Fundamental Understanding and Functionality of Silicon Oxycarbide

Ni Yang

Dissertation submitted to the faculty of the Virginia Polytechnic Institute and State University in partial fulfillment of the requirements for the degree of

Doctor of Philosophy
in
Materials Science and Engineering

Kathy Lu, Chair
Gary R. Pickrell
William Reynolds
Michael J. Bortner

Blacksburg, VA 24060
December 8, 2020

Keywords: Polymer-derived ceramics, silicon oxycarbide, phase evolution, high-temperature pyrolysis, thermophysical property

Fundamental Understanding and Functionality of Silicon Oxycarbide

Ni Yang

Abstract

Silicon oxycarbide (SiOC) is a unique polymer-derived ceramic (PDC) containing silicon, oxygen, and carbon atoms in the form of an amorphous network structure. The phase separation of SiOC is determined by polymeric precursors, pyrolysis temperatures, and atmosphere, which results in different compositions and microstructures. Because of its unique properties (high thermal stability, corrosion resistance, among others), SiOC has numerous applications in fields such as additive manufacturing, lithium-ion batteries, and advanced optics.

In the SiOC system, SiO_2 nanoclusters can be removed through the etching process, to create nanopores for increasing the surface area. By introducing the SiO_2-forming filler (perhydropolysilazane) into SiOC, more SiO_2 nanodomains with an average size of 1.72 nm were generated for an ultrahigh surface area of ~2100 m2/g material. Meanwhile, the distributions of domain wall thickness and pore distribution can be calculated by our modified model, to further understand the pore formation. The formation of porous SiOC ceramics with ultrahigh surface areas is greatly desired in numerous applications.

Transition metal-containing SiOC composites have more functional properties over pure SiOC and receive more attention in different areas. High-temperature resistant TiC/SiOC was successfully synthesized by pyrolysis of polysiloxane (PSO) and titanium isopropoxide at 1200-1400 °C in argon. It had the first reported conductivity of >1000 S/m for TiC/SiOC ceramics. Nickel-containing SiOC magnetoceramics with soft ferromagnetism was fabricated from a base PSO with the addition of nickel 2,4-pentanedionate. The effect of water vapor on the phase evolution of Ni/SiOC composites was studied at different pyrolysis temperatures, and the

formation of nickel silicides was suppressed by the effect of water vapor during the pyrolysis. Our investigation showed the catalysts from transition metals induced the generation of metal silicides, silicon carbide, and turbostratic carbon with the catalytic activity corresponding to Fe > Co > Ni, which agrees with the activation energy calculation. Also, the phase separation of SiOC was proved to be predominant than local carbothermal reduction. In addition to these findings, a novel approach was developed through the Gibbs free energy minimization method to predict the phase content in PDCs with transition metal additives. And this work provides useful guidance to fabricate the transition metal-containing SiOCs with the desired phase content.

Last, the state-of-the-art 4D-STEM technique, collaborated with Lawrence Berkeley National Laboratory, was applied to SiOC ceramics containing amorphous phase. The results showed that 4D-STEM is a valid approach to characterize the nanostructure of the amorphous phase as well as the crystallites. It solves the problem of analyzing SiOC materials at nanoscale due to the disordered atomic arrangement and properties.

Fundamental Understanding and Functionality of Silicon Oxycarbide

Ni Yang

General Audience Abstract

With the development of science and technology, some novel ceramics have begun to attract attention and become alternatives, such as polymer-derived ceramics (PDCs), due to more advantages over traditional ceramics. Silicon oxycarbide (SiOC) is the main part of the PDC family and possessing good combined thermophysical and mechanical properties. Highly porous SiOC ceramic has broad applications in the fields of catalyst, filters, and thermal insulation. A novel preparation to synthesize SiOC with a specific surface area above 2000 m^2/g was investigated. Adding transition metals into the SiOC system can enlarge its application potentials to some extent. The bright spot of nickel-containing SiOC (Ni/SiOC) composites is in the magnetic area. Ni/SiOC composites show soft ferromagnetism and can be used as magnetic sensors, transformers, and so on. In this dissertation, the effect of water vapor on the phase evolution of Ni/SiOC was illustrated. The fabrication of high-temperature-resistant Ti/SiOC composite with large than 1000 S/m conductivity was studied. To further uncover the influence of transition metals on SiOC ceramics, the effects of transition metals on the phase and microstructure evolution of polysiloxane-derived SiOC ceramics were deeply demonstrated. A novel method was even developed to predict the phase content in SiOC ceramic with different transition metals. By working with Lawrence Berkeley National Laboratory, the nanoscale structures of SiOC ceramic was studied using state-of-the-art 4D-STEM. The findings of this dissertation shed light on more potential applications for SiOC ceramics in the future.

Dedication

To my mom and dad, Xiaoduo Wang and Huaxiang Yang

To my fiancé, Anyang Hu

Acknowledgment

First of all, I would like to express the depth of my gratitude to my advisor Prof. Kathy Lu for her valuable guidance and patient support throughout my studies at Virginia Tech. I truly appreciate all of the opportunities I was given to further my research. You let me learn how to think out a meaningful research project independently and step through the project by planned outline. This research method has been had a significant influence on my academic career and driven me to a higher level, although it has been difficult and at times a painful process. You are one of the most diligent and hard-working professors I have ever met, and your perpetual enthusiasm for research is worthy for me to learn from. All I could say is thank you!

My smile and honestly thank also flow to all my other committee members, Professors William T. Reynolds, Gary R. Pickrell, and Michael J. Bortner. The *Mathematica* course that Dr. Reynolds taught has been extremely useful for me, and the Gibbs energy minimization method in Chapter 6 was developed on Mathematica software. Also, thanks to your decision to re-opening NCFL before the deadline for my revised manuscript submission to *Corrosion Science*. The reopening two days before the deadline allowed me to complete the reviewer's requirements on SEM images and was finally accepted. I am grateful to my committee members, Prof. Gary R. Pickrell and Prof. Michael J. Bortner that I was lucky to work with, for their constant support and valuable insights and suggestions on my work. Sometimes your suggestions are limited due to the different research directions, but I know that you want to do your best to help me throughout my Ph.D. work.

I am thankful to Dr. Colin Ophus, Dr. Benjamin H. Savitzky, Dr. Mary Scott, and Dr. Karen Bustillo from Lawrence Berkeley National Laboratory for collaboration on the 4D-STEM project. Thanks to Dr. Mary Scott and Dr. Karen Bustillo on 4D-STEM data collection and useful suggestions. Thanks to Dr. Colin Ophus and Dr. Benjamin H. Savitzky for data analysis by their own developed python codes. Your all developed 4D-STEM technique is so fantastic!

I would like to express my special appreciation to professor Wenjun (Rebecca) Cai, and her graduate students, Wenbo Wang and Jia Chen. Thanks for their productive collaboration and

helpful discussions on corrosion and tribocorrosion mitigation for our perhydropolysilazane-derived coatings project. Without your help, the result cannot be published in *Corrosion Science*.

I would also like to thank Dr. Jiefang li and her graduate student Min Gao, for providing magnetic property measurement by the vibrating-sample magnetometer (VSM) in their lab. I am thankful to both of you for your valuable comments and discussion on my analysis of VSM results collected.

The financial support from National Science Foundation (NSF) under grant number CMMI-1634325 is greatly appreciated. The internship at Lawrence Berkeley National Laboratory was supported by non-academic research internships for graduate students (INTERN) CMMI-1634325.

I hope to continue my sincere thanks to all my former and present friends in our group: Dr. Yi Je Cho, Dr. Sanjay Kumar, Dr. Kaustubh Bawane, Dr. Jan Tomastik, Dr. Michelle Gervasio, Dr. Ruixin Ma, Dr. Lixia Wang, Donald Erb, Bob Cheng, Advaith Rau, Jiaqi Zheng, Katie Flint, Yifeng Lin, and Rezawana Islam for their constant and patient support. It gave me the most memorable experience at Virginia Tech.

My gratitude also hopes to convey to all my professors and staff members in the MSE department and NCFL and especially Kim Grandstaff, Amy Hill, Cindy Perdue, Dr. Weinan Leng, Stephen McCartney, Ya-Peng Yu, Hesham Elmkharram, Prof. Thomas Staley, and Prof. Carlos Suchicital for their generous help.

To my dearest family, my father-Huaxiang Yang, and my mother-Xiaoduo Wang. I am excited that I am proud to be the first college student in our family. Twenty years ago, you once said that you hope that one day your daughter can get a doctorate overseas. At this moment I just want to say, this day it is here. I have only one wish in my life, that is, I hope you both will always be happy and healthy, and that is all.

Last but not least, my overwhelming love run to my beloved and cute fiancé, Anyang Hu, the most handsome, supportive, and patient person ever! The best luck in my life is I met you in September 2012 when we were freshmen. You accompanied me all the way from Hubei University, to the University of Florida, and to Virginia Tech now. Without your continuous support and encouragement, I cannot hold on till now. Half of my degree belongs to you (so you will have $Ph.D^{1.5}$ in your life). Sweet words are not enough here.

Attribution

A few colleagues assisted in different stages of my dissertation related to sample preparation, characterization. and writing/editing the manuscripts. A summary of their contributions is as follows:

Chapter 2: I performed all the experiments and characterization in this manuscript. I also wrote the manuscript and served as lead author. Prof. Kathy Lu served as the corresponding author and was involved in the editing of the manuscript.

Chapter 3: Dr. Weinan Leng (NCFL Instrument Specialist, Virginia Tech, USA) conducted the Raman spectroscopy/X-ray photoelectron spectroscopy measurements on the samples of SiOC and SiOC/M (M=Co, Ni, or Fe) pyrolyzed at 900-1300 °C. I performed all the experiments and the remaining characterization in this manuscript. I also wrote the manuscript and served as lead author. Prof. Kathy Lu served as the corresponding author and was involved in the editing of the manuscript.

Chapter 4: Dr. Min Gao (now, a researcher in Fuzhou University, China) performed the measurement related to magnetic properties of different SiOC/Ni samples pyrolyzed at 1100 °C, by using a vibrating sample magnetometer (VSM). Dr. Jiefang Li (research professor, Virginia Tech, USA) and Dr. Min Gao both gave some meaningful suggestions on the data analysis in section 4.4.5. Dr. Weinan Leng conducted the Raman spectroscopic measurement. I performed all the experiments and the remaining characterization in this manuscript. I also wrote the manuscript and served as lead author. Prof. Kathy Lu served as the corresponding author and was involved in the editing of the manuscript.

Chapter 5: Dr. Weinan Leng conducted the Raman spectroscopy/X-ray photoelectron spectroscopy measurements on the samples of SiOC-Ti-0.20 pyrolyzed at 1200-1400 °C. Dr. Christopher Winkler (now, TEM lab manager at NCSU, USA) performed the in-situ TEM characterization of SiOC/Ti sample pyrolyzed at 1300 °C. I performed all the experiments and the remaining characterization in this manuscript. I also wrote the manuscript and served as lead author. Prof. Kathy Lu served as the corresponding author and was involved in the editing of the

manuscript. I performed all the experiments and the remaining characterization in this manuscript. I also wrote the manuscript and served as lead author. Prof. Kathy Lu served as the corresponding author and was involved in the editing of the manuscript.

Chapter 6: I performed all the experiments and characterization in this manuscript. I also wrote the manuscript and served as lead author. Prof. Kathy Lu served as the corresponding author and was involved in the editing of the manuscript.

Chapter 7: Dr. Karen Bustillo (Principal Scientific Engineering Associate, NCEM, USA) performed the in-situ 4D-STEM characterization. Dr. Colin Ophus (Staff Scientist, NCEM, USA) and Dr. Benjamin H. Savitzky (post-doc, NCEM, USA) both helped to analyze the data based on the py4DSTEM python package. I performed all the experiments and the remaining characterization in this manuscript. I also wrote the manuscript and served as lead author. Prof. Kathy Lu served as the corresponding author and was involved in the editing of the manuscript.

Table of Contents

List of Figures

List of Tables

Chapter 1

Introduction

Ceramic are solid compounds comprising metallic and nonmetallic elements, such as oxides, nitrides, and carbides. The interatomic bonds of most ceramic are either entire ionic or partially ionic along with some covalent bonds [1]. The word ceramic comes from ancient Greek κεραμικός — keramikós, is an area of Athens, Greece, located to the northwest of the Acropolis, which was the potters' quarter of the city [2]. The earliest ceramics made by humans were discovered in southern China, with a history dating back to 20,000 years ago [3], which means that ancient people had mastered the practice of firing ceramics from clay at that time. Fig. 1.1 shows the fragments of ancient pottery found in Xianrendong Cave, making them the oldest known pottery in the world, even older than found in East Asia and elsewhere.

Fig. 1.1. One of the oldest pottery fragments found in Xianrendong Cave, Jiangxi Province in China [3] (Reprinted with permission. Copyright 2012, American Association for the Advancement of Science).

Starting from the 20th century, new generations of ceramic materials have been developed for use in much broader applications. A significant process has been made to develop new routes [4] for the production of novel multifunctional ceramic materials with tailored microstructures, and

they have carried huge implications on our daily lives, include electronics, aerospace, and some other industries areas.

1.1. Background and history

1.1.1. A brief review of polymer-derived ceramics (PDCs)

Polymer-derived ceramics, often abbreviated as PDCs, is a term for novel multifunctional ceramic materials formed by the pyrolysis of polymer precursors with tailored chemical composition and micro- and/or nanoscale structure controlled by crosslinking and pyrolysis processes under an inert atmosphere [5]. As early as in the 1960s, researchers-Chantrell and Ainger [6, 7] have first proposed that the non-oxide ceramic was synthesized directly from polymeric precursors. An increasing variety of ceramic materials [8-11] have been developed from organosilicon compounds, such as polysiloxane, polysilazanes, and polycarbosilanes, over the next 10 years. More than 822,000 papers resulting from a scholar search with the keyword “PDCs” have been published from 1961 up to now, demonstrating the importance of the PDCs field has been recognized in the field of material science.

It is worth mentioning that the most significant progress in the PDCs research was achieved by Yajima (1975) [12]. Based on the previous work from Fritz (1956) [13], he was the first person who synthesized the continuous silicon carbide (SiC) fiber with a high value of tensile strength ~ 350 kg/mm^2, by the means of the pyrolysis of dodecamethylcyclohexasilane polymer. To promote SiC fibers' industrialization progress, a new method was developed of synthesizing the SiC fiber from polycarbosilanes by Yajima in 1978 [14]. The study, published in Nature, has been described as a "milestone" moment that could facilitate mass production of continuous silicon carbide fiber via PDCs routes.

In the further work up to now, a variety of precursors have been applied in the PDCs field during the developments of the novel preparation route to polymeric polymers under the controlled conditions. The chemical structure of the polymeric precursor affects not only the composition but also the phases evolution as well as the microstructure of the PDCs. Thus, the chemical composition and micro- and/or nanoscale structure of PDCs can be modified through the molecular design of the preceramic polymers, which is a suitable material for the production of PDC.

Organosilicon-based polymers are one of the most promising and popular ones. Fig. 1.2 shows some common organosilicon polymers, such as polysiloxanes, polycarbosiloxanes, polyborosilanes, polysilazanes, and so on. By varying the organic substituents, the chemical structure can be directly changed, and various classes of Si-based polymers can be obtained. In order to be effective during the pyrolysis process, an idealized silicon-based precursor should consider the following aspects: 1) relatively high molecular weight and particular polymeric structure (e.g. cages) to decrease the volatilization of fragments from the matrix; 2) functional groups can be crosslinked for the shaping process.

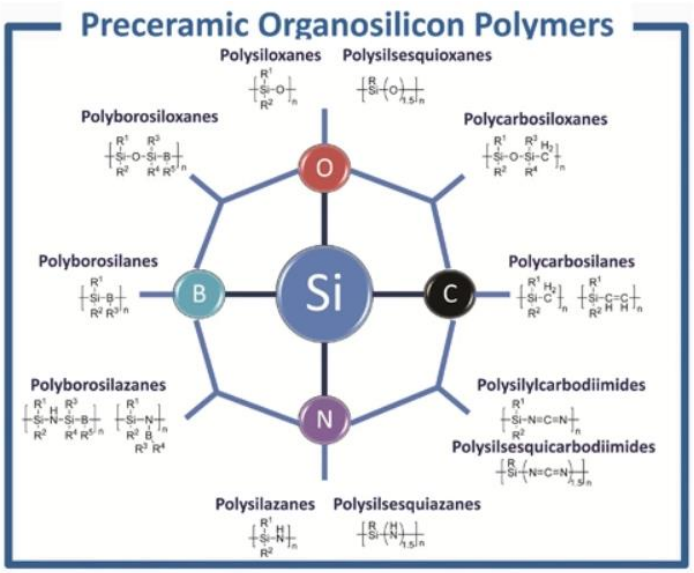

Fig. 1.2. The classes of silicon-based precursors [5] (Reprinted with permission. Copyright 2010, Wiley).

In the field of PDCs, the classes can be divided into two categories: the binary, and ternary or higher-order systems. The binary systems, for example, are silicon carbide, silicon nitride, boron nitride, and so on. The ternary systems are silicon oxycarbide, silicon oxynitride, boron carbonitride as well as quaternary systems silicon oxycarbonitride, silicon boroncarbonitride, and so on. The diversity of the chemical structural units makes the differences between the classes of PDCs. And the number of composition regimes depends on the classes of PDCs. The unusual

properties can be adjusted by the elements from the system. In other words, new systems can be designed by the various elements with specific multifunctional properties for specific applications. Thus, several higher-order systems of PDCs have been investigated in recent years [15-18].

PDCs reveals the unique glass-like structure of near ordered nanocrystalline character and exhibits extraordinary thermal stability for oxidation and crystallization up to 1600 °C and higher. Moreover, the thermal stability can be modified by the addition of an element to some extent. It is reported the improvement of the thermal stability for SiCN has been achieved by the modification of SiCN ceramic with boron [19]. Due to its high thermal stability, SiBCN ceramic can be applied in various applications in harsh environments. Since PDCs belong to conventional structural ceramics, the unique mechanical properties are not expected. However, the different processing routes result in the different mechanical behavior of the final ceramic. Compared to the traditional powder-sintered ceramic, the PDCs are much easier to synthesize in complex shapes during the curing process, and they can maintain an amorphous phase even at relatively high temperatures. As for the electrical property, in general, the microstructure of PDCs affects the conduction mechanisms. Thus, it enables the PDCs materials for the electric applications can be modified by changing the composition and structure of the final ceramic. However, the disadvantage is that the results from different labs are not comparable due to the highly processing-sensitive character. Incorporating metallic elements into the polymeric precursor opens a new world for PDCs to have potential applications in the magnetic field. In recent years, organometallic polymers have become the most attractive precursors for magnetic ceramic. It is worth to mention that the ferromagnetic material can be transformed into a superparamagnetic one when the ferromagnetic particles are less than their Weiss domains. Thus, controlling the growth of magnetic crystallites is a key issue. Because of these properties, PDCs have been systematically studied concerning exploring the development of novel materials and their potential use.

1.1.2. Fillers/PDCs development

Polymer-derived ceramics, especially for the SiOC system, has been successfully used for nearly 60 years based on producing advanced ceramics. One of their advantages is to create a variable-shape ceramic with the tailored chemical at lower temperatures than traditional ceramics. However, when PDCs were invented, one obvious disadvantage was the poor control of porosity

and shrinkage during the ceramization process [5, 20]. This is because of the decomposition and volatilization of the small organic groups at a higher temperature (600-1000 °C) [11]. The pyrolysis gas can lead to the formation of indisciplinable pores and, in severe cases, the production of cracks [20]. It makes it difficult to use the PDCs method to synthesize a dense ceramic. The introduction of fillers into the polymeric precursors has been a valid method enabling the synthesis of dense bulk ceramic to eliminate the defects (e.g. porosity, shrinkage, cracks…) during the period of polymer-to-ceramic, as shown in Fig. 1.3. Fillers can be inert, which means they can not react with precursors and conditions. Some fillers can be active because they can react with the precursor products during the ceramization process. Fillers can serve multiple purposes and effects. Greil is the pioneer of this method [20-23]. He proposed that the addition of inert or active fillers can both has a significant role in the preparation of dense and crack-free PDCs, based on a single polymer-to-ceramic step. As mentioned, inert fillers will not react with the ceramic residues at the heating atmosphere, and they can dilute the precursors to a certain extent, which can reduce the generation of pyrolysis gas, as well as volume shrinkage and cracks. As for the role of active fillers in his work, it can react with the ceramic residues to form metallic carbides, nitrides, or silicides to have an impact on the volume shrinkage due to the relatively large volume expansion from the metal-to-ceramic transformation. Thus, the fabrication of near-net-shape and crack-free ceramic becomes a reality.

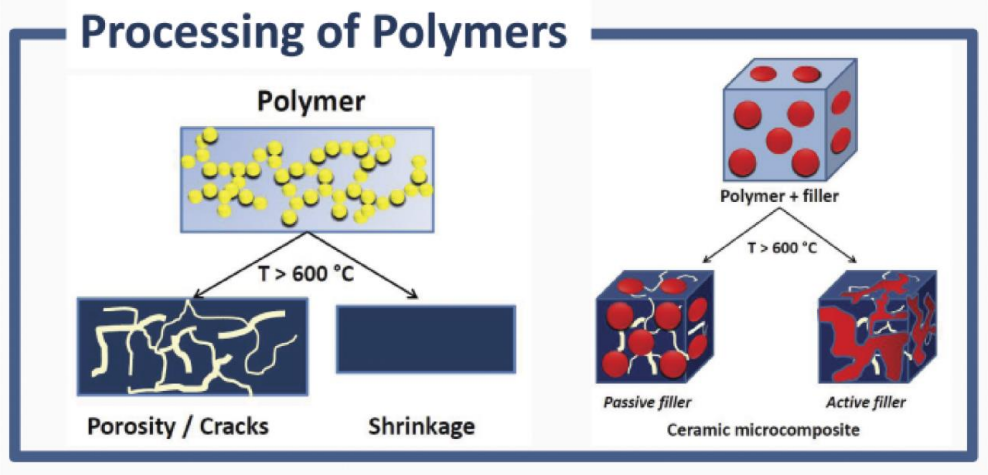

Fig. 1.3. Drawbacks of PDCs (left) and preceramic polymers containing fillers (right) [5] (Reprinted from ref. 5 with permission. Copyright 2010, The American Ceramic Society).

With the development of the times, the existing functions of ceramics can no longer meet people's needs and researchers began to dig out more versatility from ceramics. Fillers of various categories (polymer, metal…) and different dimensions (micro/meso/macro-sized powder, tubes, fibers…) play an important role in the development of multifunctionality for PDCs. For example, the potential for electrical, magnetic, and catalytic properties can be adjusted by the addition of metallic fillers [24-26]. Extensive work [27-31] has been conducted on the effects of pyrolysis temperature, microstructure, and free carbon content on the electrical properties of PDCs. It has been reported that the semiconductor is at a lower temperature due to local electron tunneling (tunneling state), while the percolation network of precipitated turbine-coated carbon provides electron conduction at a higher temperature (infiltration state) [28]. Therefore, the kinetics of carbon deposition and subsequent growth is believed to control the electrical behavior of the resultant materials when heated [28, 31]. Metallic fillers, which can react with the free carbon in the precursors to form the metallic carbides phase. It can affect the carbon content distribution in the ceramic and additionally provides new functionalities in electrical and mechanical applications. PDCs have performed the aspects of high thermal stability and chemical durability [5, 11, 32], which can be a potential candidate to be catalytic material including catalytic active component and open porosity. Two different methods can be applied for the addition of metal particles into the PDCs matrix. One is adding the pure metallic powder, or carbides, or oxides, or nitrides to the polymeric precursors at the beginning of crosslinking and then pyrolyze at the furnace in certain conditions; another is chemically grafting the metal compound into the polymer chains of precursors before the pyrolysis into the resultant ceramic.

Besides the metallic and intermetallic fillers, graphite powder [33] can also be an effective filler to enhance the electrical and mechanical properties of PDCs. Silicon carbide ceramic was synthesized from a carbon black-containing polysiloxane by the carbothermal reduction (see equation 1.1):

$$SiOC + C \rightarrow SiC + CO \uparrow \quad (1.1)$$

during the sintering. The extensive formation of the SiC phase results in high strength porous SiC ceramics. The use of an inert atmosphere leads to the generation of metal silicides, carbides, or

nitrides due to the reduction reaction with the carbon [5]. Processing in the air is more likely to oxidize the metallic components to form oxide ceramic.

1.1.3. Applications of PDCs-based materials

The use of PDCs has penetrated various fields in the past 30 years, because of their advantages over traditional ceramics due to the lower processing temperatures and the flexible precursors processing method [34, 35]. Polymer-derived technique has already been used for the synthesis of ceramic matrix composites (CMC) [36-39], bulk materials [35, 40, 41], fibers [42-44], electronics [45, 46], membranes [47, 48], and coatings [49, 50]. The versatile functionalities of PDCs upgrade the performance of the current market, and the transformation of polymer to ceramic enables substantial technological advances in the ceramic industries. Presently, plenty of companies with PDCs as the core technology have emerged one after another, such as Starfire Systems, Inc., Accuratus Corporation, Ants Ceramics Pvt Ltd., Japan Fine Ceramics Co., Ltd., Dongguan Mingrui Ceramics Technology Co., Ltd., and so on. These breakthroughs and industrialization with respect of PDCs have an extremely significant impact on further development in ceramic world.

Polymer-derived ceramic coatings are outstanding coating materials that the composition and microstructure of the coatings can be adjusted by tailoring the chemical compositions of the Si-containing precursors [51]. Also, the polymer-derived method enables a simpler synthesis when comparing to other complicated and costly techniques, such as chemical vapor deposition [52, 53] and physical vapor deposition [54-56]. The addition of fillers can extend the application of coatings based on silicon polymers. A.Schütz et al. [57] introduced the work about the introduction of glass filler particles into polysilazane-derived coatings, which are excellent material for protecting steel from abrasive wear in the harsh environment. The different types of fillers and their effects on the PDCs coatings are illustrated in Fig. 1.4. The properties of the novel coating systems based on the polymer-derived route is depending on the fillers chosen. Furthermore, the dispersion ability of filler particles in the matrix need to be enhanced to decrease the agglomeration in the suspension.

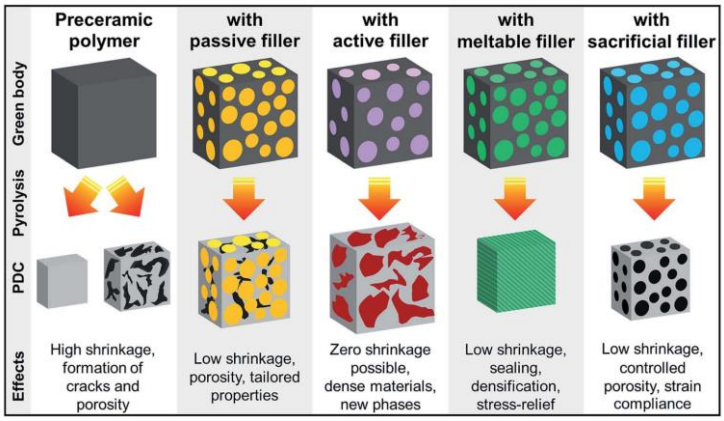

Fig. 1.4. Types of fillers and their effects in the precursor-based coating systems [51] (Reprinted from ref. 51 with permission. Copyright 2019, Royal Society of Chemistry).

Recently, polymer-derived membranes attract increasing attention in the application of gas separation [47, 58, 59], especially for the porous silicon oxycarbide (SiOC) ceramic membranes (PSCM). Microporous ceramic membranes, which have molecular sieve-like properties, can be synthesized by the polymer pyrolysis method. It has an obvious advantage of controlling the pore formations via gas evolution during the polymer to ceramic conversion, comparing to the traditional ceramic membranes. This is because the conventional ceramic powders are usually prepared by mechanical crushing, which results in a wide particle size distribution with poor filtration efficiency [60]. Several amorphous SiOC membranes were synthesized by heat treatment in an inert atmosphere of polysiloxane on zirconia support [58]. SiOC membranes prepared with a crosslinking agent in the presence of Pt catalyst showed H_2 permeance of 49.8 $m^3/(m^2hbar)$ at 300 °C, with excellent permeances in the separation of H_2/CO_2.

Polymeric precursors also provide a novel preparation method to obtain CMC, which is an advanced material that has superb strength and toughness at elevated temperatures. CMC was developed at the beginning of the 1980s for space and aeronautical applications [61]. CMC is originally intended for replacing the superalloys, but it was still put in a tight spot due to the high manufacturing costs. To build a CMC, reinforcement, interface coating, and ceramic matrix are the major three components that need to consider. For the reinforcement, the PDCs-based fibers are spun from polymeric precursors, and these fibers have a significant influence on the cost and fabrication of CMC. As for the ceramic matrix, polymer infiltration and pyrolysis (PIP) is the novel

technique to enable the manufacture of ceramic matrix inexpensively. The PIP method involves the infiltrating of a liquid polymer into a fiber preform or powder compact and pyrolyzing into ceramic material in an inert atmosphere to retain carbon [62, 63]. The advantages of PIP [11] can be concluded as the less costly fabrication, lower operating temperatures, as well as shorter cycle times.

1.2. Literature review

1.2.1. Silicon oxycarbide (SiOC)

Similar to other polymer-derived systems (silicon oxynitride, silicon carbonitride…), the compositions and microstructures of silicon oxycarbide (SiOC) can also be adjusted by the starting precursors, pyrolysis atmosphere, heat treatment, and potential fillers [64-66]. For example, the SiOC stoichiometric ratio is controlled by the different molar ratios of polymeric precursors and enabled the preparation of C-rich SiOC, Si-rich SiOC, and so on. In general, SiOC is synthesized via pyrolysis of polysiloxane, after completing the ceramization in argon at higher than 900 °C [67]. The compositions of the SiOC system (Fig. 1.5) are typically plotted onto a ternary diagram consisted of Si, O, and C. The overall composition SiO_aC_b can be firstly phase-separated into free carbon and amorphous SiO_xC_y, which is situated on the tie-line between silica and SiC parts. The chemical formula can be expressed as $SiO_{2(1-x)}C_x + yC_{free}$, with the total amount of carbon equals to x + y. After that, the SiO_xC_y phase was evolved into SiC, silica, and other intermediate SiOC intermediate compounds ($SiOC_3$, SiO_2C_2, and SiO_3C).

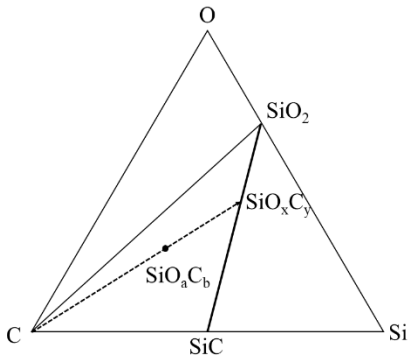

Fig. 1.5. The schematic composition diagram for the SiOC ceramic.

Structural studies of amorphous SiO_xC_y phase in SiOC system at length scales are not quite facile, since almost all spectroscopic techniques are sensitive to shorter ranges with less than 0.5 nm. Solid-state ^{29}Si nuclear magnetic resonance (NMR) technique is a useful tool to illustrate isotropic ^{29}Si chemical shifts (δ_{iso}) of SiO_4, SiO_3C, SiO_2C_2, $SiOC_3$, and SiC_4 species, at -107, -71, -34, 7, and -11 ppm, respectively [68]. The relative contents of these five species can be obtained from the corresponding area of deconvoluted peaks. However, the drawback of applying ^{29}Si NMR to SiOC is a relatively weak signal-to-noise ratio. Furthermore, the local environment of the amorphous nanostructure can be accessed by high-resolution transmission TEM mode. In Fig. 1.6, the halo rings are detected and trusted to be the nature of amorphous SiOC, which has been present in my published previous work [40]. The amorphous nature of SiOC ceramic can be displayed in the electron diffraction pattern. Spherical β-SiC crystalline precipitates with an average size of less than 5 nm are isolated dispersed in the amorphous matrix. The spacing between the lamellae for SiC is 0.25 nm. Although the information about amorphous aspects provided by HRTEM is limited, the advanced characterization-4DSTEM is applied to shed more light on detailed analysis of the amorphous structure in Chapter 7.

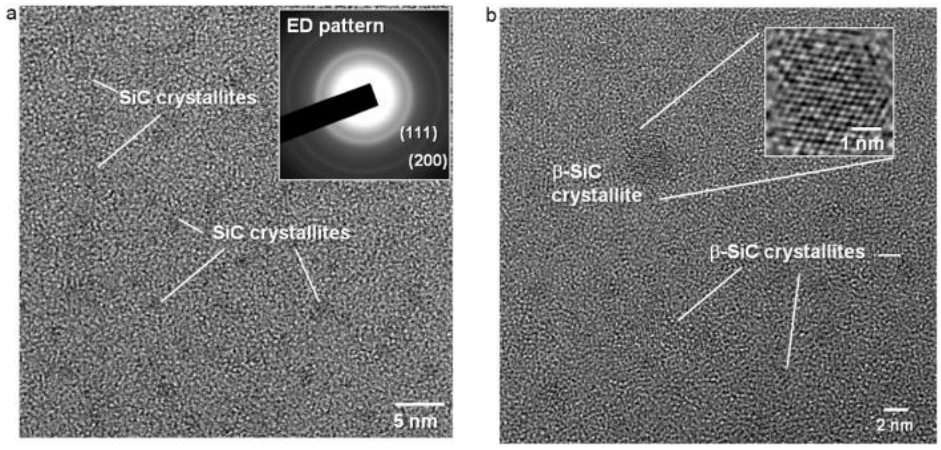

Fig. 1.6. TEM images of the distribution of SiC nanoclusters dispersed in the hot-pressed SiOC materials [69]. (Reprinted from ref. 69 with permission. Copyright 2016, Elsevier).

Another meaningful point to mention is the free carbon phase in SiOC. SiOC ceramics can be considered as the addition of carbon into silica glass, and the amount of 'free carbon' can be adjusted via the chosen precursor [70]. Many studies [71-73] on the size of regions of 'free carbon' have been done, and the HRTEM revealed the free carbon phase is consisting of turbostratic carbon with a thickness range from 4 to 10 nm. Also, Raman analysis can provide further information on the free carbon phase. The Raman spectra exhibit two main signals-D and G peaks, locating at ~1350 and 1600 cm^{-1}. To be specific, the D peak represents the sp^2 carbon atoms in carbon rings [74], and the G peak comes from the in-plane bond stretching of sp^2 carbon [75]. The lateral cluster size (L_a) of the carbon phase can be calculated using the D-to-G peak intensity ratio [39]:

$$L_a = (2.4 \times 10^{-10}) \cdot \lambda_L^4 \cdot (\frac{A_D}{A_G})^{-1} \quad (1.2)$$

λ_L is the excitation wavelength of the laser source.

1.2.2. Polymer-to-ceramic conversion in SiOC

As early as in the 1950s, Fritz et al. [76] firstly reported the preparation of SiC materials from polycarbosilane. It opened the way toward 'PDCs'. The transformation of polymeric precursors into PDCs contains a few main steps [40] that can change the compositions and properties: (a) crosslinking the monomers via catalyst (25 – 400 °C); (b) pyrolyzing the highly cross-linked preceramic materials into an infusible organic/inorganic network (400 – 1400 °C); (c) phase separation into crystallites at higher temperatures (1000 – 2000 °C). The relationship between the processing temperature and transformation is listed in Fig. 1.7.

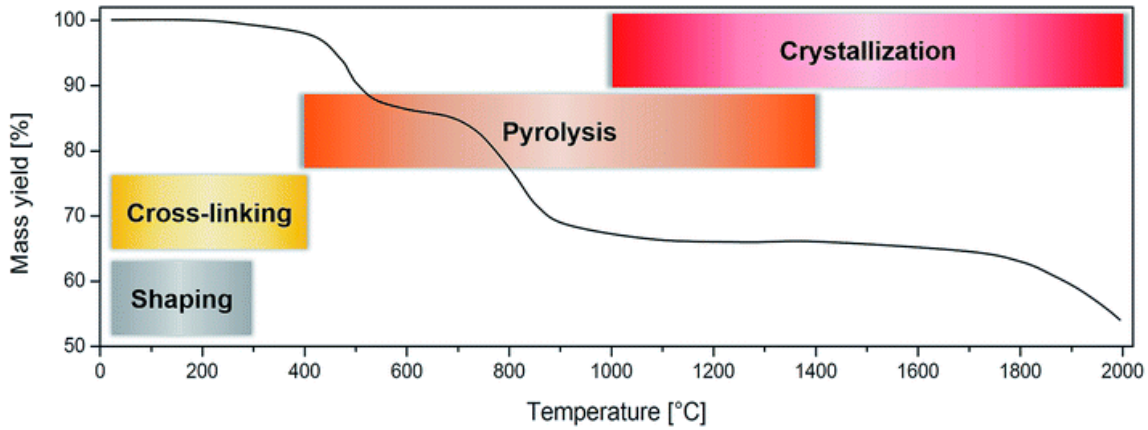

Fig. 1.7. The mass loss of polymer-derived SiOC material as the function of pyrolysis temperatures [51]. (Reprinted from ref. 51 with permission. Copyright 2019, Royal Society of Chemistry).

Crosslinking of polycarbosilanes, polysiloxanes, or polysilazanes is a very significant process for increasing the ceramic yield and retaining the bulk shape during the ceramization [77]. For the functional groups (hydroxy or alkoxy groups)-containing polysiloxanes, the corresponding crosslinking can be achieved via condensation of silanol groups to release water and generate Si-O-Si bond formation [11]. Using a suitable catalyst, such as the photoinitiator, the photo-crosslinking of polysiloxanes can even occur at room temperature [78].

After the crosslinking, the ceramization process can happen at higher temperatures for the thermolysis of the organic groups. The transformation of the organic to inorganic materials leads to the formation of an amorphous ceramic. To be specific, various [22, 79] reactions between a variety of organic groups, such as Si-O, Si-C, and Si-H, may occur and result in lower ceramic yield by the evolution of silanes. When the temperature goes higher to 600 °C, plenty of C-H, Si-O, and Si-C cleavages lead to amorphous materials containing an amorphous SiOC matrix with the free carbon dispersed. The structural investigation of the ceramization can be assessed by ^{29}Si MAS-NMR spectroscopy [80, 81] to identify the various Si sites, as discussed in section 1.2.1. The ^{13}C MAS-NMR can also provide solid evidence of the polymer-to-ceramic process concerning the C sites shown in Fig. 1.8. The Amorphous SiOC phase can be further crystallized when the pyrolysis temperature is higher than 1000 °C [39], and the compositions of final SiOC ceramic is up to the molar ratio of the O/Si [82].

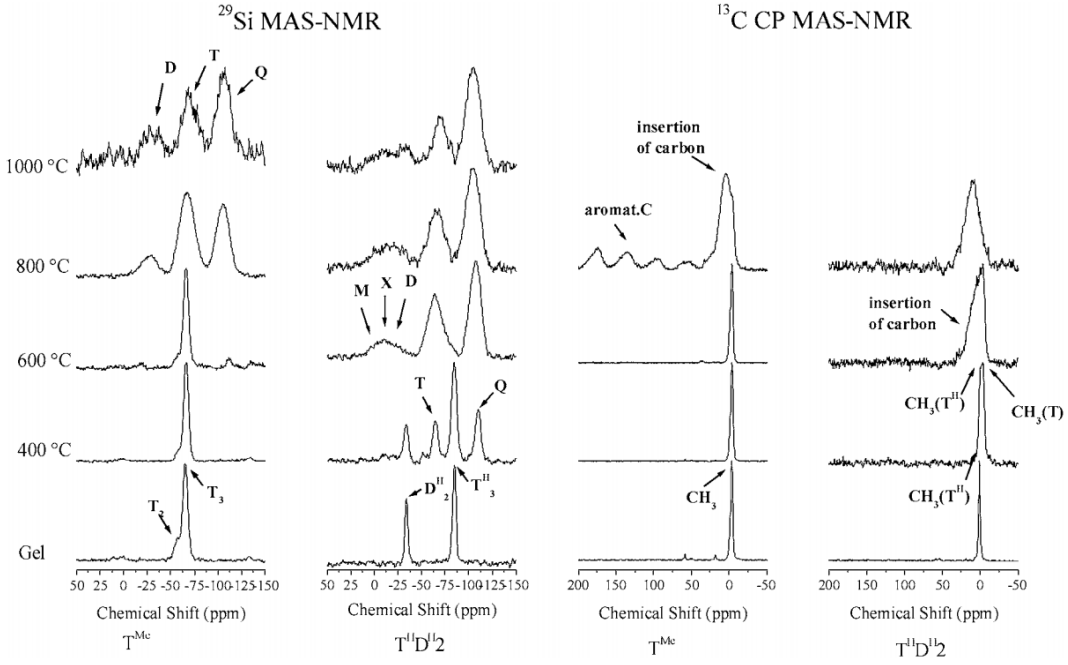

Fig. 1.8. ^{29}Si and ^{13}C CP MAS-NMR spectra of the samples calcined at different temperatures. (Contact time for CP-MAS NMR: 3 ms) [80] (Reprinted from ref. 80 with permission. Copyright 2003, Springer Nature).

Soraru et al. [83] reported some meaningful work about the pyrolysis kinetics for the polymer-to-ceramic transformation (methyltriethoxysilane → SiOC). The mechanism of the transformation reactions is determined to be first-order, consisting of the nature of solid-state. Also, the rate of the transformation is proportional to the remaining C sites, which means the composition of the final ceramic is tightly related to the geometric configuration of the cross-linked polymer. Overall, the structure of PDCs is strongly dependent on the chemical structure of the polymeric polymers, as well as the conditions for the polymer-to-ceramic transformation, such as the pyrolysis temperature, heating rate, holding time, gas atmosphere, and so on [51, 77, 84].

1.2.3. Nano/microstructure of SiOC

As mentioned in section 1.2.1, the structure and phase composition of SiOC is highly determined by their starting precursors, pyrolysis condition, heat treatment, and potential fillers. SiOC prepared between 600 – 1000 °C can be regarded as an amorphous phase and residual free carbon, after extensive Si-O and Si-C cleavage processes [11]. When the temperature is up to 1100 °C, the above amorphous part starts separating into the not well-crystallized SiO_2 nanodomains, and they will be in further growth at higher temperatures, as well as the formation of crystalline SiC phase [65].

^{29}Si MAS NMR [80] and X-ray photoelectron spectroscopy (XPS) [85] were both used to characterize the various Si structural units in the SiC_xO_{4-x} tetrahedra network. The different ^{29}Si isotropic chemical shifts [81, 86, 87] illustrates the absence of C-O bonding in the structure, which represents the existence of O-rich and C-rich SiC_xO_{4-x} units. It should be mentioned that XPS is a surface technique. However, the SiOC sample can be in a ground powder state, the tested area can be 200 µm x 200 µm in size, and each sample can be tested at multi different locations. Therefore, the XPS analysis should give reliable information- the atomic ratio of different Si sites from the bulk of the SiOC samples.

Raman spectra [39, 40, 88] can give useful information about the structural evolution of C sites, by the function-based curve fitting. A few peaks can be located in the SiOC matrix: (1) D peak from the breathing mode of sp^2-hybridized carbon; (2) G peak from the in-plane bond stretching of sp^2-hybridized carbon; and (3) T+D, 2D, and 2G bonds.

The further observation about the micro/nanostructure of SiOC can be accessed by microscopic techniques SEM and TEM [40, 78, 89]. Overall, the SEM images show the microstructure is featureless, which is corresponding to the amorphous structure of SiOC. Even the crystalline SiO_2 phase is supposed to be observed, however, the SEM cannot show the obvious feature due to the limited resolution [90]. The amorphous nature is also demonstrated in the electron diffraction pattern, by the halo rings. It is believed to be from the amorphous C and SiOC phases. Different from DEM, the crystalline SiO_2 or SiC can be clearly identified by the lattice fringe width.

The first proposed model was based on small X-ray scattering (SAXS), from Saha et al.'s work [91]. In Fig. 1.9, the SiOC system is consisting of the cellular structure of SiO_2 nanoclusters,

which is surrounded by C layers and the mixing bonds from Si, O, and C elements. The mixed SiC_xO_{4-x} layers can be altered by the fourfold coordination of Si to C and O. However, the defect of this model is the cylindrical shapes of the SiO_2 phase. The evidence from TEM images shows the spherical nature of the SiO_2, and more details related to it are described in my finished work [92] in Chapter 2.

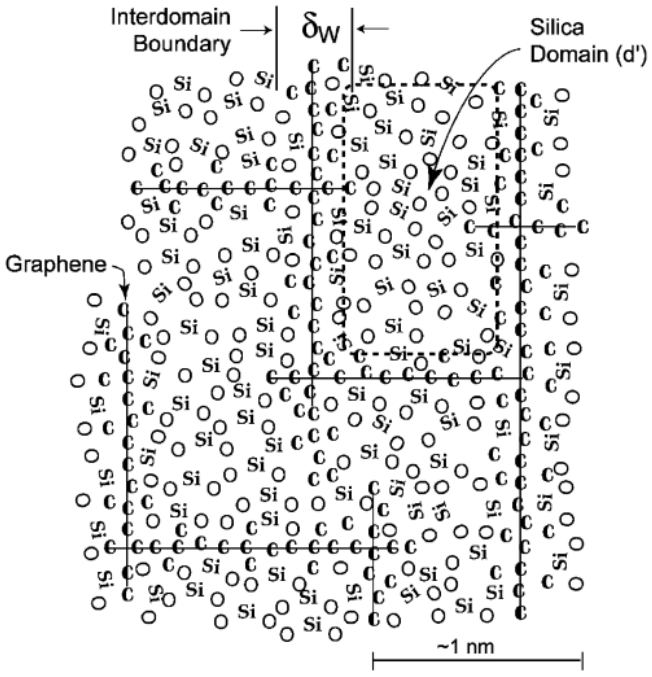

Fig. 1.9. The illustration of the structural model for the SiOC network [91] (Reprinted from ref. 91 with permission. Copyright 2006, Wiley).

1.2.4. Energetics of SiOC

Investigation of the thermodynamic aspect of SiOC materials has been important to their practical applications. However, there is not much literature to reveal the thermodynamic properties so far, due to the amorphous nature of the SiOC phase up to 1500 °C [93]. Amorphous SiOC has been reported to be thermodynamic energetically stable as an isocompositional mixture of SiO_2 (cristobalite), SiC, and C (graphite) with the pyrolysis of 1000 – 1200 °C [94, 95]. Various bonding between Si, O, and C elements and the existence of H in the interfacial areas determines the energetic stabilization of SiOC ceramics [96]. Niu et al. [97] presented thermodynamic studies to show the systematic picture of thermodynamic stability for the SiOC system. The calculated

formation enthalpies from elements for SiOC become less exothermic when increasing the temperature, and the values are less negative when decreasing the C content in the matrix. The absence of carbon within the SiOC network decreases the crystallization resistance of SiOC ceramic. Calorimetry studies demonstrated that increasing the mixed bonds and decreasing the interfacial regions caused by less free carbon species dispersed in the matrix will result in enhanced thermodynamic stability.

1.2.5. Functionalities of SiOC

SiOC can be considered as a novel and unique amorphous ceramic that carbon and oxygen share bonds with Si. The functionality of such nanostructured materials can be employed in a variety of aspects.

There is an increasing need for functional materials with high electrical conductivity and thermal stability in harsh conditions. Overall, the electrical conductivity of the Si-O-C system is highly reliant on three factors [11, 40, 90]: pyrolysis temperature, microstructure, and free carbon content. The pyrolysis temperature determines the microstructure of the SiOC system. It has been reported [98] that the amorphous SiOC phase is the main conductive part when the pyrolysis temperature is lower than 1300 °C, and the pathway formed by free carbon becomes dominating for electron conduction if the temperature goes up to 1400 °C. As shown above, electrical conductivity increases drastically with increasing the pyrolysis temperature. The effect of free carbon on the electrical properties of SiOC is controlled by the ordering of carbon atoms [30]. To be specific, the conductivity is increased with an enhanced sp^2/sp^3-ratio of the carbon. Higher pyrolysis temperature can induce the formation of a graphitic-like sp^2-carbon phase.

The optical properties of SiOC are scarcely exploited so far. In general, the SiOC glassy ceramics are black in color due to the free carbon microdomains [82, 99]. However, the fully transparent SiOC glass [100, 101] can be obtained when all the C atoms in the structure are bonded to Si by forming Si-C bonds. THE right C/Si ratio in the preceramic network is important to synthesize the suitable colorless SiOC ceramic. Luminescent SiOC [102] thin films also caught the attention of the researchers that it shows intrinsic photoluminescence in the visible range under UV lights, especially at the lower pyrolysis temperatures.

Energy materials are a topic that has received the most attention in recent years. And the investigation of the electrochemical properties for SiOC ceramic related to the lithium-ion battery has been started in the last 30 years [103, 104]. SiOC ceramic is promising anode material for lithium-ion batteries [105]. The good viscoelastic behavior of the SiOC can result in large expansion during the processes of lithiation and delithiation [106]. It has been reported [107] that the calculated capacity of SiOC anode materials is in the range of 372-1300 mA h/g. The electrochemical behavior of SiOC is tightly dependent on the chemical composition, microstructure, and pyrolysis temperature [108, 109]. For example, Lamuel et al.[108] introduced the work about the SiOC glass particles embedded graphene oxide as an electrode, and it showed an excellent charge capacity of ~588 mA h/g after a long cycle (1020^{th}) without any mechanical failure. It sheds some light on the fabrication of efficient lightweight batteries. Despite these advantages, the SiOC anodes also offer some weaknesses, like SiOC electrodes break easily after several charge/discharge cycles. Till now, still very few studies have been conducted to investigate the mechanical and fracture properties of composite SiOC-based electrodes. And there is still a long way to achieve the commercial application of SiOC electrodes in lithium ion batteries.

1.3 Motivation and objectives

Till now, there are still many problems to be solved for the versatile use of PDCs. And the major problems can be grouped into two categories. First of all, little is known about the nanoscale multiphase evolution of SiOC due to the amorphous structure of the species. Secondly, the functional use of PDCs still has technical obstacles. For example, dispersing the fillers uniformly in the precursor compounds can be challenging. To create fillers/PDCs composites with desired properties, it is necessary to control the reaction between the active fillers and residues from precursors as well as its side reaction.

1.3.1. Lack of the understanding of nanoscale multiphase evolution

Although the development of PDCs has been investigated for almost 60 years, the phase evolution from polymers to SiOC and thus the mixture of $SiOC/C/SiO_2/SiC$ phases is a very complex, and mechanistic understanding of the nucleation and phase growth process for amorphous SiO_2 and nanocrystalline SiC is severely lacking. The amorphous structure of the SiOC clusters and the similarity with the atomic number of amorphous SiO_2, so the lack of electronic contrast makes it almost impossible to perform any imaging. Nanocrystallite SiC is often buried in the amorphous SiOC and graphitic carbon matrix (Fig. 1.6). Even if nanocrystallites form, their small size (<5 nm) makes the characterization and understanding very challenging.

For such multicomponent systems where chemical compositions and pyrolysis conditions significantly affect the kinetics and thermodynamics of phase evolution, high-speed 4D STEM diffraction analysis [110, 111] will be used in my study to understand the atomistic to nanoscale evolution and multiple phase distributions. The related will be discussed in chapter 7. Developing a new 4D STEM phase and phase evolution characterization method by high-resolution electron diffraction pattern mapping and radial distribution function (RDF) analysis in order to enable phase mapping and microstructural evolution understanding of heterogeneous amorphous + nanocrystallite structure evolution for SiOC systems.

1.3.2. Limitations of functional use of PDCs

First started in 1995, Greil [21] proposed that the chemical compositions and functional properties of PDCs can be tailored by the preceramic polymer-filler mixtures. Since then more and more researchers have studied this aspect [5, 15-17, 24, 25]. Although the mixing of active fillers and preceramic precursors can be a way to expand the functional application range of SiOC ceramics, there are still many problems to be solved, especially for the fillers as transition metals. My research focuses on the following respects.

1.3.2.1. Formation of by-products in PDCs

Ni/SiOC composites are one of the most attractive candidates in the field of catalysis and magnetism [112-115]. However, in a strict sense, all of the above-mentioned Ni/SiOC ceramics

not only contain Ni crystallites but also inevitably contain nickel silicide. The previous study [114] shows the presence of Ni in the precursors induced the formation of beta-SiC, cristobalite SiO_2, graphite/turbostratic carbon, Ni, and Ni_xSi_y. The formation of nickel silicide results from the reaction of SiC and Ni at 900°C in an inert atmosphere [116, 117]. Thus, it is necessary to investigate a method to avoid the formation of Ni_xSi_y.

1.3.2.2. Issues in the preparation of PDCs

1) TiC_xO_y/SiOC [118] can possess higher values of electrical conductivity and thermal stability in harsh environments compared to pure SiOC ceramic, which makes it a lot of attention. The existence of the TiC_xO_y phase can be formed by the reaction between TiO_2 fillers and the carbon phase in the matrix during pyrolysis. To improve the dispersibility of the filler in the precursor, the Ti-containing fillers have been surface modified because the uniform dispersion of additives plays an important role in the electrical properties. However, nano-sized TiO_2 additives are still having a significant tendency of aggregation after surface modification. The uneven distribution of TiO_2 nanoparticles, especially for the high content of TiO_2 addition, is more likely to result in lower thermal stability.

2) A variety of porous SiOC materials can be generated at different heat treatments to have a high surface area and thermal stability [119, 120]. The previous study [121, 122] showed the inorganic silica powder enhances the formation of SiO_2 domains, which are selectively corroded by hydrofluoric acid (HF), leaving nanopores inside the SiOC matrix, forming an ultra-high surface area. Still, the compatible mixing of inorganic powder and polymeric precursors before crosslinking needs to be improved.

1.3.2.3. Lack of phase content prediction in PDCs

With the development of requirement variety in technology, the potential for further applications in the SiOC field is a pressing need. Metals come into the spotlight, as magnetic, catalytic, or electrical properties can be extended by the incorporation of more phases into the SiOC matrix [123, 124]. A thermodynamic model must be established to rationalize the enhanced durability of amorphous SiOC polymer-derived ceramics. However, there are no literature reports

on the thermodynamic modeling of amorphous SiOC derived from polymer precursors through a metastable phase diagram. Many questions remain about the parameters of the model Gibbs energy of the pyrolysis of multi-elements polymer derived ceramics, based on the available thermodynamic assessments.

1.3.3. Objectives

The aim of this work is to study and understand the fundamental understanding and functionality of these SiOC-based ceramics, which were synthesized on a commercially available polysiloxane ($[–Si(C_5H_6)_2O–]_3[–Si(CH_3)(H)O–]_2[–Si(CH_3)(CH=CH_2)O–]_2$. The objectives of this work are as follows:

1) Till now, the specifics of phase distribution, phase amounts, and phase evolution of amorphous SiOC materials at the nanoscale remain largely uncertain due to the limited state of current techniques. This unsolved problem can be summarized as: the local environment of the different phases, specific phase distributions, phase amounts, and the paths of phase evolutions throughout the whole structure are not clear. This dissertation will address the questions related to this field using state-of-the-art 4D-STEM equipment.

2) Adding active fillers into the SiOC system is a useful approach to enrich its application range. This dissertation will concentrate on solving the practical problems related to SiOC/fillers composites, which can be grouped into four categories: (a) microstructural evolution in Ni/SiOC magnetoceramics by preventing the reaction between SiC and Ni during the sintering; (b) the thermophysical property and electrical conductivity of TiC_xO_y/SiOC ceramics after improving the Ti fillers in the precursors; (c) ultrahigh surface area SiOC ceramics by chemically attaching Perhydropolysilazane (PHPS) filler to the precursors; and (d) the effect of transition metals of Fe, Co, and Ni on the evolution of polymer-derived Si-O-C ceramics.

3) Besides the practical problems mentioned above, there is one scientific problem that needs to solve. Quantifying polymer-derived SiOC phases, especially for transition metal-added SiOC composite is still a task of a great challenge due to the complex side reactions between metal and the SiOC matrix. In this dissertation, a thermodynamic model of Si-O-C-X (X means transition metal) multielement PDCs was created reveals the energetics related to the

quaternary systems and guides synthesizing metal-containing PDCs with desired phase contents, via a Gibbs free energy minimization method using Mathematica software.

1.4. References

1. Callister, W.D. and D.G. Rethwisch, *Materials science and engineering: an introduction*. Vol. 7. 2007: John wiley & sons New York.
2. Rice, P.M., *Pottery analysis: a sourcebook*. 2015: University of Chicago Press.
3. Wu, X., et al., *Early pottery at 20,000 years ago in Xianrendong Cave, China.* Science, 2012. **336**(6089): p. 1696-1700.
4. Kempton, W.L., *A Design Sociotechnical Making of 3D Printing*. 2017, Pan Stanford Publishing. p. 21-74.
5. Colombo, P., et al., *Polymer-derived ceramics: 40 years of research and innovation in advanced ceramics.* Journal of the American Ceramic Society, 2010. **93**(7): p. 1805-1837.
6. Chantrell, P. and P. Popper, *Inorganic polymers and ceramics.* Special Ceramics, 1965. **67**.
7. Ainger, F. and J. Herbert, *The preparation of phosphorus-nitrogen compounds as non-porous solids.* Special Ceramics, 1960: p. 168-182.
8. Verbeek, W., *Production of shaped articles of homogeneous mixtures of silicon carbide and nitride*. 1974, Google Patents.
9. Winter, G., W. Verbeek, and M. Mansmann, *Formkoerper aus homogenen mischungen von siliciumcarbid und siliciumnitrid und verfahren zu ihrer herstellung.* Ger. Offen, 1974. **2243527**.
10. Verbeek, W. and G. Winter, *Formkoerper aus siliciumcarbid und verfahren zu ihrer herstellung.* DE Patent, 1974. **2236078**: p. A1.
11. Colombo, P., *Polymer derived ceramics: from nano-structure to applications*. 2010: DEStech Publications, Inc.
12. Yajima, S., J. Hayashi, and M. Omori, *Continuous silicon carbide fiber of high tensile strength.* Chemistry Letters, 1975. **4**(9): p. 931-934.
13. Fritz, G. and B. Raabe, *Bildung siliciumorganischer verbindungen. V. Die thermische zersetzung von Si (CH3) 4 und Si (C2H5) 4.* Zeitschrift für anorganische und allgemeine Chemie, 1956. **286**(3-4): p. 149-167.

14. Yajima, S., et al., *Development of high tensile strength silicon carbide fibre using an organosilicon polymer precursor.* Nature, 1978. **273**(5663): p. 525.
15. Terauds, K., R. Raj, and P. Kroll, *Ab inito and FTIR studies of HfSiCNO processed from the polymer route.* Journal of the American Ceramic Society, 2014. **97**(3): p. 742-749.
16. Saha, A., S.R. Shah, and R. Raj, *Oxidation behavior of SiCN–ZrO2 fiber prepared from alkoxide-modified silazane.* Journal of the American Ceramic Society, 2004. **87**(8): p. 1556-1558.
17. Anand, R., B.B. Nayak, and S.K. Behera, *Coarsening kinetics of nanostructured ZrO2 in Zr-doped SiCN ceramic hybrids.* Journal of Alloys and Compounds, 2019. **811**: p. 151939.
18. Samra, H.A., et al., *Development of a new generation of amorphous hard coatings based on the Si–B–C–N–O system for applications in extreme conditions.* Surface and Coatings Technology, 2013. **223**: p. 52-67.
19. Bhandavat, R. and G. Singh, *Synthesis, characterization, and high temperature stability of Si (B) CN-coated carbon nanotubes using a boron-modified poly (ureamethylvinyl) silazane chemistry.* Journal of the American Ceramic Society, 2012. **95**(5): p. 1536-1543.
20. Greil, P., *Near net shape manufacturing of polymer derived ceramics.* Journal of the European Ceramic Society, 1998. **18**(13): p. 1905-1914.
21. Greil, P., *Active-filler-controlled pyrolysis of preceramic polymers.* Journal of the American Ceramic Society, 1995. **78**(4): p. 835-848.
22. Greil, P., *Polymer derived engineering ceramics.* Advanced engineering materials, 2000. **2**(6): p. 339-348.
23. Greil, P. and M. Seibold, *Modelling of dimensional changes during polymer-ceramic conversion for bulk component fabrication.* Journal of materials science, 1992. **27**(4): p. 1053-1060.
24. An, L., et al., *Carbon-nanotube-reinforced polymer-derived ceramic composites.* Advanced Materials, 2004. **16**(22): p. 2036-2040.
25. Cordelair, J. and P. Greil, *Electrical characterization of polymethylsiloxane/MoSi2-derived composite ceramics.* Journal of the American Ceramic Society, 2001. **84**(10): p. 2256-2259.
26. Scheffler, M., et al., *Nickel-catalyzed in situ formation of carbon nanotubes and turbostratic carbon in polymer-derived ceramics.* Materials chemistry and physics, 2004. **84**(1): p. 131-139.

27. Wang, Y., et al., *Effect of thermal initiator concentration on the electrical behavior of polymer-derived amorphous silicon carbonitrides.* Journal of the American Ceramic Society, 2008. **91**(12): p. 3971-3975.
28. Cordelair, J. and P. Greil, *Electrical conductivity measurements as a microprobe for structure transitions in polysiloxane derived Si–O–C ceramics.* Journal of the European Ceramic Society, 2000. **20**(12): p. 1947-1957.
29. Liew, L.-A., et al., *Processing and characterization of silicon carbon-nitride ceramics: application of electrical properties towards MEMS thermal actuators.* Sensors and Actuators A: Physical, 2003. **103**(1-2): p. 171-181.
30. Haluschka, C., C. Engel, and R. Riedel, *Silicon carbonitride ceramics derived from polysilazanes Part II. Investigation of electrical properties.* Journal of the European Ceramic Society, 2000. **20**(9): p. 1365-1374.
31. Wang, Y., et al., *Electron transport in polymer-derived amorphous silicon oxycarbonitride ceramics.* Journal of the American Ceramic Society, 2009. **92**(7): p. 1603-1606.
32. Monthioux, M. and O. Delverdier, *Thermal behavior of (organosilicon) polymer-derived ceramics. V: Main facts and trends.* Journal of the European Ceramic Society, 1996. **16**(7): p. 721-737.
33. Eom, J.-H., et al., *Microstructure and properties of porous silicon carbide ceramics fabricated by carbothermal reduction and subsequent sintering process.* Materials Science and Engineering: A, 2007. **464**(1-2): p. 129-134.
34. Torrey, J.D., *Polymer derived ceramic composites as environmental barrier coatings on steel*. 2006.
35. Yang, N., et al., *Nickel-containing magnetoceramics from water vapor assisted pyrolysis of polysiloxane and nickel 2, 4-pentanedionate.* Journal of the American Ceramic Society, 2020.
36. Jones, R., A. Szweda, and D. Petrak, *Polymer derived ceramic matrix composites.* Composites Part A: Applied Science and Manufacturing, 1999. **30**(4): p. 569-575.
37. King, D., et al., *Novel processing approach to polymer-derived ceramic matrix composites.* International Journal of Applied Ceramic Technology, 2018. **15**(2): p. 399-408.

38. Volkmann, E., et al., *Influence of fiber orientation and matrix processing on the tensile and creep performance of Nextel 610 reinforced polymer derived ceramic matrix composites.* Materials Science and Engineering: A, 2014. **614**: p. 171-179.
39. Yang, N. and K. Lu, *Effects of transition metals on the evolution of polymer-derived SiOC ceramics.* Carbon, 2021. **171**: p. 88-95.
40. Yang, N. and K. Lu, *Thermophysical property and electrical conductivity of titanium isopropoxide – polysiloxane derived ceramics.* Journal of the European Ceramic Society, 2019. **39**(14): p. 4029-4037.
41. Yang, N. and K. Lu, *Porous and ultrahigh surface area SiOC ceramics based on perhydropolysilazane and polysiloxane.* Microporous and Mesoporous Materials, 2020: p. 110477.
42. Miele, P., et al., *Recent developments in Polymer-Derived ceramic fibers (PDCFs): Preparation, properties and applications–A review.* Soft Materials, 2007. **4**(2-4): p. 249-286.
43. Sarkar, S., et al., *Polymer-derived ceramic composite fibers with aligned pristine multiwalled carbon nanotubes.* ACS applied materials & interfaces, 2010. **2**(4): p. 1150-1156.
44. Sarkar, S., et al., *Superhydrophobic mats of polymer-derived ceramic fibers.* Journal of the American Ceramic Society, 2008. **91**(8): p. 2751-2755.
45. Ramakrishnan, P., et al., *Silicoboron–carbonitride ceramics: A class of high-temperature, dopable electronic materials.* Applied Physics Letters, 2001. **78**(20): p. 3076-3078.
46. Ryu, H.Y., Q. Wang, and R. Raj, *Ultrahigh-temperature semiconductors made from polymer-derived ceramics.* Journal of the American ceramic society, 2010. **93**(6): p. 1668-1676.
47. Dong, B.-B., et al., *Polymer-derived porous SiOC ceramic membranes for efficient oil-water separation and membrane distillation.* Journal of Membrane Science, 2019. **579**: p. 111-119.
48. Smith, S.A., B.P. Williams, and Y.L. Joo, *Effect of polymer and ceramic morphology on the material and electrochemical properties of electrospun PAN/polymer derived ceramic composite nanofiber membranes for lithium ion battery separators.* Journal of Membrane Science, 2017. **526**: p. 315-322.

49. Torrey, J.D. and R.K. Bordia, *Processing of polymer-derived ceramic composite coatings on steel.* Journal of the American Ceramic Society, 2008. **91**(1): p. 41-45.
50. Wang, K., et al., *Corrosion resistant polymer derived ceramic composite environmental barrier coatings.* Journal of the European Ceramic Society, 2014. **34**(15): p. 3597-3606.
51. Barroso, G., et al., *Polymeric and ceramic silicon-based coatings–a review.* Journal of materials chemistry A, 2019. **7**(5): p. 1936-1963.
52. Manning, T.D., et al., *Intelligent window coatings: atmospheric pressure chemical vapor deposition of tungsten-doped vanadium dioxide.* Chemistry of Materials, 2004. **16**(4): p. 744-749.
53. Yang, R., et al., *Surface-tethered zwitterionic ultrathin antifouling coatings on reverse osmosis membranes by initiated chemical vapor deposition.* Chemistry of Materials, 2011. **23**(5): p. 1263-1272.
54. Mo, J., et al., *Comparison of tribological behaviours of AlCrN and TiAlN coatings—Deposited by physical vapor deposition.* Wear, 2007. **263**(7-12): p. 1423-1429.
55. Xu, Z., et al., *Double-ceramic-layer thermal barrier coatings of La2Zr2O7/YSZ deposited by electron beam-physical vapor deposition.* Journal of Alloys and Compounds, 2009. **473**(1-2): p. 509-515.
56. Zhang, Y., et al., *Coating of carbon nanotubes with tungsten by physical vapor deposition.* Solid state communications, 2000. **115**(1): p. 51-55.
57. Schütz, A., et al., *Characterisation of novel precursor-derived ceramic coatings with glass filler particles on steel substrates.* Surface and Coatings Technology, 2012. **207**: p. 319-327.
58. Jüttke, Y., et al., *Polymer derived ceramic membranes for gas separation.* Chem. Eng, 2013. **32**.
59. Iwamoto, Y., *Precursors-derived ceramic membranes for high-temperature separation of hydrogen.* Journal of the ceramic Society of Japan, 2007. **115**(1348): p. 947-954.
60. Lee, S. and J. Cho, *Comparison of ceramic and polymeric membranes for natural organic matter (NOM) removal.* Desalination, 2004. **160**(3): p. 223-232.
61. ç ois Christin, F., *CMC materials for space and aeronautical applications.* Ceramic Matrix Composites, 2008.

62. Li, Q., et al., *Fabrication and properties of 3-D Cf/ZrB2–ZrC–SiC composites via polymer infiltration and pyrolysis.* Ceramics International, 2013. **39**(5): p. 5937-5941.
63. Berbon, M. and M. Calabrese, *Effect of 1600° C heat treatment on C/SiC composites fabricated by polymer infiltration and pyrolysis with allylhydridopolycarbosilane.* Journal of the American Ceramic Society, 2002. **85**(7): p. 1891-1893.
64. Lu, K. and D. Erb, *Polymer derived silicon oxycarbide-based coatings.* International Materials Reviews, 2018. **63**(3): p. 139-161.
65. Erb, D. and K. Lu, *Additive and pyrolysis atmosphere effects on polysiloxane-derived porous SiOC ceramics.* Journal of the European Ceramic Society, 2017. **37**(15): p. 4547-4557.
66. Lu, K., et al., *Comparison of traditional and flash pyrolysis of different carbon content silicon oxycarbides.* Journal of the European Ceramic Society, 2019. **39**(10): p. 3035-3041.
67. Lu, K. and J. Li, *Fundamental understanding of water vapor effect on SiOC evolution during pyrolysis.* Journal of the European Ceramic Society, 2016. **36**(3): p. 411-422.
68. Widgeon, S.J., et al., *29Si and 13C Solid-State NMR Spectroscopic Study of Nanometer-Scale Structure and Mass Fractal Characteristics of Amorphous Polymer Derived Silicon Oxycarbide Ceramics.* Chemistry of Materials, 2010. **22**(23): p. 6221-6228.
69. Stabler, C., et al., *High-temperature creep behavior of a SiOC glass ceramic free of segregated carbon.* Journal of the European Ceramic Society, 2016. **36**(15): p. 3747-3753.
70. Kroll, P., *Modeling the 'free carbon' phase in amorphous silicon oxycarbide.* Journal of Non-Crystalline Solids, 2005. **351**(12): p. 1121-1126.
71. Kleebe, H.J., C. Turquat, and G.D. Sorarù, *Phase separation in an SiCO glass studied by transmission electron microscopy and electron energy-loss spectroscopy.* Journal of the American Ceramic Society, 2001. **84**(5): p. 1073-1080.
72. Kleebe, H.-J. and Y.D. Blum, *SiOC ceramic with high excess free carbon.* Journal of the European Ceramic Society, 2008. **28**(5): p. 1037-1042.
73. Kroll, P., *Searching insight into the atomistic structure of SiCO ceramics.* Journal of Materials Chemistry, 2010. **20**(46): p. 10528-10534.
74. Serrano-Esparza, I., et al., *The nature of graphene–metal bonding probed by Raman spectroscopy: the special case of cobalt.* Journal of Physics D: Applied Physics, 2016. **49**(10): p. 105301.

75. Varga, M., et al., *Diamond/carbon nanotube composites: Raman, FTIR and XPS spectroscopic studies.* Carbon, 2017. **111**: p. 54-61.
76. Fritz, G. and B. Raabe, *Die Thermische Zersetzung von Si (CH3) 4 und Si (C2H5) 4.* Z. Anorg. Allg. Chem, 1956. **286**: p. 149.
77. Ionescu, E., et al., *Polymer-derived silicon oxycarbide/hafnia ceramic nanocomposites. Part I: phase and microstructure evolution during the ceramization process.* Journal of the American Ceramic Society, 2010. **93**(6): p. 1774-1782.
78. Martínez-Crespiera, S., et al., *Pressureless synthesis of fully dense and crack-free SiOC bulk ceramics via photo-crosslinking and pyrolysis of a polysiloxane.* Journal of the European Ceramic Society, 2011. **31**(5): p. 913-919.
79. Dibandjo, P., et al., *Lithium insertion into dense and porous carbon-rich polymer-derived SiOC ceramics.* Journal of the European Ceramic Society, 2012. **32**(10): p. 2495-2503.
80. Trimmel, G., et al., *Solid state NMR and TG/MS study on the transformation of methyl groups during pyrolysis of preceramic precursors to SiOC glasses.* Journal of sol-gel science and technology, 2003. **26**(1-3): p. 279-283.
81. Mera, G., et al., *Polymer-derived SiCN and SiOC ceramics–structure and energetics at the nanoscale.* Journal of Materials Chemistry A, 2013. **1**(12): p. 3826-3836.
82. Rouxel, T., G. Massouras, and G.-D. Sorarù, *High temperature behavior of a gel-derived SiOC glass: Elasticity and viscosity.* Journal of sol-gel science and technology, 1999. **14**(1): p. 87-94.
83. Sorarù, G.D., et al., *Pyrolysis kinetics for the conversion of a polymer into an amorphous silicon oxycarbide ceramic.* Journal of the American Ceramic Society, 2002. **85**(9): p. 2181-2187.
84. Wang, X., et al., *Pyrolysis kinetics and pathway of polysiloxane conversion to an amorphous SiOC ceramic.* Journal of Thermal Analysis and Calorimetry, 2014. **115**(1): p. 55-62.
85. Yang, N. and K. Lu, *Effects of transition metals on the evolution of polymer-derived SiOC ceramics.* Carbon, 2020.
86. Stabler, C., et al., *Silicon oxycarbide glasses and glass-ceramics:"All-Rounder" materials for advanced structural and functional applications.* Journal of the American Ceramic Society, 2018. **101**(11): p. 4817-4856.

87. Sen, S. and S. Widgeon, *On the mass fractal character of Si-based structural networks in amorphous polymer derived ceramics.* Nanomaterials, 2015. **5**(1): p. 366-375.
88. Yang, N., et al., *Nickel-containing magnetoceramics from water vapor-assisted pyrolysis of polysiloxane and nickel 2, 4-pentanedionate.* Journal of the American Ceramic Society, 2020. **103**(1): p. 145-157.
89. Liu, C., et al., *High temperature structure evolution of macroporous SiOC ceramics prepared by a sol–gel method.* Ceramics International, 2015. **41**(9, Part A): p. 11091-11096.
90. Lu, K., D. Erb, and M. Liu, *Thermal stability and electrical conductivity of carbon-enriched silicon oxycarbide.* Journal of Materials Chemistry C, 2016. **4**(9): p. 1829-1837.
91. Saha, A., R. Raj, and D.L. Williamson, *A model for the nanodomains in polymer-derived SiCO.* Journal of the American Ceramic Society, 2006. **89**(7): p. 2188-2195.
92. Yang, N. and K. Lu, *Porous and ultrahigh surface area SiOC ceramics based on perhydropolysilazane and polysiloxane.* Microporous and Mesoporous Materials, 2020. **306**: p. 110477.
93. Hu, Z., L. Guo, and Q. Ma, *Effects of yttrium on structure evolution of silicon oxycarbide derived from polysiloxane.* Ceramics International, 2020.
94. Morcos, R.M., et al., *Energetics of SixOyCz polymer-derived ceramics prepared under varying conditions.* Journal of the American Ceramic Society, 2008. **91**(9): p. 2969-2974.
95. Chen, J., et al., *Thermodynamic stability of low-k amorphous SiOCH dielectric films.* Journal of the American Ceramic Society, 2016. **99**(8): p. 2752-2759.
96. Varga, T., et al., *Thermodynamically stable SixOyCz polymer-like amorphous ceramics.* Journal of the American Ceramic Society, 2007. **90**(10): p. 3213-3219.
97. Niu, M., et al., *Structure and energetics of SiOC and SiOC-modified carbon-bonded carbon fiber composites.* Journal of the American Ceramic Society, 2017. **100**(8): p. 3693-3702.
98. Engel, C., *Elektrische Eigenschaften gefüllter Pyrolyse-Keramiken im System Si-OC*. 2000: Shaker.
99. Bik, M., et al., *Protective-conducting coatings based on black glasses (SiOC) for application in solid oxide fuel cells.* International Journal of Hydrogen Energy, 2017. **42**(44): p. 27298-27307.

100. Noborisaka, M., et al., *Synthesis of transparent and hard SiOC (− H) thin films on polycarbonate substrates by PECVD method.* Surface and Coatings Technology, 2012. **206**(8-9): p. 2581-2584.
101. Dirè, S., et al., *Synthesis and characterization of the first transparent silicon oxycarbide aerogel obtained through H 2 decarbonization.* Journal of Materials Chemistry A, 2015. **3**(48): p. 24405-24413.
102. Menapace, I., et al., *Luminescence of heat-treated silicon-based polymers: promising materials for LED applications.* Journal of materials science, 2008. **43**(17): p. 5790-5796.
103. Wilson, A., et al., *Pyrolysed pitch-polysilane blends for use as anode materials in lithium ion batteries II: the effect of oxygen.* Solid State Ionics, 1997. **100**(3-4): p. 259-266.
104. Xue, J., K. Myrtle, and J. Dahn, *An Epoxy-Silane Approach to Prepare Anode Materials for Rechargeable Lithium Ion Batteries.* Journal of the Electrochemical Society, 1995. **142**(9): p. 2927.
105. Krüner, B., et al., *Silicon Oxycarbide Beads from Continuously Produced Polysilsesquioxane as Stable Anode Material for Lithium-Ion Batteries.* ACS Applied Energy Materials, 2018. **1**(6): p. 2961-2970.
106. Scarmi, A., G.D. Sorarù, and R. Raj, *The role of carbon in unexpected visco (an) elastic behavior of amorphous silicon oxycarbide above 1273 K.* Journal of non-crystalline solids, 2005. **351**(27-29): p. 2238-2243.
107. Pradeep, V., et al., *New insights in to the lithium storage mechanism in polymer derived SiOC anode materials.* Electrochimica Acta, 2014. **119**: p. 78-85.
108. David, L., et al., *Silicon oxycarbide glass-graphene composite paper electrode for long-cycle lithium-ion batteries.* Nature communications, 2016. **7**(1): p. 1-10.
109. Bhandavat, R. and G. Singh, *Stable and efficient Li-ion battery anodes prepared from polymer-derived silicon oxycarbide–carbon nanotube shell/core composites.* The Journal of Physical Chemistry C, 2013. **117**(23): p. 11899-11905.
110. Ophus, C., et al., *Recording and using 4D-STEM datasets in materials science.* Microscopy and Microanalysis, 2014. **20**(S3): p. 62-63.
111. Ophus, C., *Four-dimensional scanning transmission electron microscopy (4D-STEM): from scanning nanodiffraction to ptychography and beyond.* Microscopy and Microanalysis, 2019. **25**(3): p. 563-582.

112. Yang, N., et al., *Nickel-containing magnetoceramics from water vapor assisted pyrolysis of polysiloxane and nickel 2, 4-pentanedionate.* Journal of the American Ceramic Society, 2019.

113. Lu, P., et al., *Synthesis of Nickel Nanoparticles Supported on Nanoporous Silicon Oxycarbide (SiCO) Sheath− Core Fibers.* The Journal of Physical Chemistry C, 2010. **114**(27): p. 11776-11782.

114. Segatelli, M.G., A.T.N. Pires, and I.V.P. Yoshida, *Synthesis and structural characterization of carbon-rich SiCxOy derived from a Ni-containing hybrid polymer.* Journal of the European Ceramic Society, 2008. **28**(11): p. 2247-2257.

115. Idesaki, A. and P. Colombo, *Synthesis of a Ni-Containing Porous SiOC Material From Polyphenylmethylsiloxane by a Direct Foaming Technique.* Advanced Engineering Materials, 2012. **14**(12): p. 1116-1122.

116. Zaheer, M., et al., *Polymer derived non-oxide ceramics modified with late transition metals.* Chemical Society reviews, 2012. **41**(15): p. 5102-5116.

117. Seyferth, D., et al., *Chemical modification of preceramic polymers: Their reactions with transition metal complexes and transition metal powders.* Journal of Inorganic and Organometallic Polymers, 1992. **2**(1): p. 59-77.

118. Lu, K., D. Erb, and M. Liu, *Phase transformation, oxidation stability, and electrical conductivity of TiO 2-polysiloxane derived ceramics.* Journal of Materials Science, 2016. **51**(22): p. 10166-10177.

119. Lu, K., *Porous and high surface area silicon oxycarbide-based materials—a review.* Materials Science and Engineering: R: Reports, 2015. **97**: p. 23-49.

120. Li, J. and K. Lu, *Highly porous SiOC bulk ceramics with water vapor assisted pyrolysis.* Journal of the American Ceramic Society, 2015. **98**(8): p. 2357-2365.

121. Erb, D. and K. Lu, *Effects of SiO2-forming additive on polysiloxane derived SiOC ceramics.* Microporous and Mesoporous Materials, 2018. **266**: p. 75-82.

122. Li, J., et al., *Preparation of micro-/mesoporous SiOC bulk ceramics.* Journal of the American Ceramic Society, 2015. **98**(6): p. 1753-1761.

123. Zhang, X., et al., *Nickel silicide nanocrystal-containing magnetoceramics from the bulk pyrolysis of polysilazane and nickelocene.* Ceramics International, 2014. **40**(5): p. 6937-6947.

124. Erny, T., et al., *Microstructure Development of Oxycarbide Composites during Active-Filler-Controlled Polymer Pyrolysis.* Journal of the American Ceramic Society, 1993. **76**(1): p. 207-213.

Chapter 2

Ultrahigh surface area SiOC ceramics based on perhydro-polysilazane and polysiloxane

Ni Yang, Kathy Lu*

Department of Materials Science and Engineering, Virginia Polytechnic Institute and State University, Blacksburg, Virginia, 24061, USA

*Corresponding author: Email: klu@vt.edu

Declarations of interest: none

*This chapter has been adapted from a **published** manuscript by Ni Yang and Kathy Lu from the following reference:*

Ni Yang, and Kathy Lu. "Porous and ultrahigh surface area SiOC ceramics based on perhydropolysilazane and polysiloxane." Microporous and Mesoporous Materials 306 (2020): 110477.

Reprinted with permission from the Elsevier.

2.1. Abstract

Micro-/meso-porous ceramics with ultrahigh surface areas are highly desired in high-temperature applications. In this work, formation of porous silicon oxycarbide (SiOC) is studied based on perhydropolysilazane (PHPS) and polysiloxane (PSO) precursors. The PHPS can be chemically anchored to the PSO by hydrosilylation reaction, due to the extensive Si–H bonds from the PHPS. The presence of water vapor during pyrolysis not only accelerates the hydrolysis of the PHPS additive, but also facilitates the Si–O–Si bond formation within the SiOC. The resulting SiOC material has the highest specific surface area (SSA) of ~2000 m^2/g with an average pore size of 1.72 nm. The effects of the PHPS additive on the phase evolution and the resulting porous SiOC after hydrogen fluoride (HF) etching are investigated. 3D view of pore distributions qualitatively illustrates the PHPS effect on the SiO_2 nanocluster formation in the SiOC. The difference between the experimental and calculated SSAs is explained based on the etchability and wall thickness of the SiO_2 domains.

2.2. Introduction

Porous and high surface area ceramic materials are widely used as chemical reactors, sensors, electrodes, filters, catalyst supports, lightweight structure materials, molecular sieves, among others. The use of porous ceramics offers several excellent characteristics over other classes of porous materials [1]: good chemical stability, great specific strength and rigidity, and high thermal stability. In addition, the pore sizes and shapes of ceramics do not easily change under different stress loading conditions [2]. Proper choice of material species and techniques can make porous ceramics suitable for various harsh environments, such as under corrosive or high-temperature conditions.

In the last twenty years, preceramic polymers have been proven useful in the preparation of high-temperature materials with tailored nanostructures and complex shapes [3-5]. Due to the need for high-temperature stable and oxidation-resistant applications, much attention has been paid to silicon oxycarbide (SiOC) [6-8], in which divalent oxygen atoms are partially replaced by tetravalent carbon atoms, thus enhancing thermal properties [9]. Porous SiOC materials are an interesting system that can be prepared from pyrolysis of various polysiloxane (PSO) precursors

under different processing conditions. A wide range of unique SiOC microstructures can be adjusted to provide porous systems with a high surface area as well as thermal stability [10, 11].

Various fabrication processes [12-15], such as partial sintering, sacrificial fugitives, replica templates, and direct foaming, can create SiOC systems with a wide range of pore sizes. However, such processes can only produce micron to sub-micron sized pores; and creating ultrahigh surface area SiOCs remains a great challenge. To generate mesopores, and more desirably micropores, only controlled phase separation at the molecular level is a viable method, which can lead to pore sizes with less than 10 nm along with narrow distributions.

There have been efforts to control phase separation of polymer precursors during crosslinking. The mixing of preceramic precursors with different architectures is a developed route for one-step fabrication [14, 16-18]. When a silicone resin is crosslinked with a conventional PSO, a dense polymeric green body is formed before creating porosity by gas evolution during pyrolysis. However, the number and size of the SiO_2 nanodomains (and thus pores) in the SiOC are closely related to the preceramic precursors and processing conditions [19]. The specific surface area decreases with increasing temperature due to the sintering of transient pores. The pyrolysis temperature can also significantly influence the phase separation and separated domain sizes. At low pyrolysis temperatures (800–1100 °C), the SiOC glasses only consist of a homogeneous network of mixed Si-O-C tetrahedral and free carbon species, which can be described as a SiC_xO_y matrix within the free carbon dispersed. At >1100 °C, amorphous SiO_2 nanodomains form. The mixed Si-O-C bonds between the SiO_2 nanodomains and graphitic layers are populated by SiO_1C_3, SiO_2C_2, and SiO_3C_1 tetrahedra with different ratios. After pyrolysis, SiO_2 nanodomains can be selectively etched away by hydrofluoric acid (HF), leaving behind nano-sized pores inside the SiOC matrix to create an ultrahigh surface area.

In our work [17, 19, 20], it is noted that the presence of water vapor during pyrolysis (500-700 °C) preferentially removes the free carbon in the SiOC matrix. SiC formation is suppressed due to the less dominant presence of carbon, along with some SiO_2 being reduced to Si. Water vapor accelerates the crystallization of the SiO_2 nanodomains. After the pyrolysis, these crystallized SiO_2 nanodomains can be selectively etched away with an HF solution to form a highly porous SiOC material. Tetraethyl orthosilicate (TEOS) [19] can be used as a SiO_2-forming additive to further react with an Ar + H_2O pyrolysis atmosphere. SiO_2 domains form from the hydrolysis and condensation of the TEOS with the water vapor, as well as from the phase separation of the

SiOC matrix. After the removal of the SiO_2 domains from the HF etching, the specific surface area of the SiOC matrix increases from 1108.5 m^2/g for the base PSO to 1953.9 m^2/g for the PSO with TEOS.

Perhydropolysilazane (PHPS), an inorganic polymer composed only of Si-N, Si-H and N-H bonds [21], has been drawing more attention. PHPS can be converted to a SiO_x phase by two entirely different routes, either by reaction with water vapor or by a photolytic process with oxygen atoms [22]. In the presence of water vapor during pyrolysis, an oxidative process may occur. The hydrolysis of the massive Si-N and Si-H bonds results in the release of ammonia and hydrogen gas as well as the formation of silanol groups, before transforming into a SiO_x network in a subsequent thermally triggered condensation process. Interestingly, PHPS can be chemically attached to the PSO by hydrosilylation reaction and is potentially a desirable additive due to its cross-linking via platinum catalyzed hydrosilylation.

In this work, micro-/meso-porous SiOC ceramics are prepared through the addition of PHPS to a PSO precursor and pyrolyzed at 1100–1300 °C in an Ar + H_2O atmosphere. The SiO_2 domains can be etched away using HF to obtain high surface area SiOC bulk ceramics. The effects of the PHPS content and pyrolysis temperature on the resulting phase evolution, specific surface area, pore volume, and average pore size of the SiOC ceramics are investigated.

2.3. Experimental part

A polysiloxane (PSO) SPR-684, a member of the Polyramic® family (Starfire Systems, Inc. Schenectady, NY), was used as the polymeric precursor. A commercially available perhydropolysilazane (PHPS NN 120-20) solution in the form of 20 wt% PHPS in dibutyl ether (Clariant Advanced Materials, Sulzbach am Taunus, Germany) was used as an additive to the PSO precursor. A 2.1–2.4% platinum-divinyltetramethyldisiloxane complex in xylene (Pt catalyst, Gelest Inc. Morrisville, PA) was used as a catalyst.

First, four kinds of PHPS-containing PSO materials (Table 2.1) containing the Pt catalyst (1 wt% relative to PSO) were prepared by mixing a solution of PSO and PHPS (the molar ratio of Si in PSO: PHPS was 100:0, 100:1, 100:2, and 100:5, respectively) with magnetic stirring at 80 °C overnight in a glove box (Labstar^{pro}, MBRAUN®) until a homogeneous mixture formed. Before

being poured into aluminum foil molds, the mixtures were vacuumed for 10 min at 1500 mTorr to remove bubbles inside the solutions. A blank group without any PHPS was prepared under the same conditions. The curing of the samples was performed in an oven at 100 °C for 12 hours, and then at 150 °C for 12 hours. The sample nomenclatures were given in Table 2.1.

Table 2.1. Prepared samples and pyrolysis temperatures.

Sample	**The mole ratio of Si atoms in PSO: PHPS**	**Pyrolysis temperature (°C)**
Pure SiOC	100:0	1100/1200/1300
SiOC/PHPS-1	100:1	1100/1200/1300
SiOC/PHPS-2	100:2	1100/1200/1300
SiOC/PHPS-5	100:5	1100/1200/1300

Before pyrolysis, the crosslinked specimens (circular pieces within 10 mm of diameter and 2 mm of thickness) were placed into a zirconia crucible, covered with graphite mats, and put into a tube furnace (1730-20 Horizontal Tube Furnace, CM Furnaces Inc. Bloomfield, NJ). With a compressed argon (Industrial grade, AirGas, Inc., Radnor, PA) flow rate at 500 std cm^3/min, the samples were pyrolyzed to 1100 °C, 1200 °C, or 1300 °C at a rate of 2 °C/min with a dwelling time of 2 h at the peak temperature, before cooling to room temperature at a rate of 2 °C/min. During heating from 500°C to 700 °C, the Ar gas was bubbled through water at 60 °C, giving a gas flow with an Ar: H_2O molar ratio of approximately 5:1 [20, 23]. Etching of the pyrolyzed samples was carried out in an HF solution (20 wt% HF in water) for 72 h. After that, all the samples were rinsed with deionized water three times and vacuum dried at 120 °C.

Phase compositions of the pyrolyzed samples were investigated by using an X'Pert PRO diffractometer (PANalytical B.V.). The chemical bonding of the pyrolyzed samples was evaluated using Fourier Transform Infrared Spectroscopy (FT-IR) (Nicolet 8700 with Pike GladiATR attachment, Thermo Scientific, Waltham, MA) between 500 and 4000 cm^{-1} wavenumbers (4 cm^{-1} resolutions, 128 scans). The specific surface area, pore size distribution, and specific pore volume of the etched samples were evaluated using nitrogen adsorption at 77 K with a Quantachrome

Autosorb-1 (Quantachrome Instruments, Boynton Beach, FL). The samples were degassed before testing for 3 h at 300 °C. The specific surface areas were obtained by applying the Non-Local Density Functional Theory (NLDFT) theory to the N_2 adsorption results. The pore size distribution and specific pore volume were also derived by applying the NLDFT model and assuming cylindrical pores to the adsorption branch of the data. The 3D plots for the distribution of the SiO_2 domains were conducted using Spyder (Python 3.7).

2.4. Results and discussion

2.4.1. Polymer to ceramic conversion

For the PSO in Fig. 2.1(a), the crosslinking can be realized via a hydrosilylation catalyst, typically platinum complexes. It occurs between Si-H and $–CH=CH_2$ groups. As shown in Fig. 2.1(b), PHPS also consists of Si-H groups as well as silicon and nitrogen atoms alternating to form the basic backbone with all hydrogen substituents. The interactions between the PSO and PHPS species are illustrated in Fig. 2.1(c). Different from the physical mixing of additives and polymeric precursors [24], PHPS can be crosslinked with PSO by the hydrosilylation reaction of the Si-H bonds and the vinyl groups in the PSO. It is a fast reaction even at low temperatures (e.g., ~110 °C). The PHPS can be chemically anchored to the network of the PSO without any physical segregation. Fig. 2.1(d) indicates a structure change in the PHPS involving the reaction of − NH− with water vapor during pyrolysis [25], which can result in extensive SiO_2 formation.

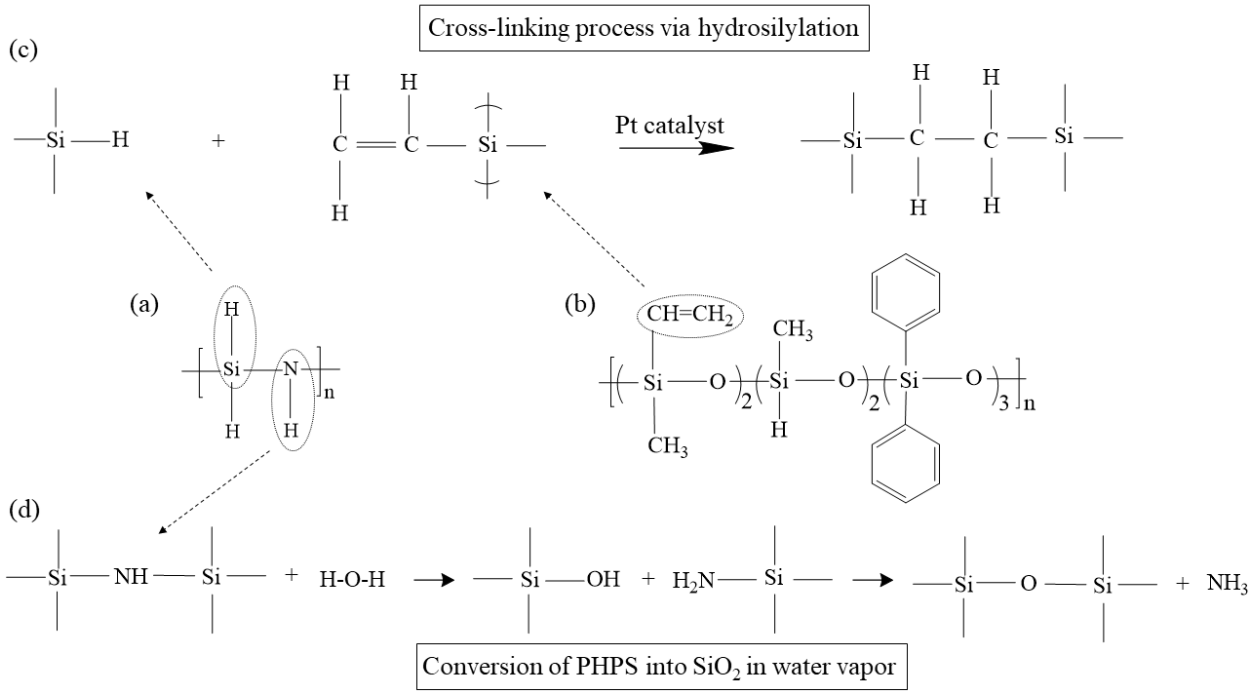

Fig. 2.1. Molecular structure of (a) perhydropolysilazane (PHPS), (b) polysiloxane (PSO) SPR-684, (c) cross-linking via platinum-catalyzed hydrosilylation, and (d) the conversion of the PHPS into SiO_2 during pyrolysis.

The pyrolysis of the cured PSO-PHPS system involves the generation and escape of NH_3, CH_4, H_2, CO, CO_2, C_2H_6, and C_2H_4 gases, as well as various redistribution reactions among the Si-C, Si-H, and Si-O bonds. In the presence of water vapor during the pyrolysis period, the polymer to ceramic transformation occurs as follows [19, 26]:

$$\text{Si-H} + \text{O-O} \rightarrow \text{Si-OH} \quad (2.1)$$

$$\text{Si-H} + \text{H-O-H} \rightarrow \text{Si-OH} + H_2 \uparrow \quad (2.2)$$

$$\text{Si-CH}_3 + \text{H-O-H} \rightarrow \text{Si-OH} + CH_4 \uparrow \quad (2.3)$$

$$\text{Si-CH}_2\text{-Si} + \text{H-O-H} \rightarrow \text{Si-OH} + \text{Si-CH}_3 \quad (2.4)$$

$$\text{Si-CH}_3 + \text{O-O} \rightarrow \text{Si-O-Si} + \text{H-O-H} + CO \uparrow + CO_2 \uparrow \quad (2.5)$$

$$\text{Si-CH}_2\text{-CH}_2\text{-Si} + \text{H-O-H} \rightarrow \text{Si-OH} + C_2H_6 \uparrow \quad (2.6)$$

$$Si\text{-}CH{=}CH_2 + H\text{-}O\text{-}H \rightarrow Si\text{-}OH + C_2H_4\uparrow \quad (2.7)$$

$$Si\text{-}C_6H_5 + H\text{-}O\text{-}H \rightarrow Si\text{-}OH + C_6H_6\uparrow \quad (2.8)$$

$$\equiv Si\text{-}NH + H\text{-}O\text{-}H \rightarrow (\equiv Si\text{-}OH + \equiv Si\text{-}NH_2) \rightarrow \equiv Si\text{-}O\text{-}Si\equiv + NH_3\uparrow \quad (2.9)$$

The oxidation and hydrolysis of the Si–H groups from PHPS in the crosslinked samples can lead to extensive Si-OH groups as shown in the above equations (2.1-2.9). Hydrogen and nitrogen are gradually released from the system, and nitrogen can be almost completely eliminated at 600 °C as reported [27]. Water vapor is not only accelerating the hydrolysis of PHPS, but also Si-O-Si bond formation from the PSO-derived SiOC matrix. The plethora of Si-OH groups can subsequently condense to generate extensive Si-O-Si bonds to form SiO_2-rich regions (Fig. 2.1(d)). Our previous study [20] also shows that water vapor preferentially removes the free carbon in the SiOC according to:

$$C_{free} + H_2O \rightarrow H_2\uparrow + CO\uparrow \quad (2.10)$$

As a result, the SiOC phase and residual free carbon form. With the less dominant presence of free carbon, SiC and crystalline carbon formation are suppressed. More importantly, water vapor promotes the crystallization of the SiO_2 nanodomains. The amount and size of the SiO_2 nanodomains can be adjusted by controlling the dwelling time and amount of water vapor during the polymer-to-ceramic conversion process.

In Fig. 2.2, the ceramic yields of the SiOC samples are displayed as a function of the PHPS content at 1100, 1200, and 1300 °C pyrolysis temperatures. For the pure SiOC ceramic, the pyrolysis temperature causes no significant change in the ceramic yield from 1100 °C to 1200 °C. From 1200 °C to 1300 °C, the ceramic yield decreases from 64.88% to 60.92% due to carbothermal reduction [17]:

$$SiO_2\ (amorphous) + C \rightarrow SiC\ (\beta) + CO\uparrow \quad (2.11)$$

It is reasonable that higher pyrolysis temperature leads to lower ceramic yield. In general, a higher percentage of PHPS addition also leads to lower ceramic yield regardless of the pyrolysis temperature. This decrease can be attributed to the hydrolysis and condensation of the Si-OH groups during the water vapor injection period, as well as the evaporation of gas species (CO, CO_2…) through equations (2.2-2.8). From 1100 °C to 1300 °C, the ceramic yield of SiOC/PHPS-

1 decreases from 65.97 % to 57.96 %. The same trend also happens for SiOC/PHPS-2 (64.47 % to 59.93 %) and SiOC/PHPS-5 (60.41 % to 55.53 %). However, the mass loss in these systems is small, suggesting that the formation of SiC is limited due to the removal of free C using water vapor in the early stage of the pyrolysis.

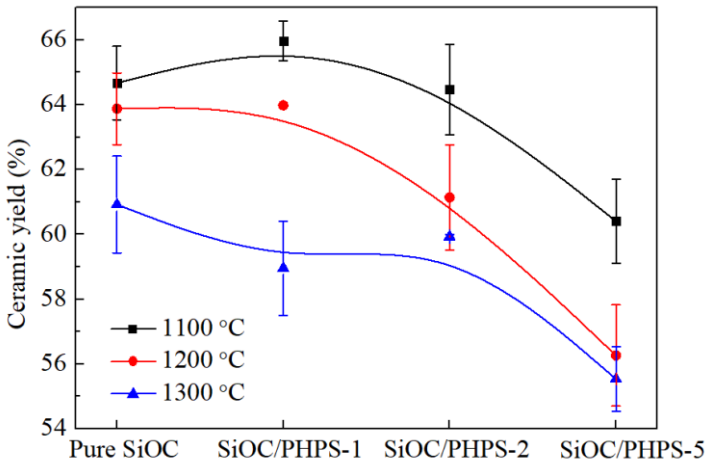

Fig. 2.2. Ceramic yield of different SiOC/PHPS samples pyrolyzed at 1100, 1200, and 1300 °C.

2.4.2. Phase evolution

Fig. 2.3 shows the FTIR spectra of the pure SiOC as well as SiOC/PHPS-1, 2, and 5 samples before the HF etching, pyrolyzed at 1200 °C. The chemical bonds in the spectra reflect the effect of the PHPS addition on the SiO_2 formation. All the pyrolyzed samples show broad peaks, except for the sharp peaks from SiOC/PHPS-5. For the pure SiOC, SiOC/PHPS-1 and 2, two broad peaks between 1000-1100 cm^{-1} and 750-850 cm^{-1} can be assigned to the vibrational bonds of Si-O [19, 28]. With further chemical addition of PHPS into the SiOC system, the peaks become sharper and are located at 804 and 1098 cm^{-1} due to the increasing amount of Si-O-Si bonds. This means that the addition of PHPS does facilitate the Si-O-Si formation in the SiOC matrix, and the amount of SiO_2 within the pyrolyzed samples increases from SiOC/PHPS-1 to 5, consistent with the mass loss changes during the HF etching (shown in Fig. 2.5).

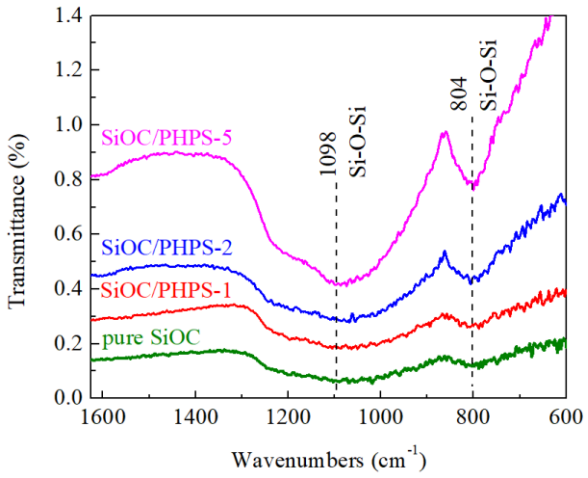

Fig. 2.3. FTIR spectra of the SiOC samples with different amounts of PHPS at 1200 °C pyrolysis temperature before the HF etching.

The effect of the PHPS addition on the phase evolution is also reflected in the XRD patterns (Fig. 2.4). All the pyrolyzed samples are amorphous. Only two broad diffraction peaks located at 43° for turbostratic carbon and 23° for amorphous SiO_2 [29] are observed. Since there are no C atoms in PHPS, the carbon content in all the samples with different amounts of PHPS should be constant. Thus the value of the intensity ratio of SiO_2 to turbostratic carbon (I_{silica}/I_{carbon}) can be represented as the level of SiO_2 formation. The value of I_{silica}/I_{carbon} increases with the PHPS addition, at 2.63, 3.03, 3.00, and 3.16 for the pure SiOC, SiOC/PHPS-1, 2, and 5, respectively. This means that the addition of PHPS accelerates the formation of Si-O-Si and nucleation of the SiO_2 nanodomains, consistent with the results in Figs. 2.2 and 2.3. A similar trend is also observed at 1200 and 1300 °C pyrolysis temperatures (Figs. 2.4(b) and (c)). All the pyrolyzed samples are amorphous in Fig. 2.4(c) without additional peaks. Even at higher pyrolysis temperatures, the samples still only show the peaks of turbostratic carbon and amorphous SiO_2. As discussed in Part 3.1, the presence of water vapor during the pyrolysis can significantly affect the subsequent phase separation of the SiOC matrix. Different from the SiOC samples pyrolyzed in pure Ar, the water vapor reacts with free carbon and certain organic species in the preceramics and generates extensive Si-OH groups to form SiO_2 nanodomains. The reduction of Si-C bonds in the matrix suppresses the precipitation of SiC at higher pyrolysis temperatures [20]. This is why there is no

significant difference between Figs. 2.18(a-c). Overall, the formation of SiO_2 is more evident for the samples with higher PHPS additions.

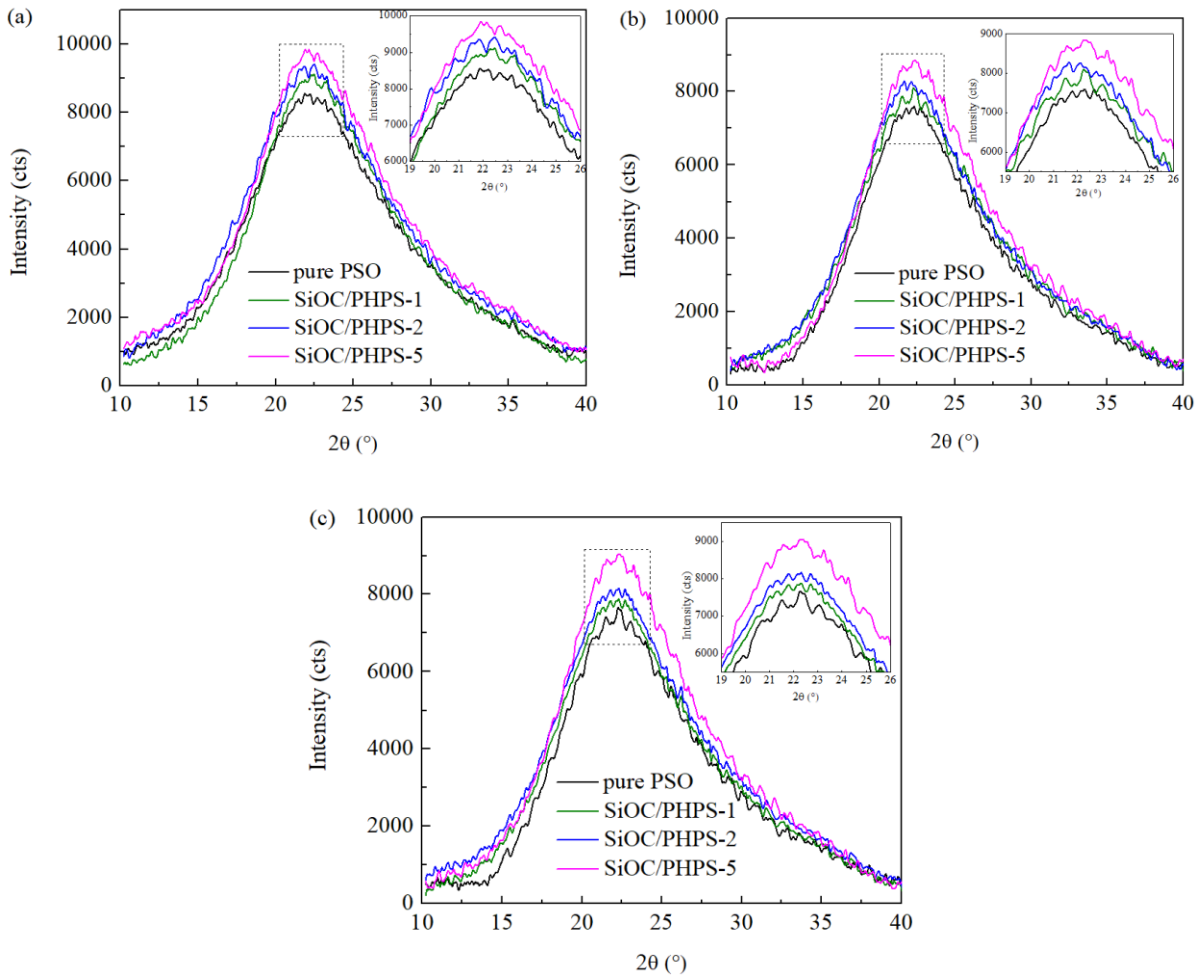

Fig. 2.4. Amorphous SiO_2 peaks of all the SiOC samples pyrolyzed at (a) 1100 °C, (b) 1200 °C, and (c) 1300 °C.

With more SiO_2 nanodomains dispersed in the SiOC matrix, highly porous microstructures can be obtained by removal of SiO_2 with HF etching:

$$SiO_2 + HF \rightarrow H_2SiF_6 + H_2O \quad (2.12)$$

Since SiOC is resistant to HF acid, presumably only the SiO_2 nanodomains can be an etched way. SiO_2 can act as a pore-forming agent for the SiOC matrix. For the pure SiOC pyrolyzed at 1100 °C, the etching mass loss is 61.9 wt% as displayed in Fig. 2.5. With the increasing addition of PHPS, the mass loss after etching slightly increases. A similar trend is also observed for the samples pyrolyzed at 1200 and 1300 °C. An addition of PHPS results in a slight increase in the mass loss after etching compared with the pure PSO in Fig. 2.5 at different pyrolysis temperatures. As a result, it is reasonable to believe that PHPS accelerates the nucleation of the SiO_2 nanodomains in the SiOC matrix. As for the effect of the pyrolysis temperature, the etching mass loss increases from 1100 °C to 1300 °C for all the samples because of the more advanced SiOC phase separation.

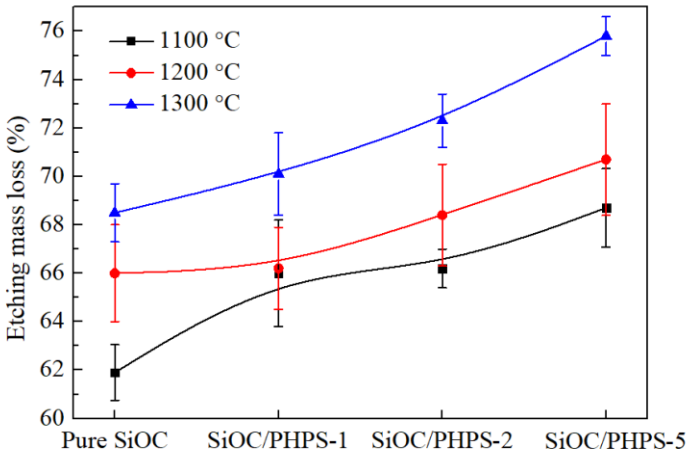

Fig. 2.5. Etching mass loss of different samples pyrolyzed at 1100, 1200, and 1300 °C.

2.4.3. Specific surface area and pore size

Fig. 2.6(a) shows the adsorption isotherms of all the samples with different PHPS contents pyrolyzed at 1200 °C after the HF etching. For all the samples, the hysteresis loop is very narrow, and the adsorption and desorption curves are almost the same. The inserted pore size distribution in Fig. 2.6(b) shows that the nanopores for the pure SiOC are in the range of 1-2 nm, whereas larger pores from ~2.3 nm to 6 nm exist in the SiOC/PHPS samples. For the pure SiOC sample, the N_2 gas adsorption volume is lowest, at 521.58 cm^3/g. For the SiOC/PHPS-1, 2, and 5 samples, the gas adsorption volumes are 832.13, 830.87, and 703.12 cm^3/g, respectively. The gas adsorption

volume decreases with the increasing addition of PHPS. The phase-separated SiO_2 leads to a maximum adsorption volume of 832.13 cm^3/g for SiOC/PHPS-1.

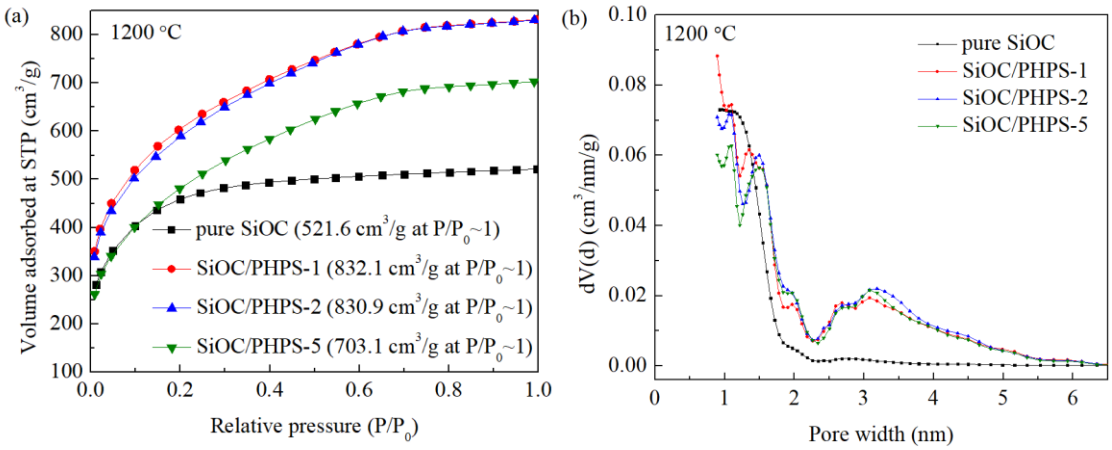

Fig. 2.6. (a) Nitrogen adsorption-desorption isotherms, (b) pore size distributions of the pure SiOC, SiOC/PHPS-1, 2, and 5 samples pyrolyzed at 1200°C after etching.

The pore size distributions of all the samples pyrolyzed at 1200 °C are displayed in Fig. 2.6(b). For the SiOC samples, the pore sizes are less than 2 nm without any pores of >2.3 nm size. With the addition of PHPS, the pore size distribution has additional high peaks at 2.3-5 nm, which is not seen for the pure SiOC sample. This indicates that the SiOC ceramics with PHPS additives consist of small (<2 nm) and large (2.3-5 nm) pores. We conjuncture that the small pores are from the SiOC phase-separated SiO_2 domains and the large ones are from the evolution of the PHPS additive.

The specific surface areas (SSA) of all the different temperature pyrolyzed samples after the HF etching are shown in Fig. 2.7, which are determined by the NLDFT theory [30]. For the pure SiOC samples, the SSA increases from 1187 to 1691 m^2/g. In comparison, the SSA of the pure SiOC pyrolyzed in pure Ar without any water vapor [24] was reported to be 44.8-630.4 m^2/g. The presence of water vapor during pyrolysis indeed accelerates the formation of SiO_2 nanodomains and then results in higher SSA. In addition, the SSA of the pure SiOC increases with the pyrolysis temperature. However, the effect of pyrolysis temperature on the SSA of the PHPS-containing

samples is more complicated. For SiOC/PHPS-1, the SSA increases from 1349.55 (1100 °C) to 2021.57 m^2/g (1200 °C), before dropping to 1803.38 m^2/g at 1300 °C. For SiOC/PHPS-2, the SSA increases from 1615.49 m^2/g to 1921.78 m^2/g, then decreases to 1765.97 m^2/g after 1300 °C pyrolysis. Overall, the SSAs of the SiOC/PHPS-1 and 2 samples increase drastically from 1100 °C to 1200 °C pyrolysis temperature and subsequently decrease from 1200 °C to 1300 °C. This can be explained based on the understanding that the continuous growth of the SiO_2 phase causes larger pore sizes and leads to a decline in the SSA. However, this explanation cannot be fitted to the SiOC/PHPS-5 sample. Different from all the other samples, the SSA of SiOC/PHPS-5 continuously decreases from 1934.21 to 1550.50 m^2/g from 1100 to 1300 °C pyrolysis temperature.

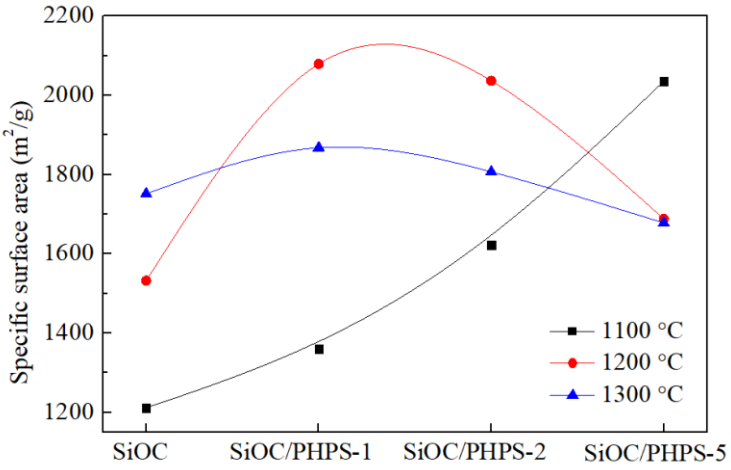

Fig. 2.7. Specific surface areas of all the samples at different pyrolysis temperatures.

At the same pyrolysis temperature, the changes in SSA depends on the amount of the PHPS additive. When the pyrolysis temperature is 1100 °C, the SSA of the samples increases with the additive content. When the additive content is highest (SiOC/PHPS-5), the SSA of the samples reaches a maximum value of 1934.21 m^2/g at 1100 °C. At 1200 and 1300 °C, the SSA increases slightly from those of the pure SiOC to SiOC/PHPS-2, and then slowly decreases from those SiOC/PHPS-2 to SiOC/PHPS-5. Again, higher pyrolysis temperature causes further phase separation of the SiOC matrix and prompts more SiO_2 nanodomain formation. If the amount of the SiO_2 phase is excessive (in the high PHPS content sample SiOC/PHPS-5), the aggregation of the

SiO_2 phase causes the SSA to decrease. This means that the PHPS additive content and the pyrolysis temperature have a convoluting effect on the SSA, depending on the specific impact on the SiO_2 nanodomain formation.

As Fig. 2.8 shows, the average pore size increases with the pyrolysis temperature and the PHPS additive amount. At 1100 °C pyrolysis temperature, the average pore size for all the samples is ~1.7 nm. With the temperature increase to 1200°C and then to 1300°C, the effect on the growth of pores becomes more obvious. The average pore size increases from ~1.7 nm to ~4 nm at 1300 °C. A possible explanation for this drastic increase in pore size for SiOC/PHPS-5 at 1300 °C is the merging of the SiO_2 domains. Higher PHPS content and pyrolysis temperature both promote the nucleation and growth of the SiO_2 phase.

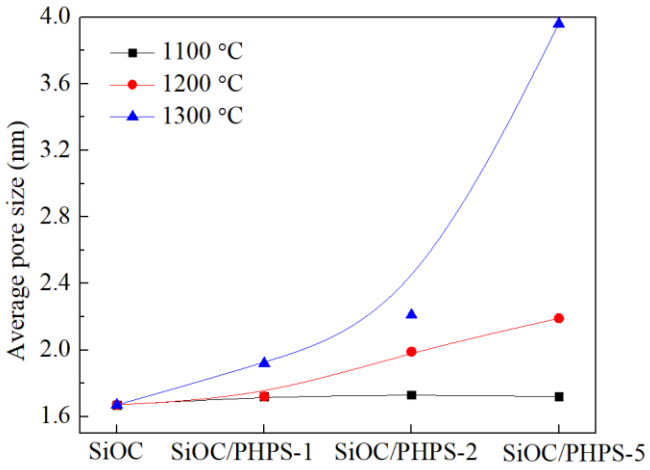

Fig. 2.8. The average pore size of all the samples at different pyrolysis temperatures.

2.4.1. Model understanding

Effects of SiO_2 nanodomains in polymer derived SiOC have been examined by small-angle X-ray scattering and small-angle neutron scattering [31-33]. The model describes a cellular structure of SiO_2 nanodomains surrounded by graphene layers and mixed bonds of Si-O-C ($SiOC_3$, SiO_2C_2, and SiO_3C). In this study, we can build on this domain model to explain the N_2-sorption results. The system can be constructed from three constituents: clusters of SiO_2 tetrahedra that form the centers of the domains, the surrounding SiC_nO_{4-n} layers, where n alters the fourfold

coordination of silicon to carbon and oxygen, and the graphene cage-like network that encases the domains.

In order to quantitatively analyze the SSA, we assume that (1) HF etching process only removes SiO_2 without the removal of carbon; (2) all the SiO_2 phases can be removed during etching; (3) the graphene layer and the mixed Si tetrahedra exist as "walls" in the etched samples; and (4) all the pores are cylindrical. The wall thickness can be calculated according to the measured pore size and pore volume. In the model [32], the radius of cylindrical pores is d_n, which can be determined from the pore size distribution in Fig. 2.6(b). The average distance between pores is s. The average volume fraction of the SiO_2 phase (V_o) is defined as:

$$V_o = \frac{\pi {d_n}^2}{(2s)^2} \tag{2.13}$$

Assuming that the total thickness of these layers and mixed bonds is δ, then the volume fraction of the 'walls' can be expressed as ($1-V_o$) [32]:

$$1 - V_o = \frac{2\pi d_n \delta}{(2s)^2} \tag{2.14}$$

Combining equations (2.13-2.14) to remove $(2s)^2$, then the wall thickness δ is

$$\delta = \frac{d_n}{2V_o} - \frac{d_n}{2} \tag{2.15}$$

V_o can be obtained from the density and specific pore volume of the N_2 adsorption measurements. In this work, the specific pore volumes and densities of the etched samples are listed in Table 2.2. The wall thickness δ, also the effective width of the interface between SiO_2 domains, varies with the amount of PHPS addition. For the pure SiOC without any additives, δ has relatively large values at an average of 0.79 nm. With the increase of the PHPS content, which means V_0 increase, δ decreases. At the low PHPS content (SiOC/PHPS-1), the SiO_2 nanodomains derived from PHPS are small enough to co-exist with the SiO_2 nanoclusters from the PSO-based SiOC phase separation. This, in turn, should produce a high SSA after etching, which is also confirmed in Fig. 2.7. Compared to the pure SiOC, SiOC/PHPS-2 and 5 samples, the average δ value of the SiOC/PHPS-1 sample is lowest at 0.26 nm. Theoretically, the thickness of the single-layer graphene is 0.345 nm. This means that the average wall between the SiO_2 domains for SiOC/PHPS-1 consists of only silicon mixed bonds without any graphene layer. Our previous

study [19] also shows that the value of SSA decreases with an increase of graphene layers, consistent with the value of SiOC/PHPS-2 (0.37 nm) and 5 samples (0.56 nm).

Table 2.2. Parameters related to the etched SiOC and SiOC/PHPS samples pyrolyzed at 1200°C.

Sample	Etched density (g/cm^3)	Specific pore volume (cm^3/g)	Average volume fraction	Average pore size (nm)	Average wall thickness (nm)
Pure SiOC	0.60	0.75	0.45	1.29	0.79
SiOC/PHPS-1	0.57	1.34	0.76	1.68	0.26
SiOC/PHPS-2	0.58	1.21	0.70	1.75	0.37
SiOC/PHPS-5	0.60	1.02	0.61	1.76	0.56

The distribution of the effective interface width between the SiO_2 domains can be obtained using equation (2.15) as shown in Fig. 2.9. The wall thickness of the pure SiOC at 1200 °C is the thickest one. With more addition of PHPS, the wall thickness distribution curve moves towards smaller values. Overall, the PHPS addition leads to pore wall thickness decrease. In order to explain this phenomenon, Fig. 2.10 displays the relation between the SiO_2 size and the domain wall thickness. Without any addition of PHPS in Fig. 2.10(a), a thicker graphene layer and a few SiC_nO_{4-n} tetrahedra separate the SiO_2 clusters. Because of the limited number of SiO_2 sites, the thickness of the domain wall (the layer between the green circle and black square) is relatively large. Since the PHPS additive creates more Si-O-Si bonds during the pyrolysis, the graphene layer and SiC_nO_{4-n} tetrahedra have to be shared among more SiO_2 sites, which results in thinner domain wall in Fig. 2.10(b). Based on equation (2.15), the wall thickness not only depends on the pore size but also on the pore volume fraction.

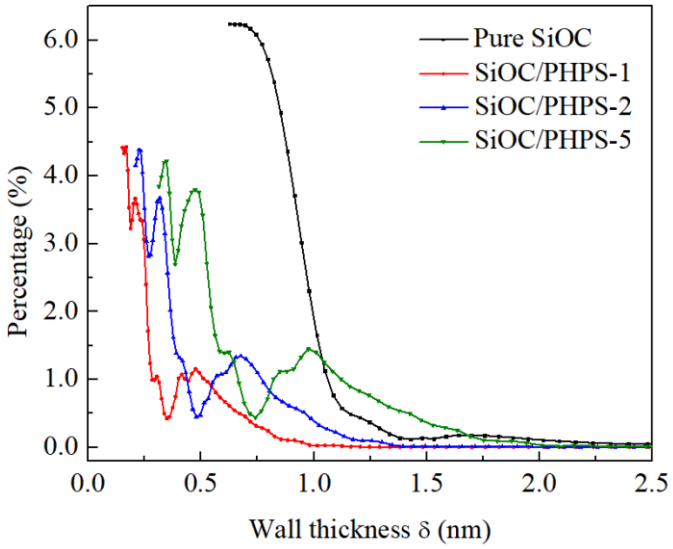

Fig. 2.9. Distribution of calculated wall thicknesses for all the etched samples pyrolyzed at 1200 °C.

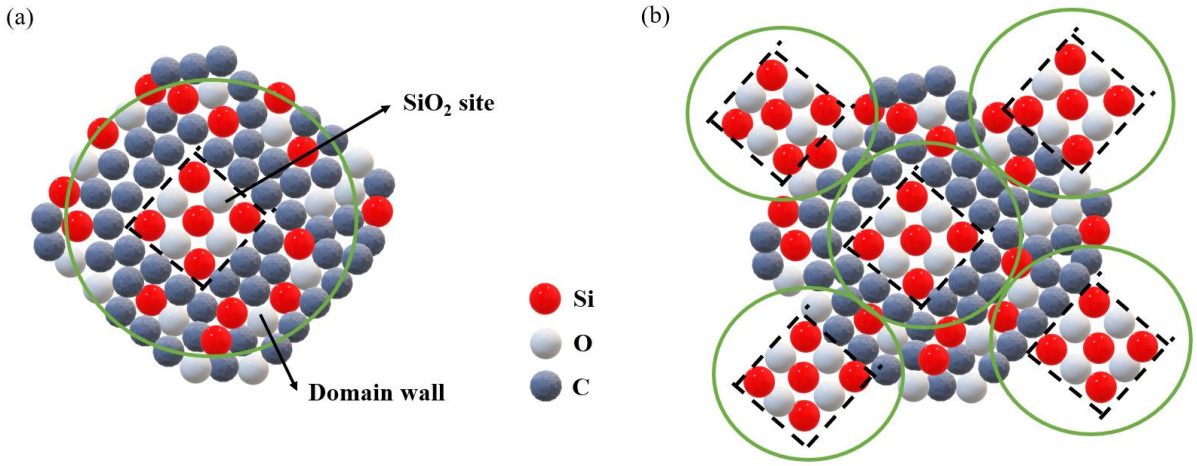

Fig. 2.10. Illustration of the etched SiOC matrix without PHPS additive (a) and with PHPS additive.

Besides Fig. 2.6(b), 3D views of SiO_2 domain distributions can also explain the effect of PHPS addition on the SSA of the etched SiOCs. Fig. 2.11 shows 3D plots of the pore distributions for the etched samples at 1200 °C. The side length of each cuboid is expressed as L and the number of SiO_2 domains n_{SiO_2} in the cuboid can be calculated based on the following equation:

$$n_{SiO_2} = \frac{L^3 \rho_b V_p \alpha}{V_{SiO_2}} \tag{2.16}$$

where ρ_b is the bulk density of the etched sample, V_{SiO_2} is the average volume for each SiO_2 tetrahedra obtained from the average pore size. α is the mole ratio of Si atoms in the PHPS: PSO precursors. V_p is the specific pore volume (cm^3/g). With more PHPS addition, n_{SiO_2} increases. For the pure SiOC, the SiO_2 nanodomains from phase separation are uniformly dispersed without any obvious aggregation, as shown in Fig. 2.11(a). Based on Fig. 2.6(b), pores larger than 2.3 nm are not evident. With an increasing amount of the PHPS additive, a greater number of SiO_2 nanoclusters are formed, along with larger sizes. The 3D simulation results show that the small pores, in the range of 1-2 nm, are more likely to aggregate after pyrolysis because of their dominance. This phenomenon is obvious in Fig. 2.11(d), which results in more connected pores to decrease the SSA. The 3D simulation also explains the results from Fig. 2.10. More SiO_2 nanoclusters are formed to decrease the wall thickness, by sharing the graphene and SiC_nO_{4-n} tetrahedra. Although a thin wall can result in a higher SSA value, the merging effect of the nanopores is more dominant in decreasing SSA. In order to create an ultrahigh SSA, small and separated SiO_2 nanoclusters should be formed during the pyrolysis by controlling a suitable amount of PHPS.

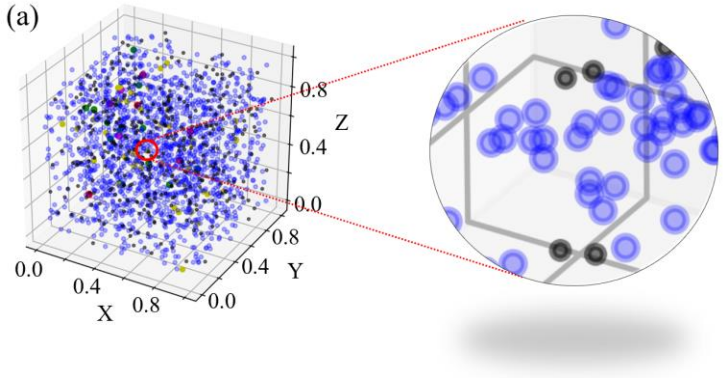

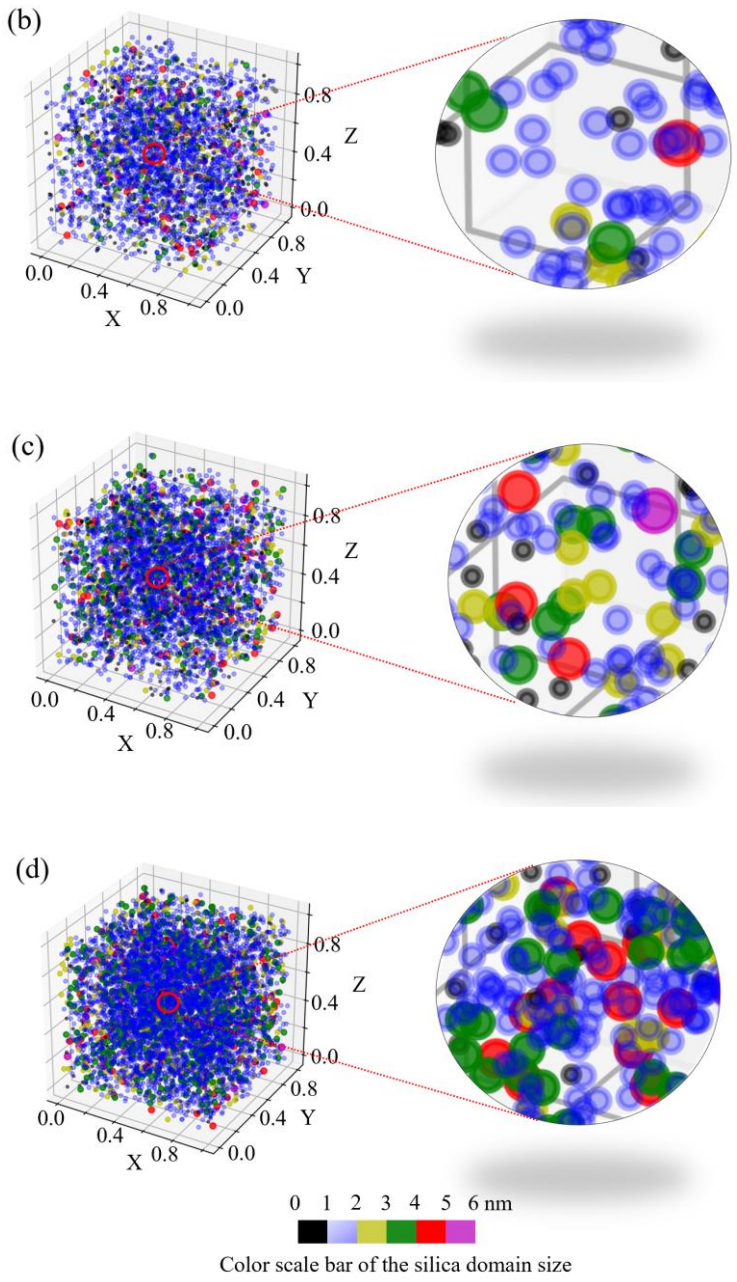

Fig. 2.11. 3D pore distributions of (a) pure SiOC, (b) SiOC/PHPS-1, (c) SiOC/PHPS-2, and (d) SiOC/PHPS-5 samples after 1200 °C pyrolysis and HF etching.

Fig. 2.12 plots the SSA and reciprocal of the average wall thickness for all the samples pyrolyzed at 1200 °C. The change for the SSA is similar to that of the reciprocal of the average wall thickness. It proves that a thicker wall results in a lower SSA. It is worth mentioning that the

specific pore volume of the pure SiOC, SiOC/PHPS-1, 2, and 5 are 0.75, 1.34, 1.21, and 1.02 cm^3/g respectively, as listed in Table 2.2. In general, the specific pore volume should increase with the additional PHPS (SiO_2) fillers. However, the experimental data only reach a maximum (1.34 cm^3/g) for SiOC/PHPS-1, before decreasing to the lowest value at SiOC/PHPS-5. In Fig. 2.9, the overall value of the wall thickness moves towards higher values, from SiOC/PHPS-1 to 5. It can be reasonably inferred that a higher wall thickness likely prevents the removal of the SiO_2 domains by the HF etching, resulting in lower values of specific pore volume and SSA with higher addition of PHPS. In order to create an ultrahigh SSA, small and separated SiO_2 nanoclusters with thin walls are necessary.

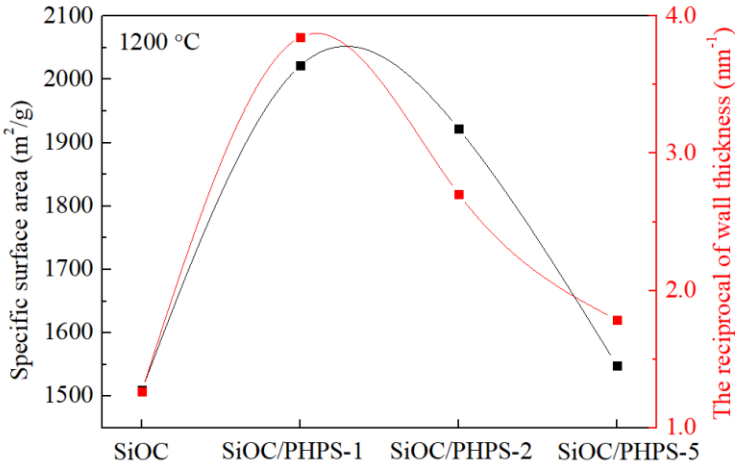

Fig. 2.12. Comparison between the experimental and simulated SSA of all the SiOC samples pyrolyzed at 1200 °C.

2.5. Conclusions

This paper reports on the creation of ultrahigh surface area SiOC ceramics based on PHPS and PSO. PHPS hydrolysis and chemical anchoring to PSO by crosslinking lead to more Si–O-Si bonds after pyrolysis. The resulting SiO_2 nanodomains can be etched to create ~2 nm size pores. The specific surface area of the SiOC/PHPS samples is up to ~2000 m^2/g. The fundamental understanding of the SiO_2 nanodomain impact is studied based on the calculation of wall thickness for graphene layers and mixed Si-O-C bonds. 3D view of SiO_2 domains can further explain the microstructural evolution. Small and separated SiO_2 nanoclusters with thin domain walls are

critical in creating ultrahigh SSA. Such high surface area and micro-/meso-porous materials should have important applications in catalysis, gas separation, molecular sieves, among others.

2.6. Supplementary data

Table S2.1. Volume shrinkage (%) for the SiOC ceramics pyrolyzed at 1100 °C, 1200 °C, and 1300 °C before the HF etching.

Pyrolysis T (°C)	*SiOC*	*SiOC/PHPS-1*	*SiOC/PHPS-2*	*SiOC/PHPS-5*
1100	23.17 ± 2.17	22.37 ± 0.58	22.04 ± 1.03	20.46 ± 0.98
1200	23.99 ± 1.23	23.01 ± 1.14	22.78 ± 0.78	22.19 ± 1.07
1300	26.76 ± 0.56	24.37 ± 2.11	23.89 ± 1.52	23.15 ± 1.63

Table S2.2. Intensity ratios of SiO_2 to turbostratic carbon (I_{silica}/I_{carbon}) for the SiOC ceramics pyrolyzed at 1100 °C, 1200 °C, and 1300 °C before the HF etching.

Pyrolysis T (°C)	*SiOC*	*SiOC/PHPS-1*	*SiOC/PHPS-2*	*SiOC/PHPS-5*
1100	2.63	3.03	3.00	3.16
1200	2.71	2.95	3.02	3.18
1300	2.69	2.81	2.97	3.10

Table S2.3. Nitrogen adsorption results for the SiOC ceramics pyrolyzed at 1100 °C, 1200 °C, and 1300 °C after the HF etching.

Pyrolysis temperature (°C)	*Sample*	*NLDFT specific surface area (m^2/g)*	*BET specific surface area (m^2/g)*
1100	Pure SiOC	1211.3	1186.5
	SiOC/PHPS-1	1359.7	1349.5
	SiOC/PHPS-2	1622.0	1565.4
	SiOC/PHPS-5	2035.6	1830.3
	Pure SiOC	1532.0	1510.0

1200	SiOC/PHPS-1	2079.3	1937.3
	SiOC/PHPS-2	2036.7	1921.8
	SiOC/PHPS-5	1688.0	1473.1
1300	Pure SiOC	1751.3	1691.0
	SiOC/PHPS-1	1867.6	1803.4
	SiOC/PHPS-2	1806.7	1766.0
	SiOC/PHPS-5	1677.7	1550.5

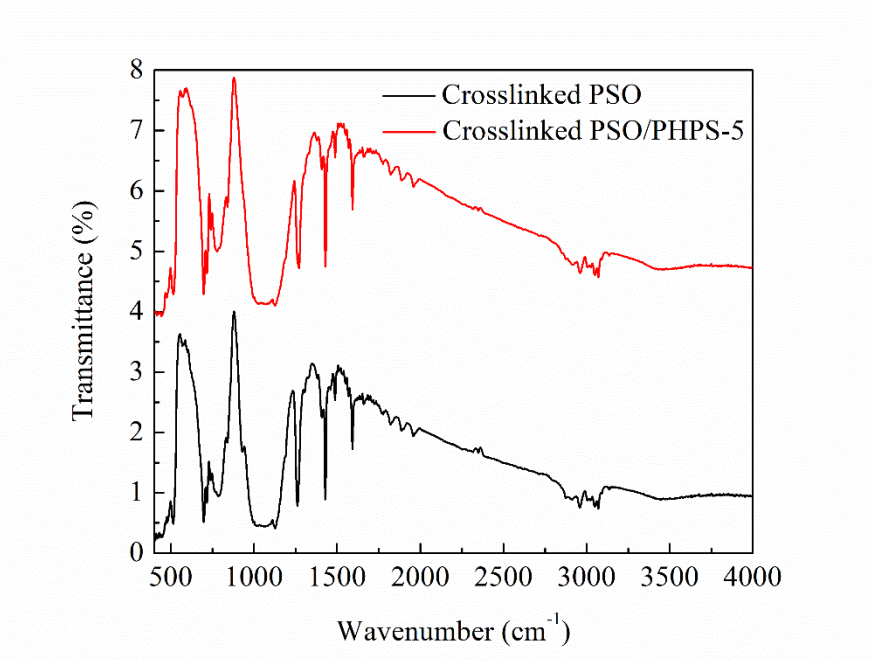

Fig. S2.1. FT-IR spectra for the pure PSO and PSO/PHPS-5 precursors after crosslinking.

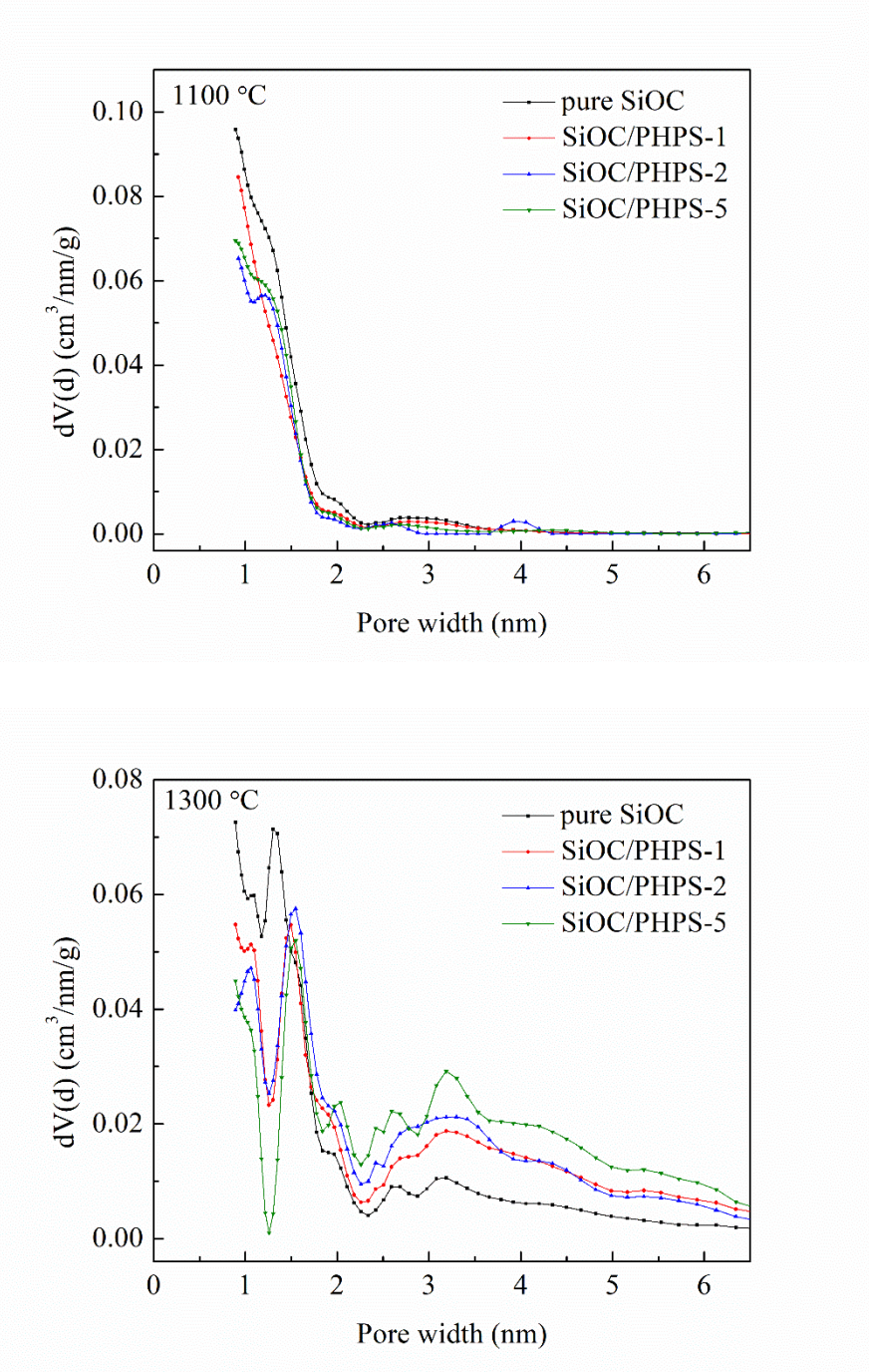

Fig. S2.2. Pore size distributions for all the etched SiOC samples pyrolyzed at 1100 °C and 1300 °C, from nitrogen adsorption (DFT method).

2.7. References

1. Liu, P.S. and G.F. Chen, *Chapter One - General Introduction to Porous Materials*, in *Porous Materials*, P.S. Liu and G.F. Chen, Editors. 2014, Butterworth-Heinemann: Boston. p. 1-20.
2. Salvini, V.R., V.C. Pandolfelli, and D. Spinelli, *Mechanical Properties of Porous Ceramics.* Recent Advances in Porous Ceramics, 2018: p. 171.
3. Bréquel, H., et al., *Systematic structural characterization of the high-temperature behavior of nearly stoichiometric silicon oxycarbide glasses.* Chemistry of materials, 2004. **16**(13): p. 2585-2598.
4. Yang, N., et al., *Nickel-containing magnetoceramics from water vapor assisted pyrolysis of polysiloxane and nickel 2, 4-pentanedionate.* Journal of the American Ceramic Society, 2020.
5. Erb, D. and K. Lu, *Synthesis of SiOC using solvent-modified polymer precursors.* Materials Chemistry and Physics, 2019. **237**: p. 121844.
6. Yang, N. and K. Lu, *Thermophysical property and electrical conductivity of titanium isopropoxide – polysiloxane derived ceramics.* Journal of the European Ceramic Society, 2019. **39**(14): p. 4029-4037.
7. Lu, K., D. Erb, and M. Liu, *Thermal stability and electrical conductivity of carbon-enriched silicon oxycarbide.* Journal of Materials Chemistry C, 2016. **4**(9): p. 1829-1837.
8. Xu, T., Q. Ma, and Z. Chen, *High-temperature behavior of silicon oxycarbide glasses in air environment.* Ceramics International, 2011. **37**(7): p. 2555-2559.
9. Pantano, C.G., A.K. Singh, and H. Zhang, *Silicon oxycarbide glasses.* Journal of Sol-Gel Science and Technology, 1999. **14**(1): p. 7-25.
10. Lu, K., *Porous and high surface area silicon oxycarbide-based materials—a review.* Materials Science and Engineering: R: Reports, 2015. **97**: p. 23-49.
11. Li, J. and K. Lu, *Highly porous SiOC bulk ceramics with water vapor assisted pyrolysis.* Journal of the American Ceramic Society, 2015. **98**(8): p. 2357-2365.
12. Naviroj, M., et al., *Directionally aligned macroporous SiOC via freeze casting of preceramic polymers.* Journal of the European Ceramic Society, 2015. **35**(8): p. 2225-2232.
13. Kumar, B.M. and Y.-W. Kim, *Processing of polysiloxane-derived porous ceramics: a review.* Science and Technology of Advanced Materials, 2010. **11**(4): p. 044303.

14. Vakifahmetoglu, C. and P. Colombo, *A Direct Method for the Fabrication of Macro-Porous SiOC Ceramics from Preceramic Polymers.* Advanced Engineering Materials, 2008. **10**(3): p. 256-259.
15. Wu, J., et al., *Simple fabrication of micro/nano-porous SiOC foam from polysiloxane.* Journal of Materials Chemistry, 2012. **22**(14): p. 6542-6545.
16. Colombo, P., *Engineering porosity in polymer-derived ceramics.* Journal of the European Ceramic Society, 2008. **28**(7): p. 1389-1395.
17. Erb, D. and K. Lu, *Additive and pyrolysis atmosphere effects on polysiloxane-derived porous SiOC ceramics.* Journal of the European Ceramic Society, 2017. **37**(15): p. 4547-4557.
18. Erb, D. and K. Lu, *Influence of vinyl bonds from PDMS on the pore structure of polymer derived ceramics.* Materials Chemistry and Physics, 2018. **209**: p. 217-226.
19. Erb, D. and K. Lu, *Effects of SiO2-forming additive on polysiloxane derived SiOC ceramics.* Microporous and Mesoporous Materials, 2018. **266**: p. 75-82.
20. Lu, K. and J. Li, *Fundamental understanding of water vapor effect on SiOC evolution during pyrolysis.* Journal of the European Ceramic Society, 2016. **36**(3): p. 411-422.
21. Morlier, A., et al., *Thin gas-barrier silica layers from perhydropolysilazane obtained through low temperature curings: A comparative study.* Thin Solid Films, 2012. **524**: p. 62-66.
22. Prager, L., et al., *Conversion of perhydropolysilazane into a SiOx network triggered by vacuum ultraviolet irradiation: Access to flexible, transparent barrier coatings.* Chemistry–A European Journal, 2007. **13**(30): p. 8522-8529.
23. Yang, N., et al., *Nickel-containing magnetoceramics from water vapor assisted pyrolysis of polysiloxane and nickel 2, 4-pentanedionate.* Journal of the American Ceramic Society, 2019.
24. Li, J., et al., *Preparation of micro-/mesoporous SiOC bulk ceramics.* Journal of the American Ceramic Society, 2015. **98**(6): p. 1753-1761.
25. Zhang, Z., et al., *Hydrophobic, transparent and hard silicon oxynitride coating from perhydropolysilazane.* Polymer International, 2015. **64**(8): p. 971-978.
26. Torrey, J.D. and R.K. Bordia, *Phase and microstructural evolution in polymer-derived composite systems and coatings.* Journal of materials research, 2007. **22**(7): p. 1959-1966.

27. Wang, K., et al., *The Conversion of Perhydropolysilazane into SiON Films Characterized by X-Ray Photoelectron Spectroscopy.* Journal of the American Ceramic Society, 2012. **95**(12): p. 3722-3725.
28. Tinio, J.V.G., et al., *Influence of OH− Ion Concentration on the Surface Morphology of ZnO-SiO2 Nanostructure.* Journal of Nanotechnology, 2015. **2015**.
29. Erb, D. and K. Lu, *Effect of additive structure and size on SiO2 formation in polymer-derived Si OC ceramics.* Journal of the American Ceramic Society, 2018. **101**(12): p. 5378-5388.
30. Kupgan, G., T.P. Liyana-Arachchi, and C.M. Colina, *NLDFT Pore Size Distribution in Amorphous Microporous Materials.* Langmuir, 2017. **33**(42): p. 11138-11145.
31. Saha, A., et al., *Characterization of nanodomains in polymer-derived SiCN ceramics employing multiple techniques.* Journal of the American Ceramic Society, 2005. **88**(1): p. 232-234.
32. Peña-Alonso, R., G.D. Sorarù, and R. Raj, *Preparation of ultrathin-walled carbon-based nanoporous structures by etching pseudo-amorphous silicon oxycarbide ceramics.* Journal of the American Ceramic Society, 2006. **89**(8): p. 2473-2480.
33. Saha, A., R. Raj, and D.L. Williamson, *A model for the nanodomains in polymer-derived SiCO.* Journal of the American Ceramic Society, 2006. **89**(7): p. 2188-2195.

Chapter 3

Effects of transition metals on the evolution of polymer-derived SiOC ceramics

Ni Yang, Kathy Lu*

Department of Materials Science and Engineering, Virginia Polytechnic Institute and State University, Blacksburg, Virginia, 24061, USA

*Corresponding author: Email: klu@vt.edu

Declarations of interest: none

*This chapter has been adapted from a **published** manuscript by Ni Yang and Kathy Lu from the following reference:*

Ni Yang, and Kathy Lu. "Effects of transition metals on the evolution of polymer-derived SiOC ceramics." Carbon 171 (2021): 88-95.

Reprinted with permission from the Elsevier.

3.1. Abstract

This study focuses on catalytic graphitization from different metals, iron (Fe), cobalt (Co), and nickel (Ni), for inducing carbon growth in silicon oxycarbides (SiOCs) during the pyrolysis. Fe, Co, and Ni-modified SiOCs were synthesized by pyrolysis to 900, 1100, and 1300°C respectively in Ar. The transition metals induced the formation of the corresponding metal silicides, β-SiC, and graphitic carbon with the catalytic activity in the order of Fe > Co > Ni, in agreement with the activation energy calculation based on the carbon types and amounts. Lateral growth of turbostratic carbon followed a 2D grain growth process and its point-like defect density decreased based on the catalytic order of the transition metals, with SiOC/Fe having the lowest defect density. Quantitative analysis of the XPS results with Rietveld refinement illustrated that the phase separation of SiOC is more dominant than local carbothermal reduction between SiO_2 and C in the SiOC/M (M=Ni, Co, or Fe) systems. Understanding the catalytic graphitization effect of Ni, Co, and Fe on polymer derived ceramics offers new strategies in increasing high temperature phase amounts and thus creating novel materials for heterogeneous catalysis, magnetic, and other applications.

3.2. Introduction

Polymer-derived ceramics (PDCs) are a new class of ceramics synthesized through solid-state pyrolysis of preceramic polymers [1-3]. Silicon oxycarbide (SiOC) is a member of the PDC family and exhibits a remarkable range of novel properties due to its covalent bonds and amorphous structure [2, 4], such as outstanding high-temperature stability [5]. excellent corrosion resistance [6], and thermochemical/mechanical durability [7]. Generally, the physical characteristics and properties of the SiOCs are directly related to and can be tuned by the chemical structures derived from the preceramic precursors [8]. Furthermore, quaternary SiOC ceramics with desired properties can be achieved via chemical modification of the polymer precursors compared to the pure SiOC ternary systems [9].

Incorporation of metallic or intermetallic phases into the SiOC matrix is greatly desired in the field of energy and catalysis [10-13], especially for transition metals. With partially filled d orbitals, transition metal oxides can be used as catalyst support(s) in harsh environments where traditional oxide-based ceramics fail due to their physical and chemical stabilities. CeO_2/SiOC nanocomposites were studied as a thermocatalyst support for CO_2 thermochemical decomposition

[12]. Ni-containing porous SiOC ceramics [13] exhibited the highest conversion efficiency from CO_2 to CH_4 with selectivity up to ~77% and good stability. Moreover, transition metals act more than a catalysis support [5, 11, 14-18]. Ni has shown to induce the formation of β-SiC, cristobalite silica, and graphitic carbon [19]. Active metal nanoparticles (M = Fe, Co, Pt, Cu, Ag, Au) promoted the growth of multiwalled carbon nanotubes [16] and SiC nanowires [11]. New combinations of transition metals and PDCs should be investigated in order to enable advancement in catalytic, magnetic, hydrogen storage, and battery applications.

Catalytic graphitization of carbon by up to 22 kinds of metals was published as early as in 1979 [20]. Al, Ti, V, Cr, Mn, Fe, Co, Ni, Mo, and W can catalyze the formation of not only graphitic but also turbostratic carbons through carbide formation-decomposition or carbon dissolution-precipitation mechanisms. In addition, there are two routes for SiC formation in carbon-rich SiOC: phase separation of amorphous SiOC at low temperatures, and carbothermal reduction between silica and carbon at high temperatures [21]. However, the effect of transition metals on these processes needs to be further understood. Although previous studies briefly reported transition metal induced formation of β-SiC, cristobalite silica, and graphitic carbon from polymeric precursors [19, 22, 23], detailed mechanisms of these accelerated processes have not been investigated.

In this study, Ni, Co, and Fe elements were incorporated into the SiOC matrix and pyrolyzed at 900 °C, 1100 °C, and 1300 °C in Ar. The catalytic effect of these transition metals and detailed phase evolution of SiOC/M (M=Ni, Co, and Fe) are quantitatively analyzed by XRD, Raman, FTIR, and XPS techniques. Gibbs free energy of the graphitization process under these transition metals is calculated, and the mechanisms of the accelerated phase separation are detailed from two aspects.

3.3. Experimental procedure

3.3.1. Chemicals

Polysiloxane SPR-684 Polyramic® (Starfire Systems Inc., Schenectady, NY) was purchased as the preceramic polymer. (3-aminopropyl)triethoxysilane (APTES) was obtained from Sigma-Aldrich (St. Louis, MO, USA) and used as the complexing agent. For metal additives, iron(II) chloride hydrate ($FeCl_2.xH_2O$, 99% pure) was purchased from Alfa Aesar (Ward Hill, MA, USA),

nickel(II) chloride hexahydrate ($NiCl_2.6H_2O$, 99.9% pure) was obtained from Eisen-Golden Laboratories (Dublin, CA, USA), and cobalt(II) chloride hexahydrate ($CoCl_2.6H_2O$, 98% pure) was acquired from Alfa Aesar (Ward Hill, MA, USA). All chemicals were used as received without further purification. Anhydrous ethanol (99.7+%, Alfa Aesar) was further desiccated by a molecular sieve (mSorb®) and used as the solvent.

3.3.2. Crosslinking and pyrolysis of metal-containing samples

Ethanol was used to dissolve $FeCl_2$, $NiCl_2$, and $CoCl_2$ in three separate beakers (the weight ratio of ethanol to metal salts was 5:1) with magnetic stirring at room temperature until all metallic salts were dissolved. A molar ratio of metal to APTES complexing agent was fixed at 1:4 [13] to ensure the complete complexation of the metal ions. Subsequently, polysiloxane was introduced into each solution and magnetically stirred at 200 rpm for 1 hour at 60°C until a homogeneous mixture was formed. The weight percents of pure iron, nickel, and cobalt contents to polysiloxane were all at 2 wt%, respectively. The homogeneous mixture was then cast into an aluminum mold and placed in a vacuum chamber until 1500 mTorr was reached to remove bubbles. A blank group without any metallic salts was prepared under the same conditions. The crosslinking procedure was performed in an oven at 50°C for 12 hours, and then at 100°C for 12 hours.

The crosslinked and polished samples were put in a zirconia boat with both sides covered by graphite felts and then placed into a tube furnace (1730–12 Horizontal Tube Furnace, CM Furnaces Inc.). With an Ar flow rate of about 500 cm^3/min, the samples were heated up to 900 °C, 1100 °C, and 1300 °C respectively with a rate of 2 °C/min and a holding time of 2 hours, and cooled down to 50°C with a rate of 2°C/min. The pyrolyzed samples were marked as SiOC/Fe, SiOC/Co, and SiOC/Ni, respectively. A blank group without any metal addition was denoted as SiOC.

3.3.3. Characterization

Phase compositions of the pyrolyzed bulk samples were investigated using an X'Pert PRO diffractometer (PANalytical B.V.). Raman spectra were recorded on a Horiba spectrometer (JY Horiba HR 800) with an excitation wavelength of 633.08 nm produced by an Ar laser in the spectral range of 0-4000 cm^{-1}. Chemical compositions were examined by X-ray photoelectron spectroscopy (XPS, PHI Quantera SXM) equipped with an Al Kα source (1486.6 eV). To quantify

the multi-component peak areas in the Si 2p band, the Lorentzian modeling method available in the Origin software was used. The chemical bonding information of the pyrolyzed samples was measured using Fourier Transform Infrared Spectroscopy (FT-IR) (Nicolet 8700 with Pike GladiATR attachment, Thermo Scientific, Waltham, MA) between 500 and 4000 cm^{-1} wavenumbers (4 cm^{-1} resolutions, 128 scans).

3.4. Results and discussion

3.4.1. Phase evolution of SiOC/M systems

Fig. 3.1 shows the XRD patterns of SiOC, SiOC/Fe, SiOC/Co, and SiOC/Ni pyrolyzed at different temperatures (900 °C, 1100 °C, and 1300 °C). At 900 °C and 1100 °C, the XRD patterns of the pure SiOC look similar and remain amorphous without any peaks, which is constant with our previous studies [5, 15]. The broad peaks centered at 20-30 ° and 40-50° for the SiOC pyrolyzed at 1300 °C are from carbon (002) and (101), respectively. Weak and poorly defined humps for the β-SiC phase are observed at 35.8°, 60°, and 72° (indexed as the (111), (220), and (311) planes). These broad peaks indicate negligible ordering for the SiC phase.

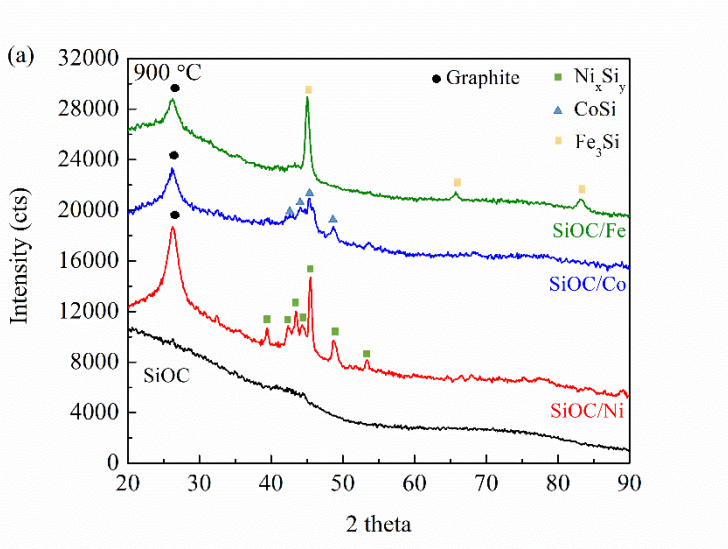

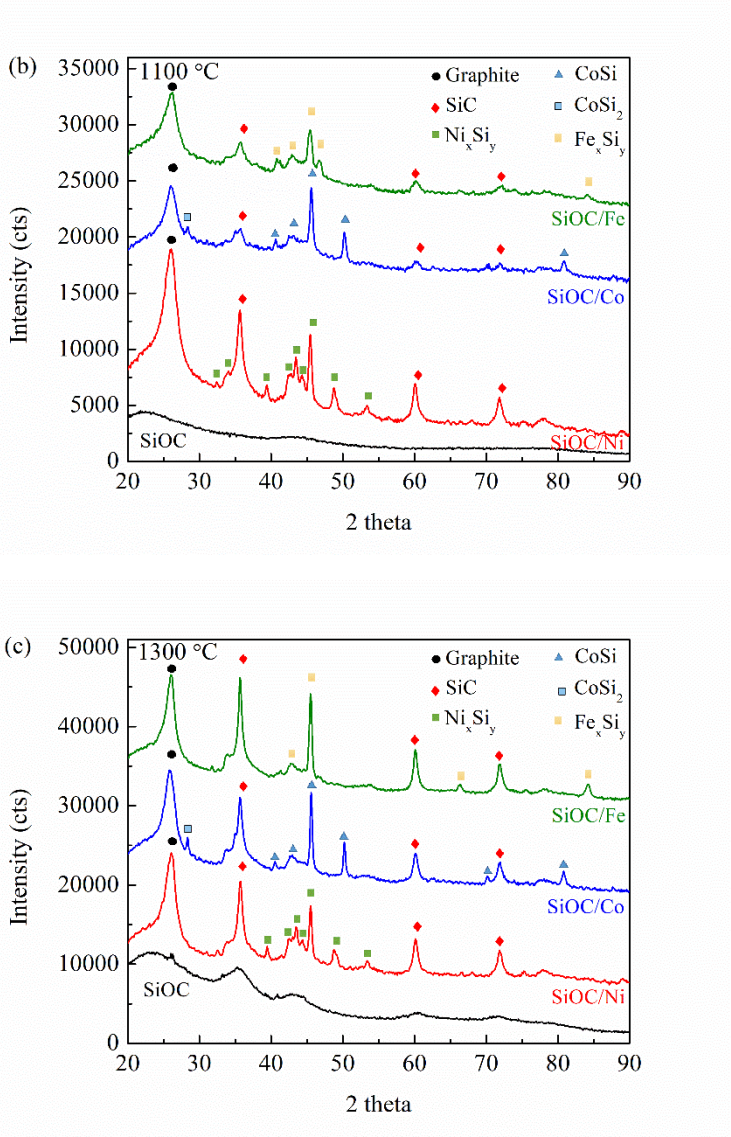

Fig. 3.1. XRD patterns of SiOC, SiOC/Ni, SiOC/Co, and SiOC/Fe pyrolyzed at (a) 900 °C, (b) 1100 °C, and (c) 1300 °C in Ar.

Different from the pure SiOC, the addition of transition metals induces distinct phase separation to form crystalline SiC, turbostratic carbon, and the corresponding metal silicides, except for the 900 °C pyrolysis condition. At 900 °C, no evident crystallization of cubic SiC is detected. The appearance of graphite at 25.2° in SiOC/M (M = Co, Ni, or Fe) is due to the catalytic graphitization of the transition metals [24]. From 1100 °C to 1300 °C, the three main peaks at 35.8°, 60°, and 72° reflect the formation of β-SiC in the SiOC/M matrix. The low-intensity peak at 33.6° belongs to SiC from the stacking faults (aggregation of vacancies) in the direction of

closed-packed (111) plane [25, 26]. It is also observed that the low-intensity peak at 28.5° belongs to the (111) plane of the $CoSi_2$ phase [27] for SiOC/Co sample.

In the XRD pattern of the SiOC/Fe sample pyrolyzed at 900 °C (Fig. 3.1(a)), the peaks for the Fe_3Si phase [28] center around 45°, 66°, and 84°, corresponding to the (022), (004), and (224) planes respectively. The formation of Fe_3Si via two possible scenarios has been reported [29]. The first process includes carbothermal reduction of unstable Fe_xO_y, which is the decomposition product of $FeCl_2$ to metallic Fe followed by reaction with SiOC to form Fe_3Si. The second possibility is the formation of intermediate cementite Fe_3C by the reaction between Fe_xO_y and carbon, before converting into Fe_3Si. Since the Gibbs free energy change for the reaction of Fe_xO_y with carbon to form Fe_3C (ΔG = -44.1 KJ/mol) is slightly more favorable than that of the formation of metallic iron ((ΔG = -43.3 KJ/mol) [22], FTIR spectra of the crosslinked samples pyrolyzed at lower temperatures are given in Fig. 3.2 to verify the presence of the Fe_3C phase. The detailed information about the main FTIR peaks that contribute to the samples has been illustrated in the supplementary Table S1. The processing temperature is chosen from 300 °C to 500 °C, based on the fact that Fe_3C decomposes at 700 °C [30]. As shown in Fig. 3.2, a peak at ~1400 cm^{-1} wavenumber is detected, which can be assigned to the vibrational mode of Fe-C [31, 32]. It also means that the second scenario is most likely to form Fe_3Si, both experimentally and thermodynamically.

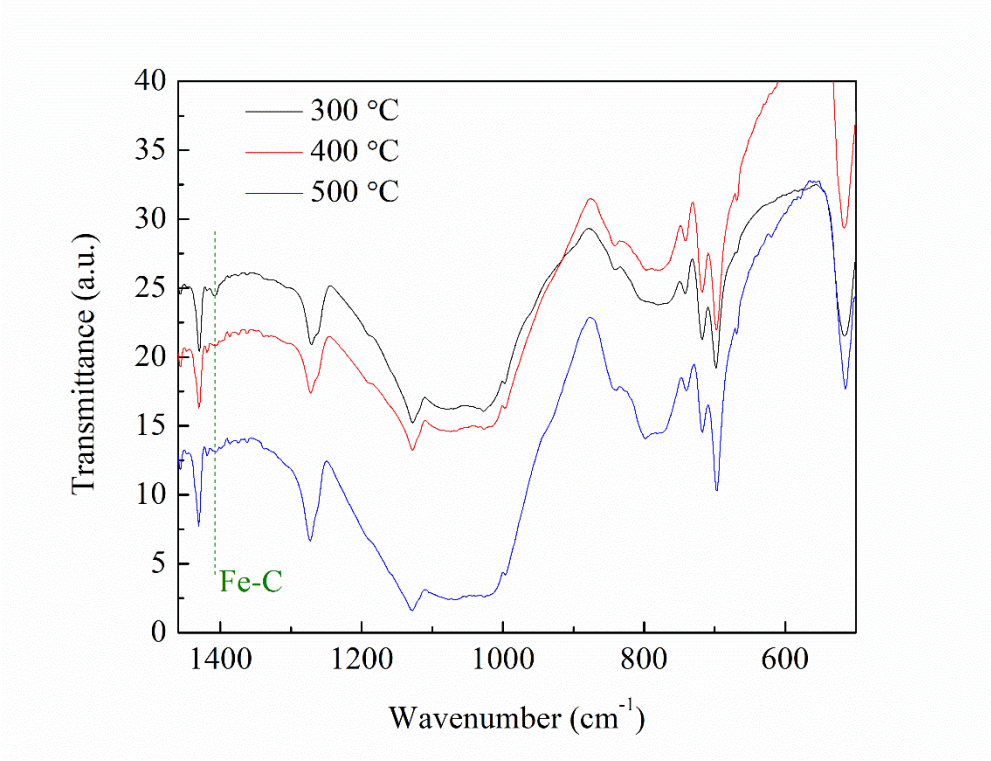

Fig. 3.2. FTIR spectra of crosslinked SiOC/Fe samples pyrolyzed at 300-500 °C.

With the pyrolysis temperature increase to 1100 °C, crystalline SiC phase forms due to the catalytic effect of Fe, Co, or Ni. The formation of cubic β-SiC can be explained by two possible processes. One is the phase separation of amorphous SiOC (Equation (3.1)) into SiO_2, SiC, and C, which commonly starts at ~1200 °C and higher [33]:

$$2SiOC \rightarrow SiO_2 + SiC + C \quad (3.1)$$

In the current study, this reaction occurs at much lower temperatures, meaning that the addition of Fe, Ni, or Co reduces the activation energy of the reaction. Another is the local carbothermal reduction between the phase-separated SiO_2 and C, which results in the formation of cubic SiC along with CO release [34]:

$$SiO_2 + 3C \rightarrow SiC + 2\,CO\uparrow \quad (3.2)$$

Between these two SiC formation processes, we can confirm that the latter is dominant, and the detailed explanation will be provided in Section 3.4.

3.4.2. Structural evolution of carbon

As shown in Fig. 3.3, the structural evolution of the carbon phases can be understood from the Raman spectra by curve-fitting using the Lorentzian function. With the pyrolysis temperature increase, the samples exhibit two main peaks with increasing separation, located at ~1350 cm^{-1} (D peak, from the breathing mode of sp^2 carbon atoms in rings [5, 35, 36]) and ~1600 cm^{-1} (G peak, from the in-plane bond stretching of sp^2 carbon [15, 37]). This phenomenon is accompanied by the decline of the minor D'' peak at 1500 cm^{-1}, which means that the amorphous carbon converts into graphitic carbon at elevated temperatures [38]. The band T at ~1200 cm^{-1} is attributed to the presence of sp^2–sp^3 C–C and C=C bonds [39]. The combined peaks at 2500 – 3000 cm^{-1} can be deconvoluted by T+D, 2D, D+G, and 2G bands. The peak positions and the area ratio A_D/A_G at different pyrolysis temperatures are listed in Table 3.1.

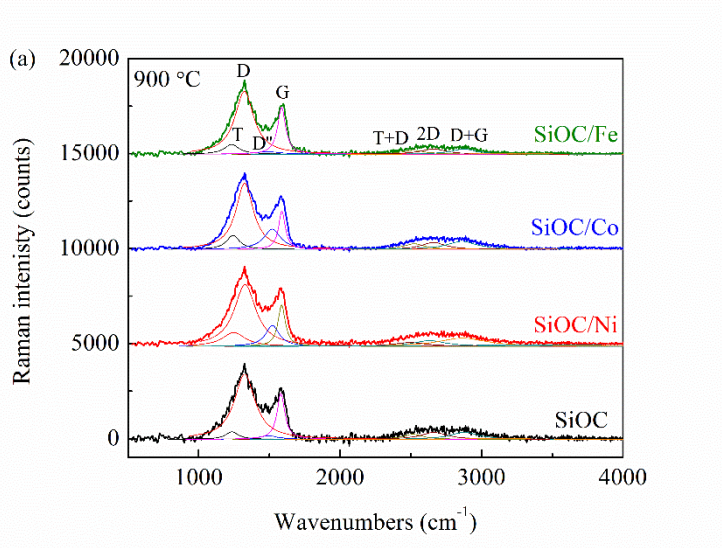

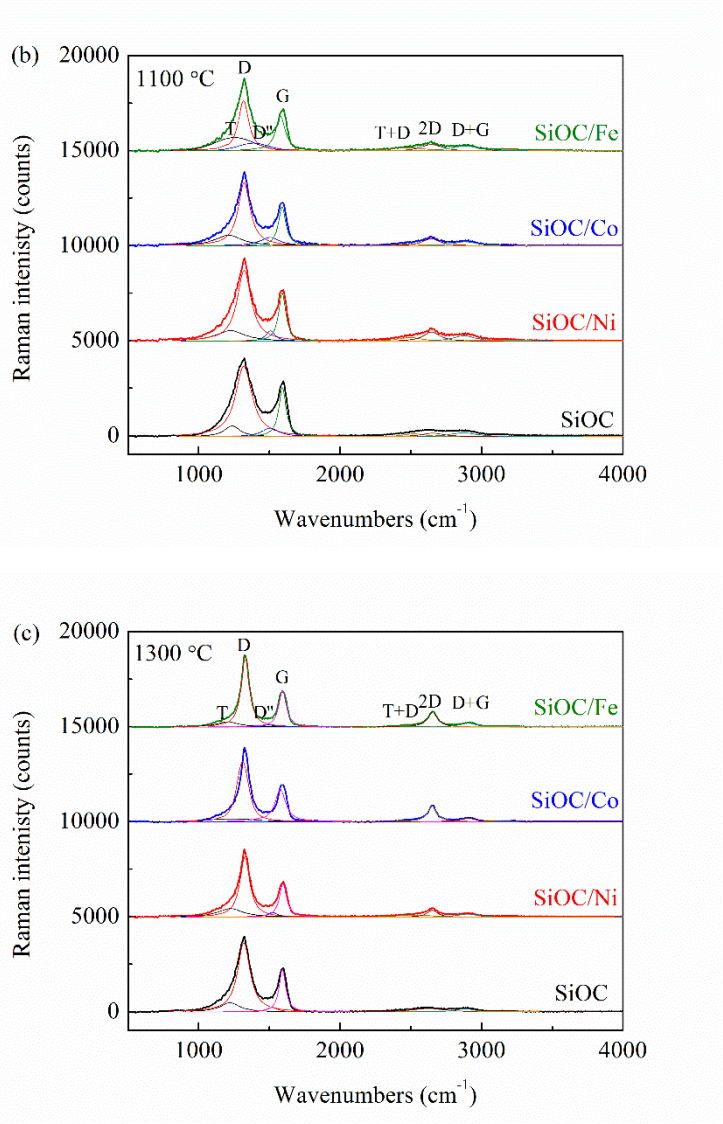

Fig. 3.3. Normalized Raman spectra of SiOC and SiOC/M (M = Co, Ni, or Fe) pyrolyzed at 900 – 1300 °C, with peak splitting by the Lorentzian function.

Table 3.1. Peak positions and area ratio A_D/A_G of the Raman spectra of the carbon species.

Peak position at 633.1 nm excitation, wavelength (cm^{-1})										
Pyrolysis temperature (°C)	Samples	T	D	D''	G	T+D	2D	D+G	2G	A_D/A_G
900	SiOC	1235	1325	1492	1581	2514	2664	2879	3121	4.61
	SiOC/Ni	1238	1327	1521	1586	2492	2632	2865	NA	4.29
	SiOC/Co	1242	1324	1520	1588	2523	2659	2860	3060	3.71
	SiOC/Fe	1233	1323	1487	1586	2520	2660	2875	3210	3.08
1100	SiOC	1236	1318	1506	1592	2524	2654	2870	3136	3.20
	SiOC/Ni	1224	1321	1508	1590	2492	2647	2875	3123	2.81
	SiOC/Co	1211	1321	1503	1589	2491	2642	2883	3179	2.66
	SiOC/Fe	1252	1317	1387	1578	2471	2645	2881	3200	2.01
1300	SiOC	1220	1319	1519	1592	2479	2623	2884	3188	2.53
	SiOC/Ni	1224	1326	1520	1595	2527	2651	2899	NA	2.46
	SiOC/Co	1228	1310	1553	1577	2551	2636	2894	3204	2.04
	SiOC/Fe	1204	1328	1494	1592	2474	2652	2906	NA	1.80

Compared with the D-to-G peak intensity ratio, the corresponding integrated intensity (peak area) ratio should be more accurate to calculate the lateral size of the carbon nanoclusters, since the area under each peak should more precisely represent the probability of the evolving phases [40]. For nano-crystalline carbon, the lateral size (L_a) can be calculated using the Cançado equation [41]:

$$L_a = (2.4 \times 10^{-10}).\lambda_L^4.(\frac{A_D}{A_G})^{-1} \quad (3.3)$$

with λ_L (633.08 nm) being the excitation wavelength of the laser source in this study. For in-plane growth of graphite nanocrystals [42]:

$$\frac{dL_a}{dT} = \frac{A}{L_a} \quad (3.4)$$

where A can be expressed as a temperature-dependent constant and T is the pyrolysis temperature. A is often described as

$$A = A_0 exp(-\frac{Q}{RT}) \quad (3.5)$$

where R is the gas constant, and Q is the activation energy. Combining Equations (3.3-3.5), we can have the following relations:

$$(\frac{A_D}{A_G})^{-2} \propto L_a^2 \propto exp(-\frac{Q}{RT}) \quad (3.6)$$

It shows a linear relationship of $In(\frac{A_D}{A_G})^{-2}$ vs. 1/T for different metal-modified SiOCs, which means that the in-plane evolution of the crystalline graphite can be classified as 2D grain growth based on the Hillert's theory [43]. According to the corresponding slopes of the fitted curves, the activation energy for the growth of the graphite from SiOC, SiO/Ni, SiOC/Co, and SiOC/Fe systems is calculated to be 66.64 ± 2.71, 66.09 ± 3.01, 62.67 ± 1.26, and 60.72 ± 4.03 KJ/mol, respectively. Compared with that of the pure SiOC, the activation energy of the transition metal modified SiOC is consistently reduced. Besides, the activation energy decreases from Q_{Ni} to Q_{Co}, and then to Q_{Fe}, which means that the graphitization activity of these three metals is in the order of Ni < Co < Fe. Also, the activation energy for the metal silicide growth is much higher (284.64 kJ/mol for NiSi [44], 154.38 kJ/mol for CoSi [45], and 350.25 kJ/mol for Fe_3Si [46]) compared to the activation energy for the graphite growth as calculated above. In general, this kind of catalytic activity should be related to the number of vacancies in the d shell of free atoms [47]. The electron configurations of Fe, Co, and Ni, as for all the metals in group VIII, are [Ar] $3d^6$ $4s^2$, [Ar] $3d^7$ $4s^2$, and [Ar] $3d^8$ $4s^2$, respectively. The d shell is occupied by 6-8 electrons, and the energy level can be adjusted by accepting extra electrons from free carbon to form covalent bonds. Overall, the graphitization activity is in the order of $Q_{Ni} < Q_{Co} < Q_{Fe}$.

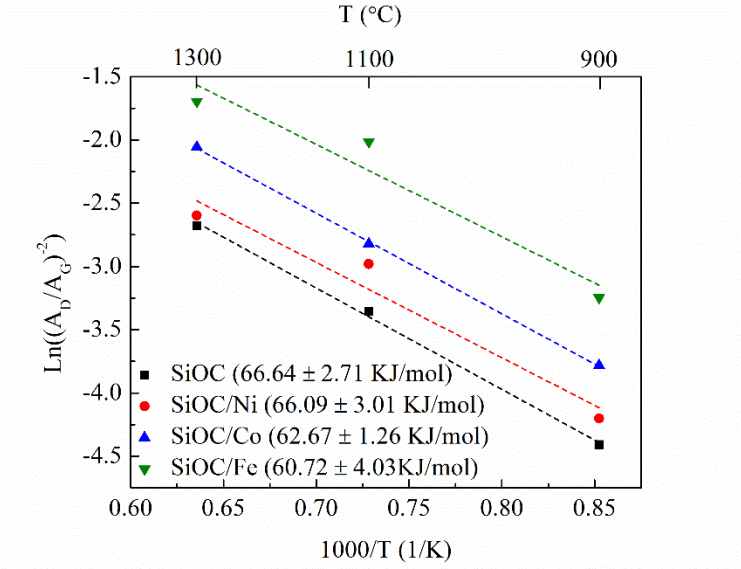

Fig. 3.4. D-to-G peak integrated intensity ratio of SiOC and different SiOC/M systems as a function of pyrolysis temperature.

To understand the effect of transition metals on the structural evolution of carbon more fully, the defect density (N_D, cm^{-2}) can be approximated by the following formula based on a phenomenological model [48, 49]:

$$N_D = \frac{2.4\times10^{22}}{\lambda_L^4}\frac{A_D}{A_G} \tag{3.7}$$

Equation (3.7) is only valid for point-like defects and not for edge defects, intercalants, and charge impurities as the latter do not change the intensity of the D-band [48] due to the symmetry-breaking nature of the edges in graphene and the associated electronic effects. Fig. 3.5 shows the effects of pyrolysis temperature and transition metals on the formation of point-like defects for carbon in the SiOC matrix. The structural defects of the graphitic carbon in the SiOC/M samples decrease compared to those of the pure SiOC samples, and this result is most pronounced in the SiOC/Co and SiOC/Fe samples. The remarkable graphitization effect achieved by Co or Fe can reduce the defects within the carbon clusters. With an increase in the pyrolysis temperature, the defect density decreases rapidly. The in-plane growth of graphite nanocrystals also causes a decrease in the boundary area (edge area), and thus a further decrease in the defect density (mostly due to the decrease in the defects at the edge).

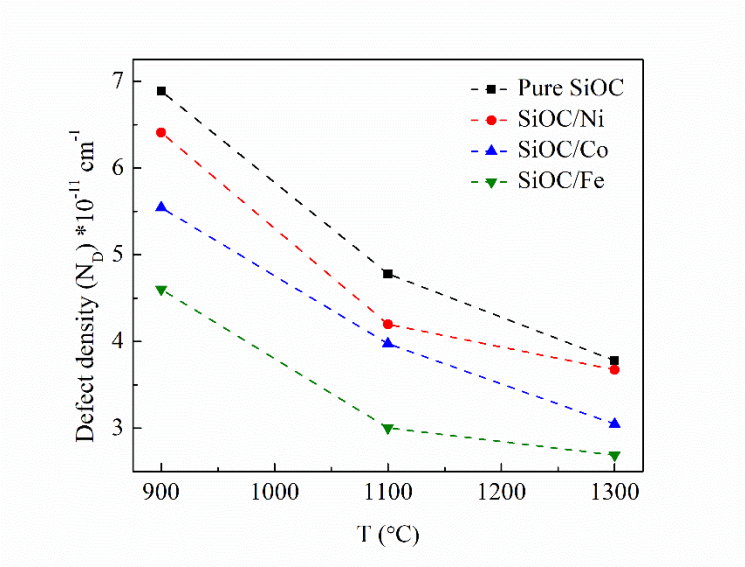

Fig. 3.5. Defect density of all the SiOC based samples pyrolyzed at 900 – 1300 °C.

3.4.3. Quantitative phase analysis

Bonding configuration in the SiOC/M (M=Co, Ni, or Fe) systems, focusing on the electronic environment (chemical bonding) of the Si 2p, is shown in Fig. 3.6. The charging effect that arises from the semi-conductivity of the SiOC matrix has been corrected using the C ls line of turbostratic/graphitic carbon [50]. Several types of phases may coexist in the high-resolution Si 2p spectra: SiO_4, SiO_3C, SiO_2C_2, $SiOC_3$ and SiC_4, with their Lorentzian-deconvoluted peaks locating at 103.2, 103, 102.2, 101.6, and 101 eV [51-54], respectively. The corresponding atomic percentage of these units can be calculated from the peak fitting curves using Equations (3.8-3.10) as shown in Table 3.2.

$$[SiO_4] = \frac{A_{SiO_4}}{A_{SiO_4}+A_{SiO_3C_1}+A_{SiO_2C_2}+A_{SiO_1C_3}+A_{SiC_4}} \tag{3.8}$$

$$[SiO_xC_{4-x}] = \frac{A_{SiO_3C_1}+A_{SiO_2C_2}+A_{SiO_1C_3}}{A_{SiO_4}+A_{SiO_3C_1}+A_{SiO_2C_2}+A_{SiO_1C_3}+A_{SiC_4}} \tag{3.9}$$

$$[SiC_4] = \frac{A_{SiC_4}}{A_{SiO_4}+A_{SiO_3C_1}+A_{SiO_2C_2}+A_{SiO_1C_3}+A_{SiC_4}} \tag{3.10}$$

where $A_{SiO_4}, A_{SiO_3C_1}, A_{SiO_2C_2}, A_{SiO_1C_3}, and\ A_{SiC_4}$ are the integrated areas underneath their corresponding peaks. Fig. 3.6 shows that the Si 2p peak shifts towards lower binding energy after the addition of transition metals, regardless of the pyrolysis temperature. The left shift gradually increases from Ni, to Co, and to Fe. This phenomenon is caused by the increasing formation of

SiC (101 eV) based on catalyst-induced phase separation, which makes the peak shifts towards lower binding nergy. It once again proves that the catalyst activity of these three metals is in the order of Ni < Co < Fe, consistent with the results in Section 3.2. The atomic percentage of SiC_4 in Table 3.2 also supports this conclusion.

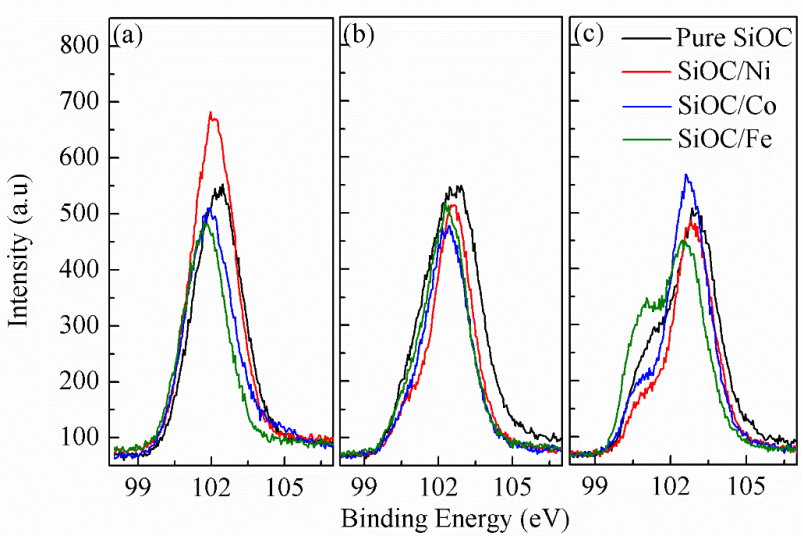

Fig. 3.6. XPS spectra of the Si 2p peaks for the SiOC and SiOC/M (M=Co, Ni, or Fe) samples pyrolyzed at (a) 900 °C, (b) 1100 °C, and (c) 1300 °C.

Table 3.2. XPS data of the SiOC and SiOC/M samples at different pyrolysis temperatures.

		Integrated areas underneath peaks			*Atomic percentage (at%)*		
Pyrolysis temperature (°C)	Sample	SiO_4	SiO_xC_{4-x} (x=1, 2, 3)	SiC_4	$[SiO_4]$	$[SiO_xC_{4-x}]$	$[SiC_4]$
900	SiOC	30.09	708.75	46.28	3.83	90.27	5.89
	SiOC/Ni	82.72	1094.61	171.16	6.13	81.17	12.69
	SiOC/Co	147.25	668.47	217.13	14.26	64.72	21.02
	SiOC/Fe	35.45	371.99	224.97	5.61	58.82	35.57
	SiOC	94.33	737.15	72.59	10.43	81.54	8.03
	SiOC/Ni	101.91	900.31	110.12	9.16	80.94	9.90

1100	SiOC/Co	76.56	754.74	134.18	7.93	78.17	13.90
	SiOC/Fe	88.88	709.46	200.47	8.90	71.03	20.07
1300	SiOC	57.68	616	88.47	7.57	80.82	11.61
	SiOC/Ni	23.56	322.31	57.39	5.84	79.93	14.23
	SiOC/Co	137.22	683.14	200.84	13.44	66.90	19.67
	SiOC/Fe	138.56	602.06	370.87	12.47	54.17	33.37

As discussed related to Equations (3.1-3.2), two reaction pathways can lead to the SiC formation. One is the phase separation of amorphous SiOC and the other is local carbothermal reduction between the phase-separated SiO_2 and C. Although transition metals induce the formation of β-SiC in polymer-derived ceramics, no studies have been able to distinguish the dominance from the two processes so far. In this study, the following method will be used to solve this challenging problem.

Unlike O and C elements, which easily form volatile gases during the ceramization process, the amount of Si atoms in the SiOC system is relatively stable and will not change significantly. In our studied systems, four Si-containing species coexist in the SiOC/M (M=Co, Ni, or Fe) samples - SiC, SiO_xC_{4-x}, SiO_2, and M_xSi_y. Together they can be regarded as clusters containing a fixed amunt of silicon atoms (100 at%). The atom ratios of SiC, SiO_xC_{4-x}, and SiO_2 are given in Table 3.2 as calculated from the peak fitting areas, except for the M_xSi_y phase, for which the content still needs to be investigated. To address this remaining issue, the ratio between M_xSi_y and SiC phases can be obtained from the XRD patterns of the SiOC-related samples (Fig. 3.1). The Rietveld analysis of the XRD patterns can be used to obtain the content of crystalline phases [55]. However, since there is no evident crystallization of SiC as shown in Fig. 3.1(a), the relationship between SiC and M_xSi_y is not available at 900 °C pyrolysis temperature. After the refinement, the atomic ratios of SiC to M_xSi_y at 1100 °C are 1.42, 0.94, and 0.47 for SiOC/Ni, SiOC/Co, and SiOC/Fe, respectively. At 1300 °C, the atomic ratios of SiC to M_xSi_y are 1.41, 1.26, and 1.05 for SiOC/Ni, SiOC/Co, and SiOC/Fe, respectively. Combining the data derived from the Rietveld refinement and Table 3.2, the corresponding Si contents from SiC, SiO_xC_{4-x}, SiO_2, and M_xSi_y are displayed in Fig. 3.7.

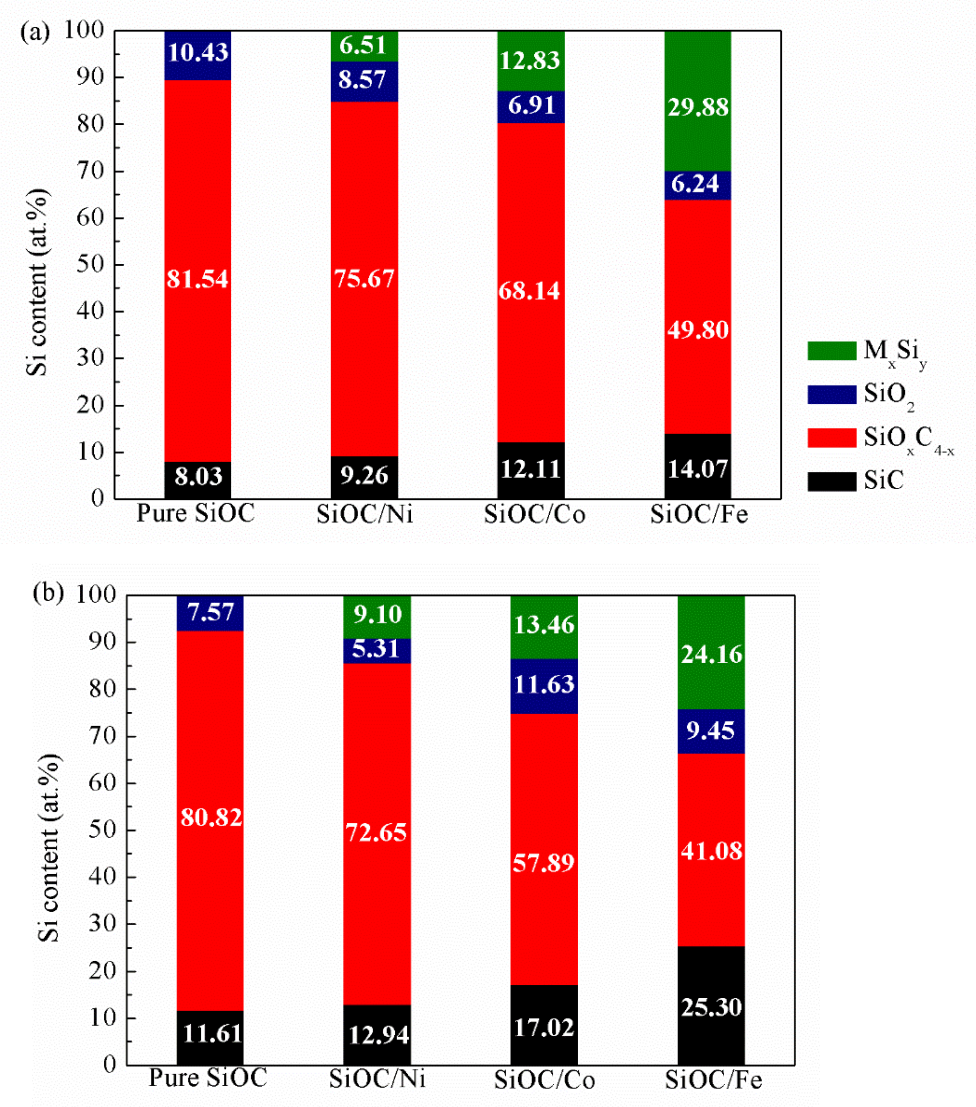

Fig. 3.7. Si contents from SiC, SiO_xC_{4-x}, SiO_2, and M_xSi_y in the samples pyrolyzed at (a) 1100 °C, and (b) 1300 °C.

According to Equation (1), one amorphous SiOC unit can convert into equal amounts of SiO_2 and SiC (1 Si → 0.5 SiC). However, different from Equation (1), one SiO_2 unit locally reacts with one C to form one SiC (1 Si → 1 SiC). In Fig. 3.7, the content of the SiO_xC_{4-x} units from the pure SiOC decreases from 81.54 at% to 80.82 at% when the pyrolysis temperature increases from 1100 – 1300 °C, meaning that 0.72 at% SiO_xC_{4-x} converts into 0.36 at% SiC and 0.36 at% SiO_2. The SiO_2 atomic content from this sample decreases from 10.43 at% to 7.57 at%, indicating that almost 5 at% SiO_2 reacts with C to form ~5 at% SiC through carbothermal reduction. Put it differently,

compared with the phase separation of SiOC, the carbothermal reduction is more dominant for the pure SiOC samples. The SiOC/Ni samples behave similarly to the pure SiOC with ~1 at% SiO_xC_{4-x} (forming 0.5 at% SiC) and ~3 at% SiO_2 (forming 3 at% SiC) loss, with the latter (carbothermal reduction) being more dominant. However, for both SiOC/Co and SiOC/Fe samples, the atomic content of SiO_2 increases from 1100 °C to 1300 °C, whereas the SiO_xC_{4-x} content decreases dramatically. This phenomenon is especially noticeable for the SiOC/Fe system in which the carbothermal reduction reaction is relatively suppressed. This means that the phase separation of SiOC is more dominant than the carbothermal reduction reaction for the SiOC/Co and SiOC/Fe systems, and the activity of these three metals is still in the order of Ni < Co < Fe.

3.4.4. Mechanism of accelerated phase separation

For the SiOC/Co and SiOC/Fe systems, the experimental and calculated results in Fig. 3.7 illustrate that the phase separation of SiOC is dominant in the SiC phase formation, which can be explained from the following two aspects.

Firstly, the formation of the more thermodynamically stable M_xSi_y (M=Ni, Co, or Fe) induces the phase separation of SiOC and leads to the crystallization of nano-sized SiC in an amorphous SiO_2 matrix, represented as Equation (3.1). According to previous studies [56, 57], SiC is chemically unstable at > 800 °C, especially in the presence of Ni, Co, and Fe. The chemical instability of SiC causes the thermodynamically favorable reactions between SiC and metals to form M_xSi_y, which is more stable than SiC. This overall reaction can be written as:

$$xM + ySiC \rightarrow M_xSi_y + yC \quad (3.11)$$

With continuous SiC formation, the forward reaction of Equation (3.11) is favored and some of the excess reactants are consumed based on the Le Châtelier's principle [58]. It explains why the phase separation reaction has accelerated in these systems.

The thermodynamic analysis of the Gibbs free energy change (ΔG_o) at 900 – 1300 °C can be used to explain the effect of different transition metals on the accelerated phase separation. Based on the reported thermodynamic data [57] for nickel silicide (NiSi), cobalt silicide (CoSi), and iron silicide (Fe_3Si), the calculated ΔG_o (J) based on the metal-silicon phase diagrams is -25469 + 19.58T (K), -8753 + 2.32T (K), and -7197 + 2.29T (K), respectively. The obtained results are plotted in Fig. 3.8.

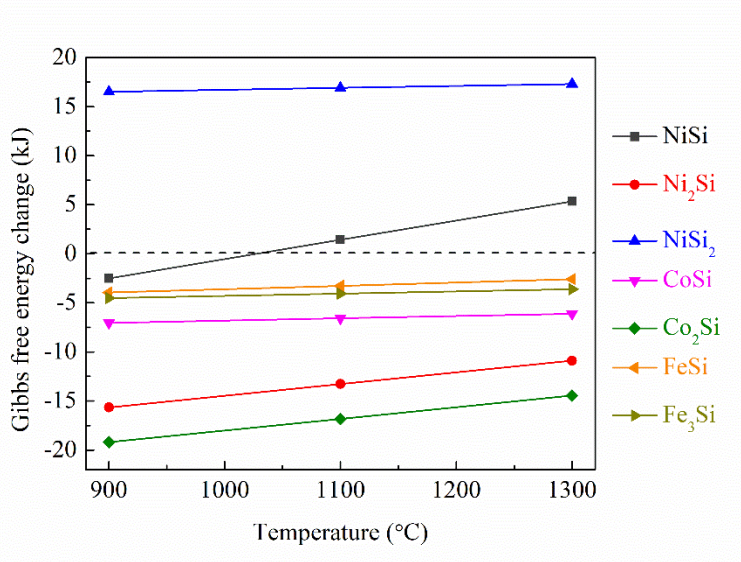

Fig. 3.8. Gibbs free energy change for the reactions between SiC and Ni, Co, or Fe as a function of temperature.

From 900 °C to 1300 °C, the Gibbs free energy for forming CoSi in the SiOC/Co system and FesSi in the SiOC/Fe system is always negative, and the difference between them is ~2 kJ/mol. This means that the reactions are favored to accelerate the SiOC phase separation. However, the Gibbs free energy for the SiOC/Ni system becomes positive when the temperature is higher than 1100 °C. This explains why the accelerated phase separation only exists for the SiOC/Co and SiOC/Fe systems, not for the SiOC/Ni system. It is also consistent with the results in Fig. 3.7. The Gibbs free energy for the SiOC/Co system is the most negative, which seems to contradict our result that the activity is in the order of Ni < Co < Fe. This contradiction can be rationalized by considering the rough estimates of the heat capacities by this method.

Secondly, the catalytic effect of the transition metals suppresses the carbothermal reduction. As shown in Equation (3.2), SiO_2 reacts with C to produce SiC. To be precise, Equation (3.1) proceeds through two steps [59]. The first step contains a solid-solid or solid-liquid reaction between SiO_2 and C leading to the formation of SiO gas, which subsequently reacts further with C to yield SiC nuclei as the second step. The C reduction of the SiO gas to SiC is reaction-rate-controlling. Based on a contracting volume shrinking core model [60], the intrinsic reaction rate (k) can be expressed as:

$$k = \frac{1-(1-X)^{1/3}}{t} = \frac{k_0}{d} exp(-E/RT) \quad (3.11)$$

where k_0 = 27.4 m/s and E = 382 ± 34 KJ/mol. The rate of this carbothermal reduction plays a significant role in influencing the carbon crystallite diameter, d. As discussed in Section 3.2, the activation energy for the growth of the graphite from SiOC, SiO/Ni, SiOC/Co, and SiOC/Fe is calculated to be 66.64 ± 2.71, 66.09 ± 3.01, 62.67 ± 1.26, and 60.72 ± 4.03 KJ/mol, respectively. It means that the lateral size of crystalline carbon (d) increases with the addition of transition metals, especially for the SiOC/Co and SiOC/Fe systems. According to Equation (3.12), the intrinsic reaction rate k decreases with increasing d values. Thus, the addition of Co or Fe into the SiOC matrix results in a high activation energy and a slower reaction rate.

Overall, the phase separation of SiOC is more dominant than carbothermal reduction to form the SiC phase in the SiOC/M (M=Ni, Co, or Fe) systems.

3.5. Conclusions

In this study, SiOC and SiOC/M (M=Ni, Co, or Fe) systems were synthesized by pyrolysis of a base polysiloxane mixed with different metal chloride salts in Ar at 900 – 1300 °C. The phase evolution of the corresponding systems varies due to the catalytic graphitization from different transition metals. The calculated activation energy for the lateral growth of the graphite phase shows that the graphitization activity is in the order of Fe > Co > Ni, which is also reflected in the formation of point-like defects. The graphitization reduces the defects within the carbon clusters and results in the lowest defect density in the SiOC/Fe samples. Two reaction pathways are responsible for the formation of SiC induced by transition metals. One is phase separation of the amorphous SiOC, and the other is the carbothermal reduction between the phase-separated SiO_2 and C. This study proves that the phase separation of SiOC is more dominant due to the following two reasons: (1) the more thermodynamically stable metal silicides induce the phase separation of SiOC, and (2) the graphitization of the transition metals suppresses the carbothermal reduction. We believe that a better understanding of catalytic graphitization by transition metal(s) for SiOC could pave the way towards more novel high temperature and harsh environment materials.

3.6. Supplementary data

Table S3.1. Main FT-IR peaks identified in the crosslinked SiOC/Fe samples pyrolyzed at 300-500 °C.

Wavenumber (cm^{-1})	*Functional Group*
693	Si-phenyl
865-750	Si-CH_3 in polysiloxanes
975-945	Si-CH_2CH_3
1190-1140, 990, 930	Si-CH_2-CH=CH_2
1259	Si-CH_3
1400	Fe-C
1410	Si-CH=CH_2

3.7. References

1. Erb, D. and K. Lu, *Additive and pyrolysis atmosphere effects on polysiloxane-derived porous SiOC ceramics.* Journal of the European Ceramic Society, 2017. **37**(15): p. 4547-4557.
2. Ionescu, E., H.-J. Kleebe, and R. Riedel, *Silicon-containing polymer-derived ceramic nanocomposites (PDC-NCs): Preparative approaches and properties.* Chemical Society Reviews, 2012. **41**(15): p. 5032-5052.
3. Lu, K., *Porous and high surface area silicon oxycarbide-based materials—a review.* Materials Science and Engineering: R: Reports, 2015. **97**: p. 23-49.
4. Kroll, P., *Modelling polymer-derived ceramics.* Journal of the European Ceramic Society, 2005. **25**(2-3): p. 163-174.
5. Yang, N. and K. Lu, *Thermophysical Property and Electrical Conductivity of Titanium Isopropoxide–Polysiloxane Derived Ceramics.* Journal of the European Ceramic Society, 2019.
6. Linck, C., et al., *Corrosion behavior of silicon oxycarbide-based ceramic nanocomposites under hydrothermal conditions.* International journal of materials research, 2012. **103**(1): p. 31-39.

7. Colombo, P., J.R. Hellmann, and D.L. Shelleman, *Mechanical Properties of Silicon Oxycarbide Ceramic Foams.* Journal of the American Ceramic Society, 2001. **84**(10): p. 2245-2251.
8. Erb, D. and K. Lu, *Influence of vinyl bonds from PDMS on the pore structure of polymer derived ceramics.* Materials Chemistry and Physics, 2018. **209**: p. 217-226.
9. Zaheer, M., et al., *Polymer derived non-oxide ceramics modified with late transition metals.* Chemical Society Reviews, 2012. **41**(15): p. 5102-5116.
10. Kockrick, E., et al., *Platinum induced crosslinking of polycarbosilanes for the formation of highly porous CeO 2/silicon oxycarbide catalysts.* Journal of Materials Chemistry, 2009. **19**(11): p. 1543-1553.
11. Pereira, J.L., et al., *Influence of pore former and transition metal on development of nanophases in porous silicon oxycarbide (SiCO) ceramics obtained by catalyst-assisted pyrolysis.* Journal of the European Ceramic Society, 2016. **36**(6): p. 1365-1376.
12. García, B., E. Casado, and A. Tamayo, *Synthesis and characterization of Ce/SiOC nanocomposites through the polymer derived ceramic method and evaluation of their catalytic activity.* Ceramics International, 2020. **46**(2): p. 1362-1373.
13. Macedo, H.P., et al., *Nickel-containing hybrid ceramics derived from polysiloxanes with hierarchical porosity for CO2 methanation.* Microporous and Mesoporous Materials, 2019. **278**: p. 156-166.
14. Cordelair, J. and P. Greil, *Electrical characterization of polymethylsiloxane/MoSi2-derived composite ceramics.* Journal of the American Ceramic Society, 2001. **84**(10): p. 2256-2259.
15. Yang, N., et al., *Nickel-containing magnetoceramics from water vapor assisted pyrolysis of polysiloxane and nickel 2, 4-pentanedionate.* Journal of the American Ceramic Society, 2019.
16. Schmalz, T., et al., *Catalytic formation of carbon phases in metal modified, porous polymer derived SiCN ceramics.* Carbon, 2011. **49**(9): p. 3065-3072.
17. Yu, Z., et al., *Polymer-derived mesoporous Ni/SiOC(H) ceramic nanocomposites for efficient removal of acid fuchsin.* Ceramics International, 2017. **43**(5): p. 4520-4526.
18. e Silva, T.C.d.A., et al., *Polymer-derived Co/Ni–SiOC (N) ceramic electrocatalysts for oxygen reduction reaction in fuel cells.* Catalysis Science & Technology, 2019. **9**(3): p. 854-866.

19. Segatelli, M.G., A.T.N. Pires, and I.V.P. Yoshida, *Synthesis and structural characterization of carbon-rich SiCxOy derived from a Ni-containing hybrid polymer.* Journal of the European Ceramic Society, 2008. **28**(11): p. 2247-2257.
20. Ōya, A. and S. Ōtani, *Catalytic graphitization of carbons by various metals.* Carbon, 1979. **17**(2): p. 131-137.
21. Blum, Y.D., D.B. MacQueen, and H.-J. Kleebe, *Synthesis and characterization of carbon-enriched silicon oxycarbides.* Journal of the European Ceramic Society, 2005. **25**(2): p. 143-149.
22. Ionescu, E., et al., *Thermodynamic control of phase composition and crystallization of metal-modified silicon oxycarbides.* Journal of the American Ceramic Society, 2013. **96**(6): p. 1899-1903.
23. Harshe, R., C. Balan, and R. Riedel, *Amorphous Si (Al) OC ceramic from polysiloxanes: bulk ceramic processing, crystallization behavior and applications.* Journal of the European Ceramic Society, 2004. **24**(12): p. 3471-3482.
24. Maldonado-Hódar, F., et al., *Catalytic graphitization of carbon aerogels by transition metals.* Langmuir, 2000. **16**(9): p. 4367-4373.
25. Pujar, V.V. and J.D. Cawley, *Effect of stacking faults on the X-ray diffraction profiles of β-SiC powders.* Journal of the American Ceramic Society, 1995. **78**(3): p. 774-782.
26. Vlaskina, S., et al., *3C-6H transformation in heated cubic silicon carbide 3C-SiC.* Semiconductor physics quantum electronics & optoelectronics, 2011(14,№ 4): p. 432.
27. Detavernier, C., et al., *The influence of Ti capping layers on CoSi2 formation.* Microelectronic Engineering, 2000. **50**(1): p. 125-132.
28. Hojamberdiev, M., et al., *Single-source-precursor synthesis of soft magnetic Fe3Si- and Fe5Si3-containing SiOC ceramic nanocomposites.* Journal of the European Ceramic Society, 2013. **33**(13): p. 2465-2472.
29. Ionescu, E., et al., *Thermodynamic Control of Phase Composition and Crystallization of Metal-Modified Silicon Oxycarbides.* Journal of the American Ceramic Society, 2013. **96**(6): p. 1899-1903.
30. Wu, A., et al., *Magnetic properties of nanocrystalline Fe/Fe 3 C composites.* CrystEngComm, 2011. **13**(3): p. 876-882.

31. Huang, J.-Q., et al., *Novel interlayer made from Fe3C/carbon nanofiber webs for high performance lithium–sulfur batteries.* Journal of Power Sources, 2015. **285**: p. 43-50.
32. Wen, Z., et al., *Nitrogen-enriched core-shell structured Fe/Fe3C-C nanorods as advanced electrocatalysts for oxygen reduction reaction.* Advanced Materials, 2012. **24**(11): p. 1399-1404.
33. Kleebe, H.J., C. Turquat, and G.D. Sorarù, *Phase separation in an SiCO glass studied by transmission electron microscopy and electron energy-loss spectroscopy.* Journal of the American Ceramic Society, 2001. **84**(5): p. 1073-1080.
34. Parmentier, J., G.D. Soraru, and F. Babonneau, *Influence of the microstructure on the high temperature behaviour of gel-derived SiOC glasses.* Journal of the European Ceramic Society, 2001. **21**(6): p. 817-824.
35. Serrano-Esparza, I., et al., *The nature of graphene–metal bonding probed by Raman spectroscopy: the special case of cobalt.* Journal of Physics D: Applied Physics, 2016. **49**(10): p. 105301.
36. Yukhnovets, O.I., A.I. Maximov, and D.S. Mazing. *Raman studies of amorphous carbon thin films*. in *2017 IEEE Conference of Russian Young Researchers in Electrical and Electronic Engineering (EIConRus)*. 2017. IEEE.
37. Varga, M., et al., *Diamond/carbon nanotube composites: Raman, FTIR and XPS spectroscopic studies.* Carbon, 2017. **111**: p. 54-61.
38. Chen, Y., et al., *Quantitative study on structural evolutions and associated energetics in polysilazane-derived amorphous silicon carbonitride ceramics.* Acta Materialia, 2014. **72**: p. 22-31.
39. Mera, G., et al., *Polymer-derived SiCN and SiOC ceramics–structure and energetics at the nanoscale.* Journal of Materials Chemistry A, 2013. **1**(12): p. 3826-3836.
40. Cançado, L.G., et al., *Disentangling contributions of point and line defects in the Raman spectra of graphene-related materials.* 2D Materials, 2017. **4**(2): p. 025039.
41. Cançado, L., et al., *General equation for the determination of the crystallite size L a of nanographite by Raman spectroscopy.* Applied Physics Letters, 2006. **88**(16): p. 163106.
42. Thompson, C.V., *Grain growth in thin films.* Annual Review of Materials Science, 1990. **20**(1): p. 245-268.

43. Hillert, M., *On the theory of normal and abnormal grain growth.* Acta Metallurgica, 1965. **13**(3): p. 227-238.
44. Ma, D., et al., *Kinetics of NiSi-to-NiSi2 transformation and morphological evolution in nickel silicide thin films on Si(001).* Acta Materialia, 2006. **54**(18): p. 4905-4911.
45. Miura, H., E. Ma, and C. Thompson, *Initial sequence and kinetics of silicide formation in cobalt/amorphous-silicon multilayer thin films.* Journal of applied physics, 1991. **70**(8): p. 4287-4294.
46. Radermacher, K., et al., *Growth kinetics of iron silicides fabricated by solid phase epitaxy or ion beam synthesis.* Thin Solid Films, 1992. **215**(1): p. 76-83.
47. Yan, Q., et al., *Catalytic graphitization of kraft lignin to graphene-based structures with four different transitional metals.* Journal of Nanoparticle Research, 2018. **20**(9): p. 223.
48. Saini, P., R. Sharma, and N. Chadha, *Determination of defect density, crystallite size and number of graphene layers in graphene analogues using X-ray diffraction and Raman spectroscopy.* Indian Journal of Pure & Applied Physics (IJPAP), 2017. **55**(9): p. 625-629.
49. Zhang, Z., et al., *Facile one-Step synthesis and enhanced optical nonlinearity of graphene-γMnS.* Nanomaterials, 2019. **9**(12): p. 1654.
50. Corriu, R.J.P., et al., *29Si NMR and XPS Investigation of the Structure of Silicon Oxycarbide Glasses Derived from Polysiloxane Precursors.* MRS Proceedings, 2011. **346**: p. 351.
51. Huang, J., et al., *An interfacial crosslinking strategy to fabricate an ultrathin two-dimensional composite of silicon oxycarbide-enwrapped silicon nanoparticles for high-performance lithium storage.* Journal of Materials Chemistry A, 2019. **7**(40): p. 22950-22957.
52. Su, D., et al., *Preparation and characterization of continuous SiZrOC fibers by polyvinyl pyrrolidone-assisted sol–gel process.* Journal of materials science, 2016. **51**(3): p. 1418-1427.
53. Shi, H., A. Yuan, and J. Xu, *Tailored synthesis of monodispersed nano/submicron porous silicon oxycarbide (SiOC) spheres with improved Li-storage performance as an anode material for Li-ion batteries.* Journal of Power Sources, 2017. **364**: p. 288-298.

54. Wheeler, D.R. and S.V. Pepper, *Angle-resolved X-ray photoelectron spectroscopy of epitaxially grown (100) β-SiC to 1300° C.* Surface and Interface Analysis, 1987. **10**(2-3): p. 153-162.
55. Ramarao, S.D. and V.R.K. Murthy, *Crystal structure refinement and microwave dielectric properties of new low dielectric loss AZrNb2O8 (A: Mn, Zn, Mg and Co) ceramics.* Scripta Materialia, 2013. **69**(3): p. 274-277.
56. Negita, K., *Effective sintering aids for silicon carbide ceramics: reactivities of silicon carbide with various additives.* Journal of the American Ceramic Society, 1986. **69**(12): p. C-308-C-310.
57. Pan, Y. and J.L. Baptista, *Chemical instability of silicon carbide in the presence of transition metals.* Journal of the American Ceramic Society, 1996. **79**(8): p. 2017-2026.
58. De Heer, J., *The principle of le chatelier and braun.* Journal of Chemical Education, 1957. **34**(8): p. 375.
59. Qian, J., J. Wang, and Z. Jin, *Preparation of biomorphic SiC ceramic by carbothermal reduction of oak wood charcoal.* Materials Science and Engineering: A, 2004. **371**(1): p. 229-235.
60. Weimer, A.W., et al., *Kinetics of carbothermal reduction synthesis of beta silicon carbide.* AIChE Journal, 1993. **39**(3): p. 493-503.

Chapter 4

Nickel‐containing magnetoceramic from water vapor‐assisted pyrolysis of polysiloxane and nickel 2,4‐pentanedionate

Ni Yang, Min Gao, Jiefang Li, and Kathy Lu*
Department of Materials Science and Engineering, Virginia Polytechnic Institute and State University, Blacksburg, Virginia, 24061, USA
*Corresponding author: Email: klu@vt.edu
Declarations of interest: none

*This chapter has been adapted from a **published** manuscript by Ni Yang Min Gao, Jiefang Li, and Kathy Lu from the following reference:*

Ni Yang, Min Gao, Jiefang Li, and Kathy Lu. "Nickel‐containing magnetoceramics from water vapor‐assisted pyrolysis of polysiloxane and nickel 2, 4‐pentanedionate." Journal of the American Ceramic Society 103.1 (2020): 145-157.

Reprinted with permission from the Wiley.

4.1. Abstract

In this study, novel ferromagnetic Ni - containing silicon oxycarbide (SiOC – Ni) was successfully fabricated from a base polysiloxane (PSO) with the addition of nickel 2,4 - pentanedionate. The resultant SiOC – Ni nanocomposite consists of in situ formed Ni nanocrystallites with a small amount of NiO uniformly dispersed in the amorphous SiOC matrix, and the corresponding nanocrystallite size increases with the increase of the pyrolysis temperature. The formation of nickel silicides (Ni_xSi_y) is completely suppressed by the effect of water vapor during the pyrolysis. The fundamental phase evolution process and mechanisms are explained. In an argon atmosphere, the SiOC–Ni materials pyrolyzed at 900°C are stable up to 1000°C with less than 6 wt% weight loss; they exhibit desirable electrical conductivity up to ~900°C with the highest electrical conductivity at ~247 S/m. This series of SiOC–Ni materials also demonstrates exciting ferromagnetic behaviors. Their new semiconducting behavior with soft ferromagnetism presents promising application potentials for magnetic sensors, transformers, actuators, etc.

4.2. Introduction

Polymer-derived ceramics (PDCs) are a novel class of materials directly prepared from the pyrolysis of hypercrosslinked polymer precursors [1, 2], without using the lengthy and sophisticated methods as for conventional ceramics, such as two-step sintering [3], hot isostatic pressing [4], or spark plasma sintering [5]. Besides that, different material formats and complex shapes can be made with the liquid processing ability of the polymer precursors, for example, thin films, hollow tubes, additively manufactured 3D objects, and bulk ceramics [6, 7]. Among the PDCs, silicon oxycarbide (SiOC) has attracted considerable interest because of its enhanced thermomechanical properties [8-10], high thermal stability [11], and superior thermal conductivity [12]. In order to expand the scope of applications for SiOC ceramics, both inert and active fillers can be incorporated into polymer precursors before cross-linking to adjust their thermomechanical properties and functional properties [13-16]. The tunable thermophysical and functional properties together with high-temperature stability and oxidation resistance make filler-containing SiOCs excellent candidates in harsh environments.

Transition metal (eg, Cr, Mn, Fe, Co, Ni, and Cu)-modified SiOCs have been among the most intensively studied as they have outstanding magnetic, catalytic, and electrical properties [17-23]. In this paper, we focus on the Ni-containing SiOCs since it is one of the most promising candidates in catalytic and magnetic areas [24-27]. However, the nonuniform distribution of Ni particles in PDCs through traditional powder mixing compromises desired properties. Therefore, chemical modification using Ni-containing precursors was studied, where Ni can be transformed from organometallic complexes to homogeneously distributed Ni nanocrystallites. A Si–Ni–C–N multiphase was synthesized by bulk pyrolysis of polysilazane and nickelocene at high temperatures [28]. Porous and magnetic SiOC(H) ceramic was obtained by the pyrolysis of allylhydridopolycarbosilane with nickel (II) acetylacetonate ($Ni(acac)_2$) [29]. Ni-containing porous SiOC was also produced from a mixture of polyphenylmethylsiloxane, azodicarbonamide, and nickel (II) acetylacetonate by direct foaming [23]. However, in a strict sense, all the aforementioned ceramics contain not only Ni crystallites but also inevitably nickel silicides. The formation of nickel silicides is believed to be caused by the reaction between silicon carbide (SiC) and Ni at 900°C in argon environments [30, 31].

We previously reported using water vapor to preferentially remove the free carbon in the SiOC matrix, thus the formation of SiC was suppressed [32]. With the less dominant presence of SiC, metal silicide formation can be potentially inhibited [33]. Water vapor pyrolysis of uniform mixtures of polymer precursors and nickel-containing compounds can be an exciting method to form Ni nanocrystallite-containing PDCs without nickel silicides even at high temperatures (eg, >900°C). It can open an exciting avenue for high-temperature functional SiOC synthesis and applications.

In this paper, the carbon-rich polysiloxane is chosen as the preceramic precursor in order to obtain desirable cross-linking ability of the precursor and the electrical conductivity of the resulting ceramic. The carbon-rich nature can effectively delay SiOC phase separation and crystallization into SiO_2 and SiC during pyrolysis [16]. which further delay the reaction products of nickel silicides due to the reaction between nickel and SiO_2. This work is focused on in situ syntheses of SiOC–Ni magnetoceramics with water vapor-assisted pyrolysis. The effects of nickel content and pyrolysis temperature on the resulting thermophysical properties, phase evolution, thermal stability, electrical conductivity, and magnetic properties are investigated.

4.3. Experimental procedure

A commercially available polysiloxane Polyramic® SPR-684 (PSO, $[–Si(C_5H_6)_2O–]_3[–Si(CH_3)(H)O–]_2[–Si(CH_3)(CH=CH_2)O–]_2$, Starfire Systems, Inc.) was used as the base precursor. Ni(II) 2,4-pentanedionate (Alfa Aesar) with 95% purity was chosen as the nickel additive. Anhydrous tetrahydrofuran (THF, 99.7+%, Alfa Aesar) was further desiccated by a molecular sieve (mSorb®) and used as the solvent. About 2% platinum-divinyltetramethyldisiloxane complex in xylene (Pt catalyst, Gelest Inc.) was used as the catalyst only for cross-linking of the pure PSO.

First, nickel (II) 2,4-pentanedionate was introduced into a beaker in an argon atmosphere in a glove box (Labstar^{pro}, MBRAUN®). A certain amount of THF was then added to dissolve the Ni (II) complex (the weight ratio of THF to Ni (II) complex was 12:1) with magnetic stirring at room temperature until a clear green solution was prepared. After that, PSO was introduced into the resultant greenish solution and magnetically stirred at 200 rpm for 2 hours to form a homogeneous mixture. The weight percent of Ni (II) 2,4-pentanedionate to PSO was 19.35, 38.70, 58.05, and 77.40 wt% (1, 2, 3, and 4 vol% Ni relative to the cross-linked bulk sample, respectively). The homogeneous mixture without any Pt catalyst was then cast into an aluminum mold and placed in a vacuum chamber until 1500 mTorr was reached to remove bubbles and THF. Afterward a viscous dark-green Ni (II)-containing precursor was obtained in each mold. A blank group without any Ni (II) complex was prepared under similar conditions. When cross-linking PSO with 0 wt% Ni (II) complex, 2.5 ppm of the diluted Pt catalyst solution (1 wt% relative to PSO) was added in order to slow down the cross-linking process and avoid defect deformation. The cross-linking of the PSO and Ni (II) 2,4-pentanedionate precursor was performed in an oven at 50°C for 12 hours, and then at 100°C for 12 hours.

To prepare the cross-linked samples for pyrolysis, the cured materials were first cut and polished to roughly 10 mm × 10 mm × 2.5 mm size. The polished samples were put in a zirconia boat with both sides covered by graphite mats and then placed into a tube furnace (1730–12 Horizontal Tube Furnace, CM Furnaces Inc.). With an Argon flow rate of about 500 cm^3/min, the samples were heated up to 500°C with a rate of 2°C/min. Water vapor was injected (Ar: H_2O molar ratio was about 5:1) at a range of 500-700°C with a heating rate of 1°C/min to reduce free carbon and SiC formation since carbon precipitation mainly occurs at 500-700°C during the polymer to

ceramic transformation. The details can be found elsewhere [32, 34, 35]. Then the temperature was raised to 800, 900, and 1100°C respectively at 2°C/min with a holding time of 2 hours, and cooled down to 50°C with a rate of 2°C/min. The samples were marked as SiOC–Ni-1, SiOC–Ni-2, SiOC–Ni-3, and SiOC–Ni-4, respectively (the numeral value represents the Ni vol%) in the cross-linked samples. A blank group without Ni was denoted as SiOC. The ceramic yield and shrinkage of the above samples were also recorded.

Phase compositions of the pyrolyzed bulk samples were investigated by using an X'Pert PRO diffractometer (PANalytical B.V.). The densities of the resulting products were measured in triplicates by a pycnometer (AccuPyc II 1340, Micromeritics®), using helium gas at an outlet pressure of 148 237 Pa in a 7.8 cm^3 sample cell. The microstructures of the Ni–SiOC samples were analyzed by a field-emission scanning electron microscope (SEM, LEO1550, Carl Zeiss MicroImaging, Inc.). The electrical conductivity of the pyrolyzed samples was measured in an Ar atmosphere from 50 to 1200°C in a four-point probe configuration using a potentiostat (Versa STAT 3, Princeton Applied Research). For the electrical conductivity measurement, palladium/silver paste (ESL Electroscience) electrodes were painted on the surfaces of the samples. The thermal stability of the samples after pyrolysis was analyzed by thermogravimetric analysis (TGA) using an STA 449C Jupiters® analyzer (Netzsch - Gerätebau GmbH) from room temperature to 1000°C at a heating rate of 5°C/min and an air flux of 40 mL/min. Raman spectra were recorded on a Horiba spectrometer (JY Horiba HR 800) with an excitation wavelength of 514 nm produced by an Ar laser in the spectral range of 0-4000 cm^{-1}.

The carbon compositions of the samples were analyzed by a combustion method, which was conducted by Galbraith Laboratories, Inc. Acid digestion and titration were used to obtain the silicon content by an ICP-OES method. The Ni content was calculated from the amount of nickel 2,4-pentanedionate used. The oxygen content was extracted based on the above results and the total mass of the samples. Specific surface area, pore size distribution, and pore volume of the pyrolyzed samples were studied by the BET method with a Quantachrome Autosorb -1 analyzer. For the testing, the samples were crushed into small pieces from the original bulk. The degassing temperature was 300°C, the degassing time was 6 hours, and the degassing pressure rise limit was controlled below 10 μm/min (0.01 mmHg/min). The average pore size and pore volume were

derived from the nonlinear density functional theory (NLDFT) model based on the adsorption isotherm, and the average pore sizes were derived from the pore volumes.

4.4. Results and discussion

4.4.1. Thermophysical evolution

Except for the SiOC–Ni-4 samples, all the other samples are intact and have good shape retention after the water-assisted pyrolysis at 800, 900, and 1100°C. The chemical formulas of the pyrolyzed SiOC and SiOC–Ni-4 samples at three different pyrolysis temperatures are measured to be $SiO_3C_{2.4}$ (SiOC, 800°C), $SiO_{1.24}C_{2.13}$ (SiOC, 900°C), $SiO_{2.2}C_{2.5}$ (SiOC, 1100°C), $SiO_{2.61}C_{1.97}Ni_{0.36}$ (SiOC–Ni-4, 800°C), $SiO_{1.75}C_{2.07}Ni_{0.54}$ (SiOC–Ni-4, 900°C), and $SiO_{1.89}C_{0.59}Ni_{0.37}$ (SiOC–Ni-4, 1100°C). The chemical compositions of the SiOC samples are consistent with those of the typical amorphous silicon oxycarbide. A drastic drop in the carbon content for the SiOC–Ni-4 samples from 900°C to 1100°C is observed. This is because the introduction of nickel makes the system more unstable at temperatures higher than 900°C, and leads to more carbon loss than the SiOC system. Table 4.1 shows the volume shrinkage, ceramic yield, and density values for all the pyrolyzed samples. The SiOC–Ni-4 samples pyrolyzed at 800°C and 1100°C have broken into pieces after pyrolysis, so no volume shrinkage values are obtained in Table 4.1. The breakage is due to the more significant decomposition of Ni(II) 2,4-pentanedionate and thus more significant pore formation along with more shrinkage-induced stress and cracking, consistent with the volume shrinkage results in Table 2.1. The unpolished surfaces of these bulk samples are black, smooth, and have shining metallic reflection.

Table 4.1. Volume shrinkage, ceramic yield, and density of the SiOC–Ni samples.

Sample	**Volumetric Shrinkage (%)**			**Ceramic Yield (%)**			**Density (g/cm^3)**		
	800 °C	900 °C	1100 °C	800 °C	900 °C	1100 °C	800 °C	900 °C	1100 °C

SiOC	25.85 ± 0.09	27.26 ± 2.27	27.80 ± 1.66	65.50 ± 1.61	63.37 ± 2.54	61.37 ± 1.55	1.70 ± 0.72	2.18 ± 0.18	2.19 ± 2.75
SiOC-Ni-1	27.16 ± 4.59	34.90 ± 0.57	33.07 ± 2.23	65.11 ± 0.57	63.55 ± 1.26	60.75 ± 1.84	1.89 ± 0.21	2.41 ± 0.85	2.42 ± 1.32
SiOC-Ni-2	39.80 ± 0.39	41.62 ± 4.93	37.02 ± 2.69	56.20 ± 2.53	55.72 ± 2.27	53.69 ± 0.30	2.05 ± 0.32	2.57 ± 1.78	2.50 ± 0.23
SiOC-Ni-3	45.35 ± 3.69	52.34 ± 2.92	50.62 ± 3.79	50.93 ± 1.61	48.47 ± 2.21	48.72 ± 0.38	2.07 ± 0.54	2.69 ± 1.51	2.51 ± 0.66
SiOC-Ni-4	N/A	64.48 ± 4.37	N/A	44.69 ± 0.35	45.57 ± 1.17	40.84 ± 0.15	2.48 ± 0.64	2.80 ± 1.52	2.84 ± 0.40

Table 4.1 shows that the volume shrinkages for the intact samples vary from ~25.85% to ~64.48%, a relatively wide range. At the same pyrolysis temperature, the volume shrinkage increases with the increase of the Ni content. This is because of the larger extent of decomposition of nickel (II) 2,4-pentanedionate during the pyrolysis. It also explains why these volume shrinkage values are higher than that of the pure SiOC systems. As a result, a higher Ni content leads to a larger shrinkage. For the same Ni content, the volume shrinkage in general increases with increasing pyrolysis temperature from 800 to 1100°C, even when the changes are not always consistent due to the small differences. Some transient pores collapse and the SiOC structure evolution complicates the volume shrinkage behavior. Thus, the volume shrinkage varies.

The ceramic yields range from ~40.84% to ~65.50%. At the same Ni content, the ceramic yield generally decreases with the temperature increase from 800 to 1100°C. This is understandable as the PSO generates more free carbon with increasing pyrolysis temperature and thus potentially experiences more weight loss through evaporative species [36]. In general, more free carbon formation leads to a lower ceramic yield. At the same pyrolysis temperature, an

increase in the Ni content results in a decrease in the ceramic yield. This is because of the formation of evaporative species (e.g., CO, CO_2) during the decomposition of nickel (II) 2,4-pentanedionate.

The densities for all the samples are in the range of 1.70-2.84 g/cm^3. At the same pyrolysis temperature, a higher Ni content generally leads to higher bulk density due to the higher density of Ni (8.91 g/cm^3). With the pyrolysis temperature increase, the density generally increases even when there is some variation within the standard deviation. This is due to further SiOC matrix and Ni evolution, which will be explained next.

4.4.2. Phase evolution

The XRD patterns in Figure 4.1 show the phases of the SiOC–Ni samples pyrolyzed in Ar+H_2O at 800, 900, and 1100°C. The crystalline phases are identified as cubic Ni (JCPDS Card No. 98-012-3814), hexagonal NiO (JCPDS Card No. 98-0044-9032), and hexagonal graphite (JCPDS Card No. 98-006-2692). All the pure SiOC samples remain amorphous at 800-1100°C pyrolysis temperatures. This has been well studied in our previous work [16, 36, 37]. In Figure 4.1(a-c), the SiOC–Ni-1, 2, 3, and 4 samples exhibit three sharp diffraction peaks at 44.49°, 51.85°, and 76.38°, which are attributed to the (111), (200), and (220) crystallographic planes of the Ni phase; and the minor shoulder peaks centering at 37.10°, 43.10°, and 62.60° are indexed to be (111), (002), and (022) crystallographic planes of NiO. Desirably, pure Ni phase is formed and no nickel silicides are detected in the materials.

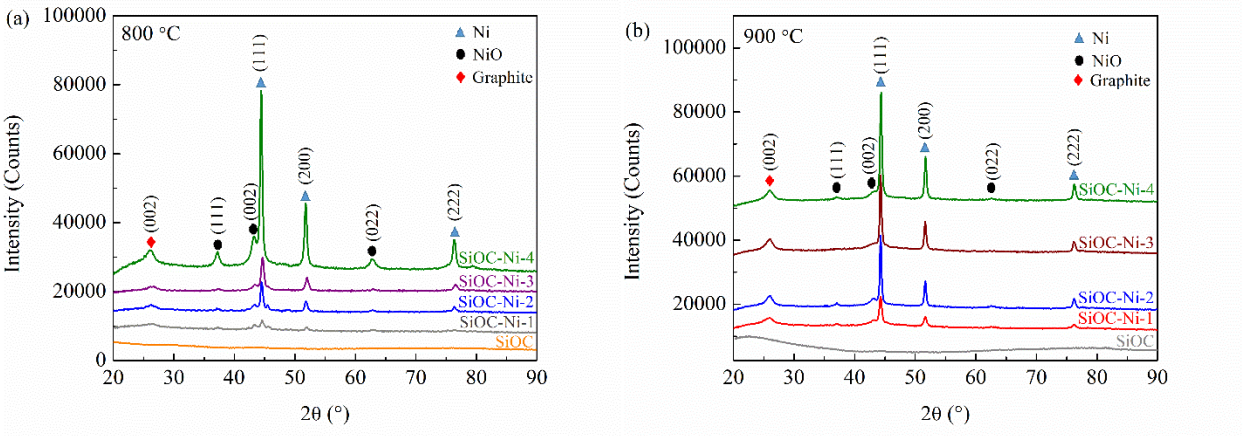

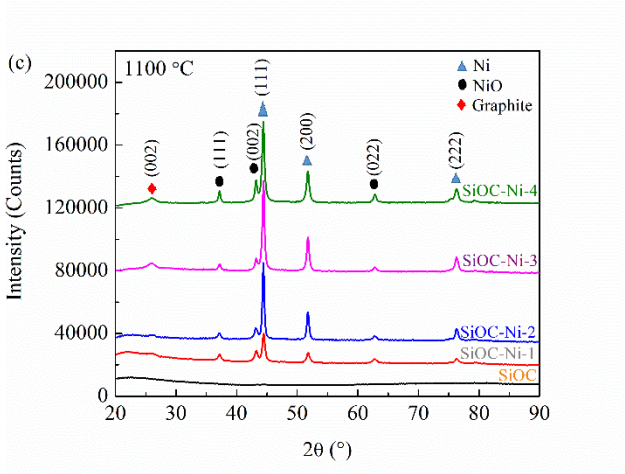

Fig. 4.1. XRD patterns of the SiOC-Ni samples pyrolyzed at (a) 800 °C, (b) 900 °C, and (c) 1100 °C for 2 h in flowing argon with water vapor.

The above observations show that nickel 2,4-pentanedionate can be carbothermally reduced to Ni in the SiOC matrix. Based on literature, the following reactions should occur [38, 39]:

$$C_{10}H_{14}NiO_4 \rightarrow Ni^{(0)}/Ni^{(2+)} + CO + C_xH_y + H_2 \quad 230\ °C \tag{4.1}$$

$$[\text{-}OSi(CH_3)_2\text{-}]_n[\text{-}OSiRO_2\text{-}]_m \rightarrow \text{Si-O-C} + H_2 + C_xH_y + \text{siloxane oligomers} \quad 400 - 600\ °C \tag{4.2}$$

$$Ni^{(0)}/Ni^{(2+)} \xrightarrow{C_xH_y/H_2} Ni^{(0)} \quad 230 - 600\ °C \tag{4.3}$$

The presence of the NiO phase can be explained in three aspects. First, water vapor dissociates into OH (ads) and H (ads) species at 500-700°C, and OH^- reacts with Ni and subsequent loss of H to form NiO [40, 41]. The reaction is believed to occur as follows:

$$5Ni + OH^-_{(ads)} + H^+_{(ads)} = NiO + 4NiH_{0.5} \quad 500 - 700\ °C \tag{4.4}$$

The Gibbs free energy of the NiO formation can be calculated with software HSC Chemistry 6.0. In the calculation, the Gibbs free energy of Equation (4.4) is from −1445.4 kJ/mol (500°C) to −1391.5 kJ/mole (700°C). It means that the formation of NiO is thermodynamically favorable. However, nickel hydride ($NiH_{0.5}$) is not stable and decomposes gradually even at room temperature with hydrogen evolution [42]. The second explanation for the NiO formation is the incomplete reduction of the oxygen-containing nickel species during the polymer-to-ceramic transformation, even in an argon atmosphere, because the precursors contain oxygen species [29]. The third

explanation is that with the increase of the pyrolysis temperature, Ni can react with the oxygen from the SiO_xC_y phase [43] and form the NiO phase.

It is important to note that the content of the NiO phase varies with the pyrolysis temperature. Figure 4.1 shows that at 900°C, the relative peak height for NiO is the lowest. This observation can be explained as follows. At 800°C, incomplete reduction of $Ni^{(2+)}$ ions has contributed more NiO in situ formation in the matrix, which is less obvious when the temperature goes higher than 800°C. With more gases (such as C_xH_y, H_2) from decomposition, at 900°C pyrolysis, more nickel crystallites form according to Equation (4.3). However, at much higher temperatures, such as 1100°C, the reaction between reduced Ni and the oxygen element in the SiOC results in more NiO formation. As a result, the optimal pyrolysis temperature for pure Ni formation is 900°C, which is consistent with the values of saturation magnetization in Table 4.2.

Table 4.2. The saturation magnetization (M_s), coercive field (H_c), and squareness ratio (M_r/M_s) of the SiOC–Ni samples at different pyrolysis temperature

Pyrolysis temperature (°C)		**800**	**900**	**1100**
Saturation magnetization (M_s) (emu/g)	SiOC-Ni-1	0.15	1.48	0.25
	SiOC-Ni-2	0.65	3.55	1.04
	SiOC-Ni-3	0.96	5.46	3.13
	SiOC-Ni-4	3.06	7.14	4.53
Coercivity (H_c) (Oe)	SiOC-Ni-1	19.96	99.98	139.92
	SiOC-Ni-2	59.97	139.96	139.95
	SiOC-Ni-3	39.94	39.93	159.96
	SiOC-Ni-4	139.96	39.92	119.91
Squareness ratio (M_r/M_s)	SiOC-Ni-1	0.07	0.28	0.20
	SiOC-Ni-2	0.26	0.29	0.26
	SiOC-Ni-3	0.24	0.14	0.19
	SiOC-Ni-4	0.35	0.10	0.15

In Figure 4.1(a-c), three small diffraction peaks indexed to be NiO are more evident in the higher Ni-containing samples, indicating that the amount of NiO is promoted with increasing Ni(II)-2,4-pentanedionate. This can be attributed to either less complete reduction of the oxygen-containing Ni precursor at lower temperatures or more extensive oxidation of the pure Ni at high temperatures.

The peak detected at 26.6° in Figure 4.1(a-c) is attributed to the (002) plane of graphitic carbon. Metal Ni can lead to the formation of turbostratic carbon by a few hundred degrees lower temperature [39]. For the SiOC–Ni systems, this means that the turbostratic carbon can form at 800°C. The amount of the turbostratic carbon also increases with the Ni content and can be explained as Ni-catalyzed in situ formations of turbostratic carbon in the SiOC matrix. The detailed mechanism will be explained in Section 3.4.

In general, different kinds of intermetallic nickel silicides can form between 850 and 1000°C [39]. Since nickel silicides are only weakly magnetic, suppressing the formation of nickel silicides can be an effective method to enhance the magnetic properties of the SiOC–Ni systems as to be discussed in Section 3.5.

From the well-known Scherrer equation the average size of the Ni nanocrystallites can be calculated as:

$$d = \frac{k\lambda}{\beta\cos(\theta)} \tag{4.5}$$

where λ is the X-ray wavelength of Cu Kα, which equals to 1.5406 Å, β is the peak width of the diffraction peak profile at half maximum intensity of the peak (FWHM) in radians, and K is a constant related to crystallite shapes, usually taken as 0.9. The average Ni size is calculated to be ~87.32 ± 26.24 nm (800°C), ~112.23 ± 22.45 nm (900°C), and ~186.32 ± 24.59 nm (1100°C).

The morphology and distribution of the Ni nanocrystallites at different pyrolysis temperatures are further investigated. Here, the SiOC–Ni-4 composition is used as the lower Ni compositions have even better Ni dispersion and Ni nanocrystallite size distribution because of the lower Ni content. Some bright, roundish species are clearly visible in Figure 4.2(a-c). We believe that these microstructures mainly show the presence of Ni nanocrystallites along with some minor NiO phase. Since Ni (8.91 g/cm^3) and NiO (6.67 g/cm^3) have much higher density than the SiOC matrix (SiOC,

2.2-2.3 g/cm^3; amorphous carbon, 1.45 g/cm^3 [13]), the bright Ni/NiO crystallites have brighter contrast than the amorphous matrix even when they cannot be clearly differentiated from each other. Thus, it can be stated that the Ni nanocrystallites are well-dispersed in the SiOC–Ni-4 samples without any aggregation. Each nanocrystallite displays a similar shape, and the diameters of these Ni nanoparticles increase with the pyrolysis temperature, consistent with the calculated result from the Scherrer equation in Equation (4.5). The SiOC matrix prevents Ni nanocrystallites from sintering to form larger aggregates [39]. The surface area (41.591, 60.249, and 64.534 m^2/g) and pore volume (0.053, 0.093, and 0.133 cc/g) of the SiOC–Ni-4 samples in Figure 4.2(a-c) increase with the pyrolysis temperature, consistent with the phase separation increase. The pyrolysis temperature has the same effect on the surface area and pore volume as that of the nickel content. It should be mentioned that pores are formed in the SiOC–Ni-4 sample at the pyrolysis temperature of 1100°C, which is believed to be due to the decomposition of nickel 2,4-pentanedionate as shown in Equations (4.1) and (4.2).

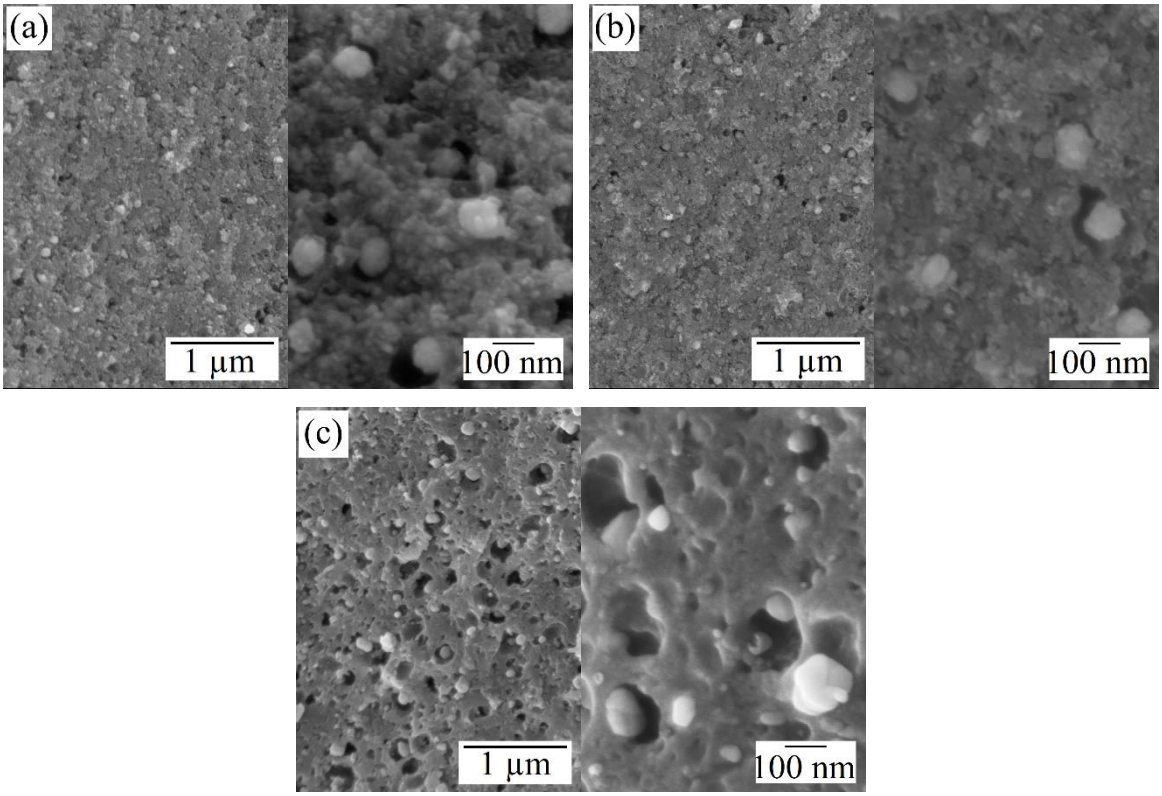

Fig. 4.2. SEM micrographs of the SiOC-Ni-4 sample at (a) 800 °C, (b) 900 °C, and (c) 1100 °C pyrolysis temperature with water vapor.

4.4.3. Thermal stability

Our previous studies about pure SiOCs [16, 32] report that the SiOC matrix is composed of a homogeneous network of Si–O–C structures and free carbon at 800°C-1100°C pyrolysis temperatures. The SiC_xO_y matrix is featureless in which the free carbon is dispersed. The free carbon can be easily oxidized, which can lead to weight loss. The specific oxidation mechanism is the combustion of the free carbon phase:

$$C_{free} + O_2 \rightarrow CO_x \quad (4.6)$$

This should lead to weight loss on the TGA curves. Along with Eq. (4.7) + (4.6), the SiOC units can become more vulnerable to oxidization to SiO_2 and result in weight gain:

$$SiOC + O_2 \rightarrow SiO_2 + CO_x \quad (4.7)$$

For the SiOC-Ni ceramics, the oxidation of Ni can also lead to weight gain and can be represented by:

$$Ni + O_2 \rightarrow Ni_xO_y \quad (4.8)$$

In Figure 4.3(a), there is a mass loss of 0.19-3.29 wt% from 25 to 100°C for the SiOC–Ni samples pyrolyzed at different temperatures, which can be caused by the evaporation of adsorbed moisture since the samples were not dried before the TGA testing. After that temperature region, there is no mass loss for all the samples at ≤600°C. It means that the SiOC–Ni systems are stable up to ~600°C in the air condition. However, there is ~26.6 wt% mass loss for the pure SiOC sample between 600°C and 1000°C, indicating a continuous deterioration of the thermal stability for the matrix. This is believed to be due to carbon burning (Equation 4.6) in the temperature range of 600°C-1000°C [44]. For the SiOC–Ni samples, however, the mass losses are 43.3, 40.4, 39.7, and 23.6 wt%, respectively at 600-1000°C from the 1 vol% to 4 vol% Ni conditions. The amount of mass loss decreases with the increase in the Ni amount. This is because more NiO is formed and results in more weight gain based on Equation (4.8). However, the Ni-containing samples are less stable than the pure SiOC sample; significant mass loss starts at around the same temperature. This is due to more free carbon formation in the SiOC–Ni samples by Ni catalysis (the detailed

mechanism will be explained in Section 3.4), which makes the SiOC–Ni samples less stable than the pure SiOC samples.

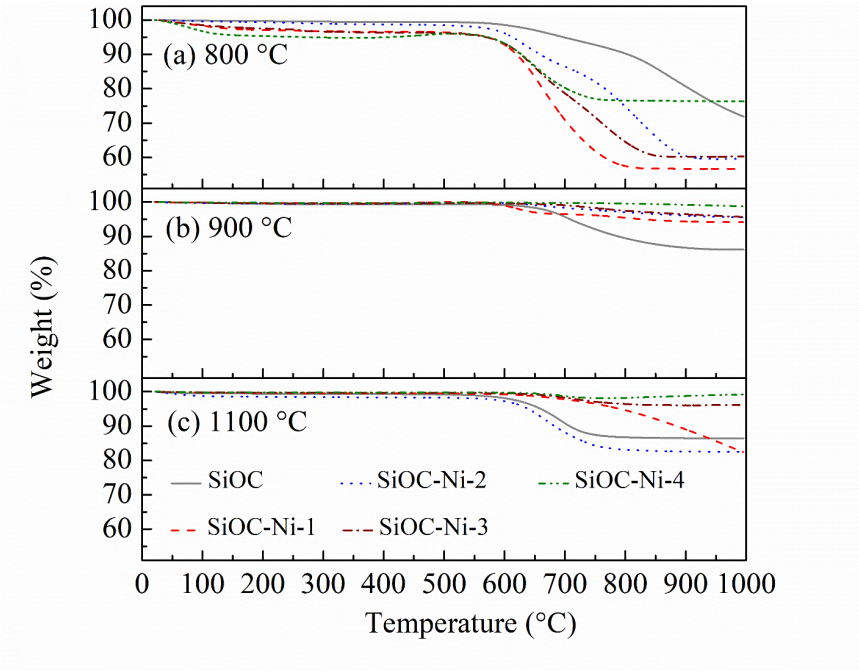

Fig. 4.3. TGA curves for the SiOCs with different Ni contents after pyrolysis at (a) 800 °C, (b) 900 °C, and (c) 1100 °C for 2 h in flowing argon with water vapor.

At 900°C pyrolysis temperature (Figure 4.3(b)), the mass losses for the pure SiOC, SiOC–Ni-1, 2, 3, and 4 samples are 13.9, 5.9, 4.5, 4.4, and 1.3 wt%, respectively. The thermal stability trend is opposite to what is shown in Figure 4.3(a). All the SiOC–Ni samples are more stable than the pure SiOC sample. This can be ascribed to more in situ formed Ni, as confirmed by the magnetic hysteresis curves (Figure 4.7(a-c)). Because of the relatively higher amount of Ni formed in the SiOC matrix at 900°C, the weight loss based on Equation (4.6) and the weight gain based on Equations (4.7) and (4.8) cancel each other out and make the TGA curves for the SiOC–Ni samples flatter. Higher Ni content leads to less overall mass loss.

When the pyrolysis temperature is 1100°C (Figure 4.3(c)), a similar trend is observed as shown in Figure 4.3(b). For the pure SiOC, there is a 13.6 wt% mass loss. For the SiOC–Ni samples, we believe that the interconnected network of sp^2 graphite carbon is embedded in clusters of tetrahedral SiOC-SiO2. Higher pyrolysis temperature results in more organized carbon

[45], promoting the ordering of turbostratic carbon layers to stacks of graphite-like layers. This explains why higher pyrolysis temperature leads to less mass loss during 900-1100°C. The weight losses of the pure SiOC, SiOC–Ni-1, 2, 3, and 4 are 13.6, 17.6, 17.5, 3.9, and 0.8 wt%, respectively. Since the weight gain effect from Equation (4.8) is more dominant for the SiOC–Ni-3 and SiOC–Ni-4 samples, the weight losses are lower than those of the other samples.

4.4.4. Electrical conductivity

For the SiOC samples with different Ni contents, the electrical conductivity between 50 and 1150°C in argon is given in Figure 4.4 as a function of temperature. The SiOC–Ni-4 samples pyrolyzed at 800 and 1100°C have broken into pieces, so no conductivity values are obtained in Figure 4.4.

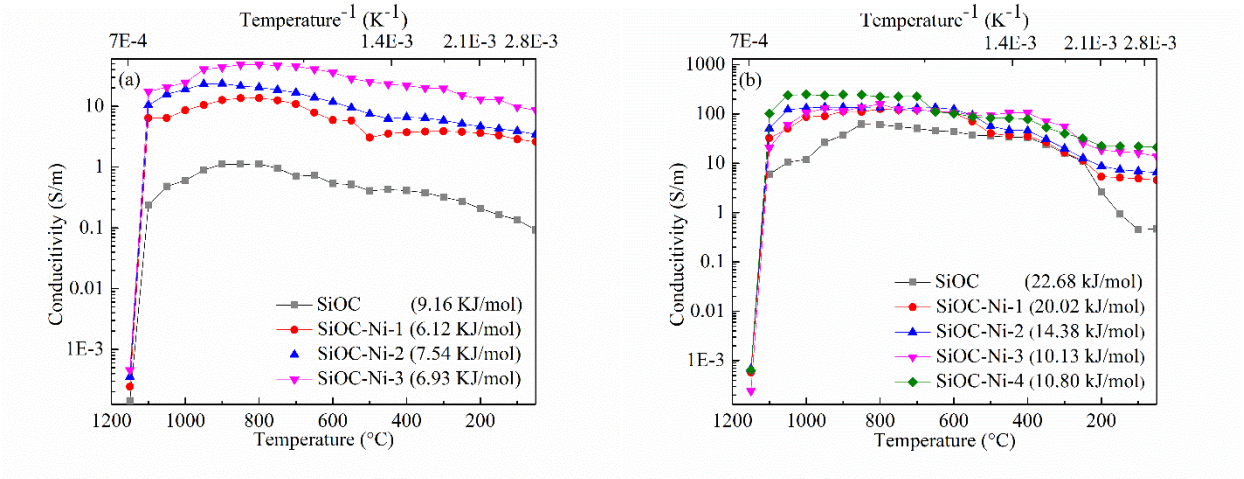

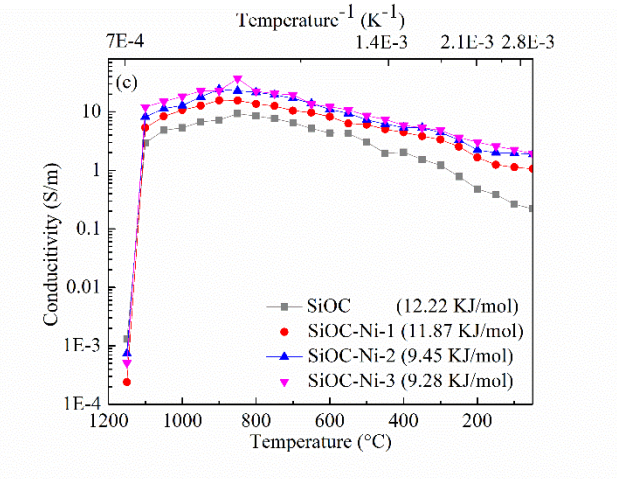

Fig. 4.4. Conductivities of the SiOC-Ni samples at different pyrolysis temperatures: (a) 800 °C, (b) 900 °C, and (c) 1100 °C.

Figure 4.4(a) shows that at 800°C pyrolysis temperature, the SiOC sample has much lower electrical conductivity compared with the SiOC–Ni samples. For the pure SiOC sample, the conductivity value changes from 0.09 S/m at 50°C to 1.13 S/m at 800°C before a marked decline at higher temperatures. For the SiOC–Ni-1 sample, the conductivity increases by two orders of magnitude, from 2.60 S/m at 50°C to 13.69 S/m at 800°C. For the SiOC–Ni-2 sample, the conductivity changes from 3.45 S/m at 50°C to 23.55 S/m at 900°C. For the SiOC–Ni-3 sample, the conductivity changes from 8.63 S/m at 50°C to 48.65 S/m at 850°C. The highest electrical conductivity value is 48.65 S/m for the samples pyrolyzed at 800°C. As seen, the electrical conductivity consistently increases with the Ni content.

At 900°C pyrolysis temperature, the SiOC and SiOC–Ni-1, 2, 3 samples have relatively lower electrical conductivity compared to the SiOC–Ni-4 composition, although some values overlap. The general trend is still valid. For the pure SiOC sample, the conductivity value changes from 0.46 S/m at 50°C to 62.07 S/m at 850°C before a marked decline at higher temperatures. Following the same trend as for the 800°C pyrolysis temperature, the electrical conductivity generally increases with the Ni content. The highest electrical conductivity value for the 900°C pyrolysis temperature is 246.69 S/m from the SiOC–Ni-4 sample, then the conductivity value decreases significantly as the test temperature becomes higher (Figure 4.4(b)).

At 1100°C pyrolysis temperature, the overall conductivity values are lower than that of the 800 and 900°C conditions. The electrical conductivity change based on the Ni content remains the same. For the SiOC sample, the conductivity increases from 0.21 S/m at 50°C to 9.29 S/m at 850°C. The conductivity of SiOC–Ni-1 changes from 1.06 S/m at 50°C to 15.75 S/m at 850°C. The conductivity of SiOC–Ni-2 increases from 1.87 S/m at 50°C to 24.20 S/m at 900°C. The conductivity of SiOC–Ni-3 increases from 1.93 S/m at 50°C to 37.01 S/m at 850°C before decreasing significantly (Figure 4.4(C)). Some of the decrease in the electrical conductivity in Figure 4.4(C) can be ascribed to the less than the fully dense structure of the samples, which has been discussed in Figure 4.2.

So far, the highest electrical conductivity is 246.69 S/m for the SiOC–Ni-4 sample pyrolyzed at 900°C.

SiOC is a favorable candidate for electrical conductivity owing to its special microstructure consisting of the semiconducting C phase [16, 46, 47]. Both the carbon content and the interconnectivity of the carbon network affect the electrical conductivity. A higher pyrolysisfsewction temperature leads to an increase in the free carbon content and ordering of the graphitic domains in the matrix, and thus higher electrical conductivity. In this study, the Ni nanocrystallites are highly conductive. However, their distribution is discrete and should not contribute directly to the electrical conductivity, especially considering the low contents. In our system, the carbon content and interconnectivity of the carbon network are believed to be the major factors for conductivity.

For the SiOC–Ni samples, Ni can accelerate the graphitization of free carbon; the sp^2 hybridization of carbon (transform from sp^3 to sp^2) increases and results in more percolating conductive network formation. Although the total carbon content is critical for the resulting electrical conductivity, the conductive carbon path formation cannot be neglected.

As seen in Figure 4.5, the most dominant features of the free carbon are the disorder-induced D band at 1350 cm^{-1} and the ordered graphite G band at 1588 cm^{-1}. The broad G′ band at 2682 cm^{-1} and the weak band at 2934 cm^{-1} can be assigned to a combination of the defect/disordering and graphitic mode (G + D). The Lorentzian curve fitting of the D and G bands can be used to extract the I_D/I_G intensity ratio, which is shown in Figure 4.5. At 1100°C pyrolysis temperature, the ratios of I_D/I_G for the pure SiOC, SiOC–Ni-1, 2, 3 and 4 samples are 1.53, 1.27,

1.25, 1.19, and 1.13, respectively. Obviously, the I_D/I_G ratios of the SiOC–Ni samples are lower than that of the pure SiOC; this ratio also decreases with the increase of the Ni content. The incorporation of Ni leads to the formation of more graphitic layers. With the increase of the Ni content, a decrease in I_D/I_G is observed because of the higher amount of graphic carbon, in agreement with the results obtained from the XRD results (Figure 4.1). Thus, it demonstrates that Ni induces ordering for the free carbon.

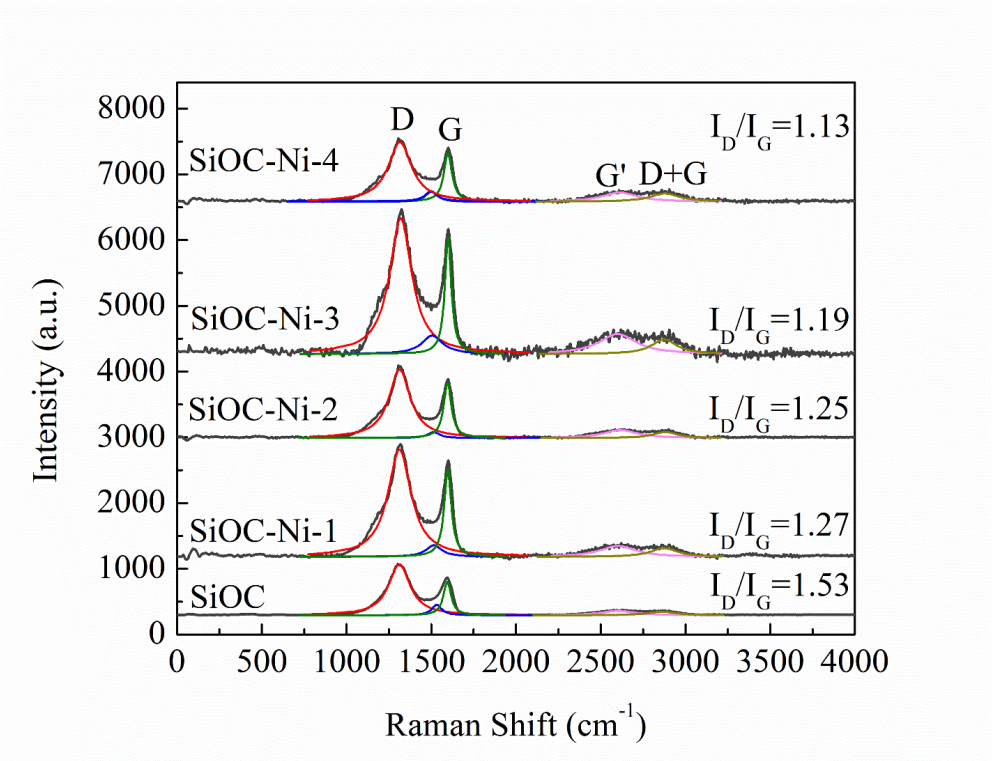

Fig. 4.5. Raman spectra of different SiOC-Ni samples pyrolyzed at 1100 °C.

The commonly perceived mechanism of nickel-induced carbon graphitization is diffusion-precipitation [48]. Without any catalyst, the conversion of disordered carbon into ordered carbon occurs between 2000°C and 3200°C [49]. In our system, the strong chemical interaction between the uniformly dispersed catalytic Ni and amorphous-free carbon breaks apart carbon-carbon bonds at a relatively low temperature of ~430°C [50]. Subsequently, carbon atoms dissolve in Ni particles (the carbon solubility of Ni is 1.15 at% at 1000°C) and precipitate as graphitic carbon between 550 and 700°C [51], as shown in Figure 4.6. During this period, Ni forms a metastable

Ni_3C compound with carbon, which has been reported to be unstable above 500°C [50, 52]. The driving force comes from the free energy difference between the disordered carbon and well-ordered graphitic carbon [53]. However, the degree of order is not high due to the limited pyrolysis temperature—thus the carbon in the SiOC samples is more likely to be turbostratic carbon. Throughout this process, the Ni surface provides a medium for the diffusion of mobile carbon atoms, thus facilitating ordered carbon growth.

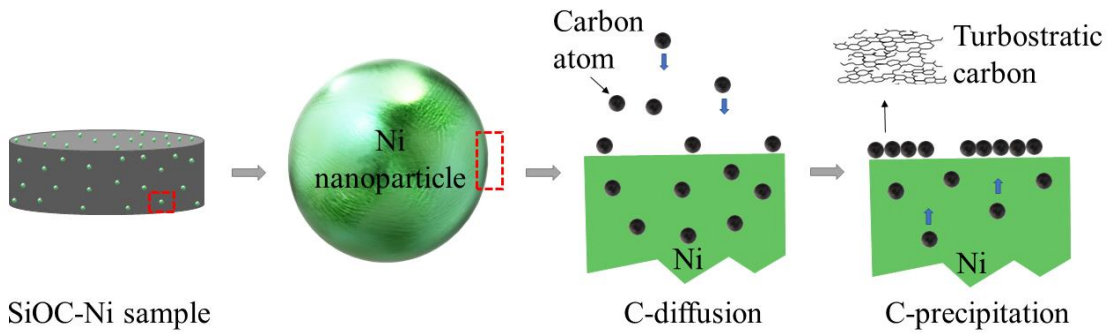

Fig. 4.6. Schematic of the formation of turbostratic carbon by diffusion-precipitation through Ni nanocrystallites.

The electrical conductivity results in Figure 4.4 follow the Arrhenius law and the activation energy can be derived from the electrical conductivity vs temperature slopes. As shown in Figure 4.4, the activation energies are fairly low; they also decrease with increasing Ni content, which proves that Ni-activated graphitization results in the percolating conductive network to enable the electrical conductivity for the SiOC–Ni systems. In our previous study [13, 16], the highest electrical conductivity values always occur at ~400°C due to the SiOC surface oxidation to SiO_2 before the sudden drop, as well as the break down of the conductive turbostratic carbon network under the electrical field. In this study, with the Ar atmosphere, the oxidation problem is not applicable and the electrical conductivity drops after 800-900°C. All the samples show a drastic conductivity decrease, which is caused by the thermal decomposition of silver/palladium pasted electrodes at around 1000°C. There is no value measured after 1150°C due to the destruction of

the conducting paste placed on the sample surface above 1100°C. The higher temperature-resistant paste is still being pursued in our study.

4.4.5. Magnetic property

The magnetic hysteresis loops of the SiOC–Ni samples pyrolyzed at 800, 900, and 1100°C are shown in Figure 4.7, from which we can summarize as (a) the hysteresis loops of all the SiOC–Ni compositions investigated are very narrow, exhibiting a "soft" ferromagnetic behavior with small values of coercivity; (b) the shape of the loop changes appreciably with the pyrolysis temperatures, which is related to the remnant Ni content.

The magnetic properties of the SiOC–Ni samples such as the saturation magnetization (M_s), coercivity (H_c), and squareness ratio (M_r/M_s) at room temperature are summarized in Table 4.2. The M_s varies from 0.15 emu/g to 7.14 emu/g. At 800°C pyrolysis temperature, the M_s values are 0.15 emu/g, 0.65 emu/g, 0.96 emu/g, and 3.06 emu/g respectively for the SiOC–Ni-1, SiOC–Ni-2, SiOC–Ni-3, and SiOC–Ni-4 samples, as shown in Figure 4.7(a). At a certain pyrolysis temperature, the value of M_s increases with the increase of the Ni content. A similar trend is also observed for the samples pyrolyzed at 900°C and 1100°C. Since the magnetization of the SiOC–Ni samples comes purely from the nickel particles, a higher amount of Ni leads to larger magnetization. It also explains why the M_s values for the 900°C pyrolyzed samples are notably higher than those of 800 and 1100°C. This is because of more Ni forms in situ inside the SiOC–Ni samples at 900°C, as discussed from mechanisms in Sections 3.2 and 3.3.

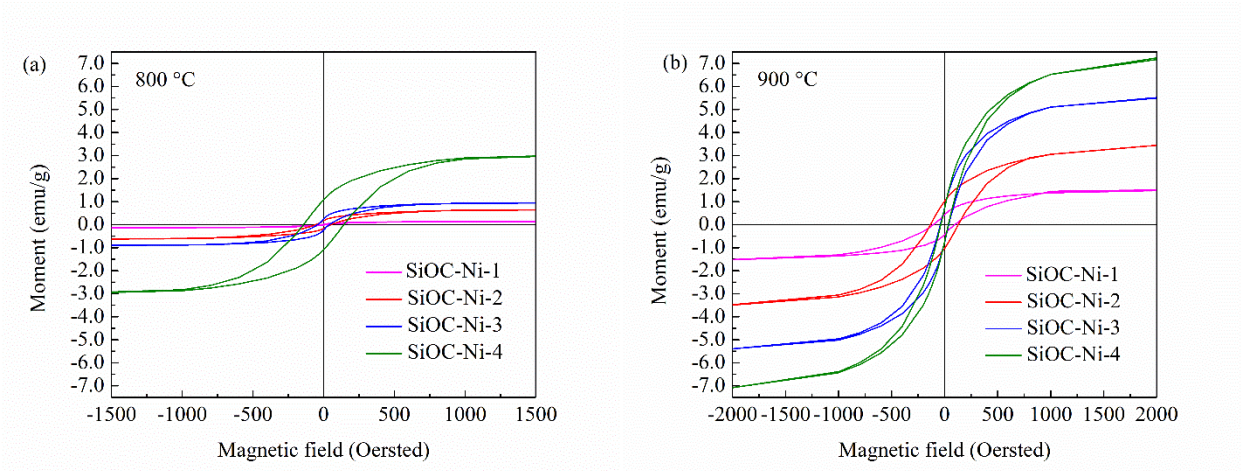

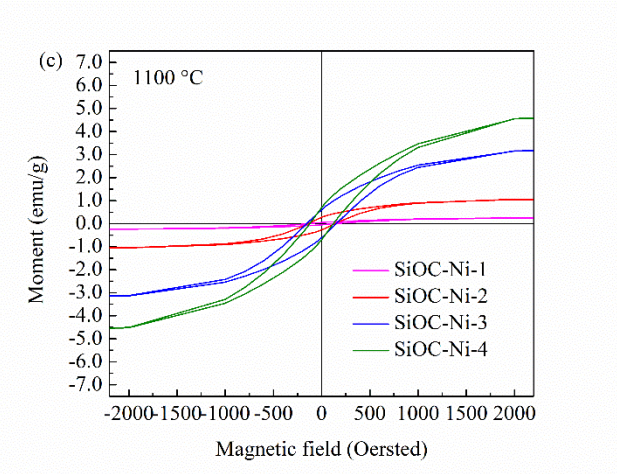

Fig. 4.7. Magnetic hysteresis loops of the SiOC-Ni ceramics pyrolyzed at (a) 800 °C, (b) 900 °C, and (c) 1100 °C.

The coercivity H_c varies from 19.96 Oe to 159.96 Oe. The variation in H_c can be interpreted based on the domain structure, critical diameter (D_c), and anisotropy of the Ni crystallites [54]. It is well-known that the formation of domain walls becomes energetically unfavorable if the nanocrystallite size is close to D_c [55-57]. Therefore, a smaller nanocrystallite size leads to a lower coercivity because of the thermal effect [58, 59]. However, at fixed pyrolysis temperature, there is no obvious relation between the coercivity and the Ni amount, indicating that the nanocrystallite size (and thus the coercivity) is more sensitive to the pyrolysis temperature than to the Ni amount. Since the hysteresis loss is dependent on the coercivity, a decrease in the size of Ni nanocrystallites can effectively decrease the hysteresis loss. In fact, the critical sizes for spherical Ni particles to exhibit superparamagnetism have been estimated to be below 20 nm [60], which is not much smaller than our results (see Section 3.2). It suggests that the SiOC–Ni samples could show almost zero coercivity by choosing the pyrolysis temperature more precisely to control the nanocrystallite size. As compared to Yu et al.'s work [29], there is not much difference between the results since both the M_s and M_r significantly increase with increasing Ni content for ferromagnetic materials. However, unlike Ni, NiO, and nickel silicide phases in the amorphous SiOC(H) matrix in Yu et al.'s work, nickel silicides are completely suppressed by the effect of water vapor during the pyrolysis.

Still, the relatively small coercivity and squareness ratio (from 0.18 to 0.26) demonstrates the "soft" ferromagnetic nature of the SiOC–Ni ceramics, indicating potentials in electronic applications like magnetic sensors and transformers [61].

4.5. Conclusions

In this study, SiOC–Ni samples are created without nickel silicide formation with the pyrolysis of a base polysiloxane with the addition of nickel 2,4-pentanedionate in an Ar+H_2O atmosphere at 800, 900, and 1100°C. The thermophysical characteristics, thermal stability, electrical conductivity, and magnetism of the SiOC–Ni samples are investigated. This SiOC–Ni samples are stable up to 600°C in air, and carbon burning occurs at 600-1000°C. In Ar, the highest electrical conductivity is 246.69 S/m at 900°C, which is two orders of magnitude higher than that of the pure SiOC. Such high electrical conductivity is closely related to the catalytic graphitization by Ni. Due to the formation of the Ni nanocrystallites in the SiOC matrix, the SiOC–Ni nanocomposites are soft ferromagnetic with the saturation magnetization in the range of 1.48-7.14 emu/g at 900°C pyrolysis temperatures. This family of materials can be used as magnetic sensors and transformers, and in hard disk drive technology.

4.6. References

1. Lu, K. and D. Erb, *Polymer derived silicon oxycarbide-based coatings.* International Materials Reviews, 2018. **63**(3): p. 139-161.
2. Ionescu, E., *Polymer Derived Ceramics*. 2012. p. 457-500.
3. Zhang, L., et al., *Alumina assisted grain refinement and physical performance enhancement of yttria transparent ceramics by two-step sintering.* Materials Science and Engineering: A, 2017. **684**: p. 466-469.
4. Jiang, N., et al., *Fabrication of highly transparent AlON ceramics by hot isostatic pressing post-treatment.* Journal of the European Ceramic Society, 2017. **37**(13): p. 4213-4216.
5. Ning, K. and K. Lu, *Ion irradiation effect on spark plasma sintered silicon carbide ceramics with nanostructured ferritic alloy aid.* Journal of the American Ceramic Society, 2018. **101**(8): p. 3662-3673.

6. Fu, Y., et al., *Multiple metals doped polymer-derived SiOC ceramics for 3D printing.* Ceramics International, 2018. **44**(10): p. 11030-11038.
7. Seo, D., et al., *Fabrication and electrical properties of polymer-derived ceramic (PDC) thin films for high-temperature heat flux sensors.* Sensors and Actuators A: Physical, 2011. **165**(2): p. 250-255.
8. Zanchetta, E., et al., *Stereolithography of SiOC ceramic microcomponents.* Advanced Materials, 2016. **28**(2): p. 370-376.
9. Tian, H., et al., *Structure and mechanical properties of porous silicon oxycarbide ceramics derived from silicone resin with different filler content.* Ceramics International, 2013. **39**(1): p. 71-74.
10. Colombo, P., J.R. Hellmann, and D.L. Shelleman, *Mechanical properties of silicon oxycarbide ceramic foams.* Journal of the American Ceramic Society, 2001. **84**(10): p. 2245-2251.
11. Nghiem, Q.D., S.J. Cho, and D.-P. Kim, *Synthesis of heat-resistant mesoporous SiOC ceramic and its hydrogen adsorption.* Journal of Materials Chemistry, 2006. **16**(6): p. 558-562.
12. Qiu, L., et al., *Thermal-conductivity studies of macro-porous polymer-derived SiOC ceramics.* International Journal of Thermophysics, 2014. **35**(1): p. 76-89.
13. Lu, K., D. Erb, and M. Liu, *Phase transformation, oxidation stability, and electrical conductivity of TiO2-polysiloxane derived ceramics.* Journal of Materials Science, 2016. **51**(22): p. 10166-10177.
14. Toma, L., et al., *Influence of nano-aluminum filler on the microstructure of SiOC ceramics.* Journal of the European Ceramic Society, 2011. **31**(9): p. 1779-1789.
15. Li, J., et al., *Preparation of micro-/mesoporous SiOC bulk ceramics.* Journal of the American Ceramic Society, 2015. **98**(6): p. 1753-1761.
16. Lu, K., D. Erb, and M. Liu, *Thermal stability and electrical conductivity of carbon-enriched silicon oxycarbide.* Journal of Materials Chemistry C, 2016. **4**(9): p. 1829-1837.
17. Guo, A., et al., *In situ carbon thermal reduction method for the production of electrospun metal/SiOC composite fibers.* Journal of materials science, 2015. **50**(7): p. 2735-2746.

18. Kolář, F., V. Machovič, and J. Svitilova, *Cobalt-containing silicon oxycarbide glasses derived from poly [methyl (phenyl)] siloxane and cobalt phthalate.* Journal of non-crystalline solids, 2006. **352**(26-27): p. 2892-2896.
19. Ionescu, E., et al., *Thermodynamic Control of Phase Composition and Crystallization of Metal-Modified Silicon Oxycarbides.* Journal of the American Ceramic Society, 2013. **96**(6): p. 1899-1903.
20. Hojamberdiev, M., et al., *Single-source-precursor synthesis of soft magnetic Fe3Si-and Fe5Si3-containing SiOC ceramic nanocomposites.* Journal of the European Ceramic Society, 2013. **33**(13-14): p. 2465-2472.
21. Pereira, J.L., et al., *Influence of pore former and transition metal on development of nanophases in porous silicon oxycarbide (SiCO) ceramics obtained by catalyst-assisted pyrolysis.* Journal of the European Ceramic Society, 2016. **36**(6): p. 1365-1376.
22. Guo, A., et al., *Hierarchically structured polymer-derived ceramic fibers by electrospinning and catalyst-assisted pyrolysis.* Journal of the European Ceramic Society, 2014. **34**(2): p. 549-554.
23. Idesaki, A. and P. Colombo, *Synthesis of a Ni-Containing Porous SiOC Material From Polyphenylmethylsiloxane by a Direct Foaming Technique.* Advanced Engineering Materials, 2012. **14**(12): p. 1116-1122.
24. Friebe, L., et al., *Pyrolysis of Polycarbosilanes with pendant nickel clusters: Synthesis and characterization of magnetic ceramics containing nickel and nickel silicide nanoparticles.* Chemistry of materials, 2007. **19**(10): p. 2630-2640.
25. Chen, X., et al., *Synthesis and catalytic properties for phenylacetylene hydrogenation of silicide modified nickel catalysts.* The Journal of Physical Chemistry C, 2010. **114**(39): p. 16525-16533.
26. Chen, X., et al., *Nickel–silicon intermetallics with enhanced selectivity in hydrogenation reactions of cinnamaldehyde and phenylacetylene.* Industrial & Engineering Chemistry Research, 2012. **51**(9): p. 3604-3611.
27. Baudouin, D., et al., *Nickel–silicide colloid prepared under mild conditions as a versatile Ni precursor for more efficient CO2 reforming of CH4 catalysts.* Journal of the American Chemical Society, 2012. **134**(51): p. 20624-20627.

28. Zhang, X., et al., *Nickel silicide nanocrystal-containing magnetoceramics from the bulk pyrolysis of polysilazane and nickelocene.* Ceramics International, 2014. **40**(5): p. 6937-6947.
29. Yu, Z., et al., *Polymer-derived mesoporous Ni/SiOC (H) ceramic nanocomposites for efficient removal of acid fuchsin.* Ceramics International, 2017. **43**(5): p. 4520-4526.
30. Zaheer, M., et al., *Polymer derived non-oxide ceramics modified with late transition metals.* Chemical Society reviews, 2012. **41**(15): p. 5102-5116.
31. Seyferth, D., et al., *Chemical modification of preceramic polymers: Their reactions with transition metal complexes and transition metal powders.* Journal of Inorganic and Organometallic Polymers, 1992. **2**(1): p. 59-77.
32. Lu, K. and J. Li, *Fundamental understanding of water vapor effect on SiOC evolution during pyrolysis.* Journal of the European Ceramic Society, 2016. **36**(3): p. 411-422.
33. Backhaus-Ricoult, M., *Solid state reactions between silicon carbide and various transition metals.* Berichte der Bunsengesellschaft für physikalische Chemie, 1989. **93**(11): p. 1277-1281.
34. Martínez-Crespiera, S., et al., *Pressureless synthesis of fully dense and crack-free SiOC bulk ceramics via photo-crosslinking and pyrolysis of a polysiloxane.* Journal of the European Ceramic Society, 2011. **31**(5): p. 913-919.
35. Wu, J., et al., *Simple fabrication of micro/nano-porous SiOC foam from polysiloxane.* Journal of Materials Chemistry, 2012. **22**(14): p. 6542-6545.
36. Erb, D. and K. Lu, *Effects of SiO2-forming additive on polysiloxane derived SiOC ceramics.* Microporous and Mesoporous Materials, 2018. **266**: p. 75-82.
37. Ma, R., K. Lu, and D. Erb, *Effect of solvent in preparation of SiOC bulk ceramics.* Materials Chemistry and Physics, 2018. **218**: p. 140-146.
38. Segatelli, M.G., A.T.N. Pires, and I.V.P. Yoshida, *Synthesis and structural characterization of carbon-rich SiCxOy derived from a Ni-containing hybrid polymer.* Journal of the European Ceramic Society, 2008. **28**(11): p. 2247-2257.
39. Scheffler, M., et al., *Nickel-catalyzed in situ formation of carbon nanotubes and turbostratic carbon in polymer-derived ceramics.* Materials chemistry and physics, 2004. **84**(1): p. 131-139.

40. Payne, B., M. Biesinger, and N. McIntyre, *The study of polycrystalline nickel metal oxidation by water vapour.* Journal of Electron Spectroscopy and Related Phenomena, 2009. **175**(1-3): p. 55-65.
41. Benndorf, C., et al., *H2O interaction with Ni (110): auto-catalytic decomposition in the temperature range from 400 to 550 K.* Applications of Surface Science, 1982. **11**: p. 803-811.
42. Hagi, H., S. Asano, and R. Otsuka, *Hydrogen Pick-up and Hydride Formation in Nickel by Cathodic Polarization.* Journal of the Japan Institute of Metals, 1976. **40**(8): p. 796-801.
43. Dernovsek, O., et al., *Reaction bonded niobium carbide ceramics from polymer-filler mixtures.* Journal of Materials Science, 2000. **35**(9): p. 2201-2207.
44. Tang, D., et al., *Preparation of alumina-coated graphite for thermally conductive and electrically insulating epoxy composites.* RSC Advances, 2015. **5**(68): p. 55170-55178.
45. Niu, M., et al., *Structure and energetics of SiOC and SiOC-modified carbon-bonded carbon fiber composites.* Journal of the American Ceramic Society, 2017. **100**(8): p. 3693-3702.
46. Duan, W., et al., *Microwave-absorption properties of SiOC ceramics derived from novel hyperbranched ferrocene-containing polysiloxane.* Journal of the European Ceramic Society, 2017. **37**(5): p. 2021-2030.
47. Li, Q., et al., *Improved dielectric and electromagnetic interference shielding properties of ferrocene-modified polycarbosilane derived SiC/C composite ceramics.* Journal of the European Ceramic Society, 2014. **34**(10): p. 2187-2201.
48. Aikawa, S., T. Kizu, and E. Nishikawa, *Catalytic graphitization of an amorphous carbon film under focused electron beam irradiation due to the presence of sputtered nickel metal particles.* Carbon, 2010. **48**(10): p. 2997-2999.
49. Fischbach, D., *Chemistry and physics of carbon.* Dekker, New York, 1971. **7**: p. 1-105.
50. Lamber, R., N. Jaeger, and G. Schulz-Ekloff, *Electron microscopy study of the interaction of Ni, Pd and Pt with carbon: I. Nickel catalyzed graphitization of amorphous carbon.* Surface Science, 1988. **197**(3): p. 402-414.
51. Zheng, G.-B., et al., *A model for the structure and growth of carbon nanofibers synthesized by the CVD method using nickel as a catalyst.* Carbon, 2004. **42**(3): p. 635-640.

52. Nagakura, S., *Study of metallic carbides by electron diffraction part I. Formation and decomposition of nickel carbide.* Journal of the Physical Society of Japan, 1957. **12**(5): p. 482-494.
53. Fitzer, E. and B. Kegel, *Reactions of Carbon Saturated Vanadium Carbide Melts with Different Order Carbons (Catalytic Graphitization).* Carbon, 1968. **6**(4): p. 433-&.
54. George, M., et al., *Finite size effects on the structural and magnetic properties of sol–gel synthesized NiFe2O4 powders.* Journal of Magnetism and Magnetic Materials, 2006. **302**(1): p. 190-195.
55. Ennas, G., et al., *Influence of metal content on size, dispersion, and magnetic properties of iron− cobalt alloy nanoparticles embedded in silica matrix.* Chemistry of materials, 2004. **16**(26): p. 5659-5663.
56. Folks, L., R. Street, and R. Woodward, *Investigation of interaction mechanisms in melt-quenched NdFeB.* Journal of Applied Physics, 1994. **75**(10): p. 6271-6273.
57. Hajihashemi, H., P. Kameli, and H. Salamati, *The effect of EDTA on the synthesis of Ni ferrite nanoparticles.* Journal of superconductivity and novel magnetism, 2012. **25**(7): p. 2357-2363.
58. Braun, H.-B., *Thermally activated magnetization reversal in elongated ferromagnetic particles.* Physical review letters, 1993. **71**(21): p. 3557.
59. Pike, C.R., A.P. Roberts, and K.L. Verosub, *First order reversal curve diagrams and thermal relaxation effects in magnetic particles.* Geophysical Journal International, 2001. **145**(3): p. 721-730.
60. Ishizaki, T., K. Yatsugi, and K. Akedo, *Effect of particle size on the magnetic properties of Ni nanoparticles synthesized with trioctylphosphine as the capping agent.* Nanomaterials, 2016. **6**(9): p. 172.
61. Lenz, J. and S. Edelstein, *Magnetic sensors and their applications.* IEEE Sensors journal, 2006. **6**(3): p. 631-649.

Chapter 5

Thermophysical property and electrical conductivity of titanium isopropoxide – polysiloxane derived ceramics

Ni Yang, Kathy Lu*

Department of Materials Science and Engineering, Virginia Polytechnic Institute and State University, Blacksburg, Virginia, 24061, USA

*Corresponding author: Email: klu@vt.edu

Declarations of interest: none

*This chapter has been adapted from a **published** manuscript by Ni Yang and Kathy Lu from the following reference:*

Ni Yang and Kathy Lu. "Thermophysical property and electrical conductivity of titanium isopropoxide–polysiloxane derived ceramics." Journal of the European Ceramic Society 39.14 (2019): 4029-4037.

5.1. Abstract

In this study, high temperature resistant Si-O-C-Ti has been successfully prepared based on the pyrolysis of polysiloxane (PSO) and titanium (IV) isopropoxide (TTIP) at 1200–1400 °C. PSO can homogeneously mix with TTIP to enhance its conversion to TiC. The carbothermal reactions between TiO_2 (product of thermal decomposition of TTIP) and carbon result in the formation of TiC. All the Si-O-C-Ti composites pyrolyzed at 1200–1300 °C are stable up to 1000 °C in an oxidizing air atmosphere. TiC leads to high electrical conductivity at elevated temperatures; the maximum conductivity is 1176.55 S/m at 950 °C, which is the first reported value of >1000 S/m conductivity for Si-O-C-Ti ceramics. However, too high a pyrolysis temperature, such as 1400 °C, can potentially 'destabilize' the Si-O-C-Ti system by consuming the free carbon and result in lower conductivities.

5.2. Introduction

Based on the homogeneous mixing of starting precursors at the molecular level, polymer-derived ceramics enable the formation of homogeneous microstructures [1] and novel properties [2, 3]. One such system is polymer-derived silicon oxycarbide (SiOC). It is a highly adjustable system for which compositions and microstructures can be tuned vastly with different crosslinking and pyrolysis conditions. With pyrolysis temperature increase, there is a phase separation into SiO_2 and then SiC domains along with free carbon formation by consuming mixed $Si_xO_yC_z$ units [4]. Stoichiometric SiOC can be described as a network of $SiC_{4-x}O_x$ ($0 \leq x \leq 4$) tetrahedra units, which are randomly distributed in the SiOC system [5]. The SiOC composition can be written as $SiC_xO_{2(1-x)}$ + y(C_{free} or Si_{free}), which means that excess free carbon or excess free silicon can be present in the matrix. SiOC material has been recently shown to display favorable properties for use in biomedical devices [6], metal-oxide-semiconductor devices [7], white light emitting devices [8], integrated pressure sensors [9], and anodes for lithium-ion batteries [10]. Owing to its diverse range of applications, the SiOC system is considered one of the most promising research areas in polymer derived ceramics.

With the increasing need for functional high temperature materials, high electrical conductivity and thermal stability in harsh environments have become especially important, stimulated by their potential applications for microelectromechanical systems and advanced

energy storage devices. However, the SiOC system is not a highly conductive material. Overall, the electrical conductivity provided by carbon-rich SiOC systems displays low values (~ 1×10^{-3} S cm^{-1}) [3]. In addition, the free carbon in the SiOC matrix leads to low thermal stability [2, 3, 11]. At high temperatures, carbothermal reduction in the SiOC system may result in weight loss and lead to deterioration of thermal stability. Many factors have been proven to have an effect on the high temperature stability, such as the content of free carbon in SiOC [12], polymer precursor type [13], SiOC microstructure [14], and pyrolysis conditions [12]. In our previous work [3, 15, 16], the most sensitive issues for the thermal stability of SiOCs are the oxidative breakdown of the SiOC structure (above 800 °C) and oxidation of free carbon (400–800 °C).

Recently, ceramic composites from SiOC systems with fillers have been reported [15, 17, 18]. Doping the Si–O–C matrix with extra elements such as B, Al, Ti, and Zr can be achieved by adding metal complexes or metal-based particles to the starting polymeric solution. In the presence of a carbide-forming transition metal (Ti, Zr, or Cr) or a transition-metal boride or silicide, the tremendous linear shrinkage encountered during the polymer pyrolysis may be drastically reduced, hence facilitating the production of bulk components [14]. More importantly, the thermal stability and electrical conductivity have been improved after introducing fillers into the SiOC matrix [15, 19]. For example, polymer derived SiOC/ZrO_2 ceramic composites have been successfully prepared by pyrolysis of polymethylsilsesquioxane and nanocrystalline ZrO_2 particles, and the thermal stability increases with respect to crystallization and decomposition at temperatures exceeding 1300 °C [19]. Functionalized TiO_2 nanoparticles promote the formation of TiC_xO_y in a SiOC-based composite, and achieve an electrical conductivity of 5.03 S/cm at 400 °C in the air [15]. SiOC/HfO_2 fibers have good thermal stability with no observable weight loss up to 1500 °C, and the electrical property of the fibers is improved due to the incorporation of carbon into the SiO_2 network [20].

In our prior work [15], SiOC-TiC_xO_y ceramic has been synthesized based on the reaction between TiO_2 nanoparticles and free carbon in the matrix during pyrolysis. In order to enhance the dispersibility of the TiO_2 nanoparticles in the polymer precursor, surface-modification has been carried out on the TiO_2 particles with surfactant sodium dodecyl sulfate (SDS). The SiOC ceramic containing the surface-modified TiO_2 has the highest electrical conductivity (~5.03 S/cm) compared to the TiO_2-SiOC ceramic without the TiO_2 surface modification (~3.07 S/cm) in air,

which proves the important effect of homogeneous dispersion of additives on the electrical properties. However, the surface chemistry incompatibility between the additives and the polymer precursor is still difficult to address because one is hydrophilic (such as the hydroxyl groups on the TiO_2 surface) and the polysiloxane precursors are hydrophobic [21]. Meanwhile, small size TiO_2 additives, such as nanoparticles, have a significant tendency of aggregation due to the high surface area. Inhomogeneous distribution of TiO_2 nanoparticles in the matrix, especially with increasing TiO_2 content, can lead to lower thermal stability.

In this study, titanium (IV) isopropoxide (TTIP) has been incorporated into phenyl and methyl containing polysiloxane to develop Si-O-C-Ti composites. The effects of the additive filler content and pyrolysis temperature on the phase evolution as well as thermophysical and electrical properties are systematically investigated. The mechanisms for phase transformation that lead to superior electrical and thermal behavior of SiOC/TiC ceramic are proposed and discussed on the basis of Raman spectroscopy, XRD (X-ray diffraction), XPS (X-ray photoelectron spectroscopy), TGA (thermogravimetric analysis), and HRTEM (high-resolution transmission electron microscopy).

5.3. Experimental procedure

Commercial polysiloxane Polyramic® SPR-684 (PSO, $[-Si(C_5H_6)_2O-]_3[-Si(CH_3)(H)O-]_2[-Si(CH_3)(CH=CH_2)O-]_2$, Starfire Systems, Inc., Schenectady, NY) was used as the polymer precursor. Titanium (IV) isopropoxide (TTIP, $Ti(OCH(CH_3)_2)_4$, Acros, NJ) with 98+% purity was chosen as the titanium-containing additive. 2.1–2.4% platinum divinyltetramethyldisiloxane complex in xylene (Pt catalyst, Gelest Inc., Morrisville, PA) diluted with toluene was used as a hydrosilylation catalyst.

TTIP/PSO mixtures with the corresponding Ti to Si molar ratios of 0.05, 0.10, 0.15, and 0.20 (marked as SiOC-Ti–0.05, SiOC-Ti–0.10, SiOC–Ti–0.15, and SiOC–Ti–0.20 respectively) were prepared in an argon atmosphere in a glove box (Labstar^{pro}, MBRAUN®, Stratham, NH). During vigorous stirring of the above mixtures at 250 rpm, 2.5 ppm of the diluted Pt catalyst solution was slowly added to the mixtures. After the mixture was stirred for 30 min, the homogeneous mix was poured into cylindrical aluminum molds and placed in a vacuum chamber at 1500 mTorr to remove all the bubbles. Before crosslinking, the mixture was a yellowish yet transparent liquid without

any bubbles. After curing at 50 °C for 12 h and 100 °C for 24 h in an oven, the cross-linked sample was hard, black, and crack–free. The cured samples were cut and polished to roughly 10 mm x 10 mm x 1.5 mm size and placed in zirconia boats with both sides covered by graphite mats before being put into a tube furnace (1730 – 12 Horizontal Tube Furnace, CM Furnaces Inc., Bloomfield, NJ) for pyrolysis. The samples were heated up to 1200 °C, 1300 °C, and 1400 °C at a rate of 1 °C/min with 2 h holding and cooled down to 50 °C with a rate of 2 °C/min. The ceramic yield and shrinkage of the above samples were recorded.

The density of the resulting products was measured in triplicate by a pycnometer (AccuPyc II 1340, Micromeritics®, Norcross, GA), using helium gas at an outlet pressure of 1.34 bars in a 7.8 cm^3 sample cell. Phase compositions of the pyrolyzed samples were examined using an X'Pert PRO diffractometer (PANalytical B.V., EA Almelo, The Netherlands). Rietveld refinement of the diffraction data was performed using X'Pert HighScore Plus. JCPDS cards 98-001-2065 and 98-009-3040 were used to index SiC and TiC phases, respectively. The thermal stability of the samples after pyrolysis was analyzed by thermogravimetric analysis (TGA) using a STA 449C Jupiters® analyzer (Netzsch - Gerätebau GmbH, Selb, Germany) from room temperature to 1000 °C at a heating rate of 10 °C/min and an air flux of 40 ml/min as well as in a furnace at 1000 °C in air for up to 100 h. The electrical conductivity of the pyrolyzed samples was measured from 50 °C to 1200 °C in an Ar atmosphere with a four-point probe configuration from a potentiostat (Versa STAT 3, Princeton Applied Research, Oak Ridge, TN). For the conductivity measurements, silver/palladium paste (ESL Electroscience, PA, USA) electrodes were painted on the surfaces of the specimens. Raman spectra were recorded on a Horiba spectrometer (JY Horiba HR 800) with an excitation wavelength of 514 nm produced by an Ar laser between the spectral range of 250–3500 cm^{-1}. The microstructures of the pyrolyzed ceramics were studied using a transmission electron microscope (JEOL 2100, JEOL USA, Peabody, MA); the TEM samples were prepared by grinding the pyrolyzed samples in a mortar and then dispersing them in absolute methanol. Chemical compositions were examined by X-ray photoelectron spectroscopy (XPS, PHI Quantera SXM) equipped with an Al K_α source (1486.6 eV).

5.4. Results and discussion

5.4.1. Thermophysical properties

Table 5.1 displays the volume shrinkage, ceramic yield, and density of the samples after pyrolysis at 1200 °C, 1300 °C, and 1400 °C. All the pyrolyzed samples are light-reflecting black and maintain good shapes and high integrity. The pure SiOC sample shows no distinction in physical appearance vs. the Si-O-C-Ti samples.

Table 5.1. Volume shrinkage, ceramic yield, and density of the pyrolyzed samples.

Samples	**Volume shrinkage (%)**			**Ceramic yield (%)**			**Density (g/cm^3)**		
	1200°C	1300°C	1400°C	1200°C	1300°C	1400°C	1200°C	1300°C	1400°C
SiOC	40.35± 2.47	47.29± 0.37	45.25± 1.10	83.34± 4.23	81.22± 5.28	74.59± 0.54	1.64±0.52	1.77±0.24	1.84±0.04
SiOC-Ti-0.05	41.04± 1.50	49.78± 0.51	46.65± 0.89	76.56± 0.07	74.15± 0.42	74.21± 1.19	1.81±0.30	1.84±0.42	1.87±0.10
SiOC-Ti-0.10	50.66± 0.55	55.06± 0.75	52.53± 1.01	71.24± 0.77	68.40± 0.85	68.39± 1.80	1.86±0.42	1.91±0.33	1.93±0.06
SiOC-Ti-0.15	53.79± 1.87	58.45± 0.83	56.92± 0.67	66.67± 0.30	63.48± 0.26	63.64± 0.70	1.90±0.40	1.96±0.32	1.98±0.36
SiOC-Ti-0.20	64.47± 0.78	59.70± 0.78	60.58± 0.91	65.59± 0.72	61.17± 1.06	63.16± 1.54	1.96±1.12	1.99±0.47	2.01±0.15

The pure SiOC sample pyrolyzed at 1200 °C shrinks at the lowest rate of ˜40%. The values for all the Si-O-C-Ti samples range from 41% to 64% at three different temperatures. At the same pyrolysis temperature, the volume shrinkage increases with the TTIP content. It is believed that the thermal decomposition of TTIP into TiO_2 as well as the carbothermal reaction between

TiO_2 and carbon leads to an increase in the volume shrinkage. The process can be described as [22, 23]:

$$Ti(O\text{-}iC_3H_7)_4 \rightarrow TiO_2 + 4C_3H_6(g) + 2H_2O(g) \quad (5.1)$$

$$TiO_2 + 3C \rightarrow TiC + 2CO(g) \quad (5.2)$$

Table 5.1 also shows that the volume shrinkage steadily increases with the TTIP content, when the pyrolysis temperature is constant. For the same TTIP content, the volume shrinkage does not have a consistent trend from 1200 °C to 1400 °C. In general, it increases from 1200 °C to 1300 °C and then decreases from 1300 °C to 1400 °C. This is because of Eq. (5.2) reacts more completely at higher temperatures, which results in larger volume shrinkage because of the evaporation of the volatile CO gas.

The ceramic yield values for all the samples in Table 5.1 range from 61 to 83%. At the same pyrolysis temperature, the ceramic yield decreases with the increase of the TTIP content. Among them, the pure SiOC samples have the highest ceramic yield (83%, 81%, and 75%) at pyrolysis temperatures of 1200 °C, 1300 °C, and 1400 °C. This is understandable as the mass loss of the pure SiOC is only dependent on the polymer decomposition. However, for the Si-O-C-Ti samples, the thermal decomposition of both the PSO and TTIP causes mass loss, especially with the consideration of the TiO_2 to TiC conversion (CO gas escape). More TTIP leads to more mass loss. At the same TTIP concentration, the ceramic yield generally decreases as the pyrolysis temperature increases because of the formation of more free carbon in the matrix and potentially more evaporative species (CO, CO_2, etc.).

The densities for all the SiOC and Si-O-C-Ti samples are in the range of 1.64–2.01 g/cm^3. At 1200 °C, as the TTIP content increases, the density slightly increases. This is because more TTIP introduces more Ti into the samples. When the pyrolysis temperature increases from 1200 °C to 1400 °C, more TiO_2 (4.23 g/cm^3) converts into TiC (4.93 g/cm^3), the density values for both of these species are much higher than those of SiOC (2.2–2.3 g/cm^3), SiO_2 (2.65 g/cm^3), and SiC (3.21 g/cm^3).

5.4.2. Phase evolution

Fig. 5.2 shows the phase evolution of the SiOC matrix with different TTIP content for different pyrolysis temperatures.

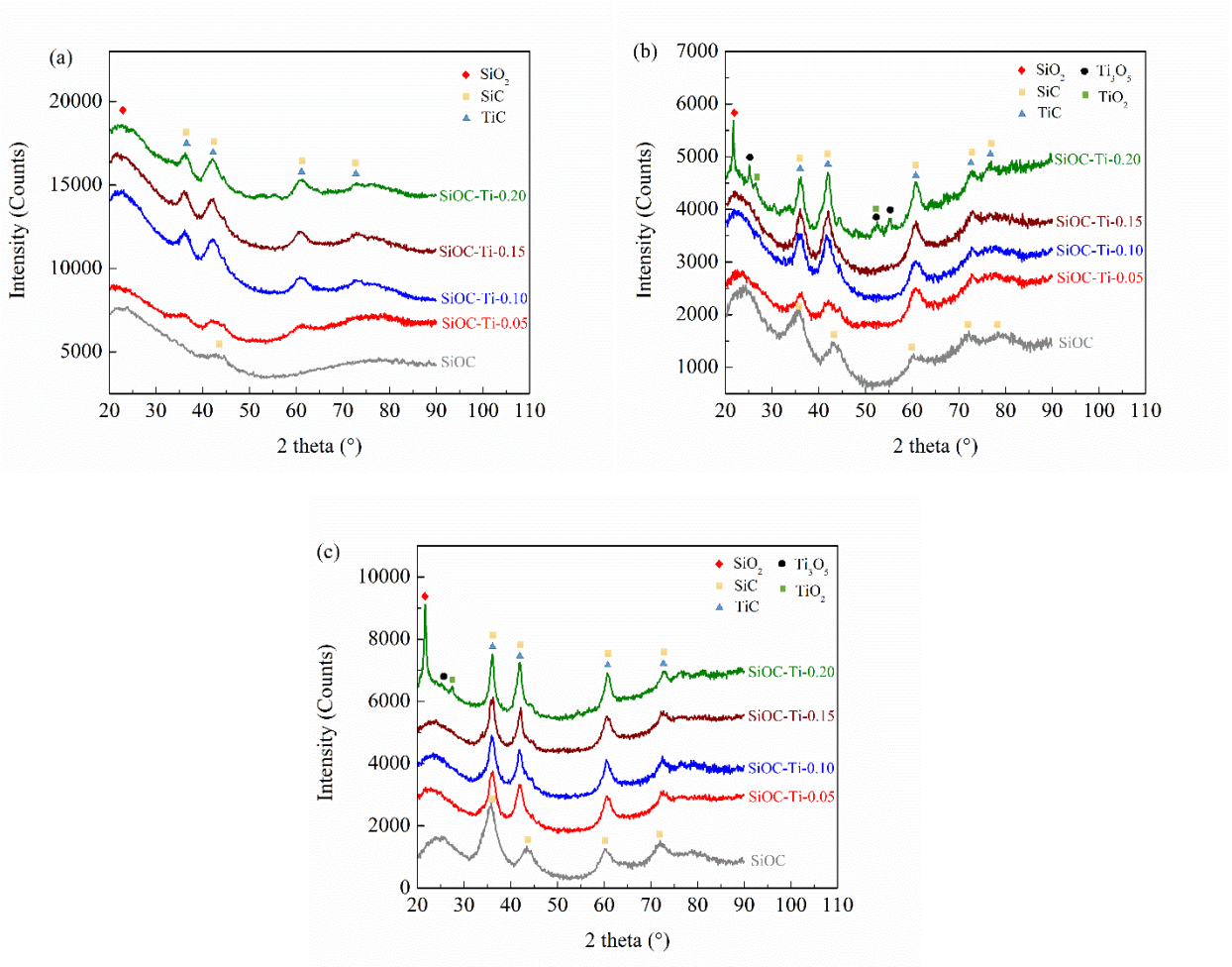

Fig. 5.1. XRD patterns of the SiOC samples with different amounts of TTIP additive after pyrolysis at (a) 1200°C, (b) 1300°C, and (c) 1400 °C for 2 h in flowing argon.

At 1200 °C (Fig. 5.2(a)), the broad 22.9° hump corresponds to the (022) plane of amorphous SiO_2. The weak and poorly defined peak at 41.4° means that the SiC content is low, which is consistent with typical SiOC systems. For the Si-O-C-Ti samples, some minor peaks appear at 36°, 41°, and 60°, consistent with the formation of TiC and SiC. With an increasing molar ratio of Ti to Si to 0.10, 0.15, and 0.20, these above-mentioned three peaks become stronger, an indication of

more TiC and/or SiC formation. The reaction paths are shown in Eqs. (5.1) and (5.2) for TiC formation are consistent with the presence of the Ti-C bonds (Ti2p, 460.7 eV) in the SiOC-Ti-0.20 pyrolyzed at 1200 °C (Fig. 5.2(b)). At the same time, the Si-C bonds shown in Fig. 5.2(a) are more related to the SiOC tetrahedrals than to SiC crystallites. The main peak of Si2p from the SiOC-Ti-0.20 system with a binding energy of 102.4 eV is attributed to the combined contribution of Si–C and Si–O bonds [24], which occurs becasue of the amorphous SiOC phase in the SiOC-Ti system. No SiC peak is detected for the SiOC-Ti-0.20 sample at 1200 °C and only a very small amount of SiC is observed at 1400 °C. It is believed that the 36°, 41°, and 60° peaks in Fig. 5.2 are more related to TiC than to SiC. The TiC content increases with the TTIP content.

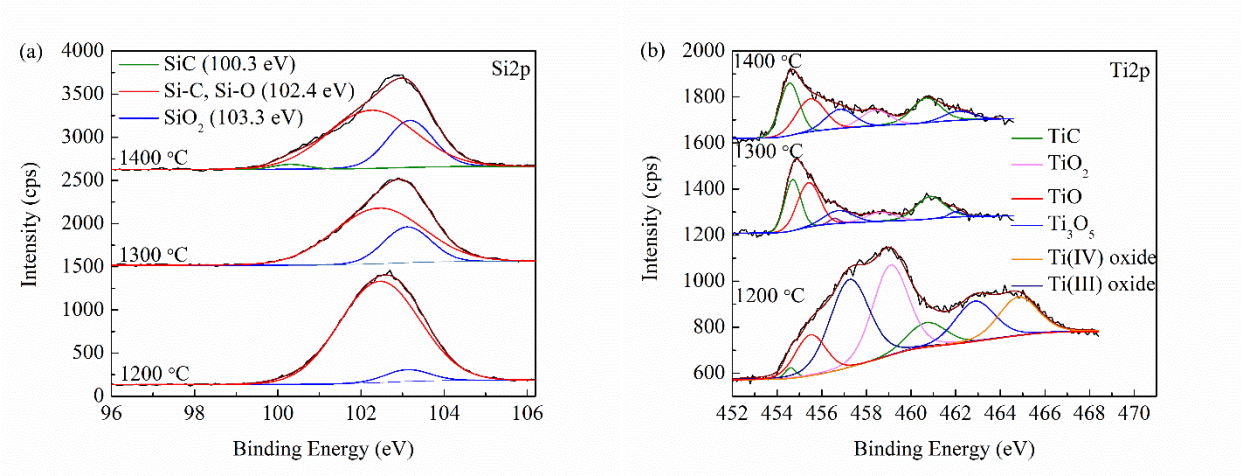

Fig. 5.2. XPS spectra of the SiOC-Ti-0.20 sample pyrolyzed at 1200, 1300, and 1400 °C showing the Si2p and Ti2p peaks.

With the pyrolysis temperature increase to 1300 °C (Fig. 5.2(b)), the 35.7°, 41.4°, 60.0°, 71.8°, and 75.5° peaks corresponding to the (111), (002), (022), (113), and (222) planes of β-SiC are clearly observed for the pure SiOC sample. Also, the SiO_2 phase crystallizes, demonstrated by the 22.9° hump change to a sharper peak. This means that a higher pyrolysis temperature accelerates the formation of SiC and the crystallization of SiO_2 in the SiOC matrix. With the increase of the TTIP addition, due to the consumption of carbon by TiO_2 through Eq. (5.3), the inhibiting effect from excessive carbon for the SiO_2 formation is decreased [15]; large SiO_2 domain sizes lead to the crystallization of SiO_2. With the TTIP addition (Fig. 5.2(b)), the peaks for the mixture of TiC

and SiC (largely TiC) centered at 36°, 41°, 60°, 72°, and 76° are more intensive. For the SiOC-Ti-0.20, both the XRD pattern from 20° to 60° and the deconvoluted XPS Ti2p peak shows a series of small peaks. These peaks result from a series of intermediate oxides due to TiO_2 reduction by carbon, such as Ti_3O_5 and TiO_2, as well as TiC, which can be expressed as:

$$3TiO_2 + C \rightarrow Ti_3O_5 + CO(g) \quad (5.3)$$

The Gibbs free energy of the above equation can be calculated with an HSC Chemistry 6.0 software. The calculation results are shown in Fig. 5.3, which indicates that only when the temperature is higher than 1100 °C (1373.15 K) is Eq. (11) thermodynamically possible (negative Gibbs free energy). However, there are no titanium intermediate oxides detected even at 1200 °C pyrolysis temperature. This may be due to the negligible amount of the predicted titanium oxides. Overall, higher TTIP content leads to more Ti_xO_y and TiC formation.

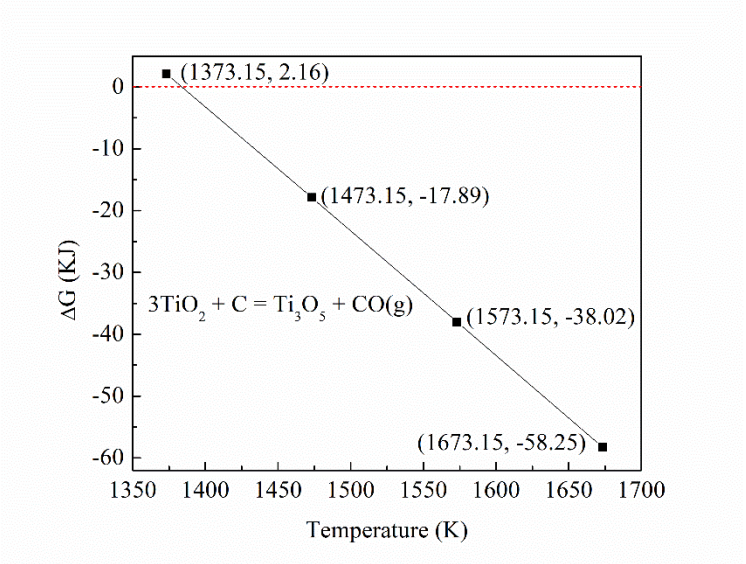

Fig. 5.3. Gibbs free energy versus absolute temperature for Eq. (11).

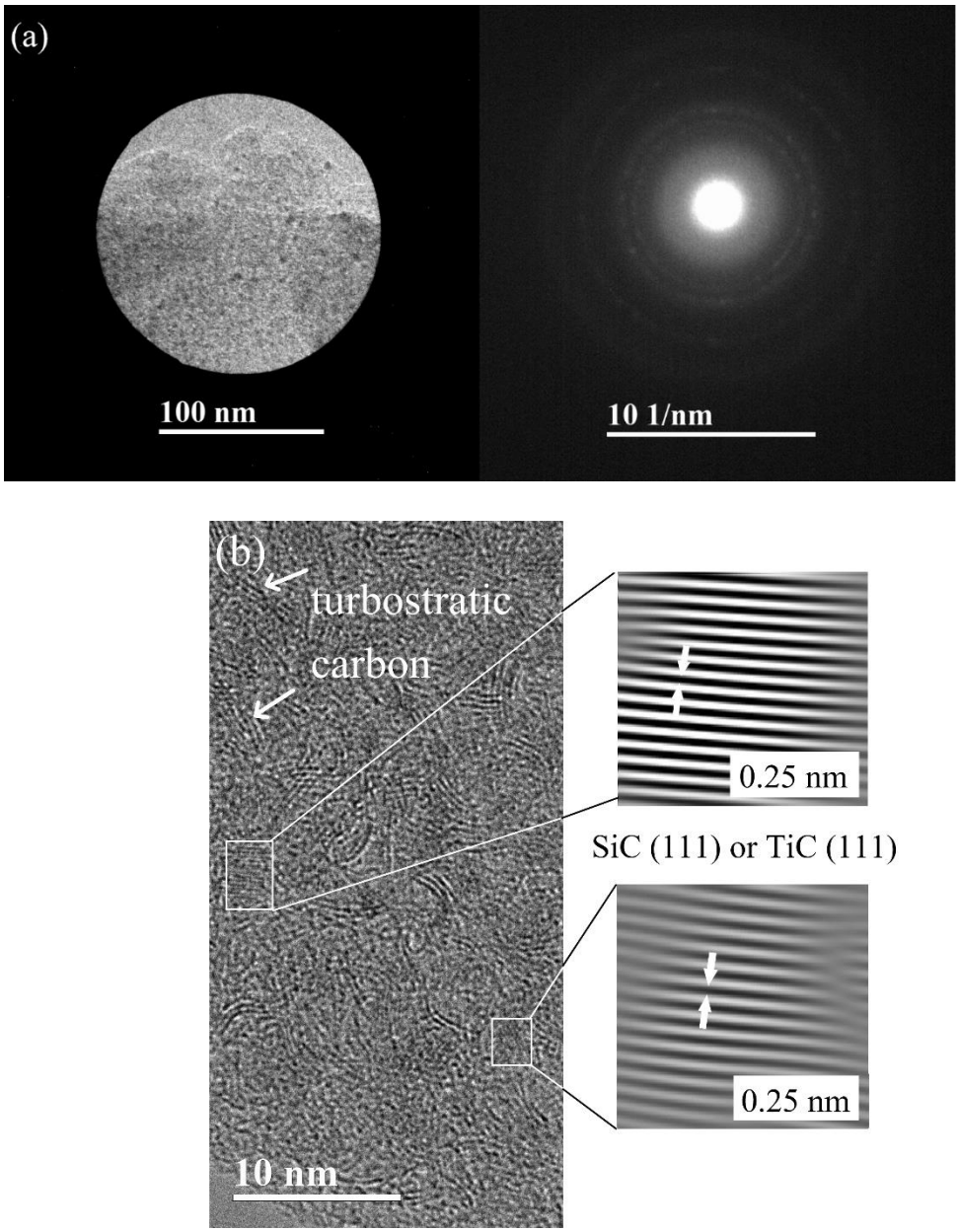

Fig. 5.4. Morphology of the SiOC–Ti-0.20 sample after pyrolysis at 1300 °C: (a) low magnification microstructure and largely amorphous diffraction pattern; (b) distribution of SiC and TiC nanocrystals in the SiOC matrix with the lattice fringe width shown.

When the pyrolysis temperature is increased to 1400 °C, the intense peak at 21.8° indicates tetragonal SiO_2 formation for the SiOC-Ti-0.20 sample. For the pure SiOC sample, there is no distinguishable difference between those of Figs. 5.1(b-c), except that the peaks become sharper

in Fig. 5.1(c). As discussed, higher pyrolysis temperature increases the transition to crystalline SiO_2. Nonetheless, the extent is much less than that with the TTIP addition. The XPS results in Fig. 5.2 also shows the strengthening of the SiO_2 peak centered at 103.3 eV from 1200 °C to 1400 °C. The SiC formed in the matrix leads to more intense peaks in Fig. 5.1(c). The mechanism can be explained as:

$$SiO_2(\text{amorphous}) + 3C(\text{graphite}) \rightarrow SiC(\beta) + 2CO\uparrow \quad (5.4)$$

The corresponding contents of TiC and SiC from the SiOC-Ti-0.05 to SiOC-Ti-0.20 samples are analyzed by Rietveld refinement. During the Rietveld refinement, several parameters are refined to generate a simulated pattern until it matches the measured profile. Table 5.2 lists the contents of TiC and SiC crystalline phases. The relative weight fraction of TiC is remarkably boosted with the increase of the Ti content in SiOC.

Table 5.2. Quantitative results of the crystalline phases by Rietveld analysis of the Si-O-C-Ti samples pyrolyzed at 1300 °C.

	Rietveld refinement (wt%)	
Sample	SiC	TiC
SiOC-Ti-0.05	92.0	8.0
SiOC-Ti-0.10	79.6	20.4
SiOC-Ti-0.15	45.1	54.9
SiOC-Ti-0.20	36.5	63.5

As seen in Fig. 5.2(a), the combined contribution from the Si-C and Si-O bonds in the amorphous SiOC phase is reduced when the pyrolysis temperature goes higher. This is because more crystalline SiC and SiO_2 evolve from the SiOC phase. The peaks centered at 454.7 eV (Ti2p3/2) and 460.7 eV (Ti2p1/2) for TiC also become stronger from 1200 °C to 1400 °C (Fig.

5.2(b)). This implies the reaction converts titanium oxides to TiC by increasingly consuming the excessive carbon, and higher temperature promotes the extent of this reaction.

From the XRD patterns in Fig. 5.1, it can be concluded that the crystallization of SiC and TiC starts at 1300 °C pyrolysis temperature. Fig. 5.4 (a) shows the electron diffraction pattern of the SiOC-Ti-0.20 samples pyrolyzed at 1300 °C. Because the amounts of the crystalline phases (e.g. SiC, TiC) are so small, the diffraction spots for these phases are not obvious. The electron diffraction pattern mainly displays the amorphous nature of the SiOC samples. The halo rings are believed to be from the amorphous carbon and SiOC, which should be widely present [25]. In order to further distinguish the TiC and SiC phases in the SiOC matrix, the high magnification microstructure is shown in Fig. 5.4(b). The width of the lattice distance is obtained by DigitalMicrograph® version 3. The results show that the lattice fringe width is 0.25 nm from both crystalline precipitates. However, the crystalline form is the same for SiC and TiC and the lattice parameters of TiC (0.249 nm) and SiC (0.251 nm) are similar, the identification between them is not definite due to the limit of the TEM measurements. The morphology of the precipitates is poorly defined, but the size is generally <5 nm. The worm-like features throughout the SiOC matrix are from the turbostratic carbon layers, which have twisted layer structures from the out-of-registry stacking of the graphene layers.

5.4.3. Thermal stability

The high temperature oxidation stability of the Si-O-C-Ti samples is shown in Fig. 5.5. At 1200 °C pyrolysis temperature, the residual masses of all the samples are more than 99.80 wt%, except for the pure SiOC sample (93.90 wt%). There is a similar trend for the samples pyrolyzed at 1300 °C. As the insert in Fig. 5.5(a) shows, there is a weight loss of 0.10 wt%, 0.16 wt%, 0.20 wt%, and 0.15 wt% for the SiOC-Ti-0.05, 0.10, 0.15, and 0.20 samples respectively from room temperature to 500 °C. This is due to the evaporation of moisture and carbon oxidation at low temperatures (400–800 °C), which causes a net weight loss for the resultant ceramic [26]:

$$C + O_2 \rightarrow CO_x \quad (5.5)$$

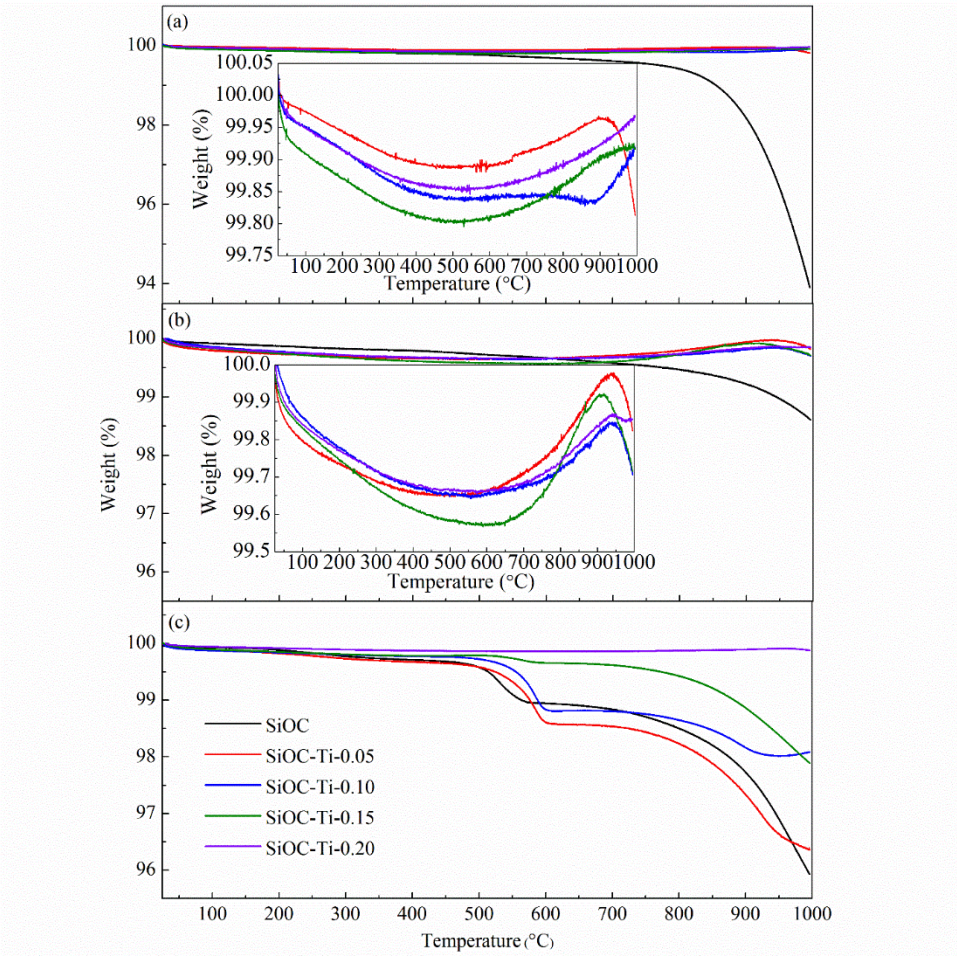

Fig. 5.5. TGA weight change curves in the air for the pure SiOC and Si-O-C-Ti samples pyrolyzed at (a) 1200 °C, (b) 1300 °C, and (c) 1400 °C.

As was discussed in our previous papers [3, 15], Eq. (5.5) involves oxidation of edge carbon atoms in the tiny graphene layers of the SiOC matrix, along with the oxidation of the radical species on the surface of free carbon.

Between 500 °C and 1000 °C, weight gains up to 0.079 wt%, 0.11 wt%, and 0.12 wt% are observed for the SiOC-Ti-0.10, SiOC-Ti-0.15, and SiOC-Ti-0.20 samples. The oxidation of the Si-C bonds in the SiOC matrix leads to net weight gain, which can be described as:

$$Si\text{-}C + O_2 \rightarrow Si\text{-}O + CO_x \quad (5.6)$$

The weight gain or loss depends on the oxidation rates of the excess carbon and the Si-C bonds in the SiOC matrix. Combining this two conflicting yet simultaneous reactions (5.5) and (5.6), and considering that TiC formation is minimal, explains why only a small weight gain is observed for the samples pyrolyzed at 1200 °C. Regardless, the high thermal stability of the SiOC-Ti-0.10, SiOC-Ti-0.15, and SiOC-Ti-0.20 samples after 1200 °C pyrolysis is clear. Compared to higher pyrolysis temperatures (1300 °C and 1400 °C), the amount of free carbon is relatively low in the SiOC matrix at 1200 °C. Moreover, SiOC oxidation should be more vulnerable at higher temperatures (500 °C–1000 °C) than at lower temperatures (< 500 °C), which results in the Si-C bond oxidation rate being comparable to that of the oxidation rate of carbon. This allows a SiO_2-like surface to build up on SiOC based on reaction (5.6), which slows all subsequent reactions due to the necessity of O_2 diffusing in and CO_x diffusing out for reactions (5.5) and (5.6) to occur. It should be noted that the mass loss is relatively small for the Si-O-C-Ti samples compared to the pure SiOC system. This is because the possible reaction between TiO_2 and SiOC will induce more Si-C bonds from the amorphous SiOC phase due to the formation of SiO_2:

$$TiO_2 + 2SiOC \rightarrow 2SiO_2 + TiC + C \quad (5.7)$$

With more oxidation of the Si-C bonds in the SiOC matrix, less net weight loss occurs for the Si-O-C-Ti samples.

The above discussion also explains the “convex” shape of the weight curves in Fig. 5.5(a), that is, the net weight loss at lower temperatures and weight gain at higher temperatures. Unlike the other samples, the weight of the SiOC-Ti-0.05 sample drops at 900 °C. Based on reactions (5.1) and (5.2), less free carbon will be consumed to form TiC. Because of the higher amount of unreacted free carbon in the SiOC-Ti-0.05 sample than in the other samples, the oxidation of free carbon becomes more prominent once again from 900 °C to 1000 °C, resulting in weight loss (0.046 wt%). The residual masses of the SiOC-Ti-0.05, 0.10, 0.15, and 0.20 samples are 99.81 wt%, 99.91 wt%, 99.92 wt%, and 99.97 wt%, respectively. Higher TTIP content leads to higher thermal stability. This is because TiC is an extremely refractory ceramic material [27] and has a positive effect on the thermal stability.

At 1300 °C pyrolysis temperature, the residual mass for the pure SiOC sample is 96.16 wt%, and for the other samples, they are all more than 99.70 wt%, as shown in Fig. 5.5(b). The thermal stability of all the Si-O-C-Ti samples is enhanced compared to the pure SiOC. Again, this is

because TiC plays an active role in improving thermal stability. At the same time, a mass loss of 3.84 wt% is observed for the pure SiOC sample between 600 °C and 1000 °C, indicating a continuous deterioration of the thermal stability due to carbon burning from 600 °C to 1000 °C [28]. However, this phenomenon is less extensive in the Si-O-C-Ti samples since part of the free carbon is consumed to support the conversion from TiO_2 to TiC (reaction (5.2)). Fig. 5.5(b) insert shows the convex-like curve, the same as in Fig. 5.5(a). The difference for the inserts in Figs. 5.5(a) and (b) is that a mass loss of 0.12 wt%, 0.11 wt%, and 0.20 wt% is detected for the SiOC-Ti-0.05, SiOC-Ti-0.10, SiOC-Ti-0.15 samples respectively from 900 °C to 1000 °C. This has been explained by the less carbon consumption in the lower TTIP-containing samples through the reduction reaction (5.2), which makes the oxidation of free carbon more prominent at a higher temperature and results in mass loss after 900 °C. In Fig. 5.5(b), the above phenomenon occurs in all the Si-O-C-Ti samples except for SiOC-Ti-0.20. In Fig. 5.5(a), the only exception is SiOC-Ti-0.05. Higher pyrolysis temperature promotes more of the free carbon phase. At 1300 °C, more free carbon in the matrix results in more prominent carbon oxidation (mass loss) than at 1200 °C. It also explains why more samples have a mass loss at a later stage in Fig. 5.5(b). The TTIP content effect is the same as at 1200 °C. Higher TiC content means higher thermal stability.

Fig. 5.5(c) shows no convex line in the mass change curves. Only mass loss from 500 °C to 1000 °C occurs. The pure SiOC sample still shows the lowest thermal stability (95.93 wt%). The residual masses of the SiOC-Ti-0.05, 0.10, 0.15, and 0.20 samples are 96.36 wt%, 98.08 wt%, 97.89 wt%, and 99.88 wt%, consistent with the observation that the thermal stability is proportional to the TiC content. All the samples show a mass loss because of the more extensive phase separation and free carbon formation at 1400 °C. The samples pyrolyzed at 1400 °C are less stable because the pyrolysis process consumes more free carbon and ‘destabilizes’ the SiOC system. As we have discussed at the beginning of this section, TiC is an extremely refractory material. Higher TiC samples mean higher thermal stability.

Table 5.3 shows that the mass loss after 1000 °C thermal treatment in the air for 25 h varies from 23.25 to 36.96 wt%. The reasons have been detailed above with extended thermal exposure. However, no weight loss is detected for all the samples during the period of 25–100 h thermal treatment. This means that after the initial mass loss, the Si-O-C-Ti system has superior thermal stability, and higher TiC content results in higher thermal stability.

Table 5.3. Mass loss of different SiOC-Ti samples with different dwelling time at 1000 °C.

Pyrolysis temperature	Sample	Mass-loss (wt%) at different dwelling time			
		0-25 h	25-50 h	50-75 h	75-100 h
1200 °C	SiOC	36.89±2.15	0	0	0
	SiOC-Ti-0.05	35.62±1.74	0	0	0
	SiOC-Ti-0.10	35.55±2.16	0	0	0
	SiOC-Ti-0.15	29.74±0.98	0	0	0
	SiOC-Ti-0.20	23.49±1.26	0	0	0
1300 °C	SiOC	36.74±0.63	0	0	0
	SiOC-Ti-0.05	35.28±1.79	0	0	0
	SiOC-Ti-0.10	32.71±2.16	0	0	0
	SiOC-Ti-0.15	24.02±0.46	0	0	0
	SiOC-Ti-0.20	23.25±1.02	0	0	0
1400 °C	SiOC	36.96±1.39	0	0	0
	SiOC-Ti-0.05	32.87±2.51	0	0	0
	SiOC-Ti-0.10	33.31±0.78	0	0	0
	SiOC-Ti-0.15	30.42±1.21	0	0	0
	SiOC-Ti-0.20	29.36±1.59	0	0	0

5.4.4. Electrical conductivity

Fig. 5.6 shows the electrical conductivity changes for the SiOC samples pyrolyzed at 1200–1400 °C with different amounts of TTIP addition.

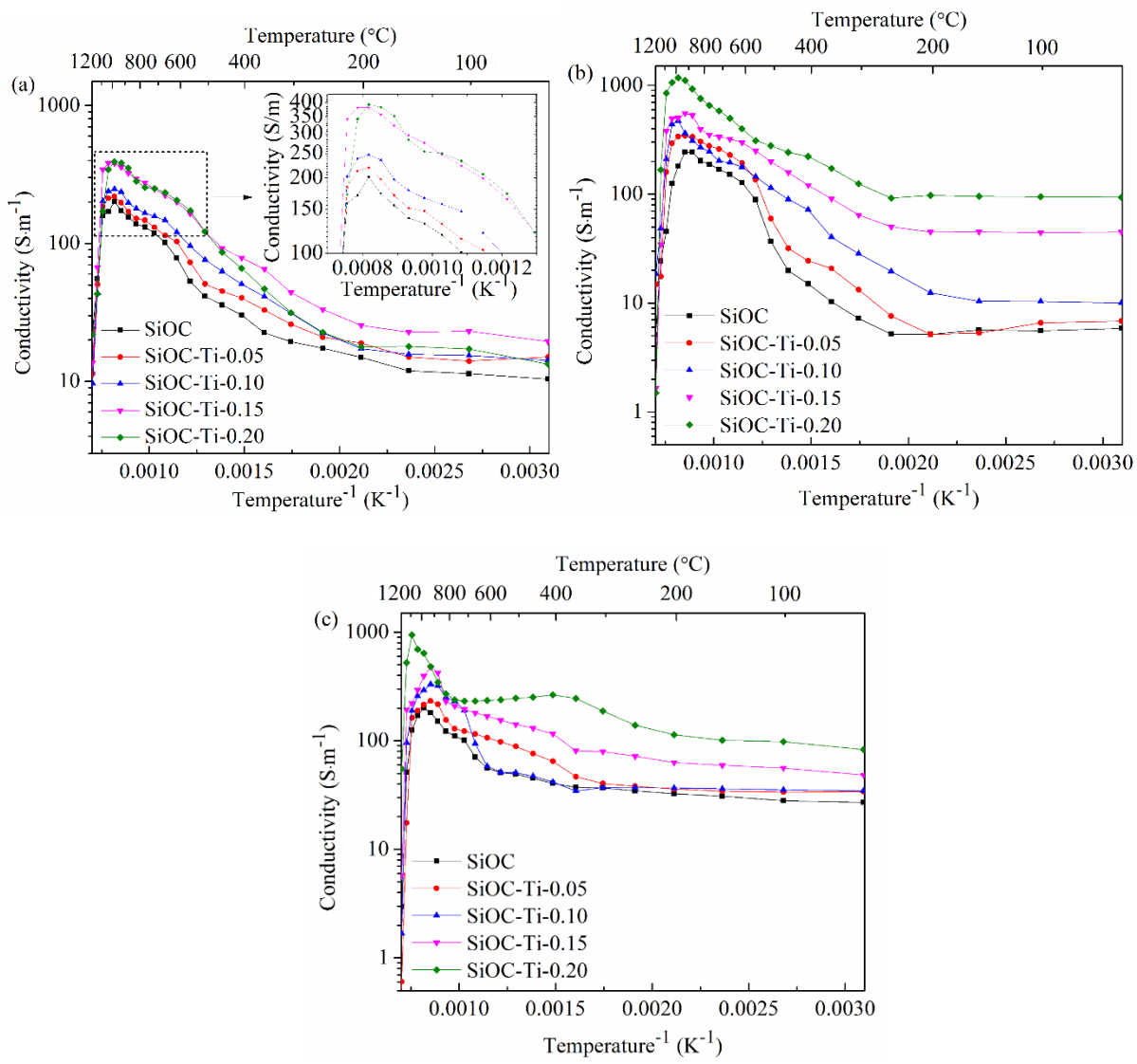

Fig. 5.6. Electrical conductivity for the SiOC, SiOC-Ti-0.05, SiOC-Ti-0.10, SiOC-Ti-0.15, and SiOC-Ti-0.20 samples after different pyrolysis temperatures in an argon atmosphere.

At 1200 °C pyrolysis temperature (Fig. 5.6(a)), for the pure SiOC sample, the conductivity increases from 10.39 to 201.49 S/m from room temperature to 950 °C, then decreases to 3.29 S/m at 1200 °C. Based on literature [29], decomposition of hydrocarbon fragments resulting from the cleavage of the functional groups bonded to silicon (e.g., Si–C_6H_5, Si–CH_3) leads to the precipitation of turbostratic carbon clusters, which are the main contributor to the electrical conductivity of Si-O-C ceramics. For SiOC-Ti-0.05, the conductivity starts from 34.02 S/m at

50 °C and achieves the highest electrical conductivity of 232.92 S/m at 900 °C before decreasing to 0.15 S/m at 1200 °C. Compared to the pure SiOC, the increasing conductivity is a result of additional TiC (3.3×10^6 S/m, 20 °C [30]) formation and free (segregated) carbon content, which has been validated by our previous work [15]. With more TiC formation, the conductivity generally shows an increase from SiOC-Ti-0.05 to SiOC-Ti-0.20, although no obvious difference is observed between SiOC-Ti-0.15 and SiOC-Ti-0.20. As mentioned in our earlier work [15], the conversion from TTIP to TiC can lead to increased free carbon content as well as the structural transformation of sp^3 carbon into sp^2 carbon. The ordering, amount, and interconnectivity of the carbon network exert a major influence on the electrical conductivity [31]. A higher fraction of carbon with sp^2 bonds leads to higher conductivity for the pyrolyzed materials.

At 1300 °C pyrolysis temperature, the electrical conductivity of the pure SiOC increases from 5.85 S/m (50 °C) to 243.53 S/m (850 °C) before decreasing to 0.94 S/m (1200 °C). An increase is observed when compared to that of the 1200 °C pyrolysis temperature. This means that higher temperature promotes carbon cluster growth; edge-to-edge linkage of neighboring structural units may coalesce to form an interconnected network (cluster size to infinity) of turbostratic carbon ribbons in the matrix [32]. As for the Si-O-C-Ti system, the electrical conductivity still increases with the TTIP content. This has been explained based on increased carbon ordering, which can be confirmed by the Raman data shown in Fig. 5.7 for selected samples pyrolyzed at 1300 °C. The two Lorentzian peaks at ~1350 cm^{-1} and 1580 cm^{-1} are assigned to the D band and G band, respectively. The D' peak centered at 1540 cm^{-1} is from the amorphous carbon structure [33]. Good curve fitting results (R^2>0.95) are achieved. The decreasing peak area ratio (A_D/A_G from 4.21 to 3.19 from the pure SiOC sample to the SiOC-Ti-0.20 sample) and the disappearance of the D' band are important indications of a higher degree of crystallization for the carbon structure in the Si-O-C-Ti samples. It is worth noting that SiOC-Ti-0.20 achieves the highest electrical conductivity of 1176.55 S/m at 950 °C. To our best knowledge, it is the first report that the conductivity for Si-O-C-Ti ceramics is over 1000 S/m. In the previous study [15], we in situ synthesized silicon oxycarbide (SiOC)–TiC_xO_y composites based on the pyrolysis of polysiloxane and carbothermal reaction between TiO_2 nanoparticles and free carbon in SiOC. However, the conductivity of the SiOC–TiC_xO_y composites is suppressed to a certain degree because of the heterogeneous dispersion of the TiO_2 particles in the polymeric precursor. In this study, the incorporation of titanium isopropoxide, which is an organic compound completely miscible with

the polysiloxane, addresses the inhomogeneity issue; the electrical conductivity of the SiOC–Ti-0.20 sample is further improved.

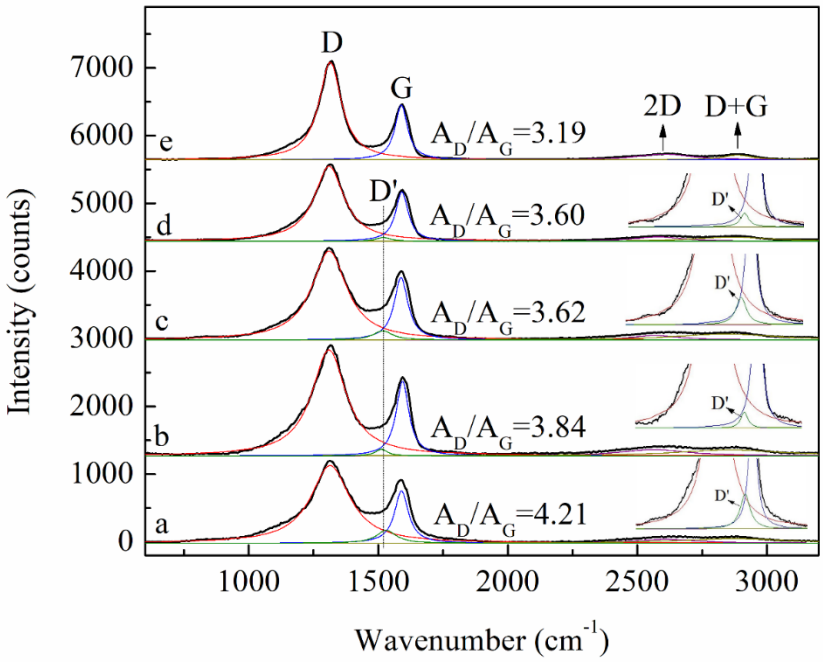

Fig. 5.7. Curve-fitting Raman spectra of different samples pyrolyzed at 1300 °C for (a) SiOC, (b) SiOC-Ti-0.05, (c) SiOC-Ti-0.10, (d) SiOC-Ti-0.15, and (e) SiOC-Ti-0.20 samples.

At 1400 °C pyrolysis temperature, Fig. 5.7(c) shows that the overall conductivity for the SiOC-Ti samples is lower than that of 1300 °C. The maximum value, from SiOC-Ti-0.20, is measured to be 946.07 S/m. With more TiC formation (Fig. 5.2), higher pyrolysis temperature should lead to higher electrical conductivity. However, the electrical conductivity of the Si-O-C-Ti samples is also dependent on the ordering, content, and interconnectivity of the carbon network. Higher pyrolysis temperature intensifies the carbothermal reaction between TiO_2 and carbon (Eq. (5.3)) and damages the interconnectivity of the carbon network, which results in lower conductivity values. It also means that overly high and low pyrolysis temperatures are not conducive to high conductivity. At higher measurement temperatures than 850–950 °C, all the samples (Fig. 5.6) show a drastic conductivity decrease. This is caused by the breakdown of the

conductive turbostratic carbon network under the electric field as well as the formation of a surface oxide layer [3, 15]. Also, the silver/palladium paste used as electrodes starts to thermally decompose at around 1000 °C. The higher-temperature resistant paste is still being pursued in our study.

5.5. Conclusions

This work focuses on using a titanium complex as an additive to synthesize superior thermal stability and high electrical conductivity Si-O-C-Ti ceramics. The volume shrinkage is 41–64.5%, the ceramic yield is 61.2–76.6% and the resultant Si-O-C-Ti composite density is 1.8–2 g/cm^3. TTIP conversion to TiC increases with the increase of the pyrolysis temperature by the carbothermal reaction. Unlike pure SiOC, all the Si-O-C-Ti composites pyrolyzed at 1200 and 1300 °C are thermally stable up to 1000 °C in the air with >99.80 wt% mass retention. However, these Si-O-C-Ti samples are less stable at 1400 °C pyrolysis temperature, especially when they consume the free carbon and 'destabilize' the SiOC system. The electrical conductivity increases from room temperature to ˜950 °C and then decreases due to the breakdown of the conductive path from the turbostratic carbon network. The maximum conductivity of 1176.55 S/m is achieved by SiOC-Ti-0.20 pyrolyzed at 1300 °C while at 950 °C, in argon, which is the highest reported for the SiOC-based systems. The conductivity of the Si-O-C-Ti composites is related to the ordering, amount, and interconnectivity of the carbon network as well as TiC formation.

5.6. References

1. Lu, K., *Porous and high surface area silicon oxycarbide-based materials—a review.* Materials Science and Engineering: R: Reports, 2015. **97**: p. 23-49.
2. Ionescu, E., H.-J. Kleebe, and R. Riedel, *Silicon-containing polymer-derived ceramic nanocomposites (PDC-NCs): Preparative approaches and properties.* Chemical Society Reviews, 2012. **41**(15): p. 5032-5052.
3. Lu, K., D. Erb, and M. Liu, *Thermal stability and electrical conductivity of carbon-enriched silicon oxycarbide.* Journal of Materials Chemistry C, 2016. **4**(9): p. 1829-1837.

4. Stabler, C., et al., *Silicon oxycarbide glasses and glass-ceramics:"All-Rounder" materials for advanced structural and functional applications.* Journal of the American Ceramic Society, 2018. **101**(11): p. 4817-4856.
5. Corriu, R., et al., *29Si nuclear magnetic resonance study of the structure of silicon oxycarbide glasses derived from organosilicon precursors.* Journal of materials science, 1995. **30**(9): p. 2313-2318.
6. Zhuo, R., et al., *Silicon oxycarbide glasses for blood-contact applications.* Acta Biomaterialia, 2005. **1**(5): p. 583-589.
7. Li, H.-F., et al., *Effect of NO annealing conditions on electrical characteristics of n-type 4H-SiC MOS capacitors.* Journal of electronic materials, 2000. **29**(8): p. 1027-1032.
8. Ding, Y. and H. Shirai, *White light emission from silicon oxycarbide films prepared by using atmospheric pressure microplasma jet.* Journal of Applied Physics, 2009. **105**(4): p. 043515.
9. Riedel, R., et al., *Piezoresistive effect in SiOC ceramics for integrated pressure sensors.* Journal of the American Ceramic Society, 2010. **93**(4): p. 920-924.
10. David, L., et al., *Silicon oxycarbide glass-graphene composite paper electrode for long-cycle lithium-ion batteries.* Nature communications, 2016. **7**: p. 10998.
11. Blum, Y.D., D.B. MacQueen, and H.-J. Kleebe, *Synthesis and characterization of carbon-enriched silicon oxycarbides.* Journal of the European Ceramic Society, 2005. **25**(2-3): p. 143-149.
12. Sorarù, G.D. and D. Suttor, *High temperature stability of sol-gel-derived SiOC glasses.* Journal of sol-gel science and technology, 1999. **14**(1): p. 69-74.
13. Sorarù, G.D., et al., *Role of precursor molecular structure on the microstructure and high temperature stability of silicon oxycarbide glasses derived from methylene-bridged polycarbosilanes.* Chemistry of materials, 1998. **10**(12): p. 4047-4054.
14. Erny, T., et al., *Microstructure Development of Oxycarbide Composites during Active-Filler-Controlled Polymer Pyrolysis.* Journal of the American Ceramic Society, 1993. **76**(1): p. 207-213.
15. Lu, K., D. Erb, and M. Liu, *Phase transformation, oxidation stability, and electrical conductivity of TiO2-polysiloxane derived ceramics.* Journal of Materials Science, 2016. **51**(22): p. 10166-10177.

16. Lu, K. and D. Erb, *Polymer derived silicon oxycarbide-based coatings.* International Materials Reviews, 2018. **63**(3): p. 139-161.
17. Chae, S.-H. and Y.-W. Kim, *Effect of inert filler addition on microstructure and strength of porous SiC ceramics.* Journal of materials science, 2009. **44**(5): p. 1404-1406.
18. Kim, Y.W., et al., *Processing of porous silicon carbide ceramics from carbon-filled polysiloxane by extrusion and carbothermal reduction.* Journal of the American Ceramic Society, 2008. **91**(4): p. 1361-1364.
19. Ionescu, E., et al., *Polymer-Derived SiOC/ZrO2 Ceramic Nanocomposites with Excellent High-Temperature Stability.* Journal of the American Ceramic Society, 2010. **93**(1): p. 241-250.
20. Yan, X., et al., *Preparation of SiOC/HfO2 fibers from silicon alkoxides and tetrachloride hafnium by a sol–gel process.* Materials Letters, 2015. **148**: p. 196-199.
21. Nguyen, V.G., et al., *Effect of titanium dioxide on the properties of polyethylene/TiO2 nanocomposites.* Composites Part B: Engineering, 2013. **45**(1): p. 1192-1198.
22. Gourinchas Courtecuisse, V., et al., *Kinetics of the titanium isopropoxide decomposition in supercritical isopropyl alcohol.* Industrial & engineering chemistry research, 1996. **35**(8): p. 2539-2545.
23. Berger, L.-M., et al., *On the mechanism of carbothermal reduction processes of TiO2 and ZrO2.* International Journal of Refractory Metals and Hard Materials, 1999. **17**(1-3): p. 235-243.
24. Tan, D., et al., *Surface passivated silicon nanocrystals with stable luminescence synthesized by femtosecond laser ablation in solution.* Physical Chemistry Chemical Physics, 2011. **13**(45): p. 20255-20261.
25. Lu, K. and J. Li, *Fundamental understanding of water vapor effect on SiOC evolution during pyrolysis.* Journal of the European Ceramic Society, 2016. **36**(3): p. 411-422.
26. Brewer, C.M., et al., *Insights into the oxidation chemistry of SiOC ceramics derived from silsesquioxanes.* Journal of sol-gel science and technology, 1999. **14**(1): p. 49-68.
27. Vallauri, D., I.A. Adrian, and A. Chrysanthou, *TiC–TiB2 composites: a review of phase relationships, processing and properties.* Journal of the European Ceramic Society, 2008. **28**(8): p. 1697-1713.

28. Tang, D., et al., *Preparation of alumina-coated graphite for thermally conductive and electrically insulating epoxy composites.* RSC Advances, 2015. **5**(68): p. 55170-55178.
29. Cordelair, J. and P. Greil, *Electrical conductivity measurements as a microprobe for structure transitions in polysiloxane derived Si–O–C ceramics.* Journal of the European Ceramic Society, 2000. **20**(12): p. 1947-1957.
30. Pang, Y., H. Xie, and R. Koc, *Investigation of electrical conductivity and oxidation behavior of TiC and TiN based cermets for SOFC interconnect application.* ECS Transactions, 2007. **7**(1): p. 2427-2435.
31. Bouillon, E., et al., *Conversion mechanisms of a polycarbosilane precursor into an SiC-based ceramic material.* Journal of materials science, 1991. **26**(5): p. 1333-1345.
32. Monthioux, M. and O. Delverdier, *Thermal behavior of (organosilicon) polymer-derived ceramics. V: Main facts and trends.* Journal of the European Ceramic Society, 1996. **16**(7): p. 721-737.
33. Bauer, F., et al., *Preparation of moisture curable polysilazane coatings: Part I. Elucidation of low temperature curing kinetics by FT-IR spectroscopy.* Progress in organic coatings, 2005. **53**(3): p. 183-190.

Chapter 6

Phase Content Prediction in Polymer-derived Ceramics with Metal Additives

Ni Yang, Kathy Lu*

Department of Materials Science and Engineering, Virginia Polytechnic Institute and State University, Blacksburg, Virginia, 24061, USA

*Corresponding author: Email: klu@vt.edu

Declarations of interest: none

*This chapter has been adapted from a manuscript by Ni Yang and Kathy Lu, with **under revision** in Composites Part B: Engineering.*

6.1. Abstract

In this study, silicon oxycarbide (SiOC) is selected as the polymer-derived ceramic matrix, and transition metals M (M=Ni, Mo, Co, and Zr) are introduced into the SiOC base to form SiMOC systems. Different ceramic phases, SiOC-Ni, SiOC-MoC_x, and SiOC-$CoSi_x$ are obtained by pyrolysis at 1100 °C, whereas SiOC-ZrO_x forms upon pyrolysis at 1400 °C. Four different phase separation pathways have been established based on their phase regions (SiC-SiO_2-C-Ni, SiC-SiO_2-C-MoC_x, SiC-SiO_2-C-$CoSi_x$, and SiC-SiO_2-C-ZrO_x). Driving force for crystallization has been analyzed using a Gibbs free energy minimization method and phase fractions of these different PDC systems are calculated based on the lever rule. This work also reveals the energetics related to the quaternary systems and provides guidance to synthesizing metal-containing PDCs with desired phase contents. In addition, we have examined the wide applicability of the phase content prediction method in a variety of other SiOC/metal systems.

6.2. Introduction

Recently, polymer-derived ceramics (PDCs) have raised great interest due to a series of advantages over other traditional ceramics, such as chemical, thermal, and oxidation stabilities [1-3]. PDCs can be divided into two categories: binary (e.g., SiC), ternary (e.g., SiCN, SiOC), or higher-order systems (e.g., SiOBC) [4]. SiOC can be described as a nanosystem composed of SiO_xC_{4-x} units with dispersed turbostratic carbon, SiO_2, or SiO_2 plus SiC [2, 5-7] and exhibits remarkable application potentials in biomedical devices [8], supercapacitors [9], optoelectronics [10], and lithium-ion batteries [11].

With the development of SiOCs, introducing metal species into the SiOC matrix becomes exciting as magnetic [12, 13], catalytic [14, 15], and electrical properties [16, 17] can be extended to intrinsically non-functional glassy systems. In our previous studies [12, 16, 18], a ferromagnetic nickel-containing SiOC with electrical conductivity up to ~247 S/m at 900°C in an argon atmosphere was successfully synthesized from the mixture of polysiloxane (PSO) and nickel (II) 2,4-pentanedionate. The in-situ formed Ni crystallites accelerate the graphitization of free carbon and result in more percolating conductive network formation. They also simultaneously offer soft ferromagnetism. Pyrolysis of polysiloxane (PSO) and titanium (IV) isopropoxide (TTIP) at 1200–1400 °C leads to high-temperature resistant Si-O-C-Ti [16], which is thermally stable up to 1000 °C in the air with >99.8 wt% mass retention. Thus, it can be stated that when more elements

are incorporated into the framework of polymer precursors, new avenues for attractive properties from SiOC-based systems become possible.

Quantifying polymer-derived SiOC phases is still a task of great challenge. ^{29}Si nuclear magnetic resonance (MAS-NMR) spectroscopy [19] is a quite powerful technique to quantify SiO_4, SiO_3C, SiO_2C_2, $SiOC_3$, and SiC_4 species by fitting five peaks around -107, -71, -34, 7, and -11 ppm ^{29}Si chemical shifts, respectively. However, due to their small amounts and low signal-to-noise ratio, the relaxation behaviors of $SiOC_3$ and SiC_4 have not been separated properly. X-ray photoelectron spectroscopy (XPS) [20] can provide information about the local environment of Si, O, and C elements in the SiOC phase. However, it is a surface analysis method for oxidation states and the resolution is never suited for quantitative phase analysis. Our earlier work [21, 22] introduced a thermodynamic method to calculate the phase contents in the SiOC system based on Gibbs free energy minimization. However, the quantitative studies were focused on pure SiOC systems without any metal additives.

Without considering metal-containing additives, the thermodynamic properties of SiOC [23] depend on precursors, pyrolysis temperatures, and phase compositions. The enthalpy of the element Si, O, and C forming a new phase decreases as the amount of free carbon increases, but as the amount of oxygen increases. As metal species are added to SiOC systems, ternary phase diagrams are not enough for quantitative phase fraction evaluation. The thermodynamics of metal-added amorphous SiOC ceramics during high-temperature pyrolysis has not been understood. Although Ionescu et al.'s work [24] predicted the stability of pure metal/metal oxide/silicide/carbide (Sn, MnO_x, LuO_x, $FeSi_x$, or VC_x) in SiOC without taking into account of phase compositions of the matrix, evaluation of phase fraction changes of SiOC with different metal-containing additives is still lacking.

In this paper, Ni, Mo, and Co elements were added into the amorphous SiOC system and pyrolyzed at 1100 °C, whereas SiOC-Zr was obtained by pyrolysis at 1400 °C. The resultant ceramics were characterized using X-ray diffraction (XRD). A thermodynamic method was developed to analyze the driving force for crystallization of the metal-containing PDCs based on Gibbs free energy minimization. Phase fractions at different pyrolysis temperatures were obtained for each system and the energetics with respect to the corresponding quaternary composition diagrams was discussed. Four different phase separation pathways have been established based on

their respective phase regions (SiC-SiO_2-C-Ni, SiC-SiO_2-C-MoC, SiC-SiO_2-C-CoSi, or SiC-SiO_2-C-ZrO_2).

6.3. Experimental procedures

To synthesize samples consisting of SiOC and Ni, Mo, Co, or Zr, a polysiloxane substituted resin Polyramic® SPR-684 (PSO, $[–Si(C_5H_6)_2O–]_3[–Si(CH_3)(H)O–]_2[–Si(CH_3)(CH=CH_2)O–]_2$, Starfire Systems, Inc.) was used. The metal species were from different metal compounds as explained below and a mass ratio of Ni (Mo, Co, or Zr) to PSO at 0.02:1 was used. At least three samples were made for each composition. Among them, anhydrous tetrahydrofuran (THF, 99.7+%, Alfa Aesar) was used as a solvent to dissolve the Ni-, Mo-, and Co-containing samples.

The SiOC/Ni samples were made as described in our previous work [12]. Ni(II) 2,4-pentanedionate (Alfa Aesar) with a purity of 95% was selected as the nickel additive. The crosslinking of all samples was carried out in an oven at 60 °C for 12 hours and then at 120 °C for 12 hours.

The Co species for the SiOC/Co samples were obtained from cobalt (II) chloride hexahydrate ($CoCl_2·6H_2O$, 98% purity, Alfa Aesar®) and (3-aminopropyl)triethoxysilane (APTES, >98%, Sigma-Aldrich®) was used as a complexing agent. The molar ratio of cobalt to APTES was fixed at 1:4 to ensure the complete complexation of the cobalt ions. More specifically, a certain amount of THF was added to $CoCl_2·6H_2O$ in a beaker and the solution turned dark blue after being placed in a sonicator bath for approximately 5 minutes. PSO was mixed with APTES and placed on a hot plate at 80°C with a stir bar set at 200 rpm. The cobalt/THF solution was added into the PSO slowly and stirred for 2 hours.
The solution was then poured into an aluminum mold and placed in a vacuum chamber until it reached 1500 mTorr.

For the SiOC/Mo samples, molybdenum(V) chloride (99.6%, Alfa Aesar®) was first dissolved in a THF solvent to form trichlorotris(tetrahydrofuran) molybdenum (III) - $MoCl_4(THF)_2$. The dissolved $MoCl_4(THF)_2$ solution was added to PSO in a beaker on a hot plate at 85°C with stirring at 250 rpm. After 2 hrs, the resultant viscous liquid was poured into an aluminum mold. The entire process was carried out in a glove box (Labstarpro, MBRAUN®) in argon gas. After that, the samples were placed in a vacuum chamber until 1500 mTor was reached.

The SiOC/Zr samples were fabricated from PSO and zirconium(IV) propoxide (70% solution in propanol, Acros®). About 2% platinum-divinyldimethyltetramethyldisiloxane complex (Pt catalyst, Gelest Inc.) in xylene was used as the catalyst. Similar to the operation performed on SiOC/Mo samples, first place the zirconia in a beaker under an argon atmosphere in a glove box, and then mix with PSO for 2 hrs under a 200 rpm stir bar. After a homogeneous mixture is obtained, the solution is poured into an aluminum mold and placed in a vacuum chamber until it reaches 1500 mTorr.

All samples were cut into 10 mm × 10 mm × 2.5 mm and polished for pyrolysis. For pyrolysis, the sample was placed in a zirconia boat with graphite felt on the side. Use a tube furnace (1730-12 horizontal tube furnace, CM Furnaces Inc.) to heat SiOC/Ni, SiOC/Mo, and SiOC/Co samples from room temperature to 1100 ℃ at a rate of 2 ℃/min. The argon flow rate is 500 cm^3/min. For the SiOC/Zr sample, the furnace temperature went up to 1400 ℃, and all the other parameters were the same as for the other samples. Only the SiOC/Ni pyrolysis used a gas mixture of Ar+H_2O and the details about water vapor settings were described in [25]). The other samples used a pure Ar pyrolysis atmosphere. The details are shown in Table 6.1.

Table 6.1. Details for the synthesis of SiOC/metal samples.

Sample name	***Composition of precursors***	***Pyrolysis condition***	***Phase composition***
SiOC/Ni	PSO + nickel(II)2,4-pentanedionate	1100 ℃, Ar + H_2O (molar ratio at Ar:H_2O=5:1)	SiOC/SiO_2/Ni
SiOC/Mo	PSO + molybdenum chloride	1100 ℃, Ar	SiOC/SiO_2/MoC
SiOC/Co	PSO + cobalt chloride + APTES	1100 ℃, Ar	SiOC/SiO_2/graphite/CoSi/CoO
SiOC/Zr	PSO + zirconium propoxide	1400 ℃, Ar	SiOC/SiO_2/ZrO_2

X'Pert PRO diffractometer (PANalytical BV) is used to analyze the phase composition of the

sample. The chemical composition was analyzed by inductively coupled plasma emission spectrometry (Agilent 5100/5110 VDV ICP-OES). The spectrometer has an axial plasma configuration with a concentric quartz atomizer. The instrument conditions are optimized to obtain sufficient sensitivity and accuracy. Standard solutions (1000 $\mu g \cdot mL^{-1}$) of carbon, silicon, nickel, molybdenum, cobalt, and zirconium were purchased from Agilent. The chosen wavelengths are shown in Table 6.2. The solutions of each sample measurement were prepared based on the lithium borate fusion-acid dissolution method [26].

Table 6.2. Wavelengths used for each element for quantification by ICP-OES.

Elements	*Si*	*C*	*Ni*	*Co*	*Mo*	*Zr*
Wavelength (nm)	251.611	193.027	231.604	238.892	202.032	343.823

6.4. Results and discussion

6.4.1. Metal-containing SiOC system

In our recent studies [21, 22], a thermodynamic model for the ternary SiOC ceramic system has been developed to calculate the amorphous phase fractions of the Si-O-C systems from the polymer-derived ceramics. The approach can be separated into two steps. First, a SiOC system phase separates into regions of free carbon and amorphous SiO_xC_y, with the latter located on the tie-line joining the phases SiC and SiO_2 in the Si-O-C composition diagram, as shown in Fig. 6.1(a). Second, the SiO_xC_y phase separates into SiC, SiO_2, and other intermediate SiOC compounds ($SiO_{\frac{3}{2}}C_{\frac{1}{4}}$, $SiOC_{\frac{1}{2}}$, and $SiO_{\frac{1}{2}}C_{\frac{3}{4}}$) located along the SiC-$SiO_2$ tie-line. The thermodynamic driving force for crystallization can be calculated from the Gibbs energy difference of the amorphous ($G^a(T)$) and crystalline ($G^{cr}(T)$) solids, at temperatures below the glass transition point. The total Gibbs free energy and phase content at different pyrolysis temperatures can be calculated based on the Gibbs free energy minimization method.

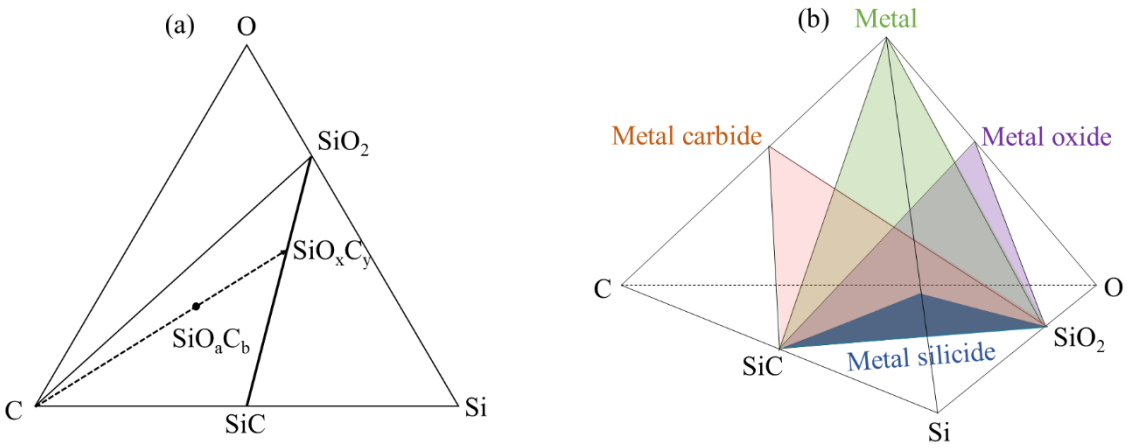

Fig. 6.1. Schematic illustration of phase separation corresponding to (a) SiOC and (b) SiOC/metal systems.

Compared to the SiOC model described above, metal-modified SiOC models have a more profound significance due to their more interesting functionalities. In general, the phase evolution of quaternary SiOC/metal systems depends on the type of metals used. The phase formation of the SiOC/metal systems can be divided into four types - pure metal, metal carbide, metal silicide, and metal oxide, as listed in Fig. 6.1(b). As to which metal compound appears in a given SiOC/metal system, it depends on the thermodynamic stability of the metallic compounds generated during pyrolysis. To explain it in more detail, the thermodynamic data (HSC Chemistry 6.0 software) of the involved metal species have been calculated as depicted in Fig. 6.2.

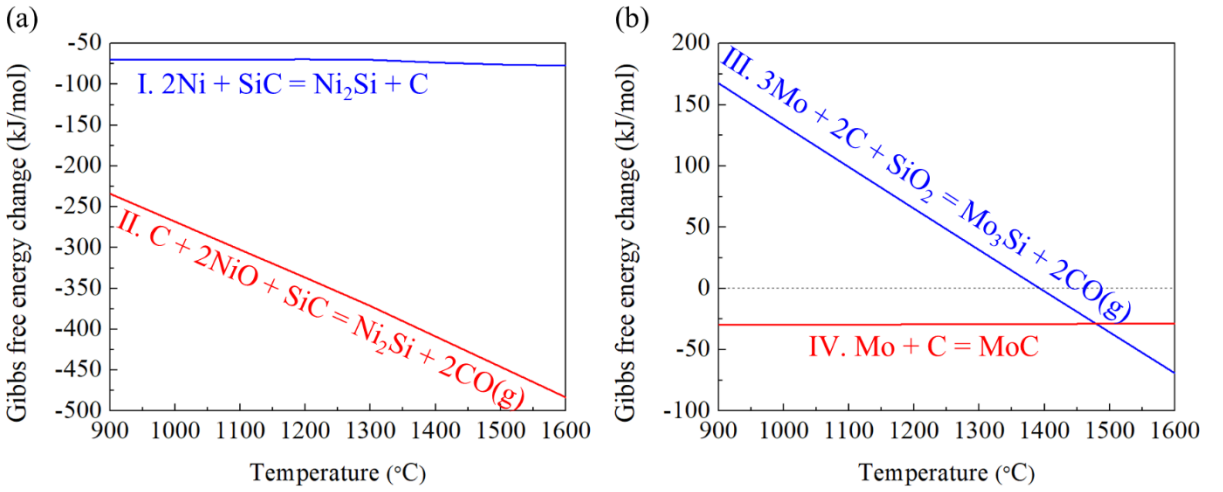

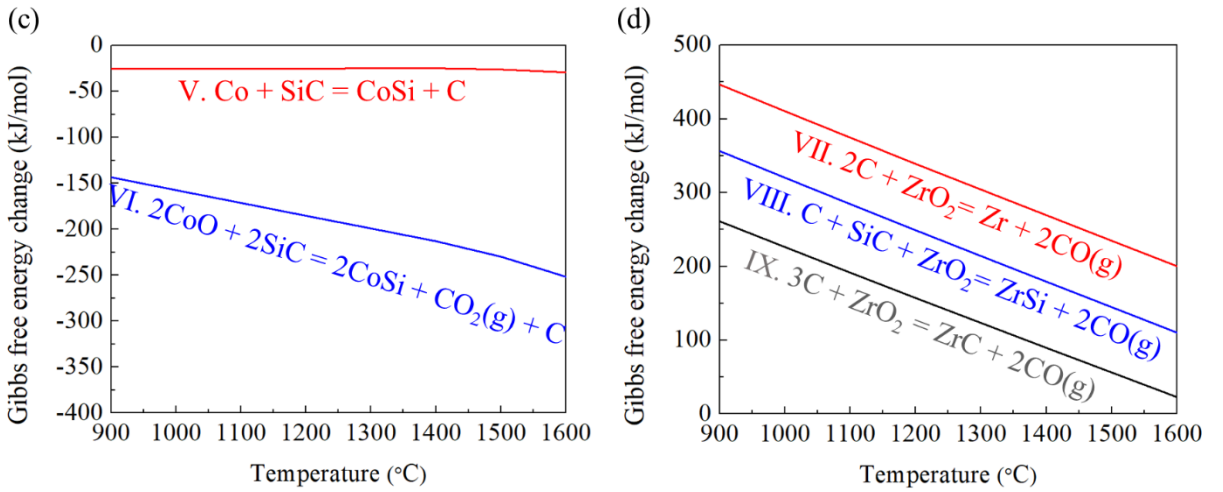

Fig. 6.2. Gibbs free energy change of different metal compounds in the SiOC systems with respect to pyrolysis temperature.

For Ni-modified SiOC systems, generally, both inorganic Ni salt and organic Ni complex can be carbothermal reduced to Ni [12, 27], which may partially react to form NiO [28] in the SiOC matrix during pyrolysis. Thus, either Ni or NiO forms upon the initial polymer-to-ceramic transformation of the Ni-modified SiOCs. At higher temperatures in an argon atmosphere, Ni_2Si formation is favored as a result of the negative ΔG (reactions I and II) due to the reaction between the Ni atoms and the Si species in the Si-O-C amorphous phase, to crystallize Ni_2Si. However, if water vapor is added into the argon atmosphere during the pyrolysis, it can effectively suppress the formation of Ni_2Si and the details have been explained in our previous work [12].

Different from Ni, the pathway for the formation of Mo-related compounds up to 1600 °C is shown in Fig. 6.2(b). Pure Mo in the SiOC matrix is more likely to convert into MoC (reaction IV) at <1460 °C pyrolysis temperature. When the temperature is higher than 1460 °C, Mo_3Si formation (reaction III) becomes dominant over the formation of the MoC phase. In Fig. 6.2(c), similar to the Ni-modified SiOC system, the Co-containing additive also generates Co and CoO products in the matrix during the polymer-to-ceramic transformation of SiOC/Co. As demonstrated by the reactions V and VI in Fig. 6.2(c), the formation of CoSi is favored after pyrolysis since the values of ΔG are strongly negative. In Fig. 6.2(d), the reaction of zirconium(iv) propoxide shows a different path. Once ZrO_2 forms by the thermal decomposition of zirconium(iv)

propoxide [29], it is stable up to 1650 °C and cannot thermodynamically react with SiC or C to form pure Zr (reaction VII), or ZrSi (reaction VIII), or ZrC (reaction IX).

From Fig. 6.2, it can be seen that the thermodynamic stability of the metal compounds plays a crucial role in the phase formation and stability of the metal-modified SiOC systems. In reality, the evolution of different metal (Ni, Mo, Co, and Zr) containing species in Fig. 6.2 based on the Gibbs free energy agrees well with the experimental results, the XRD plots in Fig. 6.3, with consideration of the effect of water vapor on the SiOC/Ni system. For all the samples, an amorphous SiO_2 halo is centered at ~22 °. The presence of this halo has been well documented [30-32] and will not be discussed further in this work.

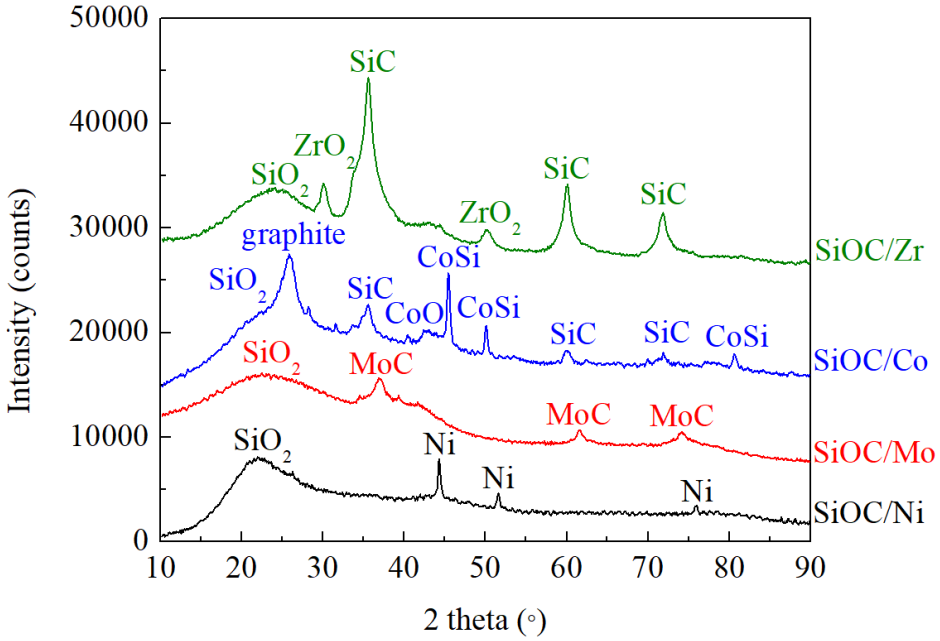

Fig. 6.3. XRD patterns for SiOC/M (M=Ni, Mo, Co) pyrolyzed at 1100 °C and for SiOC/Zr pyrolyzed at 1400 °C.

Fig. 6.3 shows various crystalline phases after the pyrolysis of the metal-containing SiOCs at 1100 °C or 1400 °C. As discussed above, since the formation of Ni_2Si was suppressed by water vapor [12], only 44.5 °, 51.9 °, and 76.4 ° peaks are observed, corresponding to the (111), (200), and (220) crystallographic planes of the cubic Ni phase with an FCC structure.

Pyrolysis of the Mo-containing polysiloxane results in a poorly crystallized SiOC/Mo system. Fig. 6.3 reveals the formation of MoC and its diffraction peaks are at 36.4 °, 61.4 °, and 77.4 ° for

the (111), (022), and (222) planes. Based on the literature [33], if the pyrolysis temperature exceeds 800 °C, MoC forms:

$$Mo + C \rightarrow MoC \quad (6.1)$$

If the temperature increases above 1400 °C, a small Mo_3Si peak will appear:

$$3Mo + 2C + SiO_2 \rightarrow Mo_3Si + 2CO \quad (6.2)$$

However, in this work, the pyrolysis temperature was only 1100 °C. Thus, these observations match with our discussion based on the thermodynamic calculation results in Fig. 6.2(b).

Different from the Ni and Mo-containing SiOCs, with the pyrolysis temperature increase, the $CoCl_2 \cdot 6H_2O$ dehydrates and degrades with the formation of Co^{2+} species, which can be easily reduced by H_2 and C_xH_y from the polymeric matrix decomposition. Also, the Co^{2+} species can react with the oxygen atoms to form CoO [34], and then cause the CoSi formation through reactions V and VI in Fig. 6.2(c). Thus, two kinds of Co compounds, CoO, and CoSi are formed. Due to the catalytic graphitization of carbon by metallic Co [35], the 26 ° peak corresponding to the (002) plane for graphitic carbon is strong. The highest X-ray intensities come from the formation of CoSi [36]. Again, the experimental results are consistent with the thermodynamic calculation in Fig. 6.2(c).

For the SiOC/Zr system, the t-ZrO_2 crystalline phase (29.7°) forms at 1400 °C pyrolysis temperature, which is also the only crystalline phase [37]. The (111), (101), and (211) diffraction peaks of β-SiC appear at 35°, 60°, and 72° respectively, after 1400°C pyrolysis. The absence of Zr, ZrSi, or ZrC phases proves that the XRD results match well with the above thermodynamic analysis (Fig. 6.2(d)).

The oxidation of SiC-based materials can be divided into two regimes [38]: active and passive oxidation, which is depending on the conditions-oxidizing types, pyrolysis temperature, pressure, and so on. Active oxidation, also called SiO gas, is formed at low oxygen partial pressures and high temperatures. As for passive oxidation, it is a protective silica layer formed at at high oxygen partial pressures and very high temperatures.

6.4.2. SiOC/M thermodynamic models

Based on Fig. 6.3, Ni, Mo, Zr, and Co represent four uniquely different phase formation paths in the SiOC system: pure metal, metal carbide, metal silicide, and metal oxide, as depicted in Fig. 1(b). These four-phase formation paths cover all the phase formation scenarios. Similar to Fig.

1(b), Fig. 6.4 illustrates the quaternary composition diagram for a specific SiOC/M (M=Ni, Mo, Co, or Zr) system. As shown, $SiO_aC_bM_c$ locates inside the four-phase equilibria of SiC-SiO_2-C-δ (δ = Ni, MoC, CoSi, or ZrO_2) and can phase-separate into two main compositions of δ-C and Si-O-C on the δ-C and SiC-SiO_2 tie lines, respectively. The formation of the δ-C domains results from the catalytic graphitization of carbon by Co, Ni, Mo, and Zr metals [35] during the pyrolysis process. They can also catalyze the formation of graphitic carbon through the formation-decomposition mechanism [39] of carbides or the carbon dissolution-precipitation mechanism [40] and the formation of the turbine layer carbon, although the complex process of graphitization catalyzed by transition metals is not fully understood. The overall phase composition of Fig. 6.4 can be formulated as:

$$SiO_aC_bM_c = f_{\delta-C} \cdot (\delta - C) + (1 - f_{\delta-C}) \cdot (Si - O - C) \quad (6.3)$$

More specifically, the details of the corresponding quaternary Si-O-C-M diagrams in Figs. 6.4(a-d) are:

$$SiO_aC_bNi_c = f_{Ni-C} \cdot (Ni_c - C_x) + (1 - f_{Ni-C}) \cdot (SiO_aC_{b-x}) \text{ for SiOC/Ni} \quad (6.3a)$$

$$SiO_aC_bMo_c = f_{MoC-C} \cdot (Mo - C_cC_x) + (1 - f_{MoC-C}) \cdot (SiO_aC_{b-c-x}) \text{ for SiOC/Mo} \quad (6.3b)$$

$$SiO_aC_bCo_c = f_{CoSi-C} \cdot (CoSi_c - C_x) + (1 - f_{CoSi-C}) \cdot (Si_{1-c}O_aC_{b-x}) \text{ for SiOC/Co} \quad (6.3c)$$

$$SiO_aC_bZr_c = f_{ZrO_2-C} \cdot ((ZrO_2)_c - C_x) + (1 - f_{ZrO_2-C}) \cdot (SiO_{a-2c}C_{b-x}) \text{ for SiOC/Zr} \quad (6.3d)$$

where the composition of each phase along the C-δ and SiC-SiO_2 tie lines can be calculated. It is well-known that SiO_AC_B can be represented as $SiO_{\frac{4-i}{2}}C_{\frac{i}{4}}$ (where i = 0 to 4) to account for the stoichiometric requirement of the SiO_2-SiC tie-line, which means the ratio of A and B in a SiO_AC_B system is

$$A = 2 - 2B \quad (6.4)$$

$f_{\delta\text{-}C}$ can be calculated from the same M composition along the δ-C-SiOC tie-line. Also, the composition of SiOC in each SiOC/M (M=Ni, Mo, Co, or Zr) system along the SiC-SiO_2 tie-line can be presented as the effective fraction of the SiO_2 and SiC phases, assuming no phase separation into intermediate compositions. The corresponding SiO_2 and SiC phases can be calculated by applying the lever rule (the negligible CoO content is not considered in this calculation in order to simplify the calculation process):

$$f_{Si-O} = f_{SiOC} \cdot \frac{\text{composition of O in } SiO_xC_y}{\text{composition of O in } SiO_2} \quad (6.5)$$

$$f_{SiC} = f_{SiOC} - f_{SiO_2} \quad (6.6)$$

Thus, for SiOC/Ni,

$$f_{Si-O} = \left(\frac{0.5a+2}{1+a+b+c}\right) \cdot \left(\frac{3a}{4+a}\right) \quad (6.7)$$

$$f_{Ni-C} = \frac{0.5a+b+c-1}{1+a+b+c} \quad (6.8)$$

$$f_C = 0.5a + b - 1 \quad (6.9)$$

For SiOC/Mo,

$$f_{Si-O} = \left(\frac{0.5a+2}{1+a+b+c}\right) \cdot \left(\frac{3a}{a+4}\right) \quad (6.10)$$

$$f_{MoC-C} = \frac{0.5a+b+c-1}{1+a+b+c} \quad (6.11)$$

$$f_C = 0.5a + b - c - 1 \quad (6.12)$$

For SiOC/Co,

$$f_{Si-O} = \left(\frac{0.5a-2c+2}{1+a+b+c}\right) \cdot \left(\frac{3a}{a-4c+4}\right) \quad (6.13)$$

$$f_{CoSi-C} = \frac{0.5a+b+3c-1}{1+a+b+c} \quad (6.14)$$

$$f_C = 0.5a + b + c - 1 \quad (6.15)$$

For SiOC/Zr,

$$f_{Si-O} = \left(\frac{0.5a-c+2}{1+a+b+c}\right) \cdot \left(\frac{3a-6c}{a-2c+4}\right) \quad (6.16)$$

$$f_{ZrO_2-C} = \frac{0.5a+b+2c-1}{1+a+b+c} \quad (6.17)$$

$$f_C = 0.5a + b - c - 1 \quad (6.18)$$

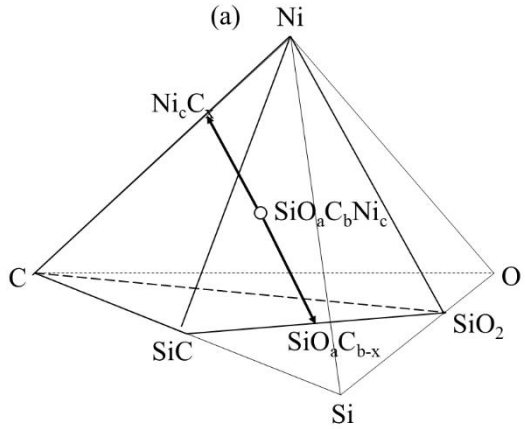

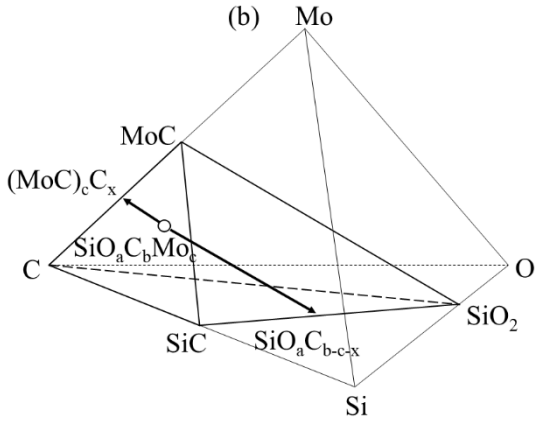

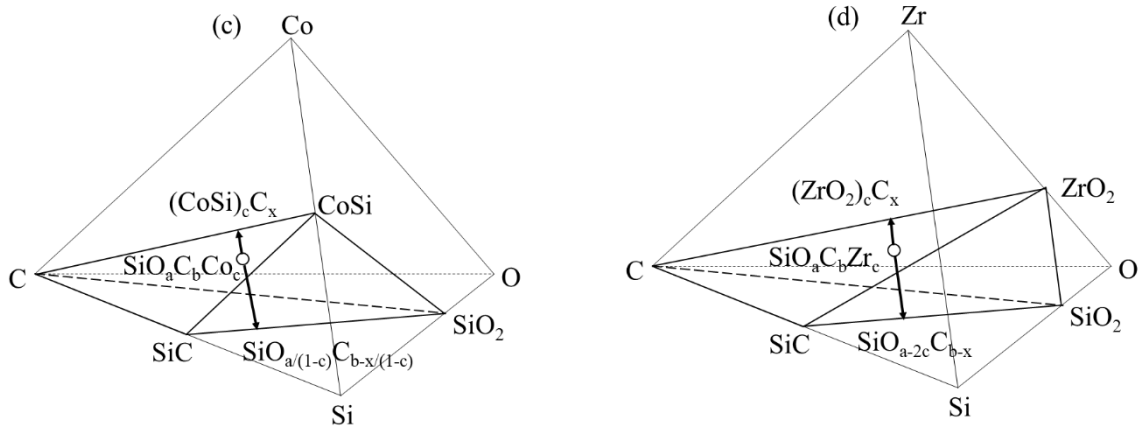

Fig. 6.4. Schematic illustration of phase separation of Si-O-C-M quaternary diagrams corresponding to (a) $SiC_aO_bNi_c$, (b) $SiC_aO_bMo_c$, (c) $SiC_aO_bCo_c$, and (d) $SiC_aO_bZr_c$.

The total amount (100%) of the phases separated from the SiOC/M matrix can be represented as (f_0, f_1, f_2, f_3, f_4, and f_5 represent the fractions of the corresponding phases):

$$f_0 \cdot (SiO_2) + f_1 \cdot \left(SiO_{\frac{3}{2}}C_{\frac{1}{4}}\right) + f_2 \cdot \left(SiO_{\frac{1}{2}}\right) + f_3 \cdot \left(SiO_{\frac{1}{2}}C_{\frac{3}{4}}\right) + f_4 \cdot (SiC) + f_5 \cdot (\delta) = 1 \quad (6.19)$$

In equation (6.19), it is noted that there is no $f_5 \cdot (\delta)$ term for the SiOC/Ni system because the Gibbs free energy for pure Ni is theoretically of zero value. The overall Gibbs free energy of the phase-separated SiOC/M (except for Ni) systems can be derived using the conventional formula:

$$G^{am-SiOC/M} = \sum_0^5 f_i(T) \cdot G_i(T) + RT \sum_0^5 f_i(T) \cdot \log f_i(T) \quad (6.20)$$

The specific fractions of various phases (f_i) at different temperatures can be calculated by the minimization of $G^{am\text{-}SiOC/M}$ method using Mathematica software based on the stoichiometric constraints for O, C, and M elements. Similar to our previous studies [21, 41], the Gibbs free energies of intermediate compositions ($SiO_{\frac{3}{2}}C_{\frac{1}{4}}$, $SiOC_{\frac{1}{2}}$, and $SiO_{\frac{1}{2}}C_{\frac{3}{4}}$) can be calculated by assuming their structures as mixed tetrahedra with $SiO_{(4-i)}C_i$ (where i = 1 to 3) compositions, which can be given as:

$$G(T)^{SiO_{\frac{3}{2}}C_{\frac{1}{4}}} = \frac{1}{4}G^{cr-SiC}(T) + \frac{3}{4}G^{cr-SiO_2}(T) \quad (6.21)$$

$$G(T)^{SiOC_{\frac{1}{2}}} = \frac{1}{2}G^{cr-SiC}(T) + \frac{1}{2}G^{cr-SiO_2}(T) \quad (6.22)$$

$$G(T)^{SiO_{\frac{1}{2}}C_{\frac{3}{4}}} = \frac{3}{4}G^{cr-SiC}(T) + \frac{1}{4}G^{cr-SiO_2}(T) \quad (6.23)$$

The thermodynamic driving force for the crystallization of the SiOC/M (M = Co, Mo, and Zr) systems can be expected from the difference between $G^{am-SiOC/M}$ and $G^{cr-SiOC/M}$, which can be calculated from:

$$G^{am-SiOC/M} = f_{\delta-C} \cdot G^{am-\delta} + (1 - f_{\delta-C}) \cdot (f_{Si-O} \cdot G^{am-SiO_2} + (1 - f_{Si-O}) \cdot G^{am-SiC}) \quad (6.24)$$

$$G^{cr-SiOC/M} = f_{\delta-C} \cdot G^{cr-\delta} + (1 - f_{\delta-C}) \cdot (f_{Si-O} \cdot G^{cr-SiO_2} + (1 - f_{Si-O}) \cdot G^{cr-SiC}) \quad (6.25)$$

For the SiOC/Ni system,

$$G^{am-SiOC/M} = f_{Si-O} \cdot G^{am-SiO_2} + (1 - f_{Si-O}) \cdot G^{am-SiC} \quad (6.26)$$

$$G^{cr-SiOC/M} = f_{Si-O} \cdot G^{cr-SiO_2} + (1 - f_{Si-O}) \cdot G^{cr-SiC} \quad (6.27)$$

Overall, for all the systems:

$$\text{Driving force for crystallization} = G^{am-SiOC/M} - G^{cr-SiOC/M} \quad (6.28)$$

The stable phase components of a specific SiOC/M (M=Ni, Mo, Co, or Zr) system can be derived from the total Gibbs free energy minimization ($G^{am-SiOC/M}$). The Gibbs free energy of the crystalline phases (SiO_2, SiC, and δ) can be obtained using an available database [21, 42-44]. The Gibbs free energy for the amorphous ones can be calculated according to

$$G^{amorphous}(T) = G^{crystalline}(T) + \Delta E \quad (6.29)$$

where ΔE is the vitrification enthalpy. The value of ΔE for SiC and SiO_2 can be found in our past paper [21]. ΔE for MoC, CoSi, and ZrO_2 are 35.5 kJ/mol [43], 7.6 kJ/mol [43], and 50.08 kJ/mol [45], respectively.

6.4.3. Phase and composition analysis

Based on the ICP measurement described in Section 6.2, the compositions for each pyrolyzed samples are given in Table 6.3. Applying the data in Table 6.3 into our thermodynamic model, the phase contents for all the samples can be calculated using Mathematica as shown in Table 6.4. No amount of nickel in Table 6.4 can be calculated due to its zero Gibbs free energy nature. The calculated values of SiC for SiOC/Ni, SiOC/Mo, and SiOC/Co are relatively lower than that from SiOC/Zr. This is because the pyrolysis temperature for SiOC/Zr (1400 °C) is much higher than that for others (1100 °C), resulting in more SiC through phase separation or carbothermal reduction. The XRD plot of SiOC/Co (Fig. 3) shows the obvious SiC peak, and the SiC content from SiOC/Co in Table 6.4 should be more than 0.05% due to the catalytic effect of cobalt. However, some SiC

was consumed by the reaction between SiC and Co (or CoO) to generate the CoSi phase (3.13%). The lowest SiC content is observed from SiOC/Ni at ~0.03%. It is well understood that water vapor induces the formation of SiO_2 nanodomains and suppresses the SiC phase, which has been reported in our past work [46]. The free carbon has reacted with water vapor and resulted in predominantly amorphous Si-rich phases, not C-rich tetrahedral or SiC. It also explains why there is the highest amount of SiO_2 in the SiOC/Ni sample.

Table 6.3. Elemental analysis (wt.%) of the pyrolyzed SiOC/Ni (1100 °C), SiOC/Co (1100 °C), SiOC/Mo (1100 °C), and SiOC/Zr (1400 °C) samples.

Samples	*Si*	*O*	*C*	*M (M=Ni, Mo, Co, or Zr)*	*Empirical Formula*
SiOC/Ni	41.2	22.4	32.1	4.3	$SiO_{0.95}C_{1.82}Ni_{0.05}$
SiOC/Mo	41.0	19.4	32.1	7.5	$SiO_{0.83}C_{1.83}Mo_{0.05}$
SiOC/Co	41.6	20.5	28.5	9.4	$SiO_{0.86}C_{1.60}Co_{0.07}$
SiOC/Zr	44.7	18.2	31.9	5.2	$SiO_{0.71}C_{1.66}Zr_{0.06}$

Table 6.4. Different phase amounts (mole fraction) of the pyrolyzed SiOC/Ni (1100 °C), SiOC/Co (1100 °C), SiOC/Mo (1100 °C), and SiOC/Zr (1400 °C) samples.

Samples	SiO_2	$SiO_{\frac{3}{2}}C_{\frac{1}{4}}$	$SiOC_{\frac{1}{2}}$	$SiO_{\frac{1}{2}}C_{\frac{3}{4}}$	*SiC*	δ
SiOC/Ni	39.46%	34.18%	14.91%	11.42%	0.03%	NA
SiOC/Mo	33.56%	31.34%	19.30%	10.92%	0.08%	4.80% (MoC)
SiOC/Co	36.54%	33.52%	17.65%	7.55%	0.05%	3.13% (CoSi), 1.56% (CoO)
SiOC/Zr	25.80%	30.93%	22.34%	16.42%	0.24%	4.27% (ZrO_2)

The phase fractions computed for the SiOC/Co and SiOC/Zr systems are both displayed in Fig. 6.5 with respect to the Si-O composition in SiO_xC_y. The corresponding plots of the SiOC/Ni and SiOC/Mo samples can be found in Fig. S1 of the supplementary file, which will not be discussed at length here. Due to the higher pyrolysis temperature (1400 °C) for SiOC/Zr, it has lower contents of metastable $SiO_{1.5}C_{0.25}$, $SiOC_{0.5}$, and $SiO_{0.5}C_{0.75}$ phases compared to the other

sample. In Table 6.4, it has been discussed that more SiC is present for the SiOC/Zr sample in Fig. 6.5(c) due to the higher pyrolysis temperature. As to the SiC content, SiOC/Co shows a little higher value than the SiOC/Ni and SiOC/Mo samples, although they look similar to each other. We believe that it can be explained by the catalytic effect from the transition metal Co [36]. Figs. 5(a-b) do not show the evident difference for the SiO_2 phase fractions, which means that the effects of transition metals and pyrolysis temperatures on the SiO_2 phase formation of the SiOC/M systems are negligible. Also, in SiOC/Zr, a peak at the lower composition of Si-O in SiOC/Zr is observed for the $SiOC_{1/2}$ phase, which we believe is related to the amount of ZrO_2. The maximum content of ZrO_2 at 0.3 (f_{si-o}) results in the decline of $SiOC_{1/2}$ phase to form peak to trough.

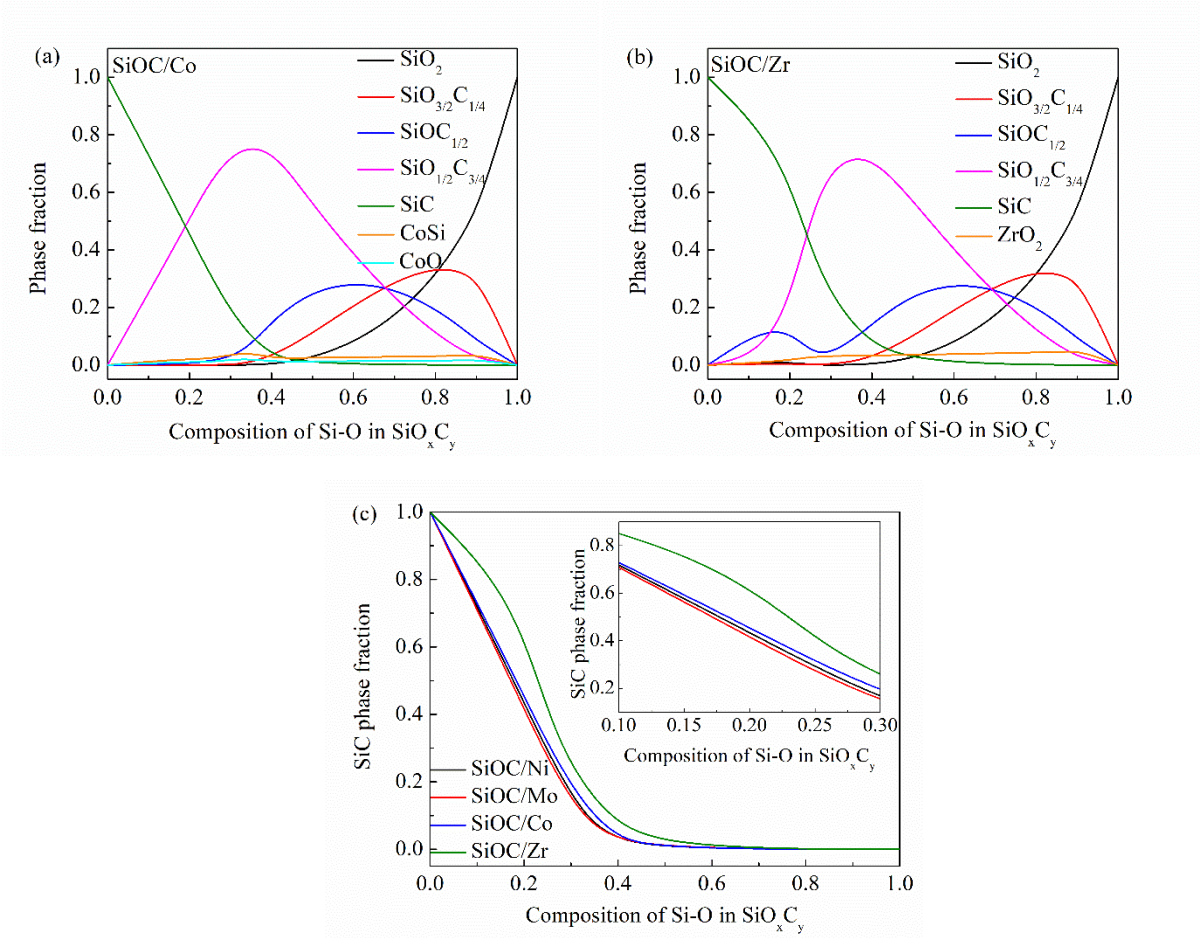

Fig. 6.5. Fraction of different phase contents in (a) SiOC/Co - 1100 °C and (b) SiOC/Zr - 1400 °C, and (c) SiC phase in all the samples.

The driving energies for crystallization have been computed for the SiOC/M ceramics. Fig. 6.6 shows the minimized Gibbs free energy for both amorphous and crystalline SiOC/M (M=Ni, Co, Mo, or Zr) materials at different f_{Si-O} in the SiO_xC_y matrix. The negative energies for crystallization are consistent with the expected thermodynamic instability of the amorphous SiOC/M phases, which vary with different f_{Si-O}. This theoretical result reflects the structural changes of the amorphous SiOC/M phases, as demonstrated by the changes in the computed phase fractions displayed in Table 6.4. In Figs. 6.6(a-c), the Gibbs free energy of SiO_xC_y is more negative than the crystalline and amorphous SiOC/M (M=Co, Ni, or Mo) after the pyrolysis of 1100 °C. It means that the system becomes more thermodynamically unstable after these metals are introduced into SiOC. A previous study [4] has reported that the average coordination number of the polymer-derived glass increases with an increasing number of transition metal sites in the glass structure, along with an increasing internal network strain and SiOC/M formation enthalpy. However, Fig. 6.6(d) shows the opposite trend for SiOC/Zr. The overall system becomes more stable after adding the Zr compound and pyrolysis at 1400 °C. The amorphous phase has further separated into the crystalline phase, which releases the network strain mentioned above. In addition, the difference between $G^{am\text{-}SiOC/M}$ and $G^{cr\text{-}SiOC/M}$ decreases with increasing Si-O composition in SiO_xC_y, except for the SiOC/Zr sample. In Figs. 6(a-d), ΔG is larger at lower f_{Si-O} values, which means that the system within this composition range has the least resistance to crystallization during pyrolysis. This is very consistent with the discussion in Figure 6.2. These metals are thermodynamically beneficial to react with SiC. When f_{Si-O} increases, the formation of SiO_2 delays the crystallization process, and the crystallization tendency decreases. Generally, this model can be used to estimate the phase separation behavior of the SiOC/M system. Based on this Gibbs free energy minimization method, the content of free carbon and other phases (from the SiC-SiO_2-δ tie line) of various SiOC/M components can be calculated.

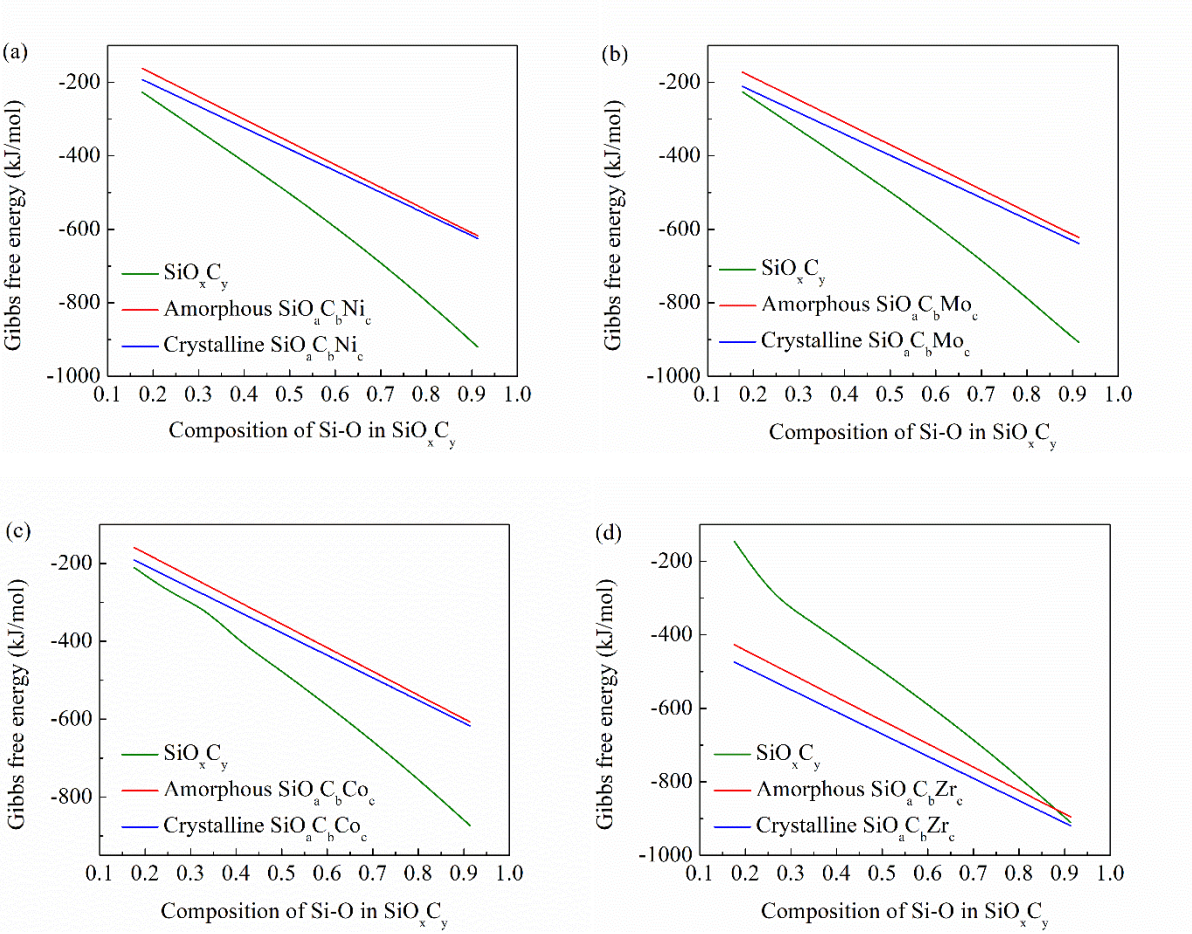

Fig. 6.6. Minimized Gibbs free energy of amorphous and crystalline phases: (a) $SiC_aO_bNi_c$-1100 °C, (b) $SiC_aO_bMo_c$-1100 °C, (c) $SiC_aO_bCo_c$-1100 °C, and (d) $SiC_aO_bZr_c$-1400 °C.

The main weakness of this model is that it is solely based on thermodynamic consideration at an ideal equilibrium state, the kinetic aspects of phase separation and crystallization are excluded. Because of this assumption, the phase amounts from the calculation and the measurements are not always consistent, especially when a system is far from equilibrium.

6.4.4. General metal-containing SiOC composites

The Gibbs free energy minimization method proposed in this study is an analysis method that can be applied to different SiOC systems. Table 6.5 shows the phase fractions of various SiOC/metal components calculated using the current method. In our past work [12], ferromagnetic SiOC/Ni was successfully fabricated from a base polysiloxane (PSO) with the addition of nickel

2,4-pentanedionate, and the generation of nickel silicides was completely suppressed by diminishing SiC formation during the pyrolysis. The method developed in this study can be used to confirm our previous conclusion quantitatively. The calculated SiC_4 values are almost zero for the SiOC/Ni samples at 800 and 900 °C, and ~2.2 wt% at 1100 °C in a water vapor plus argon condition. The values of the SiC content are clearly lower than that from the samples pyrolyzed in pure argon. As demonstrated in our previous studies [12, 25, 46], water vapor can preferentially remove free carbon in the SiOC matrix, thereby inhibiting the formation of SiC. Due to the predominance of SiC, the formation of metal silicides can be potentially inhibited.

Our quantitative analysis can be expanded to more literature reports [37, 47, 48]. Taking Liu et al.'s work [37] as an example, SiOC/metal oxide ($SiOC/ZrO_2$) ceramics were fabricated based on a hydrosilane and zirconium n-propoxide system through a classic sol-gel route. The empirical formula along with the measured percentages of SiC_4 and SiO_4 tetrahedra of Si-O-C-Zr ceramics pyrolyzed at 1200 – 1600 °C are listed in Table 6.5. In Liu's paper, only SiO_4 (-110 ppm) and SiC_4 (-15 ppm) were detected by ^{29}Si NMR, without considering the intermediate amorphous phases (SiO_xC_{4-x}) in the matrix. The SiO_2 content obtained based on equation (17) is relatively lower than the data in Liu's paper. This is because all the amorphous Si-O-C phases as well as the ZrO_2 phase are considered in our model while Liu's work only considered selected amorphous phases. Compared to the data from Liu's work, the results from our calculation above should be more reliable. For the calculations from SiOC/Sn [47] and SiOC/Hf [48] from Riedel et al.'s work, the calculated SiO_2 results are much smaller than the reported data, as well as the SiC content. The content of SiC in the literature is too high because it is difficult to produce in large quantities at lower temperatures (~ 1000 °C). As for the SiOC/Hf samples, the SiC content is much lower than the measured data. The total measured amount of SiC and SiO_2 is ~ 80% at the pyrolysis temperature of 800 – 1300 °C. This reported value is quite puzzling as it is well-known that the intermediate amorphous phases (SiO_xC_{4-x}) should be the dominating species in the matrix at < 1200 °C. Overall, from Table 6.5, the following observations can be summarized: (1) the phase fraction is affected by the polymer precursor, pyrolysis temperature and pyrolysis atmosphere, because these factors directly affect the evolution path of the phase; (2) the SiC phase content is generally low, where the SiO_2 is relatively high, as the amount of Si is fixed in a given system; (3) the quantitative analysis results from our Gibbs free energy minimization method varies from the measured data from ^{29}Si MAS NMR spectra, presumably due to the partial consideration of the

amorphous phases from the ^{29}Si MAS NMR study; (4) the value of our calculated SiC units is lower than that of measured ones, especially at lower temperatures. This calculation is consistent with the knowledge that the SiOC phases are very resistant to phase separation and SiC formation.

Table 6.5. Phase fractions were reported and calculated by our model for different SiOC/M systems in the literature.

Sample	*Pyrolysis (°C)*	*Empirical formula*	*Data from literature*		*Gibbs free energy minimization method*						*Reference*
			SiC_4	SiO_4	SiC	$SiO_{3/2}C_{1/4}$	$SiOC_{1/2}$	$SiO_{1/2}C_{3/4}$	SiO_2	δ	
SiOC/Ni	800	$SiO_{2.61}C_{1.97}Ni_{0.36}$	NA	NA	0.05	28.56	28.98	29.41	13.00	NA	[12]
	900	$SiO_{1.75}C_{2.07}Ni_{0.54}$	NA	NA	0.21	13.15	26.13	48.42	12.09	NA	
	1100	$SiO_{1.89}C_{0.59}Ni_{0.37}$	NA	NA	2.23	32.05	24.03	17.56	24.13	NA	
SiOC/Zr	1200	$SiO_{2.16}C_{0.12}Zr_{0.2}$	12	88	3.02	19.07	27.69	36.43	10.00	3.79	[37]
	1400	$SiO_{1.82}C_{0.29}Zr_{0.2}$	29	71	4.11	28.06	25.45	19.53	18.84	4.01	
	1600	$SiO_{1.74}C_{0.33}Zr_{0.2}$	33	67	4.81	27.56	25.22	18.97	19.33	4.11	
SiOC/Sn	1000	$SiO_{1.83}C_{0.57}Sn_{0.14}$	4	68	0.06	34.71	22.72	14.87	27.64	NA	[47]
	1000	$SiO_{1.71}C_{2.49}Sn_{0.25}$	5	45	0.90	9.93	24.86	52.25	12.06	NA	
	800	$SiO_{1.62}C_{0.63}Hf_{0.02}$	15	55	0.04	30.75	26.16	22.26	16.68	4.11	
	1000	$SiO_{1.54}C_{0.59}Hf_{0.02}$	17	57	0.12	29.56	25.91	22.72	17.57	4.12	

SiOC/Hf	1100	$SiO_{1.63}C_{0.54}Hf_{0.02}$	16	59	3.75	32.19	22.54	15.78	21.52	4.22	[48]
	1200	$SiO_{1.56}C_{0.63}Hf_{0.02}$	17	54	2.24	26.71	25.68	22.98	18.27	4.12	
	1300	$SiO_{1.66}C_{0.56}Hf_{0.02}$	14	59	3.19	28.29	22.41	16.05	25.79	4.27	

Regardless, the Gibbs free energy minimization model has room for improvement. For example, SiC is only assumed to form from SiOC phase separation. In reality, local carbothermal reduction [16] should be considered, especially at high temperatures, such as for the SiOC/Zr system that has been pyrolyzed at 1400 °C. During the pyrolysis, the phase-separated SiO_2 reacts with C to form cubic SiC along with CO release, and this process can be limited on a local scale and represented as:

$$SiO_2 + 3C \rightarrow SiC + 2\ CO\uparrow$$

On the development of the Gibbs free energy minimization method in Section 6.3.2, only the thermodynamics of the SiOC phase separation process is considered, dictated by the energy difference between the initial and final states for phase formation and evolution. However, this thermodynamic model ignores the carbothermal reactions that may be present under a non-equilibrium state and maybe confined at a local scale. In other words, our thermodynamic modeling of crystalline phases in the SiOC/M system does not consider the local, non-equilibrium carbothermal reduction. Without considering this influence, less SiO_2 units are consumed. That is why the calculated SiO_2 values are relatively lower in Tables 6.4 and 6.5. It is also noted that the transition metals induce the formation of β-SiC, cristobalite silica, and graphitic carbon from polymeric precursors [24, 27, 49], although detailed mechanisms of these accelerated processes have not been clearly investigated. The current model mainly applies to low or no SiC content systems. The Gibbs energy minimization method provides the theoretical limits for different phase amounts contributed from the SiOC phase separation and thus the lower pyrolysis temperature regime (such as <1300°C). Our ongoing effort is to introduce the carbothermal reduction mechanism (only applicable to high-temperature conditions) and catalytic effect (only applicable to selected systems) into the Gibbs energy minimization method and the results will be reported in future studies.

Nonetheless, the significance of this approach is to provide quantitative phase fraction data on systems that cannot be measured experimentally, especially for largely amorphous intermediate phases in polymer-derived ceramics at low pyrolysis temperatures, as well as the content of additives. Since the SiC nanocrystallites (<5 nm) formed in the SiOC matrix makes even the TEM characterization challenging and a large amount of amorphous phases in the matrix also creates almost insurmountable obstacles to XRD quantification, the models and calculations presented in this study can serve as a much needed quantitative approach for phase analysis of polymer-derived ceramics.

6.5. Conclusions

In this work, a thermodynamic approach has been developed to quantitatively analyze the phase evolution and driving force for the formation of different phases in SiOC/M systems. Based on the models, SiOC/M (M=Co, Ni, Zr, or Mo) samples were correspondingly produced by pyrolysis of a polysiloxane mixed with various metal additives. The computed driving forces for crystallization prove that the addition of M content enhances crystallization tendency. This enhancement includes the crystallization of SiC as well as the δ phases (δ= Ni, MoC, CoSi, or ZrO_2). The fraction of each particular phase, including different amorphous phases, can be calculated based on the Gibbs free energy minimization method. This phase content prediction method can also be applied to other SiOC/metal studies in the quantitative phase and composition analysis.

6.6. Supplementary data

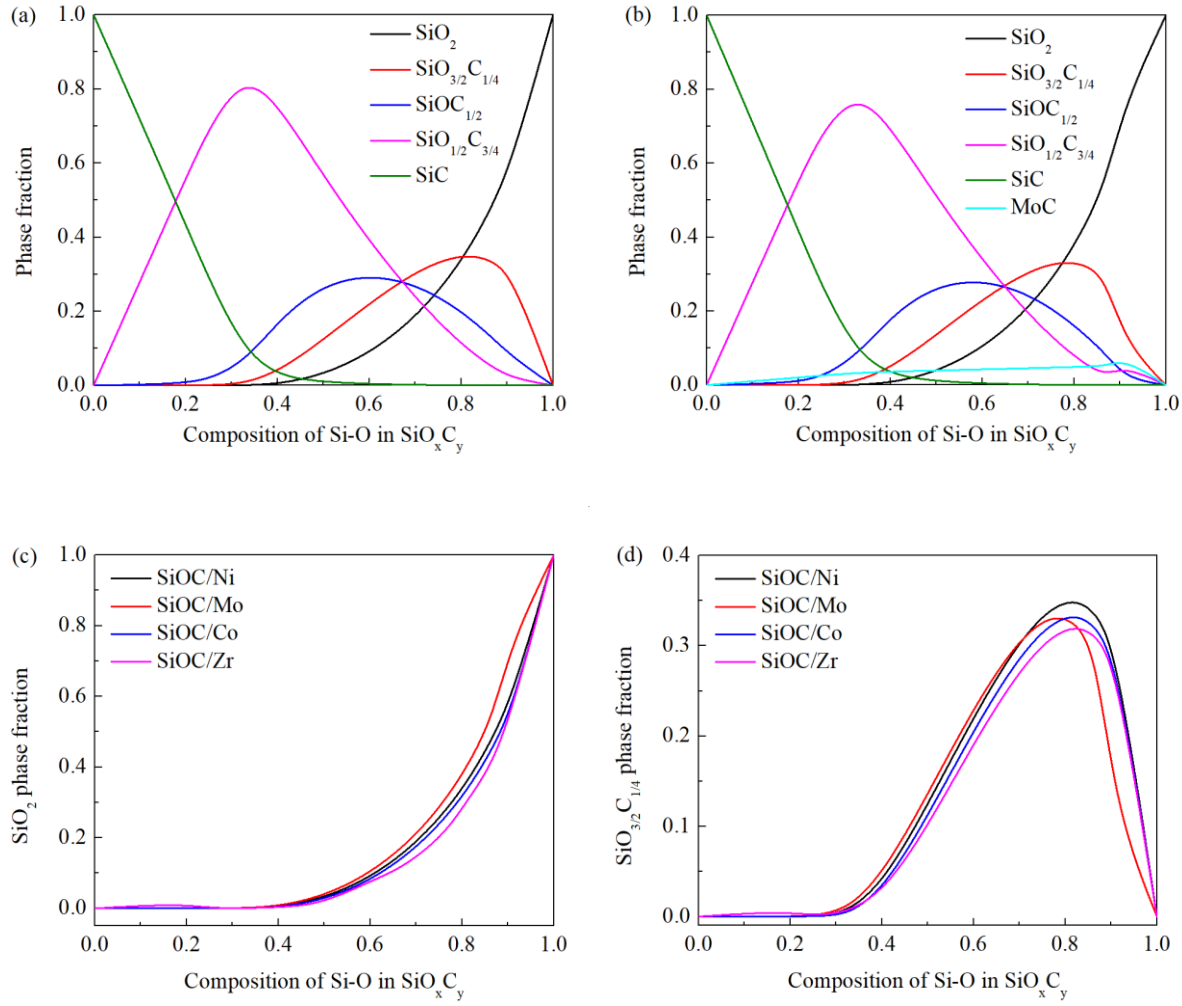

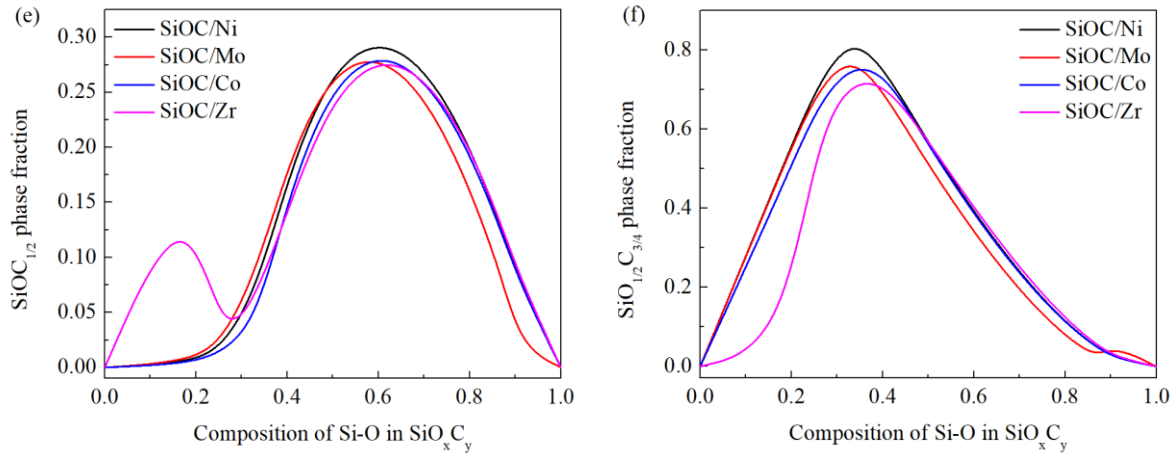

Fig. S6.1. Fraction of different phases in (a) SiOC/Ni - 1100 °C and (b) SiOC/Mo - 1100 °C; and (c) SiO_2, (d) $SiO_{3/2}O_{1/4}$, (e) $SiOC_{1/2}$, and (f) $SiO_{1/2}C_{3/4}$ phases in all the samples.

6.7. References

1. Lu, K., D. Erb, and M. Liu, *Phase transformation, oxidation stability, and electrical conductivity of TiO2-polysiloxane derived ceramics.* Journal of Materials Science, 2016. **51**(22): p. 10166-10177.
2. Lu, K., D. Erb, and M. Liu, *Thermal stability and electrical conductivity of carbon-enriched silicon oxycarbide.* Journal of Materials Chemistry C, 2016. **4**(9): p. 1829-1837.
3. Riedel, R., et al., *Silicon-based polymer-derived ceramics: synthesis properties and applications-a review dedicated to Prof. Dr. Fritz Aldinger on the occasion of his 65th birthday.* Journal of the Ceramic Society of Japan (日本セラミックス協会学術論文誌), 2006. **114**(1330): p. 425-444.
4. Colombo, P., *Polymer derived ceramics: from nano-structure to applications*. 2010: DEStech Publications, Inc.
5. Dibandjo, P., et al., *New insights into the nanostructure of high-C SiOC glasses obtained via polymer pyrolysis.* Glass Technology-European Journal of Glass Science and Technology Part A, 2008. **49**(4): p. 175-178.
6. Saha, A. and R. Raj, *Crystallization maps for SiCO amorphous ceramics.* Journal of the American Ceramic Society, 2007. **90**(2): p. 578-583.

7. Saha, A., R. Raj, and D.L. Williamson, *A model for the nanodomains in polymer-derived SiCO.* Journal of the American Ceramic Society, 2006. **89**(7): p. 2188-2195.
8. Zhuo, R., et al., *Silicon oxycarbide glasses for blood-contact applications.* Acta Biomaterialia, 2005. **1**(5): p. 583-589.
9. Meier, A., et al., *Silicon oxycarbide-derived carbons from a polyphenylsilsequioxane precursor for supercapacitor applications.* Microporous and mesoporous materials, 2014. **188**: p. 140-148.
10. Martins, R., et al. *Transport properties of doped silicon oxycarbide microcrystalline films produced by spatial separation techniques*. in *Proceedings of 1994 IEEE 1st World Conference on Photovoltaic Energy Conversion-WCPEC (A Joint Conference of PVSC, PVSEC and PSEC)*. 1994. IEEE.
11. Shen, J. and R. Raj, *Silicon-oxycarbide based thin film anodes for lithium ion batteries.* Journal of Power Sources, 2011. **196**(14): p. 5945-5950.
12. Yang, N., et al., *Nickel-containing magnetoceramics from water vapor-assisted pyrolysis of polysiloxane and nickel 2, 4-pentanedionate.* Journal of the American Ceramic Society, 2020. **103**(1): p. 145-157.
13. Zhang, X., et al., *Nickel silicide nanocrystal-containing magnetoceramics from the bulk pyrolysis of polysilazane and nickelocene.* Ceramics International, 2014. **40**(5): p. 6937-6947.
14. Macedo, H.P., et al., *Nickel-containing hybrid ceramics derived from polysiloxanes with hierarchical porosity for CO2 methanation.* Microporous and Mesoporous Materials, 2019. **278**: p. 156-166.
15. e Silva, T.C.d.A., et al., *Polymer-derived Co/Ni–SiOC (N) ceramic electrocatalysts for oxygen reduction reaction in fuel cells.* Catalysis Science & Technology, 2019. **9**(3): p. 854-866.
16. Yang, N. and K. Lu, *Thermophysical property and electrical conductivity of titanium isopropoxide – polysiloxane derived ceramics.* Journal of the European Ceramic Society, 2019. **39**(14): p. 4029-4037.
17. Eom, J.-H., et al., *Improved electrical and thermal conductivities of polysiloxane-derived silicon oxycarbide ceramics by barium addition.* Journal of the European Ceramic Society, 2018. **38**(2): p. 487-493.

18. Lu, K., D. Erb, and M. Liu, *Phase transformation, oxidation stability, and electrical conductivity of TiO 2-polysiloxane derived ceramics.* Journal of Materials Science, 2016. **51**(22): p. 10166-10177.
19. Widgeon, S.J., et al., *29Si and 13C Solid-State NMR Spectroscopic Study of Nanometer-Scale Structure and Mass Fractal Characteristics of Amorphous Polymer Derived Silicon Oxycarbide Ceramics.* Chemistry of Materials, 2010. **22**(23): p. 6221-6228.
20. Sorarù, G.D., G. D'Andrea, and A. Glisenti, *XPS characterization of gel-derived silicon oxycarbide glasses.* Materials Letters, 1996. **27**(1): p. 1-5.
21. Bawane, K., D. Erb, and K. Lu, *Carbon content and pyrolysis atmosphere effects on phase development in SiOC systems.* Journal of the European Ceramic Society, 2019. **39**(9): p. 2846-2854.
22. Lu, K., et al., *Comparison of traditional and flash pyrolysis of different carbon content silicon oxycarbides.* Journal of the European Ceramic Society, 2019. **39**(10): p. 3035-3041.
23. Mera, G., et al., *Polymer-derived SiCN and SiOC ceramics–structure and energetics at the nanoscale.* Journal of Materials Chemistry A, 2013. **1**(12): p. 3826-3836.
24. Ionescu, E., et al., *Thermodynamic control of phase composition and crystallization of metal-modified silicon oxycarbides.* Journal of the American Ceramic Society, 2013. **96**(6): p. 1899-1903.
25. Yang, N. and K. Lu, *Porous and ultrahigh surface area SiOC ceramics based on perhydropolysilazane and polysiloxane.* Microporous and Mesoporous Materials, 2020: p. 110477.
26. Feldman, C., *Behavior of traces of refractory minerals in the lithium metaborate fusion-acid dissolution procedure.* Analytical Chemistry, 1983. **55**(14): p. 2451-2453.
27. Segatelli, M.G., A.T.N. Pires, and I.V.P. Yoshida, *Synthesis and structural characterization of carbon-rich SiCxOy derived from a Ni-containing hybrid polymer.* Journal of the European Ceramic Society, 2008. **28**(11): p. 2247-2257.
28. Yu, Z., et al., *Polymer-derived mesoporous Ni/SiOC (H) ceramic nanocomposites for efficient removal of acid fuchsin.* Ceramics International, 2017. **43**(5): p. 4520-4526.
29. Inoue, M., H. Kominami, and T. Inui, *Novel synthetic method for the catalytic use of thermally stable zirconia: thermal decomposition of zirconium alkoxides in organic media.* Applied Catalysis A: General, 1993. **97**(2): p. L25-L30.

30. Erb, D. and K. Lu, *Additive and pyrolysis atmosphere effects on polysiloxane-derived porous SiOC ceramics.* Journal of the European Ceramic Society, 2017. **37**(15): p. 4547-4557.
31. Erb, D. and K. Lu, *Effect of additive structure and size on SiO2 formation in polymer-derived Si OC ceramics.* Journal of the American Ceramic Society, 2018. **101**(12): p. 5378-5388.
32. Erb, D. and K. Lu, *Synthesis of SiOC using solvent-modified polymer precursors.* Materials Chemistry and Physics, 2019. **237**: p. 121844.
33. Kaindl, A., et al., *Polymer-filler derived Mo2C ceramics.* Materials Science and Engineering: A, 1999. **260**(1-2): p. 101-107.
34. Sun, S. and C. Murray, *Synthesis of monodisperse cobalt nanocrystals and their assembly into magnetic superlattices.* Journal of applied Physics, 1999. **85**(8): p. 4325-4330.
35. Ōya, A. and S. Ōtani, *Catalytic graphitization of carbons by various metals.* Carbon, 1979. **17**(2): p. 131-137.
36. Vakifahmetoglu, C., et al., *Growth of one-dimensional nanostructures in porous polymer-derived ceramics by catalyst-assisted pyrolysis. Part II: cobalt catalyst.* Journal of the American Ceramic Society, 2010. **93**(11): p. 3709-3719.
37. Liu, C., et al., *Effects of Zr on the precursor architecture and high-temperature nanostructure evolution of SiOC polymer-derived ceramics.* Journal of the European Ceramic Society, 2016. **36**(3): p. 395-402.
38. Park, D.J., et al., *Oxidation behavior of silicon carbide at 1200°C in both air and water–vapor-rich environments.* Corrosion Science, 2014. **88**: p. 416-422.
39. Esconjauregui, S., C.M. Whelan, and K. Maex, *The reasons why metals catalyze the nucleation and growth of carbon nanotubes and other carbon nanomorphologies.* Carbon, 2009. **47**(3): p. 659-669.
40. Derbyshire, F., A. Presland, and D. Trimm, *Graphite formation by the dissolution—precipitation of carbon in cobalt, nickel and iron.* Carbon, 1975. **13**(2): p. 111-113.
41. Li, X., et al., *Structure retrieval from four-dimensional scanning transmission electron microscopy: Statistical analysis of potential pitfalls in high-dimensional data.* Physical Review E, 2019. **100**(2).

42. Golczewski, J.A. and F. Aldinger, *Thermodynamic modeling of amorphous Si–C–N ceramics derived from polymer precursors.* Journal of non-crystalline solids, 2004. **347**(1-3): p. 204-210.
43. Chase Jr, M.W., *NIST-JANAF thermochemical tables.* J. Phys. Chem. Ref. Data, Monograph, 1998. **9**.
44. Pan, Y. and J.L. Baptista, *Chemical instability of silicon carbide in the presence of transition metals.* Journal of the American Ceramic Society, 1996. **79**(8): p. 2017-2026.
45. Ranade, M.R., S.H. Elder, and A. Navrotsky, *Energetics of Nanoarchitectured TiO2−ZrO2 and TiO2−MoO3 Composite Materials.* Chemistry of Materials, 2002. **14**(3): p. 1107-1114.
46. Lu, K. and J. Li, *Fundamental understanding of water vapor effect on SiOC evolution during pyrolysis.* Journal of the European Ceramic Society, 2016. **36**(3): p. 411-422.
47. Kaspar, J., et al., *Stable SiOC/Sn nanocomposite anodes for lithium-ion batteries with outstanding cycling stability.* Advanced Functional Materials, 2014. **24**(26): p. 4097-4104.
48. Ionescu, E., et al., *Polymer-derived silicon oxycarbide/hafnia ceramic nanocomposites. Part I: phase and microstructure evolution during the ceramization process.* Journal of the American Ceramic Society, 2010. **93**(6): p. 1774-1782.
49. Harshe, R., C. Balan, and R. Riedel, *Amorphous Si (Al) OC ceramic from polysiloxanes: bulk ceramic processing, crystallization behavior and applications.* Journal of the European Ceramic Society, 2004. **24**(12): p. 3471-3482.

Chapter 7

Study of Single Nanometer and Co-Existing Amorphous and Crystalline SiOC Microstructures using 4D-STEM

Ni Yang[1], Colin Ophus[2], Benjamin H. Savitzky[2], Mary Scott[2,3], Karen Bustillo[2], and Kathy Lu[1*]

[1] Department of Materials Science and Engineering, Virginia Polytechnic Institute and State University, Blacksburg, Virginia, 24061, USA

[2] National Center for Electron Microscopy, Molecular Foundry, Lawrence Berkeley National Laboratory, 1 Cyclotron Road, Berkeley, CA, 94720, USA

[3] Department of Materials Science and Engineering, University of California, Berkeley, 94720, USA

*Corresponding author: Email: klu@vt.edu

Declarations of interest: none

*This chapter has been adapted from a manuscript with **under revision** in Materials Today.*

7.1. Abstract

Polymer-derived ceramics have great potentials in various high-temperature fields. However, lack of description and understanding of the short- to medium-range order and disorder hinders the advancement of this promising material family. In this study, poly(vinylmethylsiloxane)-derived silicon oxycarbide (SiOC) is used as a model system to address this issue. Electron diffraction-based radial distribution function (RDF) analysis is used for the first time to characterize the short- to medium-range order in the SiOC system and provide local structural data with a resolution of a few nanometers. With systematic data calibration and structural analysis, integrated 2D images of the diffraction patterns at each probe position are recorded and analyzed by a Python-based py4DSTEM toolkit; phase distributions of heterogeneous amorphous plus crystalline SiOC are obtained through 4D scanning transmission electron diffraction (4D-STEM). Local phase distributions at the single nanometer level are mapped. This approach provides never-before data for the fundamental understanding of the SiOC formation and microstructure evolution.

7.2. Introduction

Nanostructure analysis of amorphous plus crystalline materials is a great challenge due to their small sizes and mixed atomic arrangements [1]. Among these, polymer-derived silicon oxycarbide ceramics (SiOC) are X-ray amorphous but display structural heterogeneity at the nanometer length scale [2, 3]. The oxygen and carbon atoms bond randomly to silicon in a three-dimensional covalent structure - mixed SiOC units (SiC_xO_{4-x}, $1 < x < 4$) [4, 5]. Also, the structural characteristics of these SiOC units change progressively with the pyrolysis temperature, pyrolysis atmosphere, and polymeric precursors [6]. After pyrolysis at 800–1100 °C, SiOC glasses consist of a homogeneous network of mixed SiOC tetrahedrals and free carbon species. The system can be described as a nanocomposite composed of a SiOC matrix (including SiO_4, SiO_3C, SiO_2C_2, $SiOC_3$, and SiC_4 tetrahadrals) in which free carbon (amorphous C and turbostratic C) is dispersed. The microstructure is featureless. At 1100–1300 °C, amorphous SiO_2 nanodomains form. At higher temperatures (1300–1450 °C), the amorphous network undergoes further phase separation, which enhances the formation of SiO_2-rich phase and C-rich phase, the latter comprising β-SiC nanocrystals and turbostratic carbon. The microstructures at such high temperatures are amorphous plus crystalline. Due to the intriguing atomic structures and the wide application potentials of SiOCs, understanding of their continuously evolving atomic structures is highly needed.

Very few experimental techniques can provide a valid method to characterize the amorphous and crystalline mixed structures in SiOC materials. Traditional X-ray diffraction experiments with only large sample areas lack spatial resolution, especially at the nanoscale [3, 7, 8]. Neutron diffraction has great challenges in penetrating the bulk of the samples and examine discrete phases [9, 10]. High-resolution TEM shows significantly smaller β-SiC crystal (2-10 nm) precipitates in the SiOC at temperatures above 1250 °C [3] but the diffraction data can be from mixed phases.

Different from conventional STEM, recent advances in detector technologies and computational methods have enabled the recording of 2D images using a converged electron probe over a 2D grid of probe positions. This new exciting approach is termed 4D-STEM, which has been applied to virtual imaging, orientation mapping, strain mapping, and differential phase-contrast [11-15]. For example, structural mapping of organic amorphous material ([6,6]-phenyl C61-butyric acid methyl ester and poly(3-hexylthiophene-2,5-diyl)) [16] down to atomic resolution has been made possible due to the very small spatial extent of the electron probe. 4D-STEM pair distribution function analysis has provided the phase distribution of organic composites without valence states for electron energy loss spectroscopy [17]. Generally speaking, a smaller semi-convergence angle generates a higher depth-of-field [18]. However, if the semi-convergence angle is too small, the size of the electron probe in real space increase and spatial resolution is compromised [19]. Thus, a proper semi-convergence angle is critical for obtaining high-quality 4D-STEM data for quantitative analysis and varies from material to material.

In this work, we introduced 4D-STEM into the SiOC system in an attempt to characterize the well-recognized heterogeneous, nanostructured, and mixed amorphous and crystalline structures in combination with radial distribution function (RDF) mapping. We demonstrated that RDF analysis of 4D-STEM diffraction patterns in a nano volume is a critical starting point in the characterization of amorphous and crystalline mixed SiOC materials. These RDF maps can be analyzed in the short- and medium-range order in order to distinguish different glassy phases [20] as well as crystalline regions. To illustrate the potential of this approach, we applied this new method to understand the effect of carbon content on the amorphous structure of the SiOC matrix. It was shown that the method is extremely powerful to understand nanoscale structural variations in SiOC materials.

7.3. Materials and characterization

This work uses a commercially available poly(vinylmethylsiloxane) (PVMS, MW = 1000–1500 g/mol, Gelest Inc., Morrisville, PA) as the base precursor to synthesize the corresponding SiOC ceramics. Specifically, the polymeric solutions were poured into a clean zirconia crucible and placed into a tube furnace (1730-20 Horizontal Tube Furnace, CM Furnaces Inc., Bloomfield, NJ). The samples were pyrolyzed in an Ar atmosphere (AR 300, AirGas, Radford, VA) with a flow rate of about 900 std cm^3/min at 1400 °C, with a heating rate of 1 °C/min for 2 h, and then cooled to 25 °C with a rate of 1 °C/min.

A Gatan Orius CCD camera installed on an FEI TitanX operating at an accelerating voltage of 300 kV was used to record the 4D-STEM diffraction patterns [12] with an exposure time of 50ms. In real space, the scan positions were in a 50 x 50 pixel grid with a step size of ~2 nm resulting in a field of view of 100nm 100nm. A probe forming aperture below the second condenser lens had aperture size = 40 μm resulting in a quasi-parallel beam with a semi-convergence angle of 0.8 millirads. The illumination condition formed an electron probe with a full-width-half-max of 1.2 nm.

Py4DSTEM [21], a python-based software package developed by Lawrence Berkeley National Laboratory for analysis of 4D-STEM datasets, was applied to our dataset in this project. Py4DSTEM is open-source software and supports many different modes of 4D-STEM analysis.

7.4. Results and discussion

7.4.1. Data preprocessing and calibration

Several processing steps need to be applied to a 4D-STEM dataset in order to obtain an accurate analysis of the local structural information. Fig. 7.1(a) illustrates the average of all the diffraction patterns from a raw dataset (PVMS-derived SiOC) and visualizes the location of a bright-field detector (shown in red). No vertical streaks or defects are observed, and no background subtraction is needed to decrease the noise in the image.

To perform the Bragg disk detection and identify the reciprocal lattice points of the crystals in the SiOC ceramics [13, 18], the probe template in diffraction through vacuum was constructed and visualized in Fig. 7.1(b). It was generated from the average vacuum region in our 4D-STEM experimental scan, and its kernel (Fig. 7.1(c)) was formed by the Gaussian subtraction to increase the disk detectability. The Bragg disks were precisely detected by colored masks in some randomly

selected positions, as shown in Fig. 7.1(d-f). The sizes of the colored circles indicate the disk intensity. The entire dataset was recorded with a frame size of 50 × 50 pixels. The disk detections in this study were run on all the 2500 diffraction patterns collected.

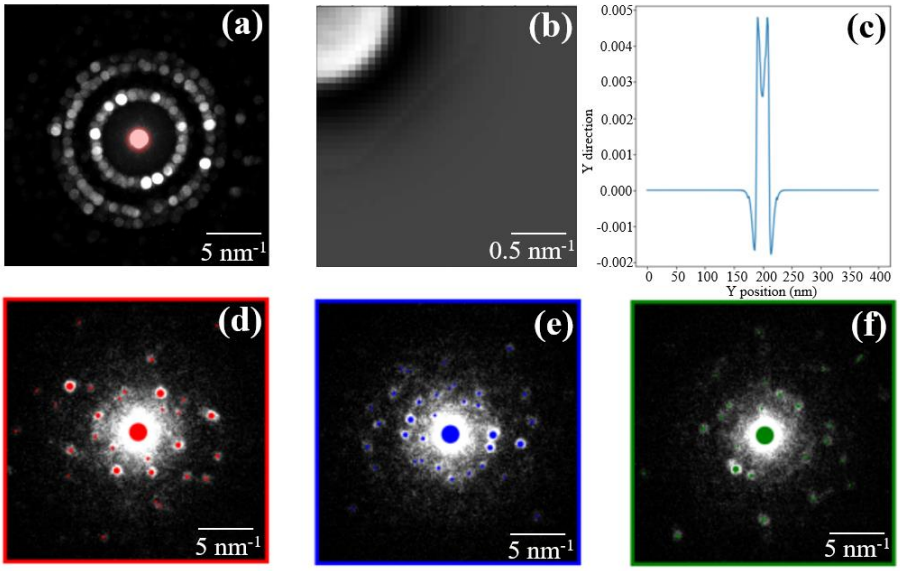

Fig. 7. 1. Bragg disk detection in the SiOC ceramic: (a) averaged diffraction pattern of 4D-STEM datacube (red shield – bright-field detector), (b) the vacuum probe template, (c) a kernel for cross correlative template matching with individual diffraction patterns, and (d-f) the detected Bragg disk positions.

Correction is the most significant step to ensure the accuracy of the analysis results [21, 22]. These include diffraction shift correction (Fig. 7.2, Fig. 7.3(a)-(f)) as well as elliptical distortion correction and pixel size calibration (Fig. 7.3 (g)-(h)).

Bragg vector maps, as a necessary part for calibration of the dataset (diffraction shift correction), can be obtained from the detected disks above (Fig. 7.1(a)). After a complete scan at every position with the function of position averaged probability distribution of reciprocal lattice points, all the peaks collapse into a single object and can be shown as the Bragg vector maps in Fig. 7.2(a). However, the diffraction shift is commonly observed because the direct electron beam slightly shifts the original position during the measurement [23], and thus the corresponding calibration should be conducted by locating the unscattered beam and calculating the shift in each position as shown on the right side of Fig. 7.2. Both before and after the diffraction shift correction, the diffraction patterns on the left side show the presence of amorphous halo rings along with

random crystal diffraction spots, which represent the mixed amorphous (SiC_xO_{4-x}, $1 < x < 4$) and crystalline (cristobalite and SiC) nature of SiOC, as discussed in the Introduction about the phase evolution of SiOC with pyrolysis temperatures. It is noted that the difference between Fig. 7.2(a) and (b) is not evident although the shape of the electron beam is more rounded on the lower right side of Fig. 2, which means that the beam shift during the data collection is not severe. The degree of the shift generally depends on the 4D-STEM parameters, such as camera length, real space scan, and instrument type [24].

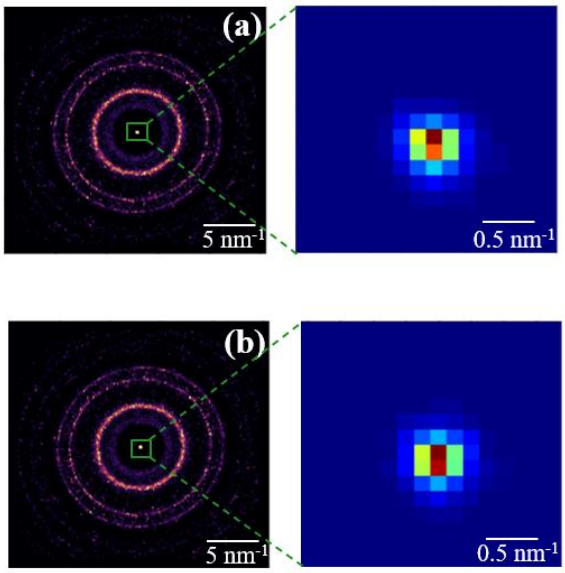

Fig. 7. 2. Bragg vector map (BVM) of the SiOC ceramic: (a) before diffraction shift correction and (b) after diffraction shift correction.

The top row images in Fig. 7.3(a-f) show the correction of diffraction shifts generated from the position optic axis from one diffraction pattern to the next. It shows the measurement of the shift histograms and images for different diffraction patterns. To be specific, Fig. 7.3(a) and (d) illustrate the initial measurements of shift at each position from the 4D-STEM images. After the diffraction shift correction for X (Fig. 7.3(h)) and Y (Fig. 7.3(e)) shifts, the corrected measurements in Fig. 7.3(e) and (f) show the shapes and pixels more clearly than before the correction (Fig. 7.3(a) and (d)). The circular features related to the optic axis are depicted in ellipses as illustrated in Fig. 7.3(g-h). These distortions must be corrected by fitting an elliptical function in the annular areas. In the amorphous material dataset, as for the SiOC sample studied

here, the polar-elliptical transform is the most common and useful tool to be applied in a coordinate system. The bottom row of Fig. 7.3(i) reveals the calibration of the diffraction pixel size by measuring the cristobalite diffraction vector with a known spacing. Fig. 7.3(i) shows the radial intensity of the elliptically corrected Bragg vector map in Fig. 7.3(h), and it matches well with the XRD reference data [8, 25], showing the expected peaks at 0.264, 0.395, 0.649, and 0.761 1/Å. The peak at 0.394 1/Å (2.53 Å) corresponds well to the brightest SiC peak in the structure [26]. SiC also has rather strong peaks at 0.646 and 0.757 1/ Å, in excellent agreement with the XRD pattern [7, 27]. The brightest SiO_2 peak is at 0.2419 1/Å, it is the only large peak that does not originate from SiC. In fact, it is much broader and supports the assertion that it is from a different phase.

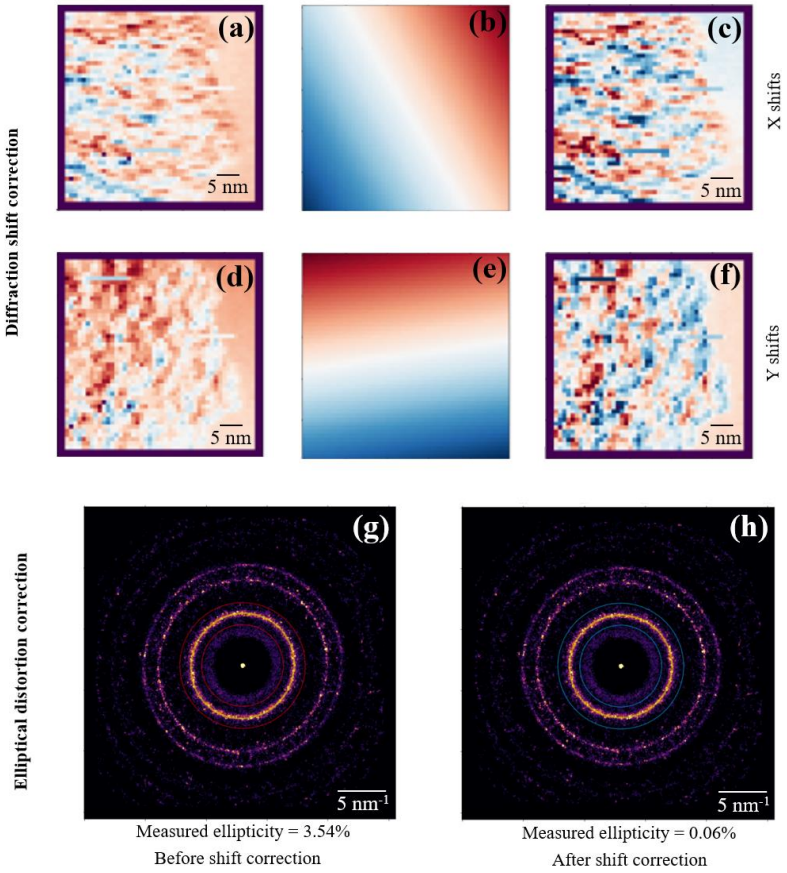

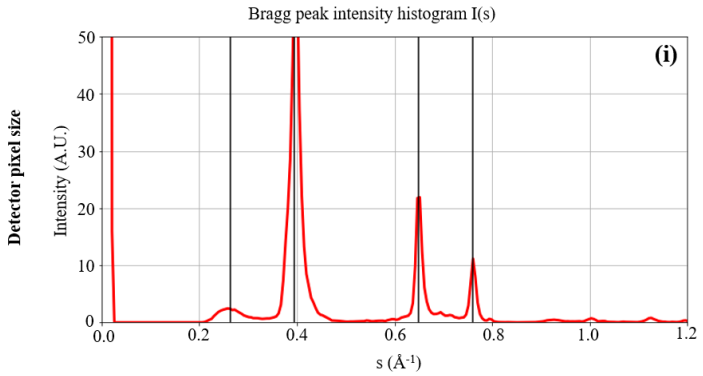

Fig. 7. 3. Calibration: (a-f) diffraction shift correction, (g-h) elliptical distortion correction, and (i) pixel size calibration.

7.4.2. Radial distribution function

Distinct features can be seen in Fig. 7.3(h) in that they are predominantly amorphous haloes and crystalline diffraction spots. The electron diffraction patterns of SiOC materials containing a substantial fraction of amorphous phases typically contain ring-like features with a radius given by a characteristic scattering length. Detailed structural information from the distance and density of neighboring shells of atoms can be obtained from an RDF analysis of the diffraction patterns. RDF [20] enables a concrete interpretation of the diffraction data in terms of interatomic distances and reveals reliable structural information of amorphous materials. The procedure for the combined 4D-STEM and RDF analysis includes data acquisition by recording the diffraction patterns in the STEM mode with a quasi-parallel nano-beam configuration (0.8 mrads semi-convergence angle and 1.2 nm probe size) over a 2D grid of probe positions. For the RDF analysis of the SiOC material, each experimental diffraction pattern is processed individually to determine a local RDF, from which detailed structural information is obtained. As explained in other studies [11, 20], the diffraction profile I(s) needs to be normalized by subtracting the single atomic scattering factor $\varphi(s)$ as expressed in Eq. (7.1):

$$\varphi(s) = \frac{I(s) - N\langle f(s)^2 \rangle}{N\langle f(s) \rangle^2} s \qquad (7.1)$$

Where N is the number of atoms within the volume sampled by the electron probe, s is the diffraction space, and f(s) is the parameterized elemental scattering factor. The corresponding RDF $G(r)$ can be obtained by a sine Fourier transformation of the structure factor $\varphi(s)$ in all the diffraction space according to Eq. (7.2):

$$G(r) = \int_0^{S_{max}} \varphi(s) sin(2\pi sr) ds \quad (7.2)$$

In reality, <f(s)> can only be treated as a rough approximation for the SiOC material. The diffraction profile I(s) should be fitted by the average scattering factor $\varphi(s)$ across a range of angles and consistent with the real structure from the SiOC matrix.

Two radial integrals can be calculated from Fig. 7.3(h) through a polar-elliptical transform as shown in Fig. 7.4(a) and Fig. 7.4(b) with a mask. It reveals the presence of a certain degree of Bragg scattering and therefore crystallinity, as well as the relationship between the diffraction intensity and optic axis distance. The resulting curve, I(q), is shown in Fig. 7.4(c). Clearly, there is a strong feature at 0.4 1/Å, and maybe another one at 0.75 1/Å, which is due to the presence of the crystalline phases. However, these two obvious features vanish (curve in red) for the median statistics based on masked Bragg peaks. Usually, the presence of crystallinities has minor effects on mean statistics, and it can be concluded that there is a very blurry boundary between the ordered and disordered phases in this SiOC system. By fitting the thermal background at low q area and atomic scattering factors at high q areas in Fig. 7.4(c), a structure factor, $\varphi(s)$, describing the arrangements of atoms in the SiOC materials, can be calculated in Fig. 7.4(d) for a given set of atomic species to the high angle scattering. Compared to the static structure factor $\varphi(s)$ above, RDF is advantageous due to its clear physical meaning and simplicity. Thus, the RDF with a real space quantity (Fig. 7.4(e)) is extracted from the structure factor $\varphi(s)$.

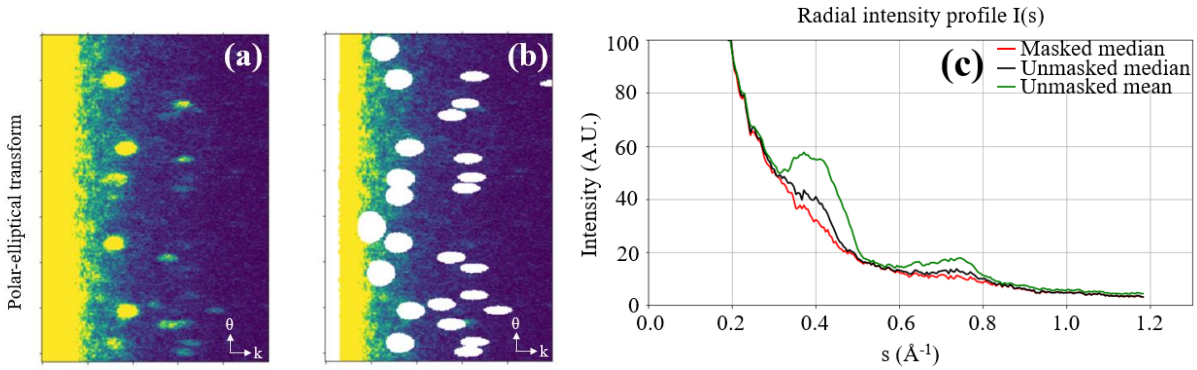

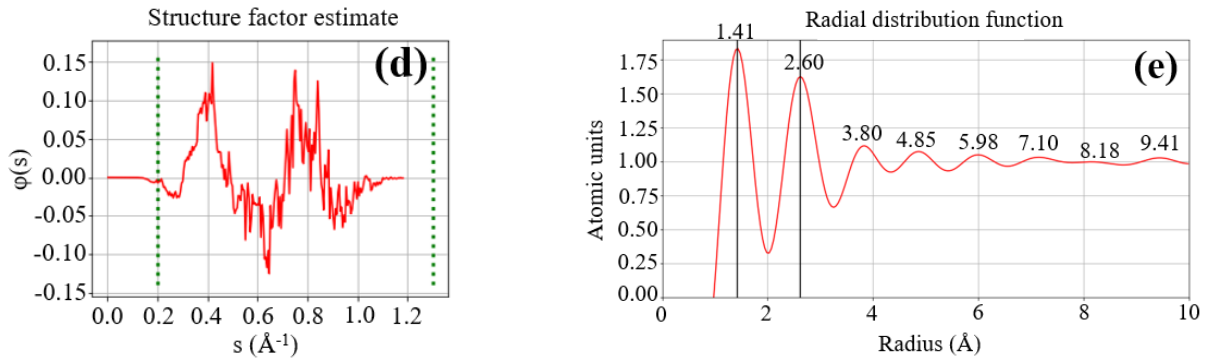

Fig. 7. 4. The radial distribution function of the SiOC sample. (a) A calculated radial integral via a polar-elliptical method, without a mask, (b) A calculated radial integral via the polar-elliptical method, with mask, (c) The radial intensity profile calculated from (a) and (b), (d) The estimated structure factor, and (e) The radial distribution function calculated from (d).

The RDF profile in Fig. 7.4(e) shows the overall features ranging from 1.41 to 9.42 Å. It is well-known that the network of the SiOC ceramic is made up of Si-C and Si-O bonds based on tetrahedral SiO_xC_{4-x} units (X = 0 - 4) [6], and the latter atomic pair being dominant [28]. The smallest feature located at 1.41 Å corresponds to the C-C bonds from the turbostratic carbon, which forms during the polymer-to-ceramic transformation process [29]. The main characteristic bond distances at 2.60 and 3.80 Å are attributed to the first nearest neighbor Si-Si and Si-O pair distances [30]. At radial distance over 5 Å, the RDF curve gradually becomes smoother, which means no apparent long-range order exists in the SiOC samples. The findings confirm the structural information of the SiO_xC_{4-x} units in the SiOC through the 4D-STEM-RDF method.

6.4.3. Crystallinity mapping in SiOC

Crystallinity mapping can be determined for the SiOC matrix, which should provide more information about the local structural information. Nanocrystalline SiC embedded in the SiOC amorphous matrix results in local crystallinity variations [31]. Compared to other characterization techniques (nuclear magnetic resonance imaging, XRD, neutron diffraction), the 4D-STEM technique [13] provides a map of crystalline phase distribution within an area. SiOC is highly suited for the nanoscale crystallinity mapping due to the low sensitivity to high electron dose bombardment. Even for radiation-sensitive materials, the small convergence angle and adjustable step size between adjacent measurements make 4D-STEM desirable. In 4D-STEM, the structures,

symmetries, and spacings of Bragg disks in the resulting four-dimensional data hypercube can be used to extract spatially resolved maps of crystalline phases [21]. Redundant information in overlapping Bragg disks can be leveraged to deconvolute the electron beam shape from the SiOC structure.

Based on the original STEM image, the radial intensity profile of the dataset in Fig. 7.4(c) indicates the partial orientation of the crystals in the SiOC matrix. In general, the mean statistics in Fig. 7.4(c) are superior and much more robust for evaluating the crystalline structure. For the crystallinity mapping, the degree of crystallinity in Fig. 7.5 carries local structural information, which can be used to characterize the structure of individual phases. Three main selected areas are shown in Fig. 7.5, and the Bragg disk features from each pixel position indicate the specific phases. The powered TEM sample prepared from solution method is relative thick and resulted in multi-layered phases. It can be seen that sp^2-bonded carbon sites (cyan) are around 10 nm upon heat treatment at 1400 °C, and they are more likely to form in the carbon-rich SiC_xO_{4-x} units (yellow) than the oxygen-rich SiC_xO_{4-x} units (green), and carbon can form between SiO_2 and SiC with high possibilities. The absence of porosity in the bulk reveals that the free carbon phase is pretty stable in this dispersion (TEM analysis), which explains the extraordinary viscoelastic properties of SiOC materials due to the interpenetrating network surrounding the silica and graphitic planes [32]. It allows to speculate that the presence of formed carbon sites behave as a diffusion barrier and thus limit the growth of the SiC and SiO_2 clusters. Also, the formation of carbon encapsulating the SiO_2 domains and connecting SiC domains resulted in a unique stable system with good thermal stability. The turbostratic carbon generates an extended region with SiC bonding at their edges and SiO_2 domains. This example highlights the importance of inspection of the diffraction images and robust statistical methods such as medians to pursue the studies of the degree of crystallinity in SiOCs.

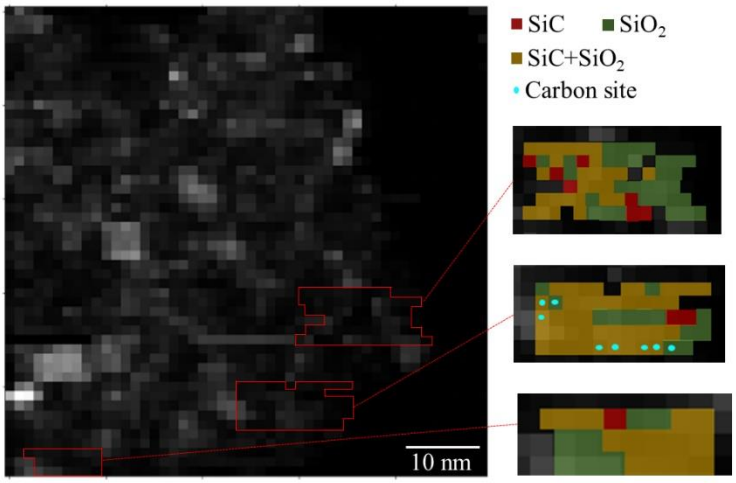

Fig. 7.5. Crystallinity mapping of predominantly SiOC pyrolyzed at 1400 °C with the presence of specific phase (red-SiC, green-SiO_2, cyan-graphite, and yellow-SiC plus SiO_2).

Polymer-derived SiOC ceramics are made up of crystalline and amorphous phases, and the corresponding structural inhomogeneity can be accessed by individual diffraction patterns in 4D-STEM mode with high-speed cameras and high-efficiency pixelated detectors. 4D-STEM-RDF enables a precise and reliable interpretation of a structure characterization for amorphous plus crystalline ceramics. However, disadvantage of the 4D-STEM mode with semi-convergence angle of 0.8 millirads is about the spatial resolution, which is limited to nm to a few angstroms, although high spatial resolution is not significantly necessary for amorphous materials. Also, because of the thick nature with irregular shape of our SiOC samples, locating the diffraction disk becomes hard and the measurement precision get affected.

7.5. Conclusion

This pioneering study focuses on an advanced 4D-STEM method for the mixed amorphous and crystalline phase analysis in SiOC. 4D-STEM data preprocessing, including calibration, Bragg disk position identification, polar-elliptical coordinate transformation, and diffraction pattern classification are carried out on a python-based py4DSTEM package. The local structure information of SiOC is presented in the RDF plot to illustrate the bonding topology of the SiOC network. The full 2D diffraction patterns at each pixel position can be extracted from the 4D-STEM dataset. This paper provides the key approaches for few nanometer phase region

quantification and should find widespread deployment for highly complex amorphous and crystalline mixed-phase analysis.

7.6. References

1. Mu, X., et al. *Radial distribution function imaging by STEM diffraction: a method development in resolving the mysteries of amorphous materials*. in *European Microscopy Congress 2016: Proceedings*. 2016. Wiley Online Library.
2. Widgeon, S.J., et al., *29Si and 13C Solid-State NMR Spectroscopic Study of Nanometer-Scale Structure and Mass Fractal Characteristics of Amorphous Polymer Derived Silicon Oxycarbide Ceramics.* Chemistry of Materials, 2010. **22**(23): p. 6221-6228.
3. Lu, K. and J. Li, *Fundamental understanding of water vapor effect on SiOC evolution during pyrolysis.* Journal of the European Ceramic Society, 2016. **36**(3): p. 411-422.
4. Erb, D. and K. Lu, *Additive and pyrolysis atmosphere effects on polysiloxane-derived porous SiOC ceramics.* Journal of the European Ceramic Society, 2017. **37**(15): p. 4547-4557.
5. Erb, D. and K. Lu, *Effects of SiO2-forming additive on polysiloxane derived SiOC ceramics.* Microporous and Mesoporous Materials, 2018. **266**: p. 75-82.
6. Yang, N., et al., *Nickel-containing magnetoceramics from water vapor assisted pyrolysis of polysiloxane and nickel 2, 4-pentanedionate.* Journal of the American Ceramic Society, 2020.
7. Yang, N. and K. Lu, *Thermophysical property and electrical conductivity of titanium isopropoxide–polysiloxane derived ceramics.* Journal of the European Ceramic Society, 2019. **39**(14): p. 4029-4037.
8. Lu, K., et al., *Comparison of traditional and flash pyrolysis of different carbon content silicon oxycarbides.* Journal of the European Ceramic Society, 2019. **39**(10): p. 3035-3041.
9. Saha, A., R. Raj, and D.L. Williamson, *A model for the nanodomains in polymer-derived SiCO.* Journal of the American Ceramic Society, 2006. **89**(7): p. 2188-2195.
10. Dixmier, J., et al., *Neutron diffraction study of the amorphous phase structure in silicon carbonitride ceramics obtained by pyrolysis of a polyvinylsilazane.* Journal of the European Ceramic Society, 1994. **13**(4): p. 293-298.

11. Mu, X., et al., *Mapping structure and morphology of amorphous organic thin films by 4D-STEM pair distribution function analysis.* Microscopy, 2019. **68**(4): p. 301-309.
12. Ophus, C., et al., *Recording and using 4D-STEM datasets in materials science.* Microscopy and Microanalysis, 2014. **20**(S3): p. 62-63.
13. Ophus, C., *Four-dimensional scanning transmission electron microscopy (4D-STEM): from scanning nanodiffraction to ptychography and beyond.* Microscopy and Microanalysis, 2019. **25**(3): p. 563-582.
14. Shukla, A.K., et al., *Study of structure of Li-and Mn-rich transition metal oxides using 4D-STEM.* Microscopy and Microanalysis, 2016. **22**(S3): p. 494-495.
15. Fang, S., et al., *Atomic electrostatic maps of 1D channels in 2D semiconductors using 4D scanning transmission electron microscopy.* Nature communications, 2019. **10**(1): p. 1-9.
16. Mu, X., et al., *4D-STEM Pair Distribution Function Mapping of the Morphology and Structure of Amorphous Organic Materials.* Microscopy and Microanalysis, 2019. **25**(S2): p. 1944-1945.
17. Mu, X., et al., *Evolution of order in amorphous-to-crystalline phase transformation of MgF2.* Journal of Applied Crystallography, 2013. **46**(4): p. 1105-1116.
18. Caplins, B.W., et al., *Orientation mapping of graphene using 4D STEM-in-SEM.* Ultramicroscopy, 2020: p. 113137.
19. Zeltmann, S.E., et al., *Patterned probes for high precision 4D-STEM bragg measurements.* Ultramicroscopy, 2020. **209**: p. 112890.
20. Mu, X., et al., *Radial distribution function imaging by STEM diffraction: Phase mapping and analysis of heterogeneous nanostructured glasses.* Ultramicroscopy, 2016. **168**: p. 1-6.
21. Savitzky, B.H., et al., *py4DSTEM: a software package for multimodal analysis of four-dimensional scanning transmission electron microscopy datasets.* arXiv preprint arXiv:2003.09523, 2020.
22. McAuliffe, T., et al., *4D-STEM elastic stress state characterisation of a TWIP steel nanotwin.* arXiv preprint arXiv:2004.03982, 2020.
23. Wan, W., et al., *Three-dimensional rotation electron diffraction: software RED for automated data collection and data processing.* Journal of applied crystallography, 2013. **46**(6): p. 1863-1873.

24. Craven, A. and T. Buggy, *Design considerations and performance of an analytical STEM.* Ultramicroscopy, 1981. **7**(1): p. 27-37.
25. Yang, N. and K. Lu, *Porous and ultrahigh surface area SiOC ceramics based on perhydropolysilazane and polysiloxane.* Microporous and Mesoporous Materials, 2020. **306**: p. 110477.
26. Yang, N. and K. Lu, *Effects of transition metals on the evolution of polymer-derived SiOC ceramics.* Carbon, 2021. **171**: p. 88-95.
27. Yang, N., et al., *Nickel-containing magnetoceramics from water vapor-assisted pyrolysis of polysiloxane and nickel 2, 4-pentanedionate.* Journal of the American Ceramic Society, 2020. **103**(1): p. 145-157.
28. Brequel, H., et al. *Radial distribution function of amorphous silicon oxycarbide compounds*. in *Journal of Metastable and Nanocrystalline Materials*. 2000. Trans Tech Publ.
29. Wen, Q., Z. Yu, and R. Riedel, *The fate and role of in situ formed carbon in polymer-derived ceramics.* Progress in Materials Science, 2020. **109**: p. 100623.
30. Su, Q., et al., *Helium Irradiation and Implantation Effects on the Structure of Amorphous Silicon Oxycarbide.* Scientific Reports, 2017. **7**(1): p. 3900.
31. Panova, O., et al., *Orientation mapping of semicrystalline polymers using scanning electron nanobeam diffraction.* Micron, 2016. **88**: p. 30-36.
32. Kleebe, H.-J. and Y.D. Blum, *SiOC ceramic with high excess free carbon.* Journal of the European Ceramic Society, 2008. **28**(5): p. 1037-1042.

Chapter 8

Summary and future work

8.1. Summary of the findings

This work deals with the processing-structure-property relationship of polysiloxane-derived SiOC and transition metals (Ni, Co, Mo, Zr, or Fe) added SiOC composites. The final compositions and structures of SiOC-based composites can be controlled by modifying and designing the preceramic polymers on the molecular level, as well as the pyrolysis condition. The followings are the main conclusions from the current work:

- The short and medium-range order and disorder of the SiOC system were revealed by unique and advanced 4D-STEM/RDF analysis, using a python-based py4DSTEM toolkit. The full 2D diffraction patterns at each pixel position from SiOC ceramic were collected in a STEM mode. The RDF profile shows the overall features range from 1.41 to 9.42 Å. More specifically, The smallest feature located at 1.41 Å was corresponding to the C-C bonds due to the turbostratic carbon. The main characteristic bond distances at 2.60 and 3.80 Å are attributed to the first nearest neighbor Si-Si and Si-O pair distances. The radial distance over 5 Å gradually becomes smoother and no apparent long-range distance was founding in our SiOC samples.

- The silica nano-size distribution in the SiOC matrix can be adjusted by pyrolysis atmosphere, temperature, and silica-forming fillers (perhydropolysilazane). Selectively etching of silica nanodomains resulted in SiOC ceramic with a high surface area. For SiOC ceramics pyrolyzed on perhydropolysilazane and polysiloxane, the silica nanodomains could be formed with an average pore size of ~ 2 nm, resulting in the specific surface area was up to $\sim 2000\ m^2/g$. 3D view of silica domain distributions further explained that the merging effect of the nanopores is predominant in decreasing the specific surface area. Small and separated silica nanoclusters with thin domain walls are the most important part to generate ultrahigh surface area.

- The effect of transition metals on the phase and microstructure evolution of the SiOC system was assessed through advanced microstructural characterizations.

Transition metals promote the formation of corresponding metal silicides, β-SiC, and graphite, and their catalytic activity is Fe>Co>Ni, which is in good agreement with the activation energy calculation based on the type and amount of carbon. The unique quantitative analysis method of XPS results shows that in SiOC ceramics with the addition of Ni, Co, or Fe, the phase separation of the SiOC matrix is more predominant than the local carbothermal reduction between silica and C.

- The phase prediction in transition metals added SiOC can be achieved using a Gibbs free energy minimization method. Four various phase calculation pathways (SiC-SiO_2-C-Ni, SiC-SiO_2-C-MoC_x, SiC-SiO_2-C-$CoSi_x$, and SiC-SiO_2-C-ZrO_x) have been built in this work. The results showed that the computed driving forces for crystallization prove that the addition of M content enhances crystallization tendency.

- Novel functional Ni-containing SiOC composites showed the soft ferromagnetic property with small values of coercivity, and the overall shape of the loop varied on the pyrolysis temperatures resulting in different contents of Ni phase. The presence of Ni enhanced the graphitization of free carbon via the diffusion-precipitation mechanism. The formation of nickel silicide was successfully avoided by the effect of water vapor in the atmosphere to avoid the reaction between SiC and Ni phases.

- The thermophysical property and electrical conductivity of Ti added SiOC were conducted on TGA and four-point probe configuration. Detailed phase composition showed that the addition of Titanium (IV) isopropoxide induced the enriched formation of TiC content. The TGA curves illustrated the TiC/SiOC composite was quite stable up to 1000 °C in an oxidizing air atmosphere with less than 0.20 wt% mass loss. Meanwhile, the existence of TiC resulted in excellent electrical conductivity that the maximum conductivity is 1176.55 S/m at 950 °C in Argon. As far as we know, this is the first paper to report that the conductivity of Si-O-C composites exceeds 1000 S/m.

8.2. Future work

Future work of this study is to be concentrated on two parts: (a) Deep understanding of nanostructure evolution in SiOC ceramics pyrolyzed at 900, 1200, and 1500 °C, through 4D-STEM technique; (b) Atomistic inquiry of SiOC structural evolution via synchrotron X-ray studies. More details about future work are depicted as follows:

- The structure of amorphous and metastable SiOC phases has not been fully studied due to the lack of advanced characterization till now. Deeply illustration the phase distribution, phase amounts, and phase evolution in SiOC materials pyrolyzed at different temperatures (900, 1200, and 1500 °C) will be investigated by the 4D-STEM technique. Through our new method, the phase distribution of amorphous or partially crystalline ceramic materials at the nanometer level will be investigated and the local atomic structure of each phase will be analyzed. These novel results, taken together, will lead to shedding light on a milestone in polymer-derived ceramics.
- A set of cutting-edge techniques, small-angle X-ray scattering (SAXS) and high-energy X-ray diffraction (HE-XRD) are to explore the nanometer-scale structure and characteristics of amorphous SiOC ceramics as a function of carbon content. Large-scale MD calculations can be conducted to simulate and investigate amorphous structures of SiOC with different carbon content. The original structures can be obtained by a cooling down method. The melt-quench technique will be used to generate the structures of SiOC from SiO2 and C phases, based on the reactive force field (ReaxFF) potential.

Original research contributions

The mixing amorphous and crystalline nature of SiOC-based ceramics raises questions related to the phase evolution in nanoscale, as well as the corresponding functionalities after the addition of transition metals. Thus, the core research particularly addresses various aspects of fundamental understanding and functionalities of SiOC-based ceramics. Following research objectives are investigated in this dissertation:

Research objective 1: To illustrate the phase evolution of pure SiOC and transition metal/SiOC composites at different pyrolysis temperatures.

Research objective 2: To calculate the phase content of transition metal/SiOC composites at different pyrolysis temperatures.

Research objective 3: To achieve superior functional performances of pure SiOC and transition metal/SiOC composites by controlling the microstructures at different pyrolysis temperatures.

The first research objective-study of single nanometer and co-Existing amorphous and crystalline SiOC was solved by using the advanced 4D-STEM technique. 4D-STEM combined RDF mapping to characterize heterogeneous nanostructured amorphous and crystalline SiOC. RDF analysis from diffraction patterns with 4D-STEM from nano volume as a critical starting point in the characterization of amorphous SiOC materials. The information related to the short- and medium-range order of the different glass phases, as well as the cluster structure, can be depicted from RDF files. To illustrate the potential of this approach, we applied this new method to investigate the effect of carbon content on the amorphous structure of the SiOCs matrix, which demonstrates that the method is extremely powerful that never reported in the field of PDCs. Our method shows a great potential to understand nanoscale structural variations in SiOC materials and shed light on deeper investigations on the structure and properties of SiOCs with the advances of technology.

As for the second objective, it is concentrating on the phase content prediction in polymer-derived SiOC ceramics with metal additives. Quantifying the phases in SiOC materials is always a task of great challenge. Small amounts and low signal-to-noise ratio from ^{29}Si nuclear magnetic resonance (MAS-NMR) spectroscopy result in difficulties for separating the relaxation behaviors of $SiOC_3$ and SiC_4. Our work introduced a thermodynamic method to calculate the phase contents

in the SiOC/metal system based on Gibbs free energy minimization. Driving force for crystallization has been analyzed using a Gibbs free energy minimization method and phase fractions of these different PDC systems are calculated based on the lever rule. Also, our solution reveals the energetics related to the quaternary systems and guides synthesizing metal-containing PDCs with desired phase contents.

The last objective can be explicitly divided into three aspects: (1) ultrahigh surface area SiOC material, (2) nickel-containing SiOC magnetceramic, and (3) conductive and thermal resistant SiOC ceramic. Our works focus on (1) the formation of porous SiOC is studied based on perhydropolysilazane (PHPS) and polysiloxane (PSO) precursors. The PHPS can be chemically anchored to the PSO by hydrosilylation reaction, due to the extensive Si–H bonds from the PHPS. The presence of water vapor during pyrolysis not only accelerates the hydrolysis of the PHPS additive but also facilitates the Si–O–Si bond formation within the SiOC. Si–O–Si formation can be selectively etched away to create nano-sized pores and ultrahigh surface area in SiOC materials; (2) novel ferromagnetic Ni‐containing SiOC can be successfully fabricated from a base preceramic polymer with the addition of nickel 2,4‐pentanedionate. The formation of nickel silicides can be completely suppressed by the effect of water vapor during the pyrolysis. The resultant SiOC–Ni nanocomposite consists of in situ formed Ni nanocrystallites with a small amount of NiO uniformly dispersed in the amorphous SiOC matrix, and the corresponding nanocrystallite size increases with the increase of the pyrolysis temperature; (3) high-temperature resistant Si-O-C-Ti can be successfully prepared based on the pyrolysis of preceramic polymer and titanium (IV) isopropoxide at 1200–1400 °C. PSO can homogeneously mix with titanium (IV) isopropoxide to enhance its conversion to TiC. The carbothermal reactions between TiO_2 and carbon result in the formation of high-temperature TiC.

The current Ph.D. thesis reveals new strategies in increasing high-temperature phase amounts, the energetics related to the quaternary systems, new semiconducting behavior with soft ferromagnetism, and novel data for the fundamental understanding of the SiOC formation and nanostructure evolution. It provides guidance to synthesizing metal-containing PDCs with desired phase contents and creating novel materials for heterogeneous catalysis, magnetic, and other applications.

List of scientific communications

Journal articles (published)

1. **Ni Yang**, and Kathy Lu. "*Effects of transition metals on the evolution of polymer-derived SiOC ceramics*." Carbon 171 (2021): 88-95.

2. **Ni Yang**, and Kathy Lu. "*Porous and ultrahigh surface area SiOC ceramics based on perhydropolysilazane and polysiloxane*." Microporous and Mesoporous Materials 306 (2020): 110477.

3. **Ni Yang**, Kathy Lu, Wenbo Wang, and Wenjun Cai. "*Corrosion and tribocorrosion mitigation of perhydropolysilazane-derived coatings on low carbon steel*." Corrosion Science 177 (2020): 108946.

4. **Ni Yang**, Min Gao, Li Jiefang, and Kathy Lu. "*Nickel-containing magnetoceramics from water vapor-assisted pyrolysis of polysiloxane and nickel 2, 4-pentanedionate*." Journal of the American Ceramic Society 103.1 (2020): 145-157.

5. **Ni Yang**, and Kathy Lu. "*Thermophysical property and electrical conductivity of titanium isopropoxide–polysiloxane derived ceramics*." Journal of the European Ceramic Society 39.14 (2019): 4029-4037.

6. Lingchen Kong, Advaith Rau, **Ni Yang**, Kathy Lu. *"ZnO Nanoparticle-Poly(methyl methacrylate) Hybrids as Flexible Ultraviolet Shielding Films"*. JOM (2020): 1-9.

7. Kathy Lu, Donald Erb, Kaustubh Bawane, and **Ni Yang**. "*Comparison of traditional and flash pyrolysis of different carbon content silicon oxycarbides*." Journal of the European Ceramic Society 39.10 (2019): 3035-3041.

Journal articles (submitted)

8. **Ni Yang**, and Kathy Lu. *"Phase Content Prediction in Multi-element Polymer-derived Ceramics",* Composites Part B (submitted), 2020.

9. **Ni Yang**, Colin Ophus, Benjamin H. Savitzky, Mary Scott, Karen Bustillo, and Kathy Lu. *"Study of Single Nanometer and Co-Existing Amorphous and Crystalline SiOC Microstructures using 4D-STEM"*, Materials Today (submitted), 2020.

Journal articles (proceeding)

10. **Ni Yang**, Benjamin H Savitzky, Colin Ophus, and Kathy Lu. *"Study of structure of polymer-derived ceramics using 4D-STEM"*, (collaborating & proceeding with Berkeley Lab), 2020.

11. **Ni Yang**, Jan Ilavsky, and Kathy Lu. *"Atomistic Inquiry of SiOC Structural Evolution via Synchrotron X-ray Studies"*, (collaborating & proceeding with Argonne Laboratory), 2020.

Conferences

1. Kathy Lu and **Ni Yang**, *Porous SiOC bulk ceramic based on perhydropolysilazane (PHPS) and polysiloxane (PSO) pyrolysis*, 44th International Conference and Expo on Advanced Ceramics and Composites, Daytona Beach, FL, Jan. 2020.

2. Kathy Lu, **Ni Yang**, and Donald Erb, *Polymer Derived Functional High Temperature Materials*, 44th International Conference and Expo on Advanced Ceramics and Composites, Daytona Beach, FL, Jan. 2020.

3. Kathy Lu, **Ni Yang**, Kaustubh Bawane, Quan Li, and Rajendra Bordia, *Polymer Derived Silicon Oxynitride (SiON) Coatings for Corrosion Protection of Steels*, 44th International Conference and Expo on Advanced Ceramics and Composites, Daytona Beach, FL, Jan. 2020.

4. Kathy Lu, **Ni Yang**, *Polymer Derived High Temperature Ti-SiOC*, Materials Science & Technology (MS&T 2019), Portland, Oregon, Sep. 2019.

5. Kathy Lu, **Ni Yang**, *Nickel-SiOC Magnetoceramics from Water Assisted Pyrolysis of Polymers*, Materials Science & Technology (MS&T 2019), Portland, Oregon, Sep. 2019.